Transactions of the ASME

The Journal of Fluids Engineering (ISSN 0098-2202) is published quarterly for $100 per year by The American Society of Mechanical Engineers, 345 East 47th Street, New York, NY 10017. Second class postage paid at New York, NY and additional mailing offices. POSTMASTER: Send address changes to The Journal of Fluids Engineering, c/o THE AMERICAN SOCIETY OF MECHANICAL ENGINEERS, 22 Law Drive, Box 2300, Fairfield, NJ 07007-2300.
CHANGES OF ADDRESS must be received at Society headquarters seven weeks before they are to be effective. Please send old label and new address.
PRICES: To members, $24.00, annually; to nonmembers, $100. Add $6.00 for postage to countries outside the United States and Canada.
STATEMENT from By-Laws. The Society shall not be responsible for statements or opinions advanced in papers or . . . printed in its publications (B7.1, Par. 3).

INDEXED by Engineering Information

Journal of Fluids Engineering

Published Quarterly by The American Society of Mechanical Engineers
VOLUME 108 • NUMBER 1 • MARCH 1986

(Contents continued on page 2)

Contents (continued)

Journal of Fluids Engineering

Editorial

Editorial Policy Statement on the Control of Numerical Accuracy

A professional problem exists in the computational fluid dynamics community and also in the broader area of computational physics. Namely, there is a need for higher standards on the control of numerical accuracy.

The numerical fluid dynamics community is aware of this problem but, although individual researchers strive to control accuracy, the issue has not to our knowledge been addressed collectively and formally by any professional society of journal editorial board. The problem is certainly not unique to the JFE and came into even sharper focus at the 1980-81 AFOSRHTTM-Stanford Conference on Complex Turbulent Flows. It was a conclusion of that conference's Evaluation Committee[1] that, in most of the submissions to that conference, it was impossible to evaluate and compare the accuracy of different turbulence models, since one could not distinguish physical modeling eerors from numerical errors related to the algorithm and grid. This is especially the case for first-order accurate methods and hybrid methods.

The practice of publishing comparisons based on coarse grid solutions, without systematic truncation error testing, may have been acceptable in the past. Certainly ten to fifteen years ago any calculation was of interest, and much of the exploratory work deserved publication, as many researchers lacked the computational power or funds to do a thorough and systematic error estimation. We are of the opinion that this practice, however understandable in the past, is outmoded and that, with powerful computers becoming more common, standards should be raised. Consequently, this journal hereby announces the following policy:

> *The Journal of Fluids Engineering will not accept for publication any paper reporting the numerical solution of a fluids engineering problem that fails to address the task of systematic truncation error testing and accuracy estimation.*

Although the formal announcement of this journal policy is new, it has been the practice of many of our conscientious reviewers. Thus the present announcement is not a change in policy so much as a clarification and standardization.

Methods are available to accomplish this task, such as Richardson extrapolation (when applicable), calculations with a high- and low-order method on the same grid, and straightforward repeat calculations with finer or coarser grids. As in the case of experimental uncertainty analysis, ". . . any appropriate analysis is far better than none as long as the procedure is explained."[2] Whatever the authors use will be considered in the review process, but we must make it clear that *a single calculation in a fixed grid will not be acceptable*, since it is impossible to infer an accuracy estimate from such a calculation. Also, the editors will not consider a reasonable agreement with experimental data to be sufficient proof of accuracy, especially if any adjustable parameters are involved, as in turbulence modeling.

We recognize that it can be costly to do a thorough study, and that many practical engineering calculations will continue to be performed on a single fixed grid. However, this practice is insufficient for publication in an archival journal.

[1] Emmons, H. W. (Chairman), "Evaluation Committee Report," pp. 979–986 in *Proc. 1980–81 AFOSR-HTTM-Stanford Conference on Complex Turbulent Flows*, Vol. II, "Taxonomies, Reporter's Summaries, Evaluation, and Conclusions," Thermosciences Division, Mechanical Engineering Department, Stanford University.

[2] Kline, S. J ., "The Purposes of Uncertainty Analysis," ASME JOURNAL OF FLUIDS ENGINEERING, Vol. 107, June 1985, pp. 153–164.

Patrick J. Roache
Kirti N. Ghia
Frank M. White
JFE Editorial Board

Shou-Rue Chen
Shanghai Power Company,
Shanghai, PRC

Samuel S. Lee

Yuan Mao Huang

Department of Mechanical Engineering,
University of Miami,
Coral Gables, FL 33124

A Mathematical Model for the Analysis of Fluid Flow in a Scroll

A three-dimensional mathematical model has been developed to simulate the flow condition in a scroll. Coordinate transformations are used as an effective tool to make the model universal, and the final governing equations are solved by the finite difference method. Three cases of scroll geometry have been investigated and the results are compared with one another to show the effects of scroll geometry on the flow condition at the outlet of the scroll.

1 Introduction

A scroll is used to either distribute fluid to or collect fluid from a rotor. Past work has focused on the design of the rotor, while the impact of the scroll configuration of the efficiency of a turbo-machine was often neglected. Recent research works have shown the importance of scroll design techniques in further improvement of the turbine machinery performance.

The main objective for designing a scroll is to provide a uniform distribution of flow parameters along the circumference at the outlet of the scroll so that the blades of the rotor or the vanes of the stator do not experience fluctuating forces. Reduction or elimination of such forces would significantly increase fatigue life.

Until recent years analytical solutions of the flow field in a turbine scroll were limited to one or two dimensional flow assumptions. Bhinder [1] provided a design procedure for a nozzleless volute casing of a radial inward-flow gas turbine. The procedure was based on the assumptions of one dimensional and isentropic flow. Chapple, Flynn, and Mulloy [2] developed a method for the design of a special series of nozzleless turbine casings. The method was based on the analysis of a flow pattern with combined a free vortex flow with a sink at the center of the scroll. It was essentially a two dimensional flow. Hamed, Baskharone, and Tabakoff [3] analyzed the flow behavior in the combined scroll-nozzle assembly of a radial inflow turbine, and they investigated the combined effects of the scroll and nozzle van geometry on the flow field based on the assumptions of two dimensional incompressible inviscid flow. The finite element method was used to obtain the numerical solutions. Their results showed that the geometry of the scroll, rather than that of the nozzle vanes, caused deviations in the amount of mass flow between different nozzle channels. For a better understanding of the three dimensional flow behavior in the scroll, Hamed, Abdallah and Tabakoff [4] investigated the two dimensional flow field on scroll cross sectional planes which were associated with various through-flow velocity profiles. Although these two investigations provided some insight about the features of the flow in a scroll, they did not provide solution for a real three dimensional flow. A true three dimensional analysis is needed since the through-flow velocity profile depends on both the cross-sectional configuration of the scroll and its location along the circumference. The complexity of the three dimensional flow field in a scroll is evidenced by an experimental study conducted by Tabakoff, Sheoran, and Kroll [5]. Hot film anenometer technique was used to measure the flow velocities in a scroll. Some work has been devoted to the theoretical study of three dimensional effects. Hamed and Baskhorone [6] conducted a study to analyze the actual three dimensional compressible inviscid flow in a scroll and the vaneless nozzle. The effects of symmetric and nonsymmetric scroll cross sectional geometries on the general flow field and the scroll exit flow condition were investigated by using the finite element method. While the finite element method has an advantage in its ability to handle irregular boundary geometry, it is more difficult for practicing designers to use because an individual grid system must be setup and analyzed for each scroll.

A universal model applicable to a wide variety of scroll configurations would be more powerful and more useful to practicing design engineers. The finite difference method can serve as a more suitable tool for this purpose. The difficulty of dealing with irregular boundary geometry can be overcome by an appropriate transformation of coordinate system. A thoughtfully prepared approach is introduced in this paper.

II Governing Equation and Its Transformation

For a steady incompressible irrotational flow, the governing equation is given by the Laplace equation:

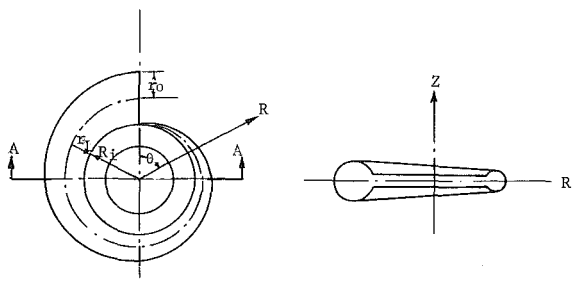

Fig. 1 A scroll shown in (R, θ, Z) cylindrical coordinates

Contributed by the Fluids Engineering Division for publication in the JOURNAL OF FLUIDS ENGINEERING. Manuscript received by the Fluids Engineering Division March 26, 1984.

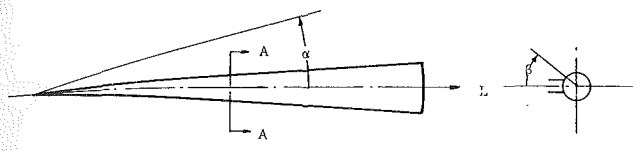

Fig. 2 A transformed straight cone shown in (L, α, β) spherical coordinates

$$\nabla^2\phi = 0 \tag{1}$$

where ϕ is the velocity potential.

Cylindrical coordinates (R, θ, Z) bound with a scroll as shown in Fig. 1 can be transformed into spherical coordinates (L, α, β) as defined in Fig. 2. The transformed spherical coordinates may be expressed in terms of the original cylindrical coordinates as follows:

$$L = L(\theta),$$

$$\alpha = \frac{\sqrt{Z^2 + (R_i + r_L(\theta) - R)^2}}{L(\theta)}, \text{ and}$$

$$\beta = \tan^{-1}\frac{Z}{R_i + r_L(\theta) - R}. \tag{2}$$

where R_i is the inner radius of a scroll and r_L is the radius of the scroll cross sections.

By using this new spherical coordinate system the scroll is unrolled or converted into a straight cone as shown in Fig. 2 and equation (1) can be transformed into the following form in the new spherical coordinates:

$$\left(\frac{L'(\theta)}{R}\right)^2 \frac{\partial^2\phi}{\partial L^2} + \left(\frac{1}{L^2} + \left(\frac{r_L'(\theta)\mathrm{Cos}\beta - L'(\theta)\alpha}{RL}\right)^2\right)\frac{\partial^2\phi}{\partial\alpha^2}$$
$$+ \left(\frac{1}{L^2\alpha^2} + \left(\frac{r_L'(\theta)\mathrm{Sin}\beta}{RL\alpha}\right)^2\right)\frac{\partial^2\phi}{\partial\beta^2}$$
$$+ \frac{2L'(\theta)(r_L'(\theta)\mathrm{Cos}\beta - L'(\theta)\alpha)}{R^2L}\frac{\partial^2\phi}{\partial L\partial\alpha}$$
$$+ \frac{2L'(\theta)(-r_L'(\theta)\mathrm{Sin}\beta)}{R^2L\alpha}\frac{\partial^2\phi}{\partial L\partial\beta}$$
$$+ \frac{2(r_L'(\theta)\mathrm{Cos}\beta - L'(\theta)\alpha)(-r_L'(\theta)\mathrm{Sin}\beta)}{R^2L^2\alpha}\frac{\partial^2\phi}{\partial\alpha\partial\beta} + \frac{L''(\theta)}{R^2}\frac{\partial\phi}{\partial L}$$
$$+ \left(\frac{1}{L^2\alpha} - \frac{\mathrm{Cos}\beta}{RL} + \frac{L\alpha(r_L''(\theta)\mathrm{Cos}\beta - L''(\theta)\alpha)}{R^2L^2\alpha}\right.$$
$$\left. - \frac{2\alpha L'(\theta)(r_L'(\theta)\mathrm{Cos}\beta - L'(\theta)\alpha) + r_L'(\theta)\mathrm{Sin}^2\beta}{R^2L^2\alpha}\right)\frac{\partial\phi}{\partial\alpha}$$
$$+ \frac{\mathrm{Sin}\beta}{RL\alpha} + \frac{-L\alpha r_L'(\theta)\mathrm{Sin}\beta + 2r_L'^2(\theta)\mathrm{Sin}\beta\mathrm{Cos}\beta}{R^2L^2\alpha^2}\frac{\partial\phi}{\partial\beta} = 0 \tag{3}$$

where $R = R_i + r_L(\theta) - L\alpha\mathrm{Cos}\beta$.

L' and r_L' are the first derivatives of L and r_L with respect to θ. L'' and r_L' are the second derivatives of L and r_L with respect to θ. By using A, B, C, E, F, G, U, W to stand for the coefficients in the above equation, equation (3) may be written in the following form:

$$A\frac{\partial^2\phi}{\partial L^2} + B\frac{\partial^2\phi}{\partial\alpha^2} + C\frac{\partial^2\phi}{\partial\beta^2} + E\frac{\partial^2\phi}{\partial L\partial\alpha} + F\frac{\partial^2\phi}{\partial L\partial\beta} + G\frac{\partial^2\phi}{\partial\alpha\partial\beta}$$
$$+ U\frac{\partial\phi}{\partial L} + V\frac{\partial\phi}{\partial\alpha} + W\frac{\partial\phi}{\partial\beta} = 0 \tag{4}$$

which is an elliptic equation. This governing equation is general in the sense that it can be used for any scroll with an arbitrary relation between r_L and θ.

In general, the cone which is unrolled-directly from the scroll along the centerline is not necessarily a straight cone because the arbitrary relation between L and θ must be set up properly. With the proper selection of the $L-\theta$ relationship the configuration after the transformation can always be converted into a straight cone. The general relation between L and θ may be derived as

$$L = \frac{r_L(\theta)}{r_0}\left[2\Pi R_i + \int_0^{2\pi} r_L(\theta)d\theta\right] \tag{5}$$

where $r_L = r_L(\theta)$ is a given condition. Let R_s represent an imaginary radius of a circle for which the length of the centerline of the scroll is $L_0 = 2\Pi R_s$. Then equation (5) can be written as

$$L = \frac{r_L(\theta)}{r_0}2\Pi R_s. \tag{6}$$

It should be noted that L is only a new coordinate and not the real length of the scroll, while L_0 is the real length of the centerline of the scroll.

Three cases of commonly used scroll geometry have been investigated, and they are described below.

Case 1. The cross-sectional radius varies linearly with θ around the circumference, i.e.,

$$r_L = r_0\frac{\theta}{2\Pi} \tag{7}$$

so that the relation between L and θ is given by

Nomenclature

R, θ, z = cylindrical coordinates for a scroll
L, α, β = spherical coordinates for a cone transformed from a scroll
n = line normal to the scroll surface
T = curve on the scroll surface S_2 corresponding to the generation line of the transformed cone
ϕ = velocity potential function
γ = angle between T and radial line from the center of cross section on θ = constant plane
γ_N = angle in the new domain corresponding to γ
L_0 = length of a scroll centerline
L' = the first derivative of L respect to θ
L'' = the second derivative of L respect to θ
r_0 = radius of scroll cross sections at the inlet of the scroll
r_L = radius of scroll cross sections
r_L' = the first derivative of r_L respect to θ
r_L'' = the second derivative of r_L respect to θ
R_i = scroll inner radius measured from center of the scroll
R_s = imaginary radius for which the length of a scroll center line is $L_0 = 2\Pi R_s$
$S_1 \sim S_6$ = boundary surfaces of a scroll
V_0 = velocity at the inlet of a scroll
V_D = discharge velocity component normal to the surfaces
α_0 = one half of the conical angle

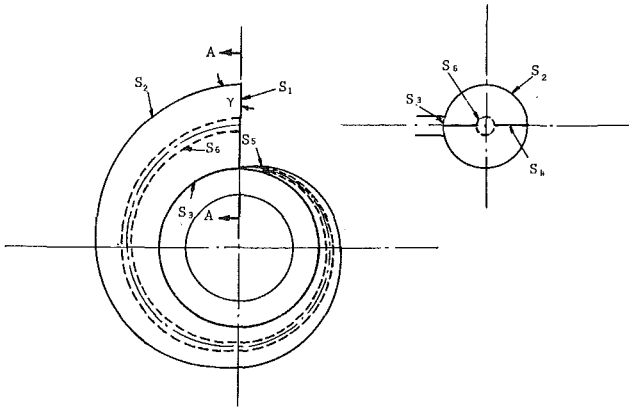

Fig. 3 Boundaries of a scroll shown in (R, θ, Z) cylindrical coordinates

$$L = R_s\theta. \tag{8}$$

Case 2. The cross-sectional area varies linearly with θ around the circumference, i.e.,

$$r_L^2 = r_0^2 \frac{\theta}{2\Pi}, \tag{9}$$

so that the relation between L and θ is given by

$$L = \sqrt{2\Pi} R_s \theta. \tag{10}$$

Case 3. The ratio of the cross-sectional area to the distance from the center of the scroll to the center-line varies with θ around the circumference, i.e.,

$$\frac{\Pi r_L{}^2}{R_i + r_L} = \frac{r_0^2}{2(R_i + r_0)}\theta. \tag{11}$$

In this case, the relation between L and θ is given by

$$L = \frac{R_s}{2(R_i + r_0)}(r_0\theta + \sqrt{r_0^2\theta^2 + 8\Pi R_i(R_i + r_0)\theta}). \tag{12}$$

If equations (7) through (12) are differentiated and then substituted into equation (3) the governing equations for these three scrolls can be obtained respectively.

If the cross section of a scroll is not circular, a further coordinate transformation for α and β is needed to convert the shape of the section from noncircular to circular. Hence, a wide range of cross section can be transformed into a circular cross section. Eventually, a straight circular cone can always be obtained. This transformation enables this approach to be applied more universally than others.

In order to increase the usability of this design tool the governing equation can be written in nondimensional form by choosing the scroll inlet flow velocity V_0 and inlet radius r_0 as the characteristic velocity and characteristic length respectively.

III Boundary Conditions

(A) In Original Coordinates. Because the governing partial differential equation is of elliptic type, all boundary conditions for the configuration are required. The solution is unique if the unknown function is described on all boundaries, or the solution is determined within an additive constant if the derivative of the function in the direction normal to the boundary is described. They are known as Dirichlet and Neumann boundary conditions respectively.

The velocity potential is an unknown variable in equation (3). The conditions which can be specified on the boundary are the normal derivatives of the function, i.e., the normal velocities on the boundary. Referring to Fig. 3, the boundary conditions of the scroll in the original domain are as follows:

1) At the inlet S_1:

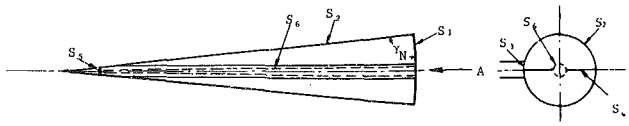

Fig. 4 Boundaries of a transformed straight cone shown in (L, α, β) spherical coordinates

$$\frac{\partial\phi}{\partial n} = \frac{1}{R}\frac{\partial\phi}{\partial\theta} = -V_0 \tag{13}$$

where V_0 is the uniform inlet velocity. The assumption of uniformity of V_0 is a simplification, since the velocity profile is uniform only at locations upstream from S_1. Since the flow considered here is a subsonic flow, any change in the flow downstream will affect that of upstream. The initially uniform velocity of V_0 at the inlet will change its value and direction after stability is achieved.

2) On the solid boundary S_2:

$$\frac{\partial\phi}{\partial n} = 0. \tag{14}$$

3) At the outlet S_3:

$$\frac{\partial\phi}{\partial n} = -\frac{\partial\phi}{\partial R}\mathrm{Cos}\beta + \frac{\partial\phi}{\partial Z}\mathrm{Sin}\beta = V_D\,\mathrm{Cos}\beta + \frac{\partial\phi}{\partial Z}\mathrm{Sin}\beta \tag{15}$$

where V_D is the discharge velocity component in the direction opposite to that of R. V_D is determined from the equation of continuity for the whole domain. The assumption of uniformity of V_D is also a simplification. The assumed uniformity will actually exist at locations downstream from S_3.

4) On the symmetric plane S_4:

$$\frac{\partial\phi}{\partial n} = -\frac{\partial\phi}{\partial Z} = 0. \tag{16}$$

For a symmetric cross section only half of the scroll needs to be analyzed, and the plane of symmetry can be considered as a solid boundary.

B) In Transformed Coordinates. The above boundary conditions should be transformed into the new spherical coordinates accordingly. Referring to Fig. 4, the boundary conditions for the new domain with new coordinates are derived as follows:

1) At the inlet S_1:

$$\frac{\partial\phi}{\partial L} \simeq -RV_0\frac{\partial\theta}{\partial L}\Big|_{s_1}. \tag{17}$$

2) On the solid boundary S_2:

Special care must be given to the boundary S_2 because the coordinate transformation used in this paper is not a conformal mapping. The right angle γ_N in the new domain as shown in Fig. 4 is not 90 degree for corresponding angle γ in the original domain as shown in Fig. 3. Therefore, the boundary S_2 in the new domain is no longer "solid" in the sense that fluid will flow in or out along the direction normal to S_2 in new domain. After a thorough consideration the boundary condition of S_2 in the new domain is derived as

$$\frac{\partial\phi}{\partial\alpha} = L\frac{\partial\phi}{\partial L}\frac{L'(\theta)}{R}\mathrm{Cos}(\alpha_0\mathrm{sin}\beta)$$

$$\mathrm{Cos}\left(\mathrm{Cot}^{-1}\frac{1}{R}\frac{dR}{d\theta}\Big|_{\text{along } T}\right) \tag{18}$$

where T is the curve on the original scroll surface corresponding to the generation line of the transformed cone.

3) At the outlet S_3:

$$\frac{\partial\phi}{\partial\alpha} = \frac{L}{\mathrm{Cos}\beta}\left(-\frac{\partial\phi}{\partial R} + \frac{\mathrm{Sin}\beta}{L\alpha}\frac{\partial\phi}{\partial\beta}\right)$$

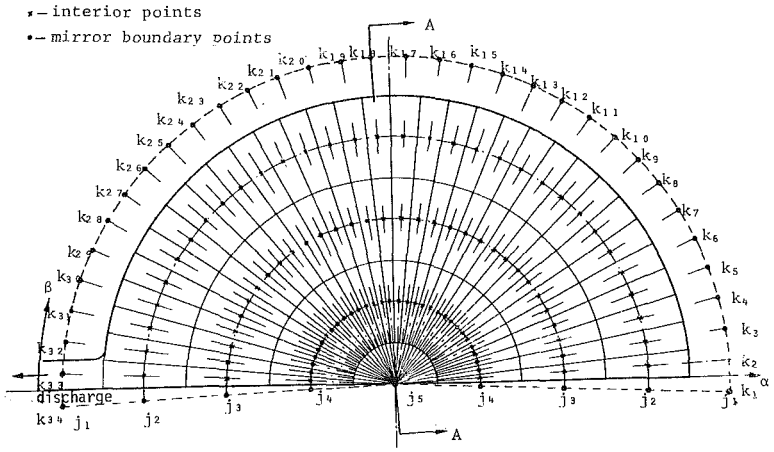

Fig. 5(a) The grid system for a straight cone in (L, α, β) spherical coordinates

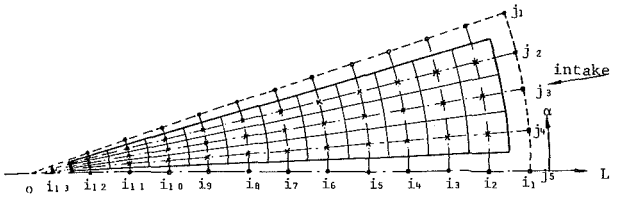

Fig. 5(b) The grid system for a straight cone cross section A-A in (L, α, β) spherical coordinates

$$= \frac{1}{\mathrm{Cos}\beta}\left(LV_D + \frac{\mathrm{Sin}\beta}{\alpha}\frac{\partial\phi}{\partial\beta}\right). \tag{19}$$

4) *On the symmetric plane* S_4:

$$\frac{\partial\phi}{\partial\beta} = 0. \tag{20}$$

In addition to the boundary conditions discussed above, there are two additional boundaries in the transformed domain. These are S_5 and S_6, which are created to avoid singularities. These are discussed below:

5) The end of cone S_5:

At location S_5 of the scroll in the original coordinates, the velocity must be specified such that the continuity of the velocity field is satisfied, i.e., the velocity at S_5 should be compatible with that at S_1. Similar to 1) at the inlet S_1, the boundary condition of S_5 is

$$\frac{\partial\phi}{\partial L} \simeq -RV_0\frac{\partial\theta}{\partial L}\Big|_{S_5}. \tag{21}$$

6) Along the centerline of the cone S_6:

Along the boundary S_6 of the scroll the normal velocity must be specified such that the net mass flux through S_6 will vanish, i.e.,

$$\int_{S_6}\frac{1}{L}\frac{\partial\phi}{\partial\alpha}dS = 0. \tag{22}$$

IV Numerical Scheme

The above coordinate transformation makes it possible to use the finite difference method in obtaining numerical solutions for a wide range of scrolls. If the scroll cross section is symmetric, only half of the scroll need be analyzed, and the dividing plane of symmetry can be considered as a solid boundary. The discretized domain of the corresponding cone is shown in Figs. 5(a) and 5(b).

(A) Finite Difference Analogy for Governing Equation. The partial differential equation (4) can be expressed in finite difference form by using centerspace finite difference scheme at any point (i, j, k) as shown in Figs. 5(a) and 5(b).

$$\begin{aligned}
&A\frac{\phi_{i-1,j,k}-2\phi_{i,j,k}+\phi_{i+1,j,k}}{\Delta L^2}\\
&\quad+B\frac{\phi_{i,j-1,k}-2\phi_{i,j,k}+\phi_{i,j+1,k}}{\Delta\alpha^2}\\
&\quad+C\frac{\phi_{i,j,k-1}-2\phi_{i,j,k}+\phi_{i,j,k+1}}{\Delta\beta^2}\\
&+E\frac{\phi_{i-1,j-1,k}-\phi_{i+1,j-1,k}-\phi_{i-1,j+1,k}+\phi_{i+1,j+1,k}}{4\Delta L\Delta\alpha}\\
&+F\frac{\phi_{i-1,j,k-1}-\phi_{i+1,j,k-1}-\phi_{i-1,j,k+1}+\phi_{i+1,j,k+1}}{4\Delta L\Delta\beta}\\
&+G\frac{\phi_{i,j-1,k-1}-\phi_{i,j+1,k-1}-\phi_{i,j-1,k+1}+\phi_{i,j+1,k+1}}{4\Delta\alpha\Delta\beta}\\
&+U\frac{\phi_{i-1,j,k}-\phi_{i+1,j,k}}{2\Delta L}+V\frac{\phi_{i,j-1,k}-\phi_{i,j+1,k}}{2\Delta\alpha}\\
&\quad+W\frac{\phi_{i,j,k-1}-\phi_{i,j,k+1}}{2\Delta\beta}=0.
\end{aligned} \tag{23}$$

In terms of the potential function of the surrounding points, it becomes

$$\begin{aligned}
\phi_{i,j,k} &= \frac{1}{\left(\frac{2A}{\Delta L^2}+\frac{2B}{\Delta\alpha^2}+\frac{2C}{\Delta\beta^2}\right)}\\
&\cdot\left(\left(\frac{A}{\Delta L^2}+\frac{U}{2\Delta L}\right)\phi_{i-1,j,k}+\left(\frac{A}{\Delta L^2}-\frac{U}{2\Delta L}\right)\phi_{i+1,j,k}\right.\\
&+\left(\frac{B}{\Delta\alpha^2}+\frac{V}{2\Delta\alpha}\right)\phi_{i,j-1,k}+\left(\frac{B}{\Delta\alpha^2}-\frac{V}{2\Delta\alpha}\right)\phi_{i,j+1,k}\\
&\quad+\left(\frac{C}{\Delta\beta^2}+\frac{W}{2\Delta\beta}\right)\phi_{i,j,k-1}+\left(\frac{C}{\Delta\beta^2}-\frac{W}{2\Delta\beta}\right)\phi_{i,j,k+1}\\
&+\frac{E}{4\Delta L\Delta\alpha}(\phi_{i-1,j-1,k}-\phi_{i+1,j-1,k}-\phi_{i-1,j+1,k}+\phi_{i+1,j+1,k})\\
&+\frac{F}{4\Delta L\Delta\beta}(\phi_{i-1,j,k-1}-\phi_{i+1,j,k-1}-\phi_{i-1,j,k+1}+\phi_{i+1,j,k+1})\\
&\left.+\frac{G}{4\Delta\alpha\Delta\beta}(\phi_{i,j-1,k-1}-\phi_{i,j+1,k-1}-\phi_{i,j-1,k+1}+\phi_{i,j+1,k+1})\right)
\end{aligned} \tag{24}$$

which consists of 19 points in this equation.

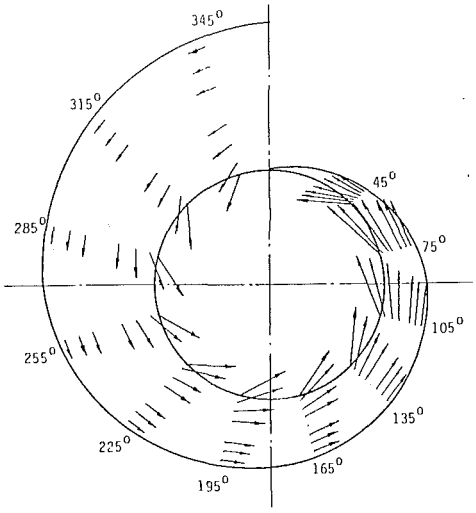

Fig. 6 Nondimensional velocity distribution on the symmetric plane of a scroll with radius of cross section varying linearly around circumference

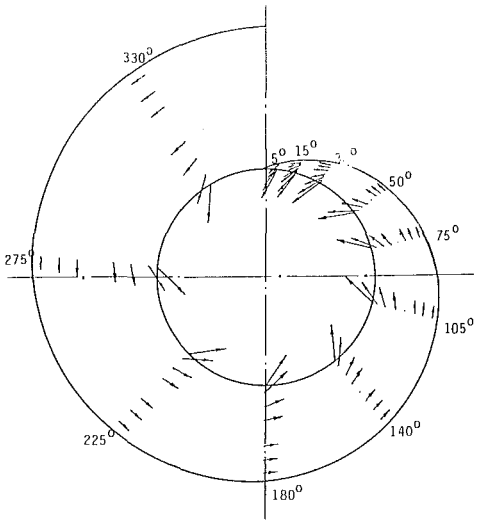

Fig. 7 Nondimensional velocity distribution on the symmetric plane of a scroll with area of cross section varying linearly around circumference.

(B) Finite Difference Analogy for Boundary Conditions. In order to obtain second order accuracy the so called "mirror boundary condition" is used everywhere in the domain. Referring to Figs. 4, 5(*a*) and 5(*b*) the discretized boundary conditions are as follows:

1) On S_1:

$$\frac{\phi_{i_1,j,k}-\phi_{i_2,j,k}}{\Delta L}=-RV_0\frac{\partial\theta}{\partial L}\Big|_{S_1}. \tag{25}$$

2) On S_2:

$$\frac{\phi_{i,j_1,k}-\phi_{i,j_2,k}}{\Delta\alpha}=L\,\frac{\phi_{i-1,j_2,k}-\phi_{i+1,j_2,k}}{2\Delta L}\cdot\frac{L'(\theta)}{R}\,\mathrm{Cos}(\alpha_0\mathrm{Sin}\beta)\mathrm{Cos}\left(\mathrm{Cot}^{-1}\frac{1}{R}\,\frac{dR}{d\theta}\Big|_{\text{along }T}\right). \tag{26}$$

3) On S_3:

$$\frac{\phi_{i,j_1,k}-\phi_{i,j_2,k}}{\Delta\alpha}=\frac{1}{\mathrm{Cos}\beta}\left(LV_D+\frac{\mathrm{Sin}\beta}{\alpha_0}\,\frac{\phi_{i,j_2,k-1}-\phi_{i,j_2,k+1}}{2\Delta\beta}\right). \tag{27}$$

4) On S_4:

$$\frac{\phi_{i,j,k_1}-\phi_{i,j,k_2}}{\Delta\beta}=0. \tag{28}$$

and

$$\frac{\phi_{i,j,k_{33}}-\phi_{i,j,k_{34}}}{\Delta\beta}=0. \tag{29}$$

5) On S_5:

$$\frac{\phi_{i_{12},j,k}-\phi_{i_{33},j,k}}{\Delta L}=-RV_0\,\frac{\partial\theta}{\partial L}\Big|_{S_5}. \tag{30}$$

6) On S_6

$$\phi_{i,j_5,k}=\frac{\sum_{k=k_2}^{K_{33}}\phi_{i,j_4,k}\left(R_i+r_L-\frac{1}{2}L\cdot\Delta\alpha\cdot\mathrm{Cos}\beta\right)}{\sum_{k=k_2}^{K_{33}}\left(R_i+r_L-\frac{1}{2}L\cdot\Delta\alpha\cdot\mathrm{Cos}\beta\right)}. \tag{31}$$

(C) Numerical Method. The successive over-relaxation iterative method is used for the numerical solution. It should be noted that if equation (24) is used for all interior grid points together with the boundary conditions equations (25) through (31) for the calculation of boundary points, the iteration may never converge, but rather drift slowly and endlessly. This may be caused by the combination of accumulation of round off error and the nature of the Neumann boundary condition. For Neumann boundary condition if ϕ is a solution and c is a constant, $\phi+c$ is still a solution even for a very small value of c. To solve this problem, following Roache [7], the boundary conditions must be incorporated implicitly into the governing equation for the interior points adjacent to the boundaries. Thus equation (24) is only used for those interior points which are more than one node away from the boundary. At the points adjacent to the boundaries, equation (24) is replaced by incorporating equations (25) to (31), respectively, according to which boundary is involved. For the points adjacent to boundary S_6, equation (24) can still be used since the hole of S_6 is very small. The effect of the uncertainty of the value ϕ at the centerline ($\phi_{i,j_n,k}$) on the whole solution is so small that it does not appreciably influence the covergence of the iteration. However, the use of equation (24) for these points instead of the replaced equation can simplify the program significantly. Another consideration for the Neumann boundary condition is that the normal derivative on boundaries should be compatible with the continuity equation numerically. Because of trun-

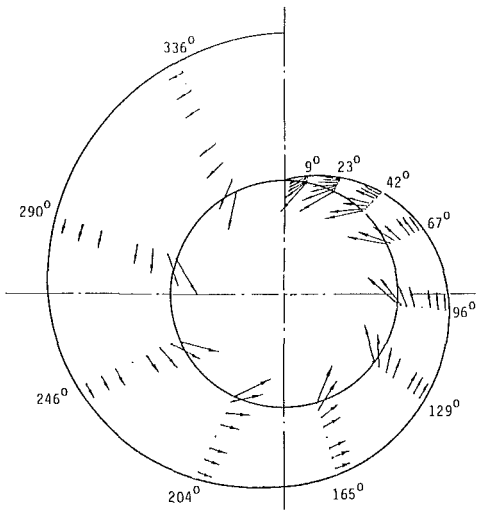

Fig. 8 Nondimensional velocity distribution on the symmetric plane of a scroll with ratio of $\Pi r_L^3/(R_i \cdot r_L)$ varying linearly around circumference

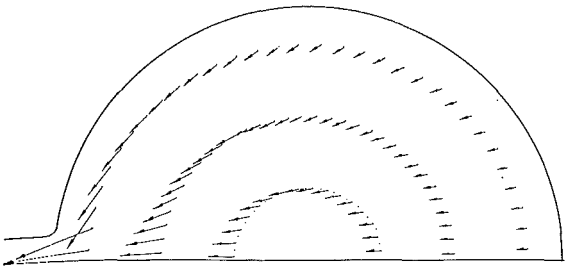

Fig. 9 Nondimensional velocity distribution on the cross-sectional plane of $\theta = 195$ deg in Fig. 6

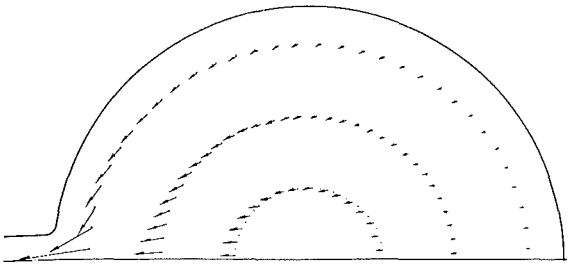

Fig. 10 Nondimensional velocity distribution on the cross-sectional plane of $\theta = 180$ deg in Fig. 7

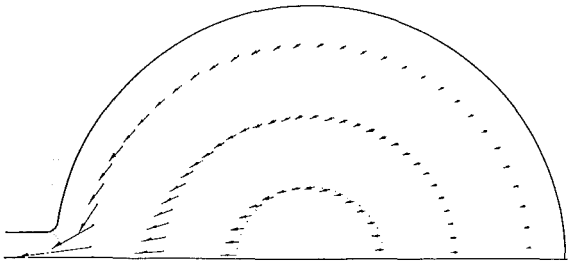

Fig. 11 Nondimensional velocity distribution on the cross-sectional plane of $\theta = 204$ deg in Fig. 8

cation error and round-off error accumulation, the value of the derivative obtained from the solution of the continuity equation over the whole domain will not meet this constraint causing a slow divergence of SOR iteration. To solve this problem, following Miyakoda [8], the boundary derivative should be modified consistently during the iteration procedure.

V Results and Discussion

The results for the three cases described above are presented here. Comparing velocity distributions on the symmetric plane for these cases as shown in Figs. 6, 7, and 8, some interesting results are revealed. For case 1, due to area over-reducing from the inlet to the end of the scroll, the through flow velocity increases consistently so that the flow angle with reference to radial direction at the scroll outlet increases as shown in Fig. 6. For case 2, one may except to obtain an even discharge condition due to the linear decrease in area. However, conservation to angular momentum indicates that if the tangential velocity at scroll exit is to be kept constant, then the average through flow velocity will increase from the inlet to the end of the scroll. To match this condition, the cross sectional area should decrease at a faster rate. In other words, the linear decreasing in area will cause the tangential velocity at the scroll outlet to decrease. This is confirmed by the decrease of discharge angle from the inlet to the end of the scroll as shown in Fig. 7. For case 3, the discharge condition as shown in Fig. 8 is most uniform among the three cases, since conservation of angular momentum has been taken into account.

From Figs. 9, 10, and 11, it can be seen that the magnitude of the velocity increases consistently from the outer wall to the inner wall of the scroll for all three cases. Case 1 has the largest magnitude of the velocity. This is compatible with the through flow velocity distribution given in Fig. 6. No significant difference in distribution pattern of velocity direction is observed among these three cases.

With the assumption of uniform radial component of velocity at the exit, V_p, the tangential velocity component and the static pressure at the exit are related. It would be very helpful to designer to have plots of static pressure variation along the outer periphery of the scroll for the comparison of the three designs on the basis of the uniformity of the exit static pressure distribution.

It is worth noting that the discussion above does not lead to the conclusion that case 3 is the best of these three cases, since the viscous effect has not yet been taken into consideration. As can be expected, the boundary layer build-up due to viscous effect will contract the flow passage.

VI Conclusion

The use of coordinate transformation turns out to be a very powerful tool in establishing a universal mathematical model. The fluid flow in scrolls with a wide range of geometry can be easily handled by the model established. The three dimensional flow field can be addressed directly and analyzed without the need of two dimensional or quasi-three dimensional assumption. The results obtained by this method look very reasonable as compared with some numerical solutions and existing experimental data.

Further research work is needed to improve the boundary conditions at inlet and outlet of the scroll and to include viscous effects on the flow. These additions would enable the model to be more realistic and practical. With further development, the model could be especially useful in the interactive computer-aided design of a scroll.

References

1 Bhinder, F. S., "Investigation of Flow in the Nozzleless Spiral Casing of Radial Inward Flow Gas Turbine," *Proc. Ins. Mechanical Engineering*, Vol. 1, 184, Part 3G (11), 1969-1970, pp. 66-71.

2 Chapple, P. M., Flynn, P. F., and Mulley, J. M., "Aerodynamic Design of Fixed and Variable Geometry Nozzleless Turbine Casings, ASME *Journal of Engineering for Power*, Vol. 102, Jan 1980, pp. 141-146.

3 Hamed, A., Baskharone, E., and Tabakoff, W., "A Flow Study in Radial Inflow Turbine Scroll-Nozzle Assembly," ASME JOURNAL OF FLUIDS ENGINEERING, Vol. 100, Mar. 1978, pp. 31-36

4 Hamed, A., Abdallah, S., and Tabakoff, W., "Flow Study in Cross Sectional Plane of a Turbine Scroll," AIAA Paper No. 77-714, AIAA 10th Fluid and Plasma Dynamic Conference, Albuquerque, N. M., June 27-29, 1977.

5 Tabakoff, W., Sheoran, U., and Kroll, K., "Flow Measurements in a Turbine Scroll," ASME JOURNAL OF FLUIDS ENGINEERING, Vol. 102, Sept. 1980, pp. 290-296.

6 Hamed, A., and Baskharone, E., "Analysis of the Three Dimensional Flow in a Turbine Scroll," ASME JOURNAL OF FLUIDS ENGINEERING, Vol. 102, Sept. 1980, pp. 297-301.

7 Pattick, J., Roache, *Computational Fluid Dynamics*, Hermosa Publishers, 1976.

8 Miyakoda, K., "Contribution to the Numerical Weather Prediction – Computation with Finite Difference," *Japanese J. of Geophysics*, Vol. 3, 1962, pp. 75-190.

Interaction Between Impeller and Volute of Pumps at Off-Design Conditions

J. A. Lorett

S. Gopalakrishnan

Byron Jackson Pump Division,
Borg-Warner Industrial Products, Inc.,
Long Beach, Calif. 90802

In a centrifugal pump of volute type, the respective characteristics of the impeller and the volute are such that at only one operating point can the flow parameters be constant along the length of the volute. At off-design conditions the mismatching of characteristics causes variations of velocity and pressure along the periphery of the impeller. This in turn forces cyclic variation of the flow in the impeller channels, introduces variations of the inlet incidence and contributes significantly to the direction and the magnitude of the radial thrust. Furthermore, below a certain pump output, a complete flow reversal occurs over a part of the impeller periphery, thus explaining the onset of recirculation. The paper describes the calculation approach used to derive this aspect of the flow behavior. Because of difficulties in obtaining a closed analytical solution, a step by step computation is employed. Beginning with arbitrarily chosen conditions at the volute tongue, the program computes the flow parameters for following segments, using the continuity and the momentum equations, until the exit from the last segment is reached. The inherent unsteadiness of the relative flow in the impeller is explicitly accounted for. Since the inflow and the velocity in the first segment depend upon the exit conditions of the last, the initial input must be modified, and the computation repeated, until the values are compatible with the exit conditions. In spite of several simplifying assumptions, the results of the calculations show very good agreement with published test results.

Introduction

The flow conditions in a volute casing of a centrifugal pump have been investigated both experimentally and analytically for a number of years. In particular, the fact is well established that, at off-design operation, static pressure is not constant along the periphery of the impeller, resulting in radial thrust. Theoretical and empirical methods of calculation exist for estimating flow fields and radial thrusts.

The theoretical models, predict the variation of static pressure along the volute passage. However, all of these methods assume that the flow in the individual impeller channels is steady, and corresponds to the mean value of the momentary pump output. Such an assumption is physically impossible. The static pressure at the exit of an impeller channel is, among other variables, a function of the flow velocity in the channel. Conversely, a variation of the impeller exit pressure, imposed by the flow characteristic of the volute, must enforce changes in the channel flow. For example, flow in an impeller channel passing from a region of higher into a region of lower exit pressure will be subjected to an additional unsteady acceleration, superimposed over the steady mean flow velocity. Further, at a sufficiently low overall flow, the impeller channels approaching the volute tongue can operate with reverse flow.

Analytical calculation of the actual flow conditions is quite complicated. It requires simultaneous solution of the continuity and momentum equations in the volute, and the Euler, relative unsteady motion and continuity in the impeller. The method chosen in this investigation was that of step by step calculation of the flow parameters in discrete peripheral segments of the volute/impeller system. Based on assumptions of volute and impeller flows and static pressure at the beginning of the volute passage, conditions at the exit are computed. The initial assumptions are tested for compatibility with the end conditions, and adjusted by iteration until satisfactory agreement is obtained.

From a then known pressure and impeller flow distribution

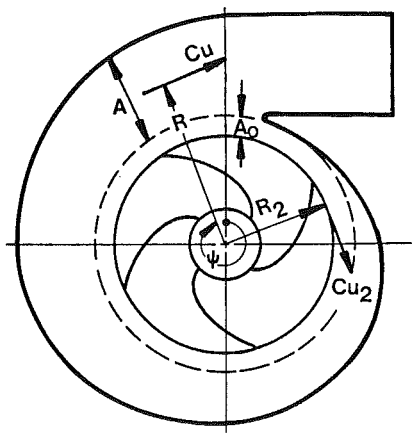

Fig. 1 Volute geometry and velocity notation

Contributed by the Fluids Engineering Division for publication in the JOURNAL OF FLUIDS ENGINEERING. Manuscript received by the Fluids Engineering Division, January 30, 1984.

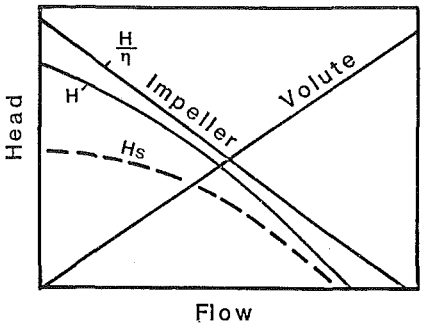

Fig. 2 Volute—impeller matching

the radial thrust and the local impeller inlet incidences can be calculated.

The following sections describe the basic equations and the calculation sequence, and quote comparisons between calculated and measured data.

Volute Flow at Design Point

The volute cross sectional areas are usually designed to produce at design point of the pump constant velocity and pressure along the periphery of the impeller. When the effects of fluid friction are ignored, the volute area at any radial position can be calculated as follows:

A radial section of a volute, shown in Fig. 1, at an angular distance ψ from the volute tongue, has to pass the flow quantity:

$$Q_\psi = Q\,\psi/2\pi \tag{1}$$

and the net flow area, that is the area over the initial tongue clearance area Ao, should be:

$$A_\psi = \frac{Q_\psi}{Cu} \tag{2}$$

The local value of the average velocity follows the angular momentum equation, so that:

$$Cu = Cu_2\,\frac{R_2}{R} \tag{3}$$

where Cu_2 is the absolute tangential exit velocity at the impeller periphery. This velocity is determined by the Euler equation (without inlet prewhirl) to be:

$$Cu_2 = \frac{gH}{\eta\omega R_2} \tag{4}$$

Combining equations (2), (3), and (4) results in a simple expression for the flow area of a volute:

$$\left(\frac{A}{R}\right)_\psi = \frac{Q\omega\eta}{gH}\,\frac{\psi}{2\pi} \tag{5}$$

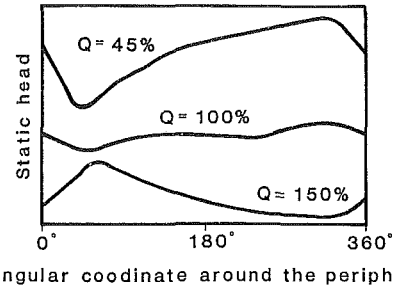

Fig. 3 Typical experimental observation of static head variations around impeller periphery

Putting $\psi = 2\pi$, yields the value of A/R at the volute throat.

In practice one finds that higher specific speed volutes can be designed with sections smaller than those given by equation (5), and volutes designed with a constant value of Cu are often used. Some textbooks offer purely empirical equations for the volute areas.

Volute Flow at Off-Design Conditions

At constant speed, the volute characteristic given by the equation (5) represents, in the H/Q plane, a straight line through the origin:

$$H = \frac{\eta\omega}{g}\,\frac{Q}{(A/R)} \tag{6}$$

In contrast to it, a pump impeller with backward leaning vanes, has a characteristic of the type:

$$H/\eta = H_0 - \text{const.}Q \tag{7}$$

As illustrated in Fig. 2, the respective characteristics intersect at the design point of the pump, but at other operating points they do not match. This mismatch forces a variation of velocity and pressure around the periphery of the impeller at off-design conditions.

Pressure distributions along the volute passage, and the associated radial thrust are well documented in the literature. A typical plot of volute pressures at different flows is that published in 1962 by B. Eck, [1] shown in Fig. 3. It should be noted that, while the pressure at the end of the volute is dictated by the pump exit pressure, at the beginning of the volute the pressure departs relatively little from that at the design point of the pump. More recent and detailed data of pressure variation around the periphery can be seen in [2].

Much of the existing work on volute flow behavior has been aimed at developing the magnitude of radial forces. References [3] and [4] document experimental results of radial thrust measurements. More recent work has concentrated on the effects of impeller eccentricity on forces, [5] and pressure

Nomenclature

A = area of volute
Ao = area under volute tongue
B = impeller exit width
C = flow velocity in volute
Cu = absolute tangential velocity
Cm = meridional velocity
C_2 = absolute impeller exit velocity
D = diameter
D_h = hydraulic diameter
E = total energy
g = gravity acceleration
H = total head
Hs = static head in volute section
Hs_m = steady flow static head at impeller exit
L = length
M = number of tongues
N = number of segments
P = radial force
Q = flow quantity
R = radius
t = time
U = peripheral speed
W = relative velocity
β = impeller blade angle
η = hydraulic efficiency
ψ = angular distance
λ = friction coefficient
ξ = loss coefficient
ρ = density
ω = angular velocity

Subscripts

1 = at I.D. of impeller, also first volute station
2 = at O.D. of impeller
0 = at shutoff condition
m = steady state
M = due to momentum
MR = due to meridional momentum
MT = due to tangential momentum
N = last volute station
P = due to pressure
s.f. = due to skin friction

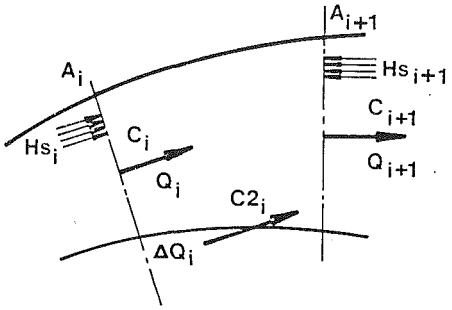

Fig. 4 Velocity and head conditions around a peripheral element in a pump volute

distribution [6]. Analytical calculations of radial forces recognize the variation of pressure around the periphery. In [7], the volute casing is treated as an "equivalent" log spiral, which experiences a lift force at off-design conditions, just as a single blade of a radial cascade at non-zero incidence. In [8], the volute pressure distribution is computed using a step-by-step integration of the momentum equation. Most calculation methods assume that, at off-design conditions, the impeller flow is still distributed uniformly around its circumference. However, since the static pressure along the volute is not constant, such an assumption is invalid.

At off-design conditions an individual impeller channel experiences a relatively constant inlet pressure, but the pressure at the exit varies cyclically with the momentary angular position of the channel in relation to the volute. This variation of the pressure difference, imposed by the characteristic of the volute, introduces unsteady accelerations and decelerations of the relative velocity in the impeller channels.

The unsteady velocity changes can be calculated from the static characteristic of the impeller and the channel dimensions. Their magnitude depends primarily upon the steepness of the static pressure gradients along the volute; at very low overall flow the gradients can be steep enough to cause complete flow reversal in the impeller channels while they approach the volute tongue. The reverse flows is returned into the impeller inlet region and introduces inlet prerotation.

Even before flow reversal occurs, the impeller velocity oscillates around the mean value corresponding to the overall flow, and so do the inlet incidence angles. This is significant when predicting the incipient cavitation behavior.

An indirect experimental proof of the unsteady impeller flow follows from the fact that calculations of the magnitude and direction of radial thrust, based on integration of the pressure field alone, do not generally agree with test results.

The calculation method described below explicitly recognizes the unsteadiness of the impeller relative velocity.

Flow Equations for an Element of Volute Length

Figure 4 shows a peripheral element of volute and the notations used for the flow areas, velocities and static pressures.

It is assumed that average tangential velocities and radial pressure gradients obey the preservation of angular momentum. To simplify the calculation process, all velocities, pressures and flow areas are therefore normalized to the values corresponding to the outer diameter of the impeller. This assumption preserves the values of (A/R) and of total pressures, and has no effect upon the interaction between the impeller and the volute. Variations in the axial direction are ignored. It is also assumed that the momentum exchange between the flow in the volute and the flow added by the impeller within the length of the segment is completed before the exit from the segment. Since only linear equations of continuity and momentum are used, this assumption should not introduce any errors, and the mixing effect of the impeller meridional velocity lends it validity.

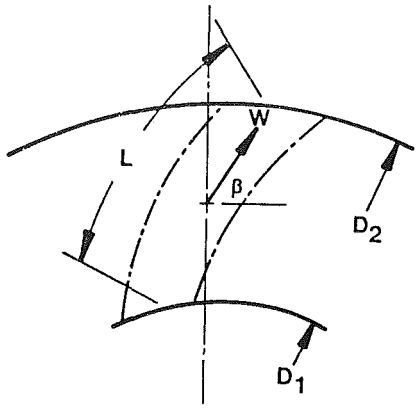

Fig. 5 Typical flow channel

A flow quantity Q_i enters the segment through the flow area A_i at a velocity C_i and static pressure Hs_i. The meridional velocity in this segment is denoted by Cm_i. Within the length of the segment, the impeller introduces an additional flow quantity ΔQ_i, at the local impeller exit velocity C_{2i}. The quantity and the velocity of the flow contributed by the impeller within the length of the segment are functions of the local static pressure at the impeller periphery.

From the impeller geometry and the slip factor one can express:

$$C_{2i} = f(CM_i)$$

so that the flow entering the volute segment from the impeller is:

$$\Delta Q_i = Cm_i \frac{\pi D_2 B}{NM} \tag{8}$$

The exit flow of the segment is then:

$$Q_{i+1} = Q_i + \Delta Q_i \tag{9}$$

and the exit velocity follows from the continuity equation to:

$$C_{i+1} = \frac{Q_{i+1}}{A_{i+1}} \tag{10}$$

If the velocities C_i, C_{2i}, and C_{i+1} are not equal, the difference in momentum of the flows entering and leaving the element must cause a change in the static pressure within the length of the element.

Furthermore, friction at the walls of the volute will also cause a pressure loss. This loss depends on the flow velocity, friction coefficient and channel geometry, and can be expressed as follows:

$$\Delta H_{\text{s.f.}} = \lambda \frac{\Delta L}{D_h} \cdot \frac{C_i^2}{2g} \tag{11}$$

The static pressure at the exit from the element can be determined by combining the momentum equation and the friction loss, and expressed as follows:

$$Hs_{i+1} = \frac{2}{g} [Q_i C_i + \Delta Q_i C_{2i} - Q_{i+1} \cdot C_{i+1}] / (A_i + A_{i+1}) - \Delta H_{\text{s.f.}} + Hs_i \tag{12}$$

If the static pressure along the element does not alter, the impeller exit velocity in the next element remains unchanged. However, at off-design conditions, there usually is a change of static pressure along the element. This reflects upon the impeller and must alter its operating point.

Figure 5 shows an impeller channel and the notations used.

The length of the channel can be approximated by:

$$L = (D_2 - D_1)/2 \operatorname{Sin} \beta \tag{13}$$

and the average relative velocity in the channel by:

$$\bar{W} = Cm/\text{Sin}\,\beta \tag{14}$$

The steady state static characteristic of the impeller has a general form of:

$$Hs_m = \frac{1}{g}\left(U \cdot Cu - \frac{C_2^2}{2} - \xi\,\frac{W_1^2}{2}\right) \tag{15}$$

and can be solved for:

$$Hs_m = f(C_m) \tag{16}$$

At design point of the pump, the local value Hs is, by definition, equal to Hs_m and the local values of the relative velocity W and the relative acceleration dW/dt are therefore constant. Together with the two other components of the absolute acceleration, the centrifugal and the Coriolis, they determine the pressure rise along the channel and the work input to the impeller.

At off-design conditions the pressures Hs and Hs_m are generally not equal, and a transient change of the static pressure at the exit of the channel causes a further, transient acceleration of the impeller flow. Since the centrifugal acceleration is constant at constant speed, and the Coriolis acceleration acts at right angles to the channel walls, the only term affected by the transient pressure is the term dW/dt. Expressed in finite differences and averaged over the length of the channel, the change in the relative velocity is:

$$\frac{\Delta W}{\Delta t} = g\left\{\frac{H_s - Hs_m}{L}\right\}_{i+1} \tag{17}$$

The time interval is:

$$\Delta t = \frac{60}{\text{RPM} \cdot N \cdot M} \tag{18}$$

Equation (17) can be transcribed as:

$$\frac{\Delta W}{\Delta t} = \frac{2g\ \text{Sin}\ \beta}{D_2 - D_1}\ (Hs - Hs_m)_{i+1} \tag{19}$$

and the change in the impeller output within a segment, caused by the transient mismatching of the pressures, becomes:

$$\Delta Cm_i = \frac{2g\ \text{Sin}^2\ \beta}{D_2 - D_1}\ \frac{60}{\text{RPM} \cdot N \cdot M}\ (Hs - Hs_m)_{i+1} \tag{20}$$

The impeller meridional velocity at the entry to the next element, $(i+1)$, becomes:

$$Cm_{i+1} = Cm_i + \Delta Cm_i \tag{21}$$

The entire calculation can then be repeated for the following segments, until the end of the volute is reached.

Closing Conditions

The process described above allows calculation of the flow parameters at the exit from the volute, provided that the conditions at the beginning of the volute are known.

It is necessary therefore to begin the calculation process by selecting the value of Hs_1 and assuming values of C_1 and Cm_1. Since experimental evidence suggests a single valued relationship between the pump output Q and the pressure Hs_1, it is convenient to arbitrarily select Hs_1 as an independent parameter. The associated selection of Cm_1 and C_1 is, however, by no means obvious.

A convenient starting point is to select Cm_1 and C_1 corresponding to the steady state value of Hs_1. Flow parameters of the subsequent sections are calculated by equations (9) through (21) until section N is reached.

It is then necessary to test the compatibility of the assumed values of Cm_1 and C_1 with the values of Cm_N and C_N in the way explained below.

At the junction of sections N and 1, some of the flow leaving section N reenters section 1 through the tongue clearance area Ao. For this flow the energy and the continuity equations should be satisfied, so that:

$$C_1^2 = C_N^2 + 2g\,(Hs_N - Hs_1)(1 - \xi) \tag{22}$$

The reason for using the energy equation, rather than that of momentum, is the realization that the process is not instantaneous but that it extends over a finite region of the volute periphery. Reasonably orderly diffusion or acceleration should therefore be possible without losses associated with pure momentum mixing. The value of the loss coefficient is difficult to choose, but an estimate of the shape of the stagnation line at the tongue can be of help, particularly if separation at the tongue is expected.

Equation (22) suggests a new value C_1 for the next run of computation. The new value of Q_1 for the next run is then:

$$Q_1 = C_1 Ao \tag{23}$$

A second change in the initial assumptions concerns the impeller velocity Cm_1 and the associated values of Q_1 and C_{21}. In this case the transition $N/1$ is taken as instantaneous, and the value of Cm_N is input for Cm_1 for the next run of the program.

The program is rerun with the initial assumptions adjusted, and the compatibility is tested again. Usually there will still be a significant discrepancy, but the results will indicate the direction and magnitude of further adjustments. The iterations can form part of the program, but great care is needed in the selection of the steps and of the limit at which no further adjustments of the input become necessary.

A point requiring some care is the correct estimate of the tongue clearance area Ao, as large axial gaps between the impeller and the casing walls definitely contribute to its magnitude.

After the final run of the program, the net flow and the total head of the pump amount to:

$$Q_{\text{TOT}} = Q_N - Q_1 \tag{24}$$

and

$$H_{\text{TOT}} = Hs_N + \frac{C_N^2}{2g} \tag{25}$$

Volute Loss

The energy losses in the volute consist of the mixing losses of the unequal momentum within the segments of the volute, and of the pressure drops caused by wall friction.

In each segment of the volute the impeller contributes an energy:

$$\Delta E_i = \Delta Q_i \left(Hs_i + \frac{C_{2i}^2}{2g}\right) \tag{26}$$

while the total energy available at the exit from the volute is:

$$E_N = Q_{\text{TOT}} \cdot \left(Hs_N + \frac{C_N^2}{2g}\right) \tag{27}$$

The overall loss of the volute is then the difference between the sum of the impeller energy inputs of equation (9), and the exit energy of equation (10).

$$L = \Sigma \Delta E_i - E_N \tag{28}$$

Radial Thrust at Off-Design Operation

The net radial force acting upon the impeller can be regarded as the sum of two distinct effects.

The well documented nonuniformity of the static pressure around the periphery of the impeller causes a net radial force, which can be expressed as follows:

$$\Delta P_P = \rho g Hs_i\ \frac{\pi D_2 B}{N.M} \tag{29}$$

Vector sum of the elements of equation (29) gives the static pressure contribution to the radial thrust.

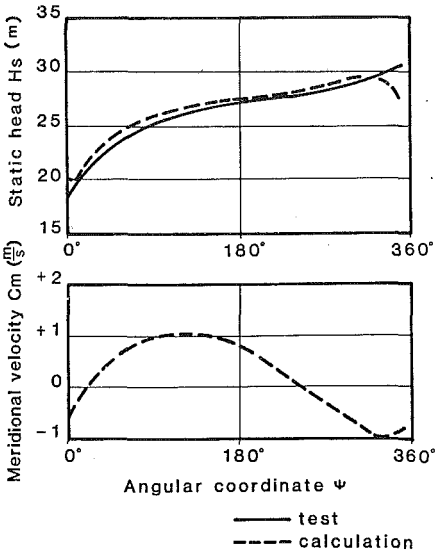

Fig. 6 Comparison between calculated and measured static pressure for the low specific speed pump of reference [9] (no test data are available for the meridional velocity distribution). Flow is 10 percent of design flow.

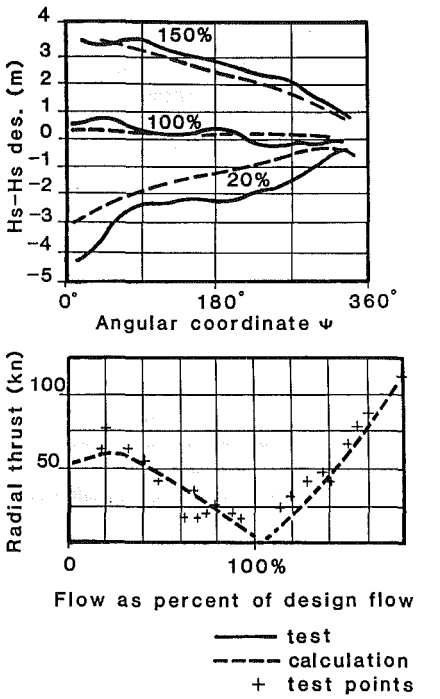

Fig. 7 Comparison between calculated and measured values for static head and radial thrust

The elements of momentum reacting upon the impeller are:

$$\Delta P_M = \rho . \Delta Q_i (C_{2i} - C_{1i}) \tag{30}$$

At design point Q_i, C_{2i}, and C_{1i} are all constant, their vector sum results in a torque upon the shaft, (and an axial force if C_1 has an axial component), but no radial resultant is present.

At off design the values in equation (30) alter around the periphery and their summation yields also a radial thrust.

The contribution due to meridional momentum is

$$\Delta P_{MR} = \rho \Delta Q_i C m_i \tag{31}$$

and that due to tangential momentum is

$$\Delta P_{MT} = \rho \Delta Q_i C u_i \tag{32}$$

The total net radial thrust upon the impeller results from the vector summation of the elements of equations (29), (31), and (32).

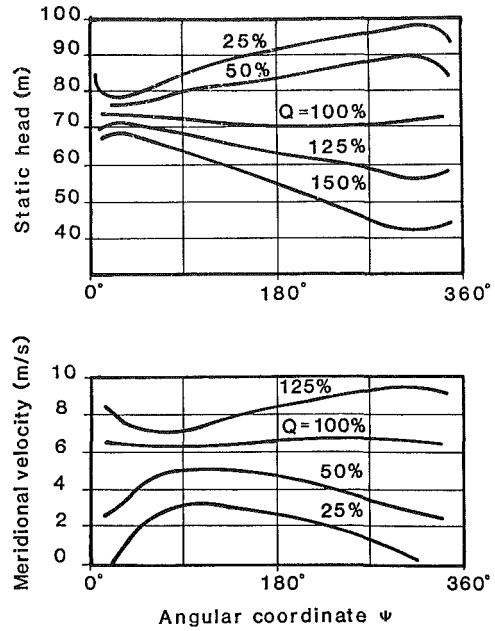

Fig. 8 Calculated flow distributions for a conventional volute with a low specific speed, high head pump

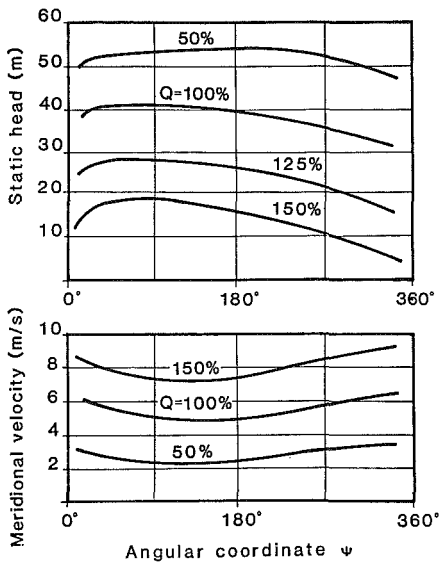

Fig. 9 Calculated flow distribution for a rotationally symmetric casing with a centrifugal pump

In the computation process it is more convenient to project the elements of the forces on to rectangular X and Y coordinates before their summation.

It is interesting to note that inclusion of the momentum terms has a significant effect upon the magnitude and direction of the predicted radial thrust, similar to the conclusion that was reached in (2).

Calculation Results and Comparisons With Test Data

The validity of the approach described above was verified by comparing available experimental data with the predictions of the computer program. In spite of many simplifying assumptions, the agreement was on the whole very good indeed. In cases of significant discrepancy the suspeceted reason was the uncertainty of estimated tongue clearance area Ao. As will be evident from some examples, the relative magnitude of Ao has a very strong effect upon the steepness of the velocity

and pressure gradients, and is often difficult to estimate in cases of tests published in the literature.

Figure 6 shows pressure measurements in a volute of a low specific speed pump at approximately 10 percent of design flow, published in Stepanoff's textbook [9]. As can be seen, the calculated pressure distributions compare very well with the test data.

To illustrate the variation of the impeller flow, the figure also shows a plot of calculated values of Cm versus angular distance from the volute tongue. At this low flow the distortion of the relative field is very strong indeed, over 30 percent of the impeller periphery shows a complete reversal of the velocity. In these regions the volute forces the fluid back into the impeller channels. It is discharged into the inlet casing at tangential velocity somewhat larger than Cu_1, and mixing with the suction flow, it imparts to it a positive prewhirl, usually referred to as inlet prerotation.

Comparison of calculated values with tests published in 1960 by Iversen [8] is shown in Fig. 7. At high flow the agreement is quite good. At low flow the relatively smooth calculated curve lies from 10 to 30 percent above the test plot. On the other hand, the test curve shows local irregularities, possibly caused by unsteady changes in the volute sections. The thrust values compare very well, particularly if the scatter of the test points is smoothed out. An interesting feature of the calculated thrust curve is the reversal of its slope near to the shut-off point. The fact that some published thrust curves show a similar character leads one to believe that the change of slope is real rather than a peculiarity of the program.

Repeated calculations suggest that, in general, complete flow reversal in the impeller is unlikely to occur above 30 to 40 percent of the design capacity. Significant variations in channel velocity do however, appear at already much smaller departures from design point operation. This is illustrated in the next example.

In Fig. 8 are plotted calculated values of static pressure and impeller channel velocity versus volute angle in a relatively high head, medium specific speed pump. The pressure plots for different operating points show the familiar character, remaining close together at the beginning, and diverging to meet the system resistance at the exit of the volute. Velocity plots suggest that flow reversal in the impeller channels begins to take place at approximately 30 percent of the design capacity, but strong departures from constant velocity are evident already in the curves for 50 and 125 percent capacity. For example, at 50 percent overall capacity, the channel velocity alternates between 30 and 75 percent of the design value. More important is the implication that, at 125 percent of design capacity, the local channel velocity can reach almost 150 percent of design value.

The conclusion must be that calculations of off-design cavitation behavior based on average channel velocities can be seriously misleading. It is suggested therefore that, in applications where accurate prediction of the cavitation inception is of importance, cyclic changes in channel velocity and impeller inlet incidence be taken into account.

The previously mentioned influence of the tongue clearance area Ao upon the pressure and velocity distribution is illustrated very clearly in the next example.

Centrally symmetrical spherical outlet casings are sometimes used in nuclear pumps and in applications where the stress considerations are of paramount importance. Figure 9 shows calculated pressure and velocity plots of such a casing, in which the tongue clearance area Ao equals A_N.

The slopes of the curves are much smaller than of those in spiral volutes, and, not unexpectedly, velocity and pressure are almost uniform at very low flows.

Mixing losses will be relatively low, but the shape of the exit branch will influence the overall loss. However, such casings are more often used at high specific speeds, at which the kinetic energy at the impeller exit is relatively low, and correct shape of the exit can reduce the loss to an acceptable level.

Sources of Errors

The calculation method described above contains a number of assumptions and simplifications which must introduce errors into the final results. Already mentioned has been the uncertainty in the interpretation of the contribution the meridional velocity Cm can make to the energy of the volute flow. In a typical centrifugal pump, the kinetic energy of Cm lies between 10 and 20 percent of that of C_2. It does reach higher proportions in high specific speed pumps, but there the kinetic energy of C_2 itself is relatively low in relation to the total head of the pump.

A hypothetical rectangular volute of the same width as the width of the impeller exit, would preserve the energy of Cm, but would be somewhat impractical and would suffer high wall friction losses.

Several published velocity traverses in pump volutes show a very strong turbulence in the axial plane, which makes any orderly radial diffusion very unlikely. In view of this it was decided to ignore the momentum of Cm in the equation (12) and use the tangential components of C_2 only.

The second simplifiction concerns the transition region between the last and the first element of the volute. The inherent character of the adopted step by step calculation approach postulates an abrupt change of parameters at this point. In physical terms, however, it is clear that the influence of the volute tongue must extend for several elements in front of it. To compensate for the inability to correctly interpret this aspect of the flow, the change in parameters is calculated by the energy rather than by the momentum equation. The magnitude of the error should not be very significant. Large changes in parameters across the $N/1$ boundary occur only in volutes with a small clearance area Ao, in which the energy content of the recirculated flow is not very significant, and in those with large tongue clearances the change in parameters and the relative error should be small.

Flow separation at the tongue can introduce errors. Its likelihood and extent can be judged from a rough estimate of the shape of the stagnation line, based on calculated values of C_N and C_1. Inputs for the first few volute elements should then be adjusted to the extent of separated flow. Again, fortunately, separation is more likely to occur at sharp volute tongues with small clearance areas Ao, that is those in which the flow quantity Q_1 is relatively less significant.

Conclusions

A method is proposed for a step by step calculation of the flow and velocity fields in volutes and impellers of centrifugal pumps at off design operation. Good agreement between results of calculations and available test data for static pressures and radial thrust proves its validity and shows that errors inherent in the necessary simplifying assumptions are not significant.

In particular, the method illustrates that the velocity in the impeller channel varies as the channel rotates. Consequently, the classical assumption, that the relative flow in the impeller is steady, is no longer valid. In this proposed method, the effect of the unsteadiness of the relative flow is explicitly taken into account. Further, it is postulated that cyclical variations of velocity will affect predictions of the inception of cavitation.

The calculations also show that, depending on volute geometry, at flows below approximately 40 percent of design capacity, discharge recirculation i.e., complete flow reversal occurs in channels passing the first quadrant of the volute. For incompressible flow, this provides a valid physical explanation of the appearance of inlet recirculation.

Acknowledgments

The authors wish to express their thanks to Prof. Dr. A. J. Acosta of the California Institute of Technology for very helpful suggestions and criticisms, as well as for encouragement to proceed with the publication of this paper, and to the management of Byron Jackson Pump Division, Borg-Warner Industrial Products, Inc., for permission to publish.

References

1 Eck, B., *Ventilatoren*, Springer, 1962.

2 Chamieh, D. S., "Forces on a Whirling Centrifugal Pump Impeller," Ph.D. thesis, Division of Engineering and Applied Science, California Institute of Technology, Pasadena, Calif., 1983.

3 Biheller, H. J., "Radial Force on the Impeller of Centrifugal Pumps with Volute, Semi Volute, and fully Concentric Casings," ASME *Journal of Engineering for Power*, July 1965.

4 Agostinelli, A., Nobles, D., and Mockridge, C. R., "An Experimental Invesigation of Radial Thrust in Centrifugal Pumps," ASME *Journal of Engineering for Power*, Apr. 1960.

5 Hergt, P., and Krieger, P., "Radial Forces in Centrifugal Pumps with Guide Vanes," *Proc. Inst. of Mech. Engineers*, Vol. 184, Part 3, 1969–1970.

6 Kanki, H., Kawata, Y., and Kawatani, J. T., "Experimental Research on the Hydraulic Excitation Force on the Pump Shaft," ASME Paper No. 81-DET-71.

7 Csanady, G. T., "Radial Forces in a Pump Impeller caused by a Volute Casing," ASME *Journal of Engineering for Power*, Oct. 1962.

8 Iverson, H. W., Rolling, R. E., and Carlson, J. J., "Volute Pressure Distribution, Radial Force on the Impeller, and Volute Mixing Losses of a Radial Flow Centrifugal Pump," ASME *Journal of Engineering for Power*, Apr. 1960.

9 Stepanoff, A. J., *Centrifugal and Axial Flow Pumps*, John Wiley, 1957.

D. L. Rhode
Assistant Professor.

J. A. Demko
Graduate Student.

U. K. Traegner
Graduate Student.

G. L. Morrison
Associate Professor.

S. R. Sobolik
Graduate Student.

Mechanical Engineering Department,
Texas A&M University,
College Station, TX 77843

Prediction of Incompressible Flow in Labyrinth Seals

A new approach was developed and tested for alleviating the substantial convergence difficulty which results from implementation of the QUICK differencing scheme into a TEACH-type computer code. It is relatively simple, and the resulting CPU time and number of numerical iterations required to obtain a solution compare favorably with a previously recommended method. This approach has been employed in developing a computer code for calculating the pressure drop for a specified incompressible flow leakage rate in a labyrinth seal. The numerical model is widely applicable and does not require an estimate of the kinetic energy carry-over coefficient for example, whose value is often uncertain. Good agreement with measurements is demonstrated for both straight-through and stepped labyrinths. These new detailed results are examined, and several suggestions are offered for the advancement of simple analytical leakage as well as rotordynamic stability models.

Introduction

Labyrinth seals play a vital role in gas and steam turbines, compressors, and high-capacity pumps. In pumps the sealing objective is generally to minimize the leakage flow around the impellers, whereas for turbines it is often to maintain a minimal leakage flow for cooling hot parts. The seal designer accomplishes this by providing a highly dissipative flow path between high and low pressure regions. The flow passage through a labyrinth is illustrated in Fig. 1 for a simple straight-through seal configuration. Each tooth converts a portion of the available pressure head into mean flow kinetic energy, some of which is dissipated within the cavity immediately downstream.

Numerical simulation of labyrinth seal leakage employing the governing partial differential equations is relatively complicated and expensive. A recent literature search indicated that only Stoff [1] and Rhode, et al. [2] have reported such an investigation. Stoff's solution, which utilized the upwind Hybrid scheme, corresponded to his large scale experimental water facility consisting of a straight-through series of generic cavities as illustrated in Fig. 1. He compared a single radial profile of predicted mean swirl velocity, rms swirl velocity and turbulence dissipation rate with his corresponding measurements for an axial station midway between adjacent teeth. Rhode, et al. developed a finite difference procedure to compute the compressible flow cavity pressure drop at various leakage Mach numbers. These values were subsequently used in a Fanno analysis to predict the leakage rate and cavity-to-cavity stator wall pressure distribution.

For incompressible flow, several investigators have developed simple algebraic leakage models ranging from experimental data correlations to purely analytical expressions involving friction factor for example. One example of an analytical model is that developed by Bilgen and Akgungor [3]. They assumed turbulent couette and Poiseuille flows in the tangential and axial directions, respectively. In estimating the shear stress along the free shear layer, Han [4] recently considered the leakage flow energy consumed in driving the cavity vortex while estimating the wall shear stresses using Prandtl's flat plate boundary layer solutions. Another example is the work of Nikitin and Ipatov [5], who approximated frictional losses via analysis and data correlation, showing how the friction coefficient varies with tooth width, etc.

Objective

Depending on flowfield details, labyrinth seal solutions using the finite difference procedure of Stoff [1] may suffer from false diffusion numerical error, which is discussed in a later section. Simple analytical models often predict leakage rates only within about a factor of two, even for simple straight-through seal geometries such as that of Fig. 1. However, these modellers have done well considering the flowfield complexity and the limited detailed information available regarding rotating cavity flows. Thus there is a need for a leakage model of improved accuracy which is widely applicable and does not involve the uncertainty of an assumed kinetic energy carry-over coefficient for example. The present threefold objective is: to present a new approach for alleviating the convergence difficulty that occurs upon implementation of the QUICK scheme; to demonstrate the widely applicable capability for obtaining realistic labyrinth seal flowfield solutions; and to provide additional flowfield details to allow more realistic approximations for the refinement of simple analytical models.

Contributed by the Fluids Engineering Division of THE AMERICAN SOCIETY OF MECHANICAL ENGINEERS and presented at the Energy-Sources Technology Conference and Exhibit, New Orleans, La., February 12–16, 1984. Manuscript received the Fluids Engineering Division, May 4, 1984.

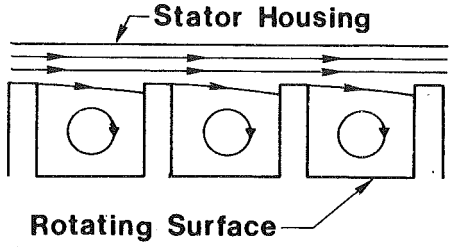

Fig. 1 Labyrinth seal with generic cavities illustrating the expected streamline pattern

Numerical Procedure

General Methodology. The numerical procedure employed is based on that of the TEACH computer program of Gosman and Pun [6]. The recent QUICK convective differencing scheme of Leonard, which is described below, was implemented in a version of the code which had previously been extended by Lilley and Rhode [7] to include swirl momentum. The computational domain consists of a single cavity as shown in Fig. 2.

The governing equations for this axisymmetric flow may be expressed in the general form

$$\frac{1}{r}\left[\frac{\partial}{\partial x}(\rho u r\phi)+\frac{\partial}{\partial r}(\rho v r\phi)-\frac{\partial}{\partial x}\left(r\Gamma_\phi\frac{\partial\phi}{\partial x}\right)-\frac{\partial}{\partial r}\left(r\Gamma_\phi\frac{\partial\phi}{\partial r}\right)\right]=S^\phi$$

where ϕ represents any of the dependent variables, and the equations differ primarily in their final source terms S^ϕ [7]. It is the standard high Reynolds number version of the two-equation k-ϵ turbulence model [8] which has been employed thus far. The presence of swirl momentum directly influences the values of k and ϵ, and in turn, the values of turbulent viscosity through the swirl velocity derivatives in the expression for turbulence energy production.

Boundary values at the inlet of a particular cavity are naturally very important, but unfortunately were unknown, as necessary quantitative flow measurements were unavailable even at a single operating condition. Due to this lack of inlet boundary data, for each numerical iteration the inlet values of each variable (except pressure) were assumed equal to the latest corresponding outlet values. This practice assumes the presence of a series of geometrically identical cavities and a streamwise periodic flow occurring downstream of the first two or three cavities.

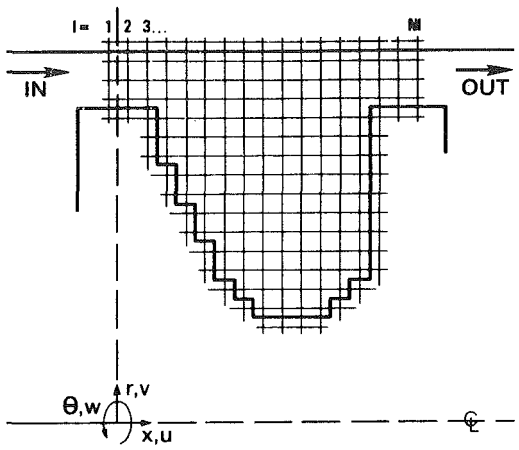

Fig. 2 Computational domain for a typical labyrinth seal cavity with a coarse grid illustrating the stairstep approximation

The user specifies a desired leakage flow rate, and the computer code calculates the associated cavity bulk pressure drop. Observe that by making several such computations, each with a different leakage rate, one may plot the leakage-pressure drop characteristic which is of considerable interest to the designer.

There are several techniques for simulating sloping wall boundaries such as that of the typical cavity geometry shown in Fig. 2. Sophisticated approaches include utilization of a body-fitted coordinate system or a coordinate transformation for mapping the physical plane onto an idealized computational domain. These methods require extensive reformulation of the governing differential equations, boundary conditions and formulae for length, area and volume. Moreover, expected numerical instabilities using the new coordinates along with the added complexity of the QUICK scheme render this a difficult task. Thus, in view of computer budget and manpower limitations the simpler stairstep approximation illustrated in Fig. 2 was adopted for the typical cavity configuration.

Locally, wall shear stress and heat flux on such a simulated wall will not generally agree closely with measurements. However, bulk as well as local velocities, etc. a slight distance

Nomenclature

A = coefficient of finite difference equation
B = auxiliary coefficient
c = tooth clearance
d = radial distance from cavity base to stator wall
HDS = hybrid upwind/central differencing scheme
k = turbulence kinetic energy
L = axial length of seal cavity
Pe = grid Péclet number
R = stator wall radius
r_{sh} = shaft radius to the base of a cavity
Re = Reynolds number
S_p,S_U = components of linearized source term
S = source term
Ta = Taylor number
U = bulk axial velocity at flow inlet
$V=(u,v,w)$ = time-mean velocity (in x, r, θ direction)
W = bulk swirl velocity
x,r,θ = axial, radial, azimuthal cylindrical polar coordinates
Γ = turbulent exchange coefficient
Δ = internodal mesh spacing
ϵ = turbulence dissipation rate
ϕ = generalized dependent variable
ρ = time-mean density
ν = kinematic viscosity
τ = shear stress
Ω = shaft speed

Subscripts

n,s,e,w = north, south, east, west faces of a control volume
N,S,E,W = first, i.e., immediately adjacent neighboring grid points to the North, South, East, West
NN,SS, . . . = second neighboring grid points to the North, South, East, West
eff = effective
lam = laminar

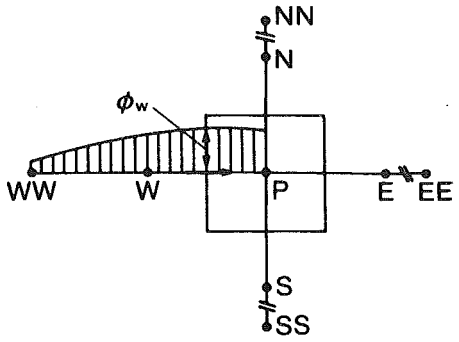

Fig. 3 Illustration of quadratic upwind interpolation for ϕ_w on the west face of a control volume with flow from left to right

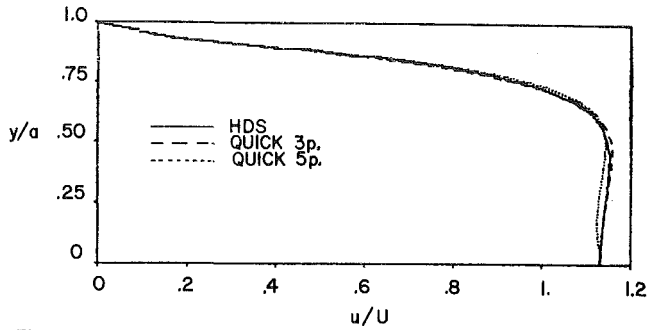

Fig. 4 Predicted axial velocity values at $x/a = 1.0$ using: (*a*) Hybrid; (*b*) three-point QUICK; and (*c*) five-point QUICK schemes for laminar flow between parallel plates separated by distance 2a

away from the wall have been found to be surprisingly accurate if careful attention is devoted to stairstep implementation details. For example Rhode, et al. [9] and Syed [10] found close agreement with measurements using this approach for flow past a backstep with a sloping wall. Also, Sindir [11] employed nearly the same implementation details and obtained close agreement with experiment for backstep flows with a deflected wall. Further, the flow along the simulated sloping wall exhibits extremely low velocity and is far removed from the all-important leakage flow region.

Implementation of QUICK Differencing Scheme. False diffusion is a second-order truncation numerical error. The upwind portion of the previous Hybrid upwind/central differencing scheme can result in an erroneous solution which is overly diffusive. This difficulty occurs where convection dominates (i.e., where the grid Peclet number $\mathrm{Pe} = |V|\Delta/\Gamma_\phi$ exceeds 2.0) in the presence of both streamline-to-grid skewness and diffusive transport normal to the flow direction. Recall that the upwind scheme is based on the uniform ϕ distribution assumption in evaluating ϕ at any face of a control volume. The recent QUICK (Quadratic Upstream Interpolation for Convective Kinematics) scheme of Leonard [12] greatly reduces false diffusion by utilizing either a five-point or a three-point, upwind-shifted quadratic interpolation formula in evaluating ϕ. Figure 3 graphically illustrates the three-point formula for a west face for example. The three-point interpolation expressions for this face, using a uniform grid for simplicity, are

$$\phi_w = \frac{1}{2}(\phi_p + \phi_W) - \frac{1}{8}(\phi_E - 2\phi_p + \phi_W)$$

if u_w is positive and

$$\phi_w = \frac{1}{2}(\phi_P + \phi_W) - \frac{1}{8}(\phi_P - 2\phi_W + \phi_{WW})$$

if u_w is negative. The first term in these expressions represents the centered difference formula, and the second is the crucial stabilizing upstream-weighted curvature contribution.

The QUICK expressions for an arbitrary non-uniform grid were incorporated by expressing each convected quantity ϕ in the convection terms of the difference equations with the appropriate interpolation formula. The standard expressions were used for all other quantities in the equation. Upon collecting terms the conventional difference equation of the form

$$A_P^\phi \phi_P = \sum_j A_j^\phi \phi_j + S_U^\phi$$

where

$$A_P^\phi = \sum_j A_j^\phi - S_P^\phi$$

was obtained. However, using the three-point expressions the summation occurs over

$$j = \mathrm{E, W, N, S, EE, WW, NN, SS}$$

where the last four neighbors were not involved previously using the Hybrid scheme.

The method of solving the equations is the same as for the previous Hybrid scheme formulation. For the solution of the difference equations for a vertical column of cells, the neighbor values along adjacent vertical columns are assumed to be temporarily known. Thus the equation for each cell involves only three unknowns, and the equation is arranged so that these appear on the left-hand side as

$$-A_N^\phi \phi_N + A_P^\phi \phi_P - A_S^\phi \phi_S = A_{EE}^\phi \phi_{EE} + \ \ldots\ + S_U^\phi$$

The set of these equations for the column of cells forms a tridiagonal coefficient matrix which is solved using an iterative, line-by-line application of the well known tridiagonal matrix algorithm.

Numerical convergence may be impaired as the A_j^ϕ coefficients may become negative when using QUICK. No false source transient terms are employed as a remedy as in reference [13]. Instead, for each iteration the difference equation for certain cells is re-arranged as needed to promote diagonal dominance of the tridiagonal coefficient matrix. This re-arrangement is applied to every cell for which any coefficient, for example A_{EE}^ϕ, is negative. In effect, this ad hoc procedure subtracts $B^\phi A_{EE}^\phi \phi_P$ from both sides of the difference equation in a very economical fashion. Observe that if $B^\phi = 1.0$, A_{EE}^ϕ no longer makes a negative contribution to the diagonal coefficient A_P^ϕ, and thus the diagonal dominance of the coefficient matrix is enhanced.

The source term S_U^ϕ becomes

$$S_U^\phi = S_U^\phi - B^\phi A_{EE}^\phi \phi_p^+$$

where ϕ_p^+ is the current "in-store" value of ϕ_P. Values of 1.0 have routinely been used without difficulty for B^u, B^v, and B^w even though this value allows the possibility that $A_P^\phi = 0.0$. If necessary this can easily be precluded by specifying values near 0.8 for example.

At present the k and ϵ equations employ the Hybrid scheme for computational economy reasons. Leschziner and Rodi [14] have supported this practice in explaining that solutions for k and ϵ were found to be unaffected by the convected differencing scheme, espeically in the shear layer bordering a recirculation zone. They attribute this to the fact that the source terms of these equations are dominant.

Numerical Testing

The implementation of QUICK was extensively checked by comparison with corresponding Hybrid scheme results and measurements where available. The test problems selected include elliptic and parabolic problems with and without turbulence and with and without swirl momentum. The simplest of these concerns laminar flow in the boundary layer development region between parallel plates separated by a distance of $2a$. The flow enters with a uniform velocity profile at $\mathrm{Re} = 150$. This problem exhibits very slight streamline-to-grid skewness, and thus negligible false diffusion, so that the solu-

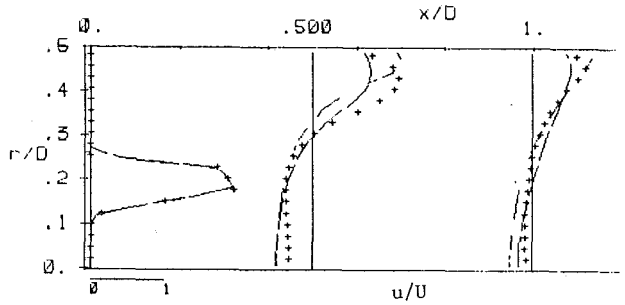

Fig. 5 Axial velocity of swirling flow through a pipe expansion showing predictions using (*a*) the Hybrid (——) and (*b*) the three-point QUICK scheme (---) along with previous measurements [16] (+ + +)

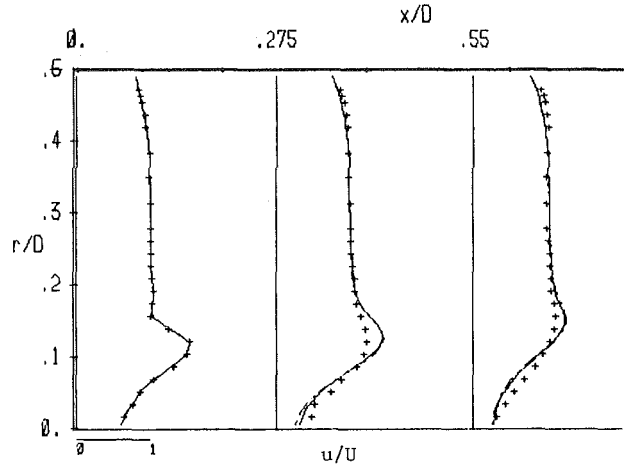

Fig. 6 Axial velocity of coswirling annular jets in a pipe showing predictions using (*a*) the Hybrid (——) and (*b*) the three-point QUICK scheme (— — —) along with previous measurements [17] (+ + +)

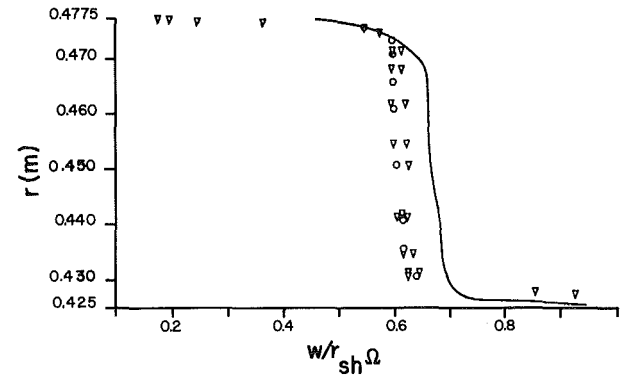

Fig. 7 Comparison of present prediction (——) of dimensionless swirl velocity with corresponding LDA measurements (o o o, ▽ ▽ ▽) of Stoff [1] at $x/L = 0.5$

tion from both the three-point and five-point QUICK formulations should agree with that of the Hybrid approach. Figure 4 indeed shows a maximum deviation among these solutions of only 1.6 percent using a 48×20 grid. The value is only half this much farther downstream.

This flow problem, grid distribution, boundary condition data, etc. is precisely identical to that used by Pollard and Siu [15] in evaluating their important implementation approaches of the three-point QUICK scheme. Their formulation named QUICKE would not always converge to a solution, and thus they recommend their QUICKER approach. By normalizing the required CPU time and number of numerical iterations by the corresponding Hybrid scheme values, somewhat meaningful comparisons between the previous QUICKER and the present formulations are possible. These values are found in Table 1. Observe that the present three-point implementation using diagonal dominance enhancement seems to be somewhat more desirable.

Table 1 Convergence data for flow between parallel plates

Scheme	T/T_{HDS}	N/N_{HDS}	$(T/N)/(T_{HDS}/N_{HDS})$
HDS	1.00	1.00	1.00
QUICK 3 p.	1.34	0.99	1.34
QUICK 5 p.	1.76	1.05	1.66
QUICKE	0.84	0.60	1.41
QUICKER	1.85	1.32	1.40

T-computational time
N-number of iterations

Table 2 Convergence data for flow through pipe expansion

Scheme	T/T_{HDS}	N/N_{HDS}	$(T/N)/(T_{HDS}/N_{HDS})$
HDS	1.00	1.00	1.00
QUICK 3 p.	1.31	1.00	1.31
QUICK 5 p.	1.62	0.99	1.64

T – computational time
N – number of iterations

Laminar flow through an abrupt pipe expansion of diameter ratio 2.0 constitutes a more complicated case in which a large recirculation eddy exists behind the step. A fully developed laminar velocity profile was specified at the inlet where $Re = 200$. Once again, there was little false diffusion in the Hybrid scheme solution resulting in no significant deviations among the three solutions employing a 34×22 grid. Table 2 shows the relative convergence data to be very similar to that for the case of parallel plates. Note that the three-point scheme is naturally more economical. Since Leonard also found little loss of accuracy in using the three-point as opposed to the five-point version of QUICK, the five-point formula was discontinued.

The next case is that measured by Rhode, et al. [16]. Here again the flow passes through an abrupt pipe expansion of diameter ratio 2.0. However, this problem is much more complicated, involving turbulent swirling flow with an inlet $Re = 1.1 \times 10^5$ and upstream swirl vane angles oriented at 38 degrees from the downstream direction. A nonuniform 40×25 grid was utilized. Figure 5 shows the improvement of the QUICK results over that of the Hybrid scheme for the annular peak value of axial velocity at $x/D = 0.5$ and $r/D = 0.4$. This improvement was anticipated because substantial false diffusion arises at $x/D = 0.25$ from the slope of the streamlines which is near 45 deg. However, closer agreement with measurements was expected. One possible reason for this is error in the measurement of inlet boundary values due to adverse conditions there, a location immediately downstream of the swirler where a non-axisymmetric region of low velocity occurs.

The turbulent co-swirling concentric jet flow in a pipe measured by Vu and Gouldin [17] constitutes another test case. In this flow, however, measurements were available for use as inlet boundary values for every quantity including k and ϵ. Based on chamber diameter and bulk velocity, $Re = 2.96 \times 10^5$ and the swirl parameter for the inner and outer jets was 0.58 and 0.54, respectively. A highly nonuniform 35×30 grid was employed. Streamline skewness is very slight, and as shown in Fig. 6, the two solutions are almost identical. Also, observe that both solutions are in good agreement with measurements.

Results and Discussion

Experimental Verification for Labyrinth Seals. A literature search indicated that only the paper by Stoff [1] gives detailed quantitative velocity measurements within a labyrinth seal cavity. He utilized a large scale test section model of a straight-through seal with rectangular cavities through which water flowed. The Reynolds number

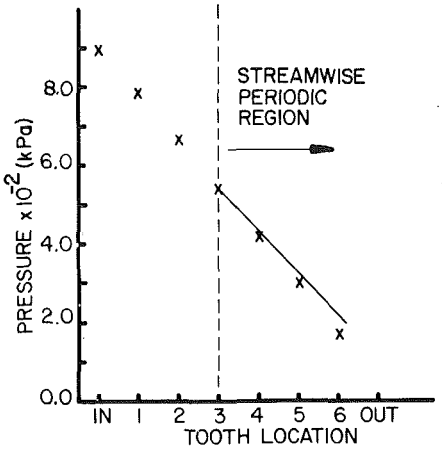

Fig. 8 Measured tooth-to-tooth pressure distribution (× × ×) the streamwise periodic prediction (——) plotted to match the measured pressure at the third tooth

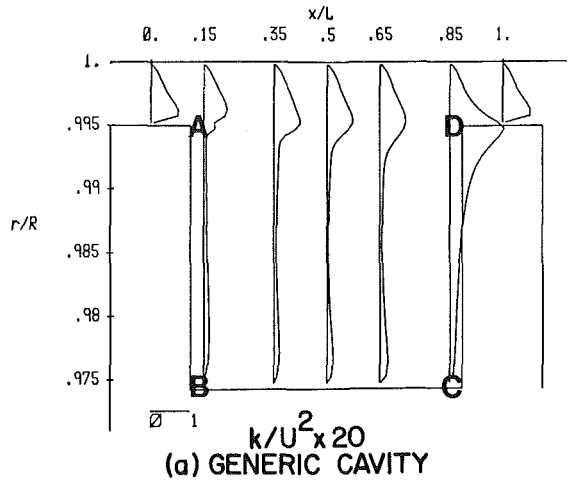

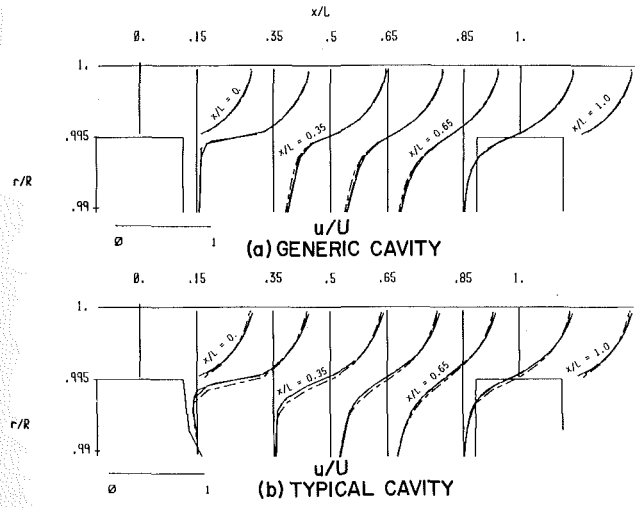

Fig. 9 Axial velocity prediction for (*a*) the generic and (*b*) the typical seal cavity employing 33 × 31 QUICK (——), 53 × 53 Hybrid (— —) and 33 × 31 Hybrid (—·—) solutions

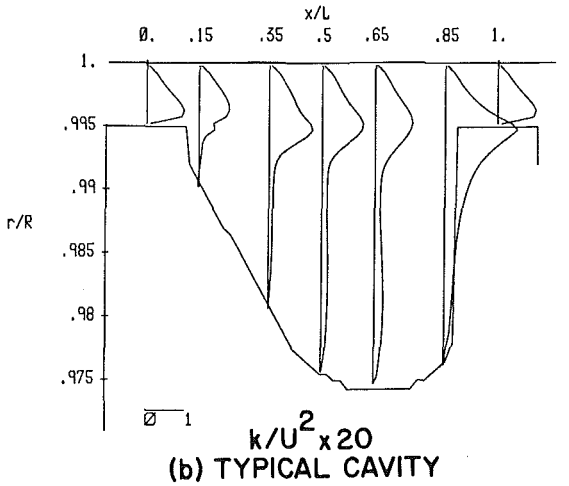

Fig. 10 Predicted turbulence kinetic energy for (*a*) the generic and (*b*) the typical seal cavity using the QUICK scheme

$\mathrm{Re} \equiv 2Uc/\nu \approx 3.4 \times 10^2$ and the Taylor number $\mathrm{Ta} \equiv (Wd/\nu)(d/r_{sh})^{1/2} \approx 1.1 \times 10^4$. Figure 7 shows that swirl velocity predictions are within 6.0 percent of Stoff's corresponding measurements.

The measurements of Morrison, et al. [18] for the tooth-to-tooth pressure distribution of stepped labyrinth seals flowing water were employed in a series of further prediction tests. In the experimental facility, a single static pressure tap was located at each tooth on the stator wall. The dimensionless flow parameters were $\mathrm{Re} = 4.95 \times 10^3$ and $\mathrm{Ta} = 6.7 \times 10^3$. The result for one case with six cavities is given in Fig. 8. The predicted value of bulk pressure drop per cavity for the streamwise periodic cavities was 105 kPa. This was translated into the predicted streamwise periodic pressure distribution, which was plotted by graphical construction using this slope while matching the pressure measured at the third tooth. Note that streamwise periodicity commences at approximately the third tooth. The measured pressure drop per cavity averaged 123 kPa in this region, yielding a discrepancy of under 15.0 percent.

Seal Flowfields Considered. The operating conditions of the two cavity geometries investigated are identical. Liquid hydrogen at 42°R enters a cavity with tooth-clearance bulk velocity $U = 338$ m/s. The primary dimensionless flow parameters are $\mathrm{Re} = 1.0 \times 10^6$ and $\mathrm{Ta} \equiv 1.3 \times 10^5$. Other conditions are: shaft speed $\Omega = 35{,}410$ rpm, cavity axial length $L = 1.113$ mm, stator wall radius $R = 42.89$ mm, tooth radial clearance $c = 0.216$ mm, radial distance from cavity base to stator wall $d = 1.105$ mm, and kinematic viscosity $\nu = 1.462 \times 10^{-7}$ m^2/s.

Not included here are the streamline plots, which show that the dividing streamline exhibits a reattachment stagnation point which is very slightly below the peripheral corner of the downstream tooth. This occurs for both cavity geometries. In both cases the slope of a straight line approximation for the dividing streamline is near 2 degrees below horizontal. This serves to aid the developers of simple analytical models, as an assumed value near 7 degrees has been employed by Jerie [19] for example.

Axial velocities from several solutions for the generic case are shown in Fig. 9(*a*) which reveals that the 33 × 31 QUICK and 53 × 53 Hybrid solutions are essentially identical. The 33 × 31 Hybrid and 53 × 53 Hybrid solutions differ very slightly. As with the generic cavity, Fig. 9(*b*) shows that the 33 × 31 QUICK and the 53 × 53 Hybrid solutions of axial velocity for the typical cavity are nearly identical. Note that in this case the 33 × 31 Hybrid solution is not grid independent in the free shear layer. The axial velocity values of this solution deviate from those of the other two by as much as 20 percent.

Observe at this point that the QUICK approach exhibits an

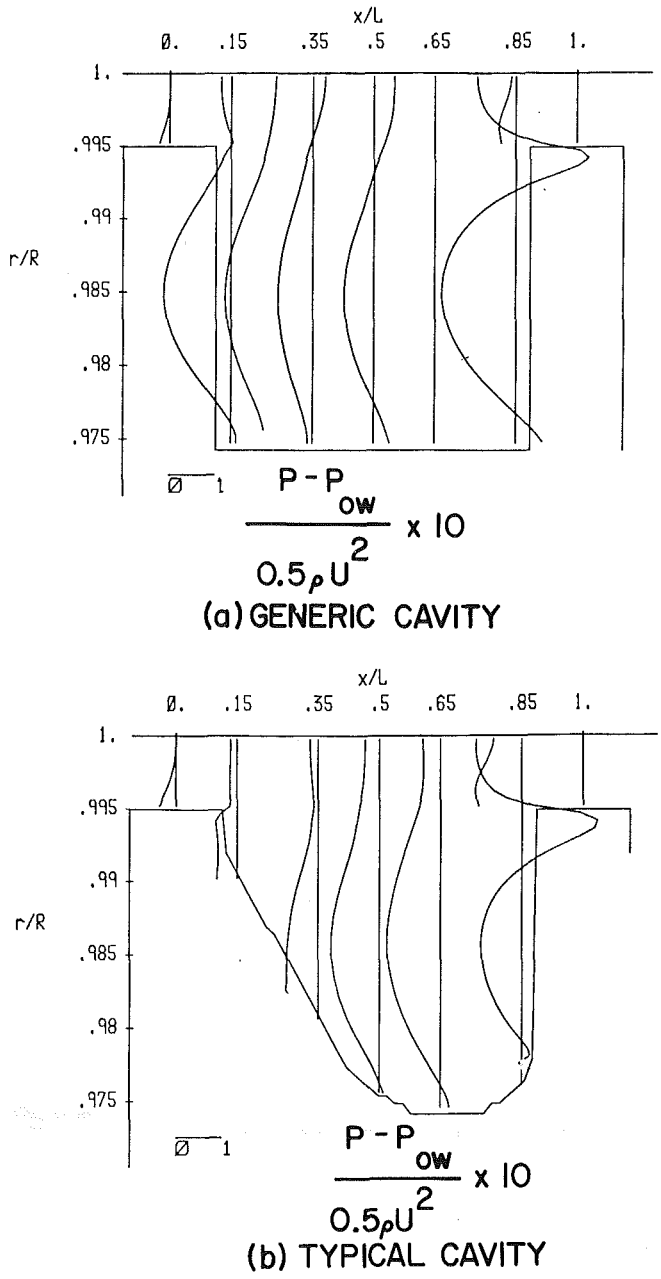

Fig. 11 Predicted relative pressure for (*a*) the generic and (*b*) the typical seal cavity using the QUICK scheme

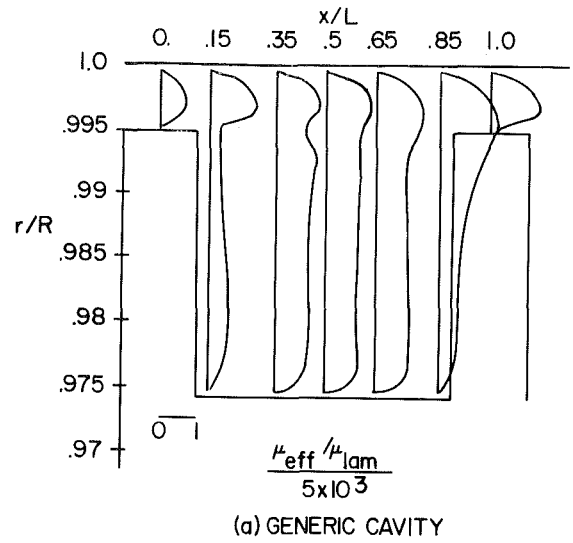

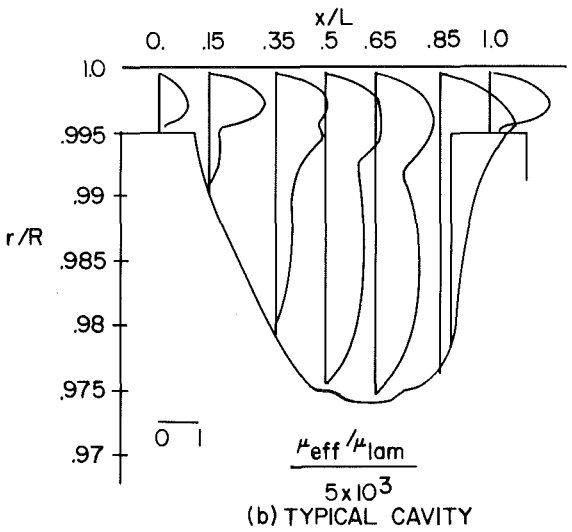

Fig. 12 Predicted effective viscosity from the k-ϵ model for (*a*) a generic and (*b*) a typical seal cavity using the QUICK scheme

economic advantage over the Hybrid approach. In obtaining a grid independent solution, utilization of the Hybrid method requires 53×53 grid points whereas utilization of QUICK requires only 33×31 points. The execution time required for the QUICK solution is only 44% of that required by the Hybrid version. This is mostly attributed to the well known apparent sluggish response to grid refinement of the upwind portion of the Hybrid scheme. As demonstrated by Han, et al. [13], this lack of response is actually a false diffusion effect.

Figures 10(*a*) and 10(*b*) illustrate the fundamental physical mechanism of labyrinth seal performance. The large value of $\partial u/\partial r$ in the free shear layer yields a high generation rate of turbulence kinetic energy in this region. A portion of this turbulence energy is transported into the recirculation region which is clearly seen to act as an effective region of viscous dissipation. This turbulence generation and dissipation within each cavity is the basic means by which the upstream total mechanical energy is irreversibly converted into heat. Observe in these figures that the typical cavity is expected to achieve a higher pressure drop due to higher levels of turbulence energy.

The distribution of pressure relative to the cavity inlet stator wall pressure P_{OW} is shown in Figs. 11(*a*) and 11(*b*). In the leakage flow region of the generic cavity, the pressure variation is partly a reflection of the Bernoulli effect of pressure decrease at constrictions in flow area. A sharp positive pressure peak, which occurs in an annular fashion near $x/L = 0.85$, results from the flow stagnation on the downstream tooth. The overall pressure drop from inlet to outlet of this cavity is predicted as approximately 6.0×10^2 kPa.

The pressure distribution within the typical cavity is seen in Fig. 11(*b*) to exhibit similar trends. However, leakage flow pressure varies in the streamwise direction much more gradually for this geometry upstream of $x/L = 0.65$. Downstream of this location it decreases more rapidly than for the generic case as the flow area constricts in passing over the downstream tooth. The predicted bulk pressure drop for this cavity is approximately 8.0×10^2 kPa, an increase of 33 percent over the generic geometry.

Swirl velocity distributions are not included here. They are quite uniform with values of 0.65 and 0.69 for the generic and typical configurations, respectively, when nondimensionalized by the circumferential velocity of the cavity base. Simple

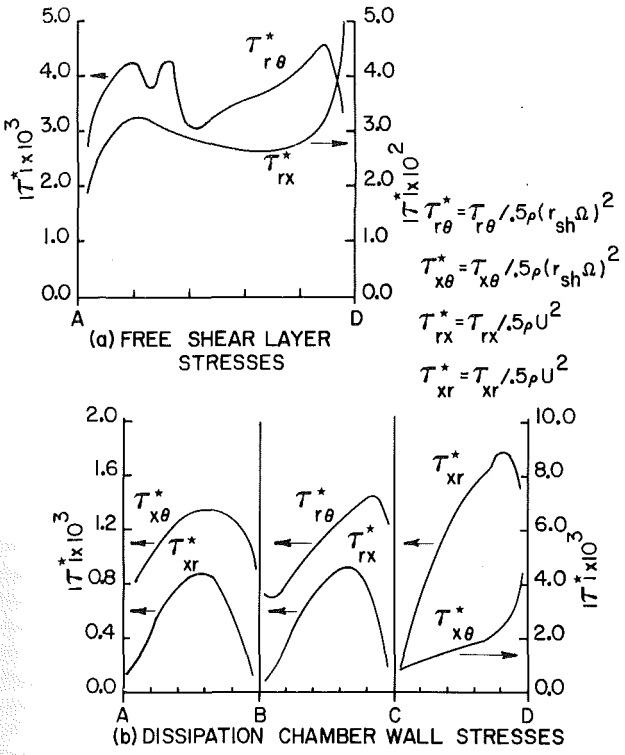

Fig. 13 Predicted shear stress components along various planes (see Fig. 10) of the generic cavity

models may employ uniform values in this range for similar configurations.

The isotropic turbulent viscosity values resulting from the k-ϵ turbulence model via

$$\mu_{\text{eff}} = C_\mu \rho k^2/\epsilon + \mu_{\text{lam}}$$

are given in Fig. 12(*a*) and 12(*b*). In accordance with turbulence energy values, the typical cavity exhibits the greater viscosity values. Viscosity profiles are much more uniform than turbulence energy profiles because, even though μ_{eff} varies with turbulence energy squared, the dissipation values in the free shear region are more than a hundred times larger than in the recirculation zone.

Figure 13(*a*) gives the magnitude of both components of shear stress coefficient for the generic cavity along plane AD of the free shear layer as labeled in Fig. 10(*a*). Observe that the axial component is an order of magnitude larger than the circumferential component. Further, it drastically increases near the reattachment point, as the flow undergoes large gradients in this region of maximum effective viscosity.

The shear stress components along each of the three walls of the dissipation chamber have been evaluated in simple analytical models [4] using Prandtl's flat plate turbulent boundary layer solution for example. The upstream corner of each wall was taken as the leading edge. Figure 13(*b*) shows the present predictions which indicate different behavior. The peaks arising midway along CB and BA are largely attributed to the significant pressure gradients which have not been accounted for in the boundary layer solution. The abrupt variation near point D results from the high viscosity near the stagnation point.

Conclusion

A new and relatively simple method was developed for alleviating the convergence difficulty which arises upon implementation of the QUICK scheme. The required CPU time and number of numerical iterations, as a percentage of that required by the previous Hybrid scheme, are shown to compare favorably with a previously recommended approach. Due to space limitations, the solutions presented here are only a sample of those computed in evaluating this approach.

The labyrinth seal computer code is seen to provide realistic results for both straight-through and stepped labyrinths. There is no worrisome uncertainty of assuming a value for the mean flow kinetic energy carry-over coefficient for example. The present solutions allow the advancement of simple analytical leakage models via refinement of various important approximations. Results of particular interest in this regard for generally similar cavities are:

(i) the dimensionless swirl velocity is accurately represented by a uniform value near 0.65;

(ii) the slope of the dividing streamline may be approximated as 2 degrees below the horizontal;

(iii) the predicted shear stress distributions on planes where they are often required by analytical methods are presented for modelling approximations as appropriate.

Acknowledgment

The developments and results presented here are a by-product of two studies for which the financial support of AFOSR and NASA Marshall Space Flight Center are gratefully acknowledged. Also, the expert typing skills of Ms. Bich-N. Ho are greatly appreciated.

References

1 Stoff, H., "Incompressible Flow in a Labyrinth Seal," *Journal of Fluid Mechanics*, Vol. 100, 1980, pp. 817–829.

2 Rhode, D. L., and Sobolik, S. R., "Simulation of Subsonic Flow in Labyrinth Seals," accepted for publication in ASME *Journal of Engineering for Gas Turbines and Power*, Vol. and page nos. unavailable.

3 Bilgen, E., and Akgungor, A. C., "Leakage and Frictional Characteristics of Large Diameter Labyrinth Seals," National Conference on Fluid Power, 1972, pp. 85–101.

4 Han, J. T., "A Fluid Mechanics Model to Estimate the Leakage of Incompressible Fluids through Labyrinth Seals," ASME Paper 79-FE-4, presented at the Joint ASME/CSME Applied Mechanics, Fluids Engineering and Bioengineering Conference, Niagra Falls, June 18–20, 1979.

5 Nikitin, G. A., and Ipatov, A. M., "Design of Labyrinth Seals in Hydraulic Equipment," *Russian Engineering Journal*, Vol. 53, No. 10, 1973, pp. 26–30.

6 Gosman, A. D., and Pun, W. M., "Calculation of Recirculating Flows," Rept. No. HTS/74/2, 1974, Dept. of Mech. Engr., Imperial College, London, England.

7 Lilley, D. G., and Rhode, D. L., "A Computer Code for Swirling Turbulent Axisymmetric Recirculating Flows in Practical Isothermal Combustor Geometries," NASA CR-3442, Feb. 1982.

8 Launder, B. E., and Spalding, D. B., "The Numerical Computation of Turbulent Flows," *Comp. Methods in Appl. Mech. and Engrg.*, Vol. 3, 1974, pp. 269–289.

9 Rhode, D. L., Lilley, D. G., and McLaughlin, D. K., "On the Prediction of Swirling Flowfields Found in Axisymmetric Combustor Geometries," ASME *Journal of Fluids Engineering*, Vol. 104, 1982, pp. 378–384.

10 Syed, S. A., personal communication, 1984.

11 Sindir, M., "Calculation of Deflected-Walled Backward-Facing Step Flows: Effects of Angle of Deflection on the Performance of Four Models of Turbulence," ASME paper No. 83-FE-16.

12 Leonard, B. P., "A Stable and Accurate Convective Modelling Procedure Based on Quadratic Upstream Interpolation," *Comp. Meths. Appl. Mech. Eng.*, Vol. 19, 1979, pp. 59–98.

13 Han, T., Humphrey, J. A. C., and Launder, B. E., "A Comparison of Hybrid and Quadratic-Upstream Differencing in High Reynolds Number Elliptic Flows," *Comp. Meths. Appl. Mech. Eng.*, Vol. 29, 1981, pp. 81–95.

14 Leschziner, M. A., and Rodi, W., "Calculation of Annular and Twin Parallel Jets Using Various Discretization Schemes and Turbulence-Model Variations," ASME JOURNAL OF FLUIDS ENGINEERING, Vol. 103, 1981, pp. 352–360.

15 Pollard, A., and Siu, A. L., "The Calculation of Some Laminar Flows Using Various Discretization Schemes," *Comp. Meths. Appl. Mech. Eng.*, Vol. 35, 1982, pp. 293–313.

16 Rhode, D. L., Lilley, D. G., and McLaughlin, D. K., "Mean Flowfields in Axisymmetric Combustor Geometries with Swirl," *AIAA Journal*, Vol. 21, No. 4, 1983, pp. 593–600.

17 Vu, Bach T., and Gouldin, F. C., "Flow Measurements in a Model Swirl Combustor," *AIAA Journal*, Vol. 20, No. 5, 1982, pp. 642–651.

18 Morrison, G. L., Rhode, D. L., Cogan, K. C., Chi, D., "Labyrinth Seals for Incompressible Flow," Final Report for NASA Contract NAS8-34536, November 1983.

19 Jerie, J., "Flow Through Straight-Through Labyrinth Seals," *Proceedings of the Seventh International Congress of Applied Mechanics*, 1948, Vol. 2, pp. 70–82.

Y. Tsujimoto
Research Associate,
Doctor of Engineering.

K. Imaichi
Professor Emeritus,
Doctor of Engineering.
Mem. ASME

Osaka University,
Faculty of Engineering Science,
Toyonaka, Osaka, Japan

T. Tomohiro
Research Engineer,
Matsushita Housing Equipment.

M. Gotoo
Research Engineer,
Ebara Research Co., LTD.

A Two-Dimensional Analysis of Unsteady Torque on Mixed Flow Impellers

A new method is given for the analysis of unsteady flows through mixed flow impellers under an assumption of a two-dimensional flow in a representative flow surface of revolution. The flow is mapped to one around a two-dimensional annular cascade. If the thickness of the impeller flow passage changes in a certain functional form, the flow can be represented by using a two-dimensional potential flow in the mapping plane. For impellers with such a thickness distribution, small sinusoidal and/or large transient fluctuations of flow rate and/or rotational velocity are considered. Special attention is paid to the unsteady torque on the impeller. The unsteady torque is divided into three components – quasisteady, apparent mass and wake, and the effects of the geometry of the flow surface on each component are discussed. Apparent mass torque coefficients are determined for fluctuations of flow rate and rotational velocity. Stability of torsional vibration and surging are discussed from energy considerations.

Introduction

The development of computing methods of three-dimensional flows in turbomachinery impellers has been the subject of extensive investigation in recent years. For the analysis of steady flows, quasi-three-dimensional methods [1, 2] consisting of successive solutions of meridional and blade to blade flows have been developed to the extent that they are widely used in the designing stage of turbomachinery. More recently, three-dimensional numerical methods [3, 4] are beginning to be used in combination with the quasi 3-D methods.

On the other hand, most existing methods for the analysis of unsteady flows have been limited to cases of axial flow turbomachines [5–8, 20]. Recently, several unsteady flow analyses have been made for two-dimensional centrifugal impellers involving transient characteristics during start up [9], vibration of vanes [10] and whirling instability of rotors [11]. For mixed flow impellers, the authors are aware only of analyses by MacCormack methods [12] and by finite element methods [13].

This paper treats unsteady flows through mixed flow impellers when the flow rate and/or the rotational velocity change periodically and/or transiently. *We assume that the thickness of the impeller flow passage is small and the flow can be represented by a two-dimensional flow in a representative flow surface.* We apply a stream function formulation similar to that used by Hoffmeister [14] for an analysis of steady flow. The flow in the representative flow surface is mapped to one around a two-dimensional *annular* cascade. If the thickness of the impeller flow passage changes in a certain functional form, the flow can be expressed by using a two-dimensional potential flow in the mapping plane. We consider impellers with such a thickness distribution and apply a singularity method in the mapping plane for the determination of the flow.

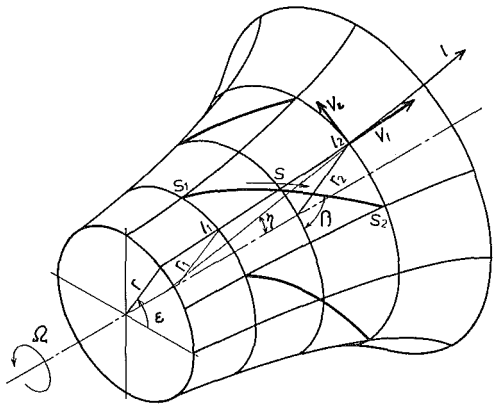

Fig. 1 Representative flow surface

This paper is an extension of the author's analysis [15, 16] for 2-D centrifugal impellers. Among the various unsteady characteristics, we take a special interest in the unsteady torque on the impeller. It is directly related to the stability of the torsional vibration of the impeller. Stability against surging can also be discussed from energy considerations. The unsteady torque is divided into three components – quasisteady, apparent mass, and wake. It is shown that the wake component is usually smaller than the other components. Hence, a rough estimate of the total unsteady torque is obtained by simply adding the quasisteady and apparent mass components. Apparent mass torque coefficients are defined and calculated for the angular velocity and flow

Contributed by the Fluids Engineering Division for publication in the JOURNAL OF FLUIDS ENGINEERING. Manuscript received by the Fluids Engineering Division, March 28, 1985.

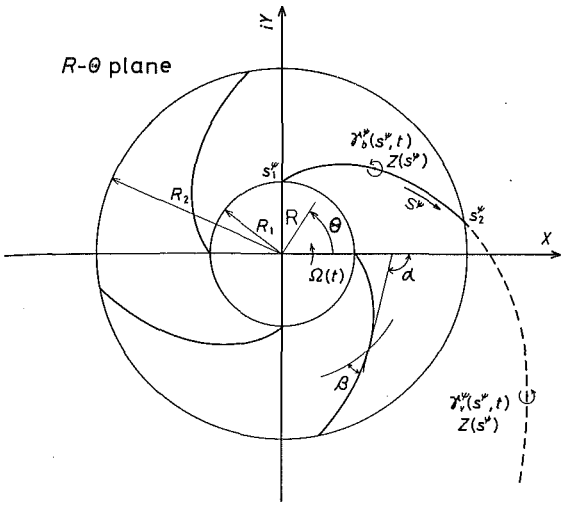

Fig. 2 Mapping plane

rate fluctuations. The effect of the geometry of the flow surface on each component is discussed.

It is assumed that the flow is inviscid, incompressible and free from separation and cavitation. We treat only the cases in which the thickness of the vanes and the effects of the volute can be neglected.

Basic Equations and Mapping

We consider the cases where the thickness b of the impeller flow passage is small and the flow can be represented by a two-dimensional flow in a representative flow surface as shown in Fig. 1. We call this surface a "physical plane." For incompressible flows, the equations of continuity and irrotationality can be expressed as follows.

$$\frac{\partial}{\partial l}\left(v_l \frac{b}{b_2} r\right)+\frac{\partial}{\partial \epsilon}\left(v_\epsilon \cdot \frac{b}{b_2}\right)=0 \tag{1}$$

$$\frac{\partial}{\partial l}(v_\epsilon \cdot r)-\frac{\partial}{\partial \epsilon} v_l=0 \tag{2}$$

We introduce a stream function Ψ defined by

$$\frac{\partial \Psi}{\partial \epsilon}=\frac{b}{b_2} r v_l, \quad \frac{\partial \Psi}{\partial l}=-\frac{b}{b_2} v_\epsilon. \tag{3}$$

Then the continuity equation (1) is automatically satisfied and the basic equation for Ψ is derived by substitution of equations (3) into equation (2). Assuming that r and b are functions of l and not of ϵ, we obtain

$$\frac{\partial^2 \Psi}{\partial l^2}+\frac{1}{r^2}\frac{\partial^2 \Psi}{\partial \epsilon^2}+\frac{\partial \Psi}{\partial l}\left\{\frac{1}{r}\frac{dr}{dl}-\frac{b_2}{b}\frac{d}{dl}\left(\frac{b}{b_2}\right)\right\}=0. \tag{4}$$

Hoffmeister [14] mapped the flow to that around a linear cascade but we map it to one around a circular cascade in $R-\Theta$ plane (see Fig. 2) by using the following mapping relations.

$$\frac{d\Theta}{d\epsilon}=\frac{\Theta}{\epsilon}=1, \quad \frac{dl}{r}=\frac{dR}{R} \tag{5}$$

Then the basic equation (4) can be represented in the mapping plane by:

$$\frac{\partial^2 \Psi}{\partial R^2}+\frac{1}{R^2}\frac{\partial^2 \Psi}{\partial \Theta^2}+\frac{\partial \Psi}{\partial R}\left\{\frac{1}{R}-\frac{b_2}{b}\frac{d}{dR}\left(\frac{b}{b_2}\right)\right\}=0 \tag{6}$$

Here we assume that the stream function Ψ is expressed by

$$\Psi=f(R)\psi+\frac{Q(t)}{2\pi b_2}\Theta \tag{7}$$

using a harmonic function ψ and a function $f(R)$ to be determined.

Considering that ψ is harmonic, we can easily find that the stream function of equation (7) satisfies the basic equation (6) if the function $f(R)$ and the thickness distribution $b(R)$ are solutions of the following simultaneous differential equations.

$$f''+f'/R-f'b'/b=0$$

$$2f'-fb'/b=0$$

After integration we obtain

$$f(R)=1/\{1+P\ln(R/R_2)\}=H(R)^{-1} \tag{8}$$

$$b/b_2=f^2=1/\{1+P\ln(R/R_2)\}^2 \tag{9}$$

where

$$P=(1-\sqrt{b_2/b_1})/\ln(R_2/R_1) \tag{9'}$$

Hence, for impellers with thickness distribution given by equation (9), the stream function Ψ can be represented by equation (7) using the function $f(R)$ of equation (8) and the harmonic function ψ. We treat here impellers of such thickness distribution. As can be easily seen for centrifugal ($R = r = l$) or axial flow ($R = R_1 e^{l/r}$, r = constant) impellers, the thickness distribution given by equation (9) is a realistic one. Hence, it is expected that there are many cases where the present method

Nomenclature

A = constant, representing the slope of head-capacity characteristic
b = thickness of impeller flow passage
C_a^Ω, C_a^φ = apparent mass torque coefficients, equations (26), (27)
E = energy transferred to the fluid owing to one cycle of fluctuations
F = fluctuating torque coefficient
$f(R), H(R)$ = functions of R, equation (8)
g = gravitational acceleration constant
H_{th} = theoretical head
h = $h_s - A\varphi$, head coefficient
h_s = shut-off head coefficient
i,j = imaginary units with respect to space and time
k = ω/Ω_0, nondimensional frequency
l,ϵ = meridional and angular coordinates in physical plane
L = $(l_2 - l_1)/r_2$, relative length of the flow surface
M = number of vortex points
N = number of vanes
P = constant, equation (9)'
$Q(t), Q_0$ = volumetric flow rate and its steady component
r = radius of the representative flow surface of revolution
R,Θ = radial and angular coordinates of mapping plane
s = coordinate along vane or trailing vortex surface
t = time
t^* = $t/(2\pi/\Omega_1)$, nondimensional time
T = torque
v = absolute velocity in physical plane

can be applied by appropriately giving the outer to inner thickness ratio b_2/b_1.

Now the problem is reduced to determining the harmonic function ψ so that the total flow satisfies the boundary conditions on the vane surface and in the upstream. From equations (3), (5), and (7), the absolute velocity in the physical plane is expressed as follows.

$$\left.\begin{aligned} v_l &= \frac{Q(t)}{2\pi r b_2} H^2 + \frac{R}{r} H V_R^\psi \\ v_\epsilon &= \frac{P}{r}\psi + \frac{R}{r} H V_\Theta^\psi \end{aligned}\right\} \tag{10}$$

where

$$V_R^\psi = \frac{1}{R}\frac{\partial \psi}{\partial \Theta} \quad \text{and} \quad V_\Theta^\psi = -\frac{\partial \psi}{\partial R}.$$

Expression of ψ and Boundary Conditions

For the determination of the harmonic function ψ, we apply a singularity method in the mapping plane. For infinitely thin vanes, we should use singularities in the mapping plane such that no normal velocity difference is induced across the vanes or wakes in the physical plane. From equation (10), we find that a vortex distribution γ^ψ in the mapping plane represents a flow with continuous normal velocity and with a tangential velocity discontinuity $\gamma = R/r\, H\gamma^\psi$ in the physical plane. In the case of unsteady flows, free vortices are shed from the trailing edges and form trailing vortex sheets. Representing the vortex distribution on the vane surface by γ_b^ψ and the trailing vortex distribution by γ_v^ψ, we can express ψ in terms of $z = x + iy = Re^{i\Theta}$ as:

$$\psi(z,t) = \psi_0 - \frac{1}{2\pi}\sum^N \left[\int_{s_1^\psi}^{s_2^\psi} \gamma_b^\psi(s^\psi,t)\{\ln|z - z(s^\psi)| - \ln|z(s^\psi)|\}ds^\psi + \int_{s_2^\psi}^{\infty} \gamma_v^\psi(s^\psi,t)\{\ln|z - z(s^\psi)| - \ln|z(s^\psi)|\}ds^\psi\right] \tag{11}$$

where $\sum^N$ represents the summation for all of the vanes. Correspondingly we have

$$V_x^\psi - iV_y^\psi = \frac{\partial \psi}{\partial y} + i\frac{\partial \psi}{\partial x} = (V_s^\psi - iV_n^\psi)e^{-i\alpha} = (V_R^\psi - iV_\Theta^\psi)e^{-i\Theta}$$

$$= \frac{1}{2\pi i}\sum^N \left[\int_{s_1^\psi}^{s_2^\psi} \frac{\gamma_b^\psi(s^\psi,t)}{z - z(s^\psi)}\, ds^\psi + \int_{s_2^\psi}^{\infty} \frac{\gamma_v^\psi(s^\psi,t)}{z - z(s^\psi)}\, ds^\psi\right] \tag{12}$$

where α is the angle between the tangent of the vortex surface and the x-axis.

The component of the rotational velocity normal to the vane surface is given by $r\Omega(t)\sin\beta$ and the normal velocity should coincide with this value. By using equation (10), we can express this condition as

$$r\Omega(t)\sin\beta = \frac{Q(t)}{2\pi r b_2} H^2 \cos\beta + \frac{P}{r}\psi \sin\beta + \frac{R}{r} H V_n^\psi \tag{13}$$

where ψ and V_n^ψ can be expressed in terms of γ_b^ψ and γ_v^ψ by using equations (11) and (12). As will be shown in the next section, the strength and the position of γ_v^ψ are determined by using the value of γ_b^ψ in the past. Hence equation (13) gives an integral equation to determine γ_b^ψ. This equation is solved for γ_b^ψ with the complementary use of an unsteady Kutta condition.

Let us consider the flow upstream of the impeller. If we let $R \to 0$ in equation (10) after the substitution of equation (12), we see that

$$v_l \to \frac{Q(t)}{2\pi r b_2} H^2 = \frac{Q(t)}{2\pi r b} \quad \text{and} \quad v_\epsilon \to \frac{P}{r}\psi_0.$$

This means that $Q(t)$ is the volumetric flow rate through the impeller and that ψ_0 is proportional to the strength of prerotation. In this study, we consider only cases without prerotation.

Treatment of Free Vortex Sheet

Applying the unsteady pressure equation in a frame rotating with the impeller on the upper and lower surfaces of the free vortex sheet and assuming that the pressure is continuous across the sheet, we obtain the following equation.

$$\frac{\partial}{\partial t}\int_{s_1}^{s_2} \gamma_b(s,t)ds + \frac{\partial}{\partial t}\int_{s_2}^{s} \gamma_v(s,t)ds + w_m\gamma_v(s,t) = 0 \tag{14}$$

where w_m is the average of the tangential component of the relative velocities on the upper and lower surfaces of the vortex sheet. This equation means that the free vortices move with average relative velocity, w_m, keeping the total circulation constant. By setting $s = s_2$, we obtain the unsteady Kutta

Nomenclature (cont.)

V^ψ = velocity in mapping plane
w_m = average of relative velocities on the upper and lower surfaces of the free vortex sheet
W_m = ditto, in mapping plane
$z = x + iy$ = complex coordinate in mapping plane
β = vane angle
η = semivertex angle of conical flow surface
γ = vortex distribution
Γ = circulation
γ_b, γ_v = vortex distributions on the vane surface and on the free vortex sheet
Δ = increment in a time interval Δt (transient case) or amplitude (sinusoidal case)
ρ = density
$\varphi, \varphi_0, \varphi_e$ = flow coefficient, mean flow coefficient and shockless flow coefficient
ψ, ψ_0 = harmonic function and a constant, equation (11)
Ψ = stream function
$\Omega(t), \Omega_0$ = angular velocity of the impeller and its steady component
ω = angular velocity of fluctuations

Superscripts

ψ = values in mapping plane
$*$ = nondimensional value

Subscripts

1,2 = inlet and outlet of the impeller
l, ϵ, R, Θ = component in l, ϵ, R, Θ direction
n, s = normal and tangential component
0,1,2 = component of vortex distribution
s, qs, a, w = steady, quasisteady, apparent mass, and wake component, equations (22)–(25)

condition. The Kutta condition expressed with variables in the mapping plane is

$$\gamma_v^\psi(s_2^\psi,t)=\gamma_b^\psi(s_2^\psi,t)=-\frac{\partial}{\partial t}\int_{s_1^\psi}^{s_2^\psi} H\gamma_b^\psi(s^\psi,t)ds^\psi \Big/\left\{\left(\frac{R_2}{r_2}\right)^2 W_m(s_2^\psi,t)\right\} \tag{15}$$

where $W_m = \frac{r}{R}\ w_m$.

When the unsteady components are sufficiently small, we may assume that the free vortices flow along a steady streamline. For simplicity we further assume that the steady harmonic function $\psi = \psi_s(R)$ is given by

$$\psi_s(R)=-\frac{N}{2\pi}\Gamma_s^\psi \ln R+\frac{N}{2\pi}\int_{s_1^\psi}^{s_2^\psi}\gamma_{bs}^\psi(s^\psi)\ln R(s^\psi)ds^\psi \tag{16}$$

where $\Gamma_s^\psi = \int_{s_1^\psi}^{s_2^\psi}\gamma_{bs}^\psi ds^\psi$ and γ_{bs}^ψ is the vortex distribution corresponding to the steady flow. This simplified flow is given by concentrating γ_{bs}^ψ at the origin of the mapping plane. Then, the position R, Θ of the vortex sheet and the transfer velocity $(R/r)^2\ W_m$ in the mapping plane are given by

$$\Theta=\int_{R_2}^{R}\left(\frac{d\Theta}{dt}\Big/\frac{dR}{dt}\right)dR+\Theta_2$$

$$\left(\frac{R}{r}\right)^2 W_m=\frac{ds^\psi}{dt}=\sqrt{\left(\frac{dR}{dt}\right)^2+\left(R\frac{d\Theta}{dt}\right)^2} \tag{17}$$

where

$$\frac{dR}{dt}=\frac{R}{r^2}\frac{Q_0}{2\pi b_2}H^2 \quad\text{and}\quad \frac{d\Theta}{dt}=\frac{R}{r^2}\left[\frac{P}{R}\psi_s+\frac{N\Gamma_s^\psi}{2\pi R}H\right]-\Omega_0$$

and Θ_2 is the angular coordinate of the trailing edge, Q_0 and Ω_0 are the steady flow rate and the angular velocity of the impeller. The strength of the free vortex sheet is given by the integration of equation (14) after the replacements of the variables with those in the mapping plane. The result is

$$\gamma_v^\psi(s^\psi,t)=\left[-\frac{\partial}{\partial t}\int_{s_1^\psi}^{s_2^\psi} H\,\gamma_b^\psi(s^\psi,t-\delta t)ds^\psi\right]\Big/\left[\left(\frac{R}{r}\right)^2 W_m H\right]_{s^\psi} \tag{18}$$

where

$$\delta t=\int_{s_2^\psi}^{s^\psi}\frac{ds^\psi}{\left(\frac{R}{r}\right)^2 W_m(s^\psi)}.$$

In cases where the unsteady disturbance is not small, the flow is solved stepwise in time with a time interval Δt. The effect of the free vortex sheet is estimated by assuming that the free vorticity shed within the time interval Δt is concentrated in a free vortex of strength

$$\Delta\Gamma_j=w_m\gamma_v|_{s=s_2}\Delta t=-\int_{s_1^\psi}^{s_2^\psi}H\{\gamma_b^\psi(s^\psi,t_j+\Delta t)-\gamma_b^\psi(s^\psi,t_j)\}ds^\psi \tag{19}$$

This free vortex flows down in the physical plane with the instantaneous local velocity keeping the circulation $\Delta\Gamma_j$ constant. The strength $\Delta\Gamma_j^\psi$ of the corresponding free vortex in the mapping plane is determined from

$$\Delta\Gamma_j=\gamma_v\Delta s=H\gamma_v^\psi\Delta s^\psi=H\Delta\Gamma_j^\psi \tag{20}$$

and the displacement of the vortex within the time interval Δt is

$$\Delta R=\frac{R}{r}\Delta l=\left(\frac{R}{r}\right)^2\left(\frac{Q(t)}{2\pi R b_2}H^2+HV_R^\psi\right)\Delta t$$
$$\Delta\Theta=\Delta\epsilon=\left\{\frac{R}{r^2}\left(\frac{P}{R}\psi+HV_\Theta^\psi\right)-\Omega\right\}\Delta t \tag{21}$$

which is used at each time step to determine the new position of $\Delta\Gamma_j^\psi$. The infinite integrals in equations (11) and (12) are replaced by summations with respect to $\Delta\Gamma_j^\psi = \gamma_v^\psi\Delta s^\psi$.

In both cases the value of γ_v^ψ is determined using the value of γ_b^ψ in the past. Hence, if we use equations (11) and (12) for ψ and V_n^ψ in the boundary condition (13), we obtain an integral equation for the unknown quantity γ_b^ψ. This equation can be solved for γ_b^ψ using the unsteady Kutta condition (15).

Unsteady Torque on the Impeller

The unsteady torque on the impeller can be determined from the consideration of the balance of the angular momentum in the physical plane. In order to get an expression suitable for physical understanding, we separate γ_b^ψ into the following components.

1) $\gamma_s^\psi(s^\psi)$: Steady component due to the steady flow rate Q_0 and the rotational velocity Ω_0, with a circulation Γ_s in the physical plane.
2) $\gamma_1^\psi(s^\psi,t)$: Unsteady component cancelling the normal component of assumed velocity disturbance, without circulation.
3) $\gamma_0^\psi(s^\psi,t)$: Unsteady component inducing no normal velocity in the physical plane with a circulation $\Gamma_0(t)$, which is determined so as to satisfy $\gamma_0^\psi(s_2^\psi,t)+\gamma_1^\psi(s_2^\psi,t)=0$.
4) $\gamma_2^\psi(s^\psi,t)$: Unsteady component cancelling the unsteady velocity due to free vortices, satisfying equation (15) with $\gamma_b^\psi=\gamma_2^\psi$.

Then the unsteady torque can be expressed as follows.

$$T=T_s+T_{qs}+T_a+T_w \tag{22}$$

where

$$T_s+T_{qs}=\frac{\rho Q(t)}{2\pi}\left(\sum^N\Gamma_s+\sum^N\Gamma_0\right) \tag{23}$$

$$T_a=\rho\sum^N\int_{R_1}^{R_2}\frac{r^2}{R}b\left(\int_{s_1^\psi}^{s^\psi}H\frac{\partial\gamma_1^\psi}{\partial t}ds^\psi\right)dR \tag{24}$$

$$T_w=\frac{\rho Q(t)}{2\pi}\sum^N\Gamma_2+\frac{\rho b_2}{2}\,\mathrm{Real}\left[\frac{1}{\pi i}\sum_{j=1}^{N}\int_{s_1^\psi}^{s_2^\psi}\gamma_b^\psi(s_j^\psi,t)z(s_j^\psi)\left\{\sum_{k=1}^{N}\int_{s_2^\psi}^{\infty}\frac{\gamma_v^\psi(s_k^\psi,t)}{z(s_j^\psi)-z(s_k^\psi)}ds_k^\psi\right\}ds_j^\psi\right]$$
$$+\rho\sum^N\int_{R_1}^{R_2}\frac{r^2}{R}b\left\{\int_{s_1^\psi}^{s^\psi}H\left(\frac{\partial\gamma_0^\psi}{\partial t}+\frac{\partial\gamma_2^\psi}{\partial t}\right)ds^\psi\right\}dR \tag{25}$$

and $T_s + T_{qs}$, T_a and T_w are quasisteady, apparent mass and wake components respectively. Each component has the same characteristics as those of two-dimensional centrifugal impellers [15]. We define the apparent mass coefficients $C_a^{\Omega,\varphi}$ as follows.

For angular velocity fluctuation

Table 1 Steady characteristics

$N=6$ $\beta=30°$ $L=0.6$ $h=h_s-A\varphi$

η	b_2/b_1	φ_e	A	h_s
30°	0.4	0.654	1.478	0.866
	0.7	0.437	1.610	0.865
	1.0	0.332	1.719	0.865
60°	0.4	0.365	1.519	0.792
	0.7	0.239	1.633	0.793
	1.0	0.179	1.729	0.794

$$C_a^{\Omega}=T_a/(\rho r_2^4 b_2 d\Omega/dt)$$

$$=\sum^{N}\int_{R_1^*}^{R_2^*}\frac{r^{*2}}{R^*}\,b^*\left\{\int_{s_1^{\psi}*}^{s^{\psi}*}H\frac{\partial\gamma_1^{\psi}*}{\partial\Omega^*}\,ds^{\psi}*\right\}dR^* \tag{26}$$

For flow rate fluctuation

$$C_a^{\varphi}=T_a/\left(\rho r_2^4 b_2\Omega_0\frac{d\varphi}{dt}\right)$$

$$=\sum^{N}\int_{R_1^*}^{R_2^*}\frac{r^{*2}}{R^*}\,b^*\left\{\int_{s_1^*}^{s^*}H\frac{\partial\gamma_1^{\psi}*}{\partial\varphi}\,ds^{\psi}*\right\}dR^* \tag{27}$$

where * indicates that the velocity has been normalized by $r_2\Omega_0$, the lengths by r_2 and the thickness by b_2. Since γ_1^{ψ} can be determined independently of other components, we can calculate the apparent mass component separately. For impellers with a large number of vanes, we can assume that the flow is perfectly guided by the vanes. In such cases we obtain the following expressions.

$$C_{a\,N=\infty}^{\Omega}=2\pi\int_{l_1^*}^{l_2^*}r^{*3}b^*dl^* \tag{28}$$

$$C_{a\,N=\infty}^{\varphi}=-2\pi\int_{l_1^*}^{l_2^*}r^*\cot\beta\,dl^* \tag{29}$$

It should be noted that $C_{a\,N=\infty}^{\Omega}$ is independent of the vane angle $\beta(l^*)$ and that $C_{a\,N=\infty}^{\varphi}$ is independent of the impeller thickness $b^*(l^*)$.

Method of Solution and Examples

The linear integral equation for γ_b^{ψ} obtained from equation (13) can be solved by a singularity method. We put M vortex points on a vane surface in the mapping plane and specify the values of γ_b^{ψ} on the vortex points as unknowns assuming a linear distribution between them. We apply equation (13) on $M-1$ downwash points midway between the vortex points. After carrying out the integrations included in the expressions of ψ and V_n^{ψ}, we obtain $M-1$ linear equations for the M unknowns. By the complementary use of the unsteady Kutta condition (15), we have M linear equations for M unknowns, from which we can determine the γ_b^{ψ} distribution.

As is apparent from equations (11) and (12), the integral equation obtained from equation (13) contains integrals of order $\log(x)$ and of order x^{-1} in the expressions of ψ and V_n^{ψ}, respectively. The logarithmic singularity should be integrated analytically assuming a linear distribution of γ_b^{ψ}. Cauchy's principal value should be taken for the x^{-1} singularity in the evaluation of V_n^{ψ}.

In the analyses of flows with large unsteady fluctuations, we solve the resulting M simultaneous linear equations at each time step. The free vortices are treated as described in the last section. For small sinusoidal fluctuations the unsteady components can be represented by complex amplitudes times $\exp(j\omega t)$. The infinite integrals in equations (11) and (12) relating to γ_b^{ψ} are truncated at sufficiently large R so that the relative error due to the truncation is within 1 percent. In the analyses

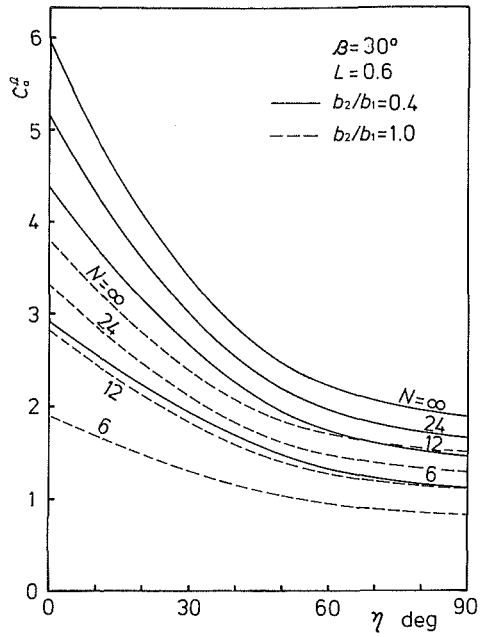

Fig. 3 Apparent mass torque coefficient C_a^{Ω} for angular velocity fluctuation

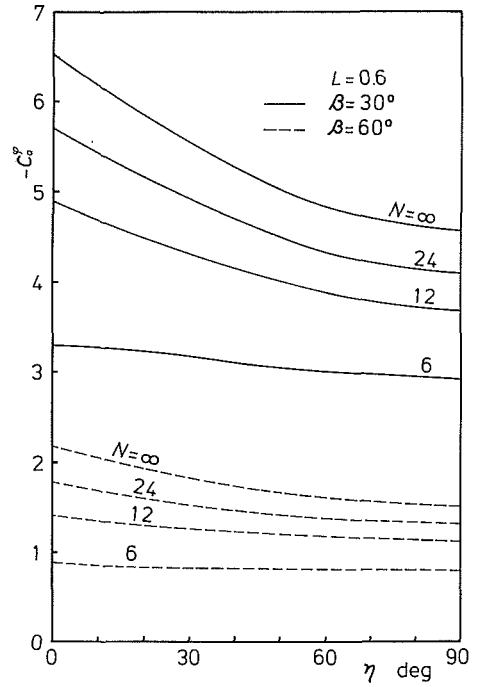

Fig. 4 Apparent mass torque coefficient C_a^{φ} for flow rate fluctuation

of $\partial\gamma_1^{\psi}*/\partial\Omega$ and $\partial\gamma_1^{\psi}*/\partial\varphi$, which are needed to calculate C_a^{Ω} and C_a^{φ}, the boundary conditions are given by equation (13) with $Q=0$, $\Omega=1$ or $Q=1$, $\Omega=0$. The definition of γ_1^{ψ} indicates the use of the condition that circulation in the physical plane should be zero instead of the Kutta condition.

For all of the examples presented in this paper, $M=40$ is used. We consider impellers with conical flow surface with a semi vertex angle η and a constant vane angle β. The parameter $L=(l_2-l_1)/r_2$ is used to represent the length of the flow surface in the impeller.

Steady Characteristics. For later use in the analysis of unsteady flows, we determine steady characteristics for impellers for which unsteady analyses are made. The flow coeffi-

Table 2 Effect of b_2/b_1 on C_a^φ (η = 60 deg, N = 6, β = 30 deg, L = 0.6)

b_2/b_1	1.0	0.7	0.4
C_a^φ	-3.013	-2.999	-2.997

cient φ and the head coefficient h are defined by $\varphi = Q/2\pi r_2^2 b_2 \Omega$ and $h = gH_{th}/(r_2\Omega)^2$, respectively, where H_{th} is the theoretical head and g the gravitational acceleration constant. We represent the head-capacity characteristic by $h = h_s - A\varphi$ and the values of the constants h_s and A are shown in Table 1. The values of the shockless flow coefficient φ_e (*the flow coefficient for which the velocity at the leading edge is finite*) are also shown in the table. The accuracy of the steady analysis has been checked by comparisons with the results in [17] for centrifugal impellers, and with those in [18] for axial flow impellers.

Apparent Mass Torque Coefficients. Figures 3 and 4 show the results for the apparent mass torque coefficients. The accuracy has been confirmed by comparisons with the results in [15, 16] for centrifugal impellers and with those in [19] for axial flow impellers. The values for $N=\infty$ are given by equations (28) and (29), to which the calculated values tend as N increases. Both C_a^Ω and $-C_a^\varphi$ decrease with increasing η. The effect of η is smaller for impellers with a smaller number of vanes, and is smaller for $-C_a^\varphi$ than for C_a^Ω. As shown in Table 2, the effect of b_2/b_1 on C_a^φ is quite small and the values in Fig. 4 can be used for impellers with any realistic values of b_2/b_1. Although not shown here, the effect of β is smaller for C_a^Ω than for C_a^φ, and impellers with smaller L have smaller values of C_a^Ω and $-C_a^\varphi$. The above mentioned tendencies concerning the effects of η and b_2/b_1 are valid also for impellers with other values of β and L.

Unsteady Flows With Small Sinusoidal Fluctuations. We consider the cases in which the flow rate Q and the angular velocity Ω are given by

(i) $Q=Q_0$, $\Omega=\Omega_0 + \Delta\Omega e^{j\omega t}$ $(\Delta\Omega \ll \Omega_0)$

(ii) $\Omega=\Omega_0$, $Q=Q_0 + \Delta Q e^{j\omega t}$ $(\Delta Q \ll Q_0)$

The unsteady torque $\Delta T e^{j\omega t}$ is given by equations (22)–(25) after linearization with respect to the unsteady components. The fluctuating torque coefficients are defined by

(i) $F=\Delta T/(\rho r_2^4 \Omega_0 b_2 \Delta\Omega)$ for angular velocity fluctuation

(ii) $F=\Delta T/(\rho r_2^4 \Omega_0^2 b_2 \Delta\varphi)$ for flow rate fluctuation.

Figures 5 and 6 show the fluctuating torque coefficient F as functions of the normalized frequency $k=\omega/\Omega_0$. The validity of the present results has been confirmed by comparisons with those in [15] and [16] for centrifugal impellers and with those in [20] for axial flow impellers. In these examples, the shockless flow coefficient φ_e is used as the mean flow coefficient φ_0. The torque coefficient F is divided into quasisteady F_{qs}, apparent mass F_a and wake F_w components. The apparent mass component is given by $F_a = jkC_a^{\Omega,\varphi}$ using $C_a^{\Omega,\varphi}$ as given in the preceding section. The quasisteady component coincides with F for $k=0$ and are given by $F_{qs} = 2\pi h_s \varphi_0$ or $2\pi(h_s - 2A\varphi_0)$ for angular velocity or flow rate fluctuations, respectively. The following tendencies are observed.

(1) The wake component is smaller than the other components, and the effect of the geometry of the flow surface manifests itself mainly in the quasisteady and apparent mass components.

(2) The wake component is smaller for impellers with a smaller outer to inner thickness ratio b_2/b_1.

(3) The wake component is smaller for impellers with a smaller semi-vertex angle β of the flow surface.

Let us consider the stability of the torsional vibration of the impeller. In the case of angular velocity fluctuation, the energy E transferred to the fluid owing to one cycle of the fluctuation is given by

$$E=\int_0^{2\pi/\omega} \mathrm{Real}(\Delta T e^{j\omega t})\,\mathrm{Real}(\Delta\Omega e^{j\omega t})\,dt$$
$$=\rho r_2^4 \Omega_0 b_2 \Delta\Omega^2 (\pi/\omega)\{F_{qs} + \mathrm{Real}(F_w)\}. \quad (30)$$

This shows that the energy is proportional to the real part of F. From Fig. 5 we see that the unsteady fluiddynamic torque

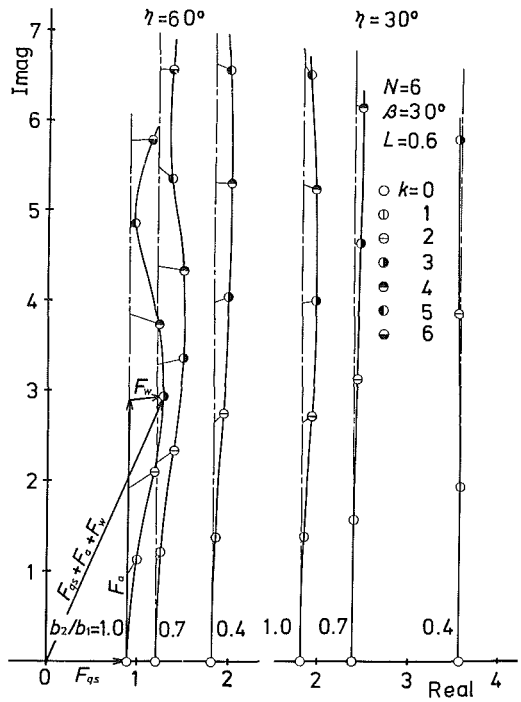

Fig. 5 Fluctuating torque coefficient F for small sinusoidal angular velocity fluctuation

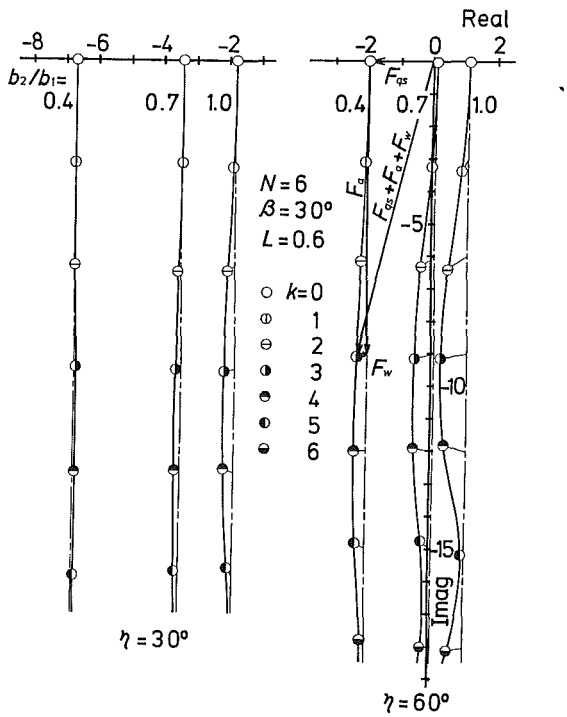

Fig. 6 Fluctuating torque coefficient F for small sinusoidal flow rate fluctuation

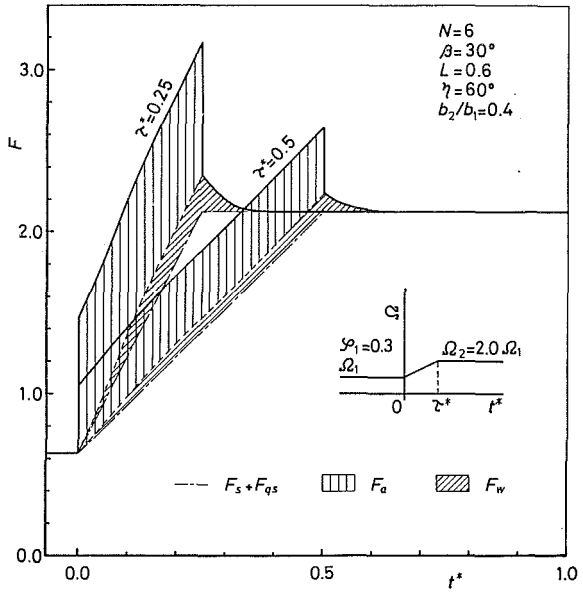

Fig. 7 Response of the torque coefficient F when the angular velocity is increased

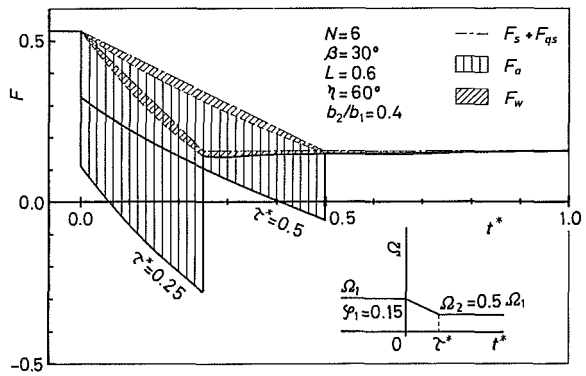

Fig. 8 Response of the torque coefficient F when the angular velocity is decreased

has a stabilizing effect for torsional vibrations. The wake component has an effect of enhancing the stability in most of the present examples. Since $F_{qs} = 2\pi h_s \varphi_0$, the stability will be reduced if we reduce the mean flow coefficient φ_0.

For the discussion on the stability for surging, let us assume that the energy relation $T\Omega = \rho g Q H_{th}$ can be used for the estimation of the amplitude ΔH_{th} of the unsteady head from the unsteady torque ΔT due to the flow rate fluctuation. Then the energy E transferred to the fluid owing to one cycle of the flow rate fluctuation is given by

$$E = \rho g \int_0^{2\pi/\omega} \mathrm{Real}(\Delta H_{th} e^{j\omega t}) \mathrm{Real}(\Delta Q e^{j\omega t}) dt$$

$$= \rho r_2^4 \Omega_0^2 b_2 \pi (\Omega_0/\omega)(\Delta\varphi^2/\varphi_0)\{-2\pi A \varphi_0 + \mathrm{Real}(F_w)\}. \quad (31)$$

From this expression we find that the stability for surging is mainly determined by the slope $-A$ of the steady head-capacity characteristic. Figure 6 shows that the wake component has a stabilizing effect in most of the present examples but its contribution is small compared with the first term of equation (31). This assures the validity of the quasisteady application of the steady head-capacity characteristic in the analyses of surging of systems including turbomachines.

Unsteady Flows With Large Transient Fluctuations. The following four types of transient flows are considered for an impeller with $N = 6$, $\beta = 30$ deg, $L = 0.6$, $\eta = 60$ deg and

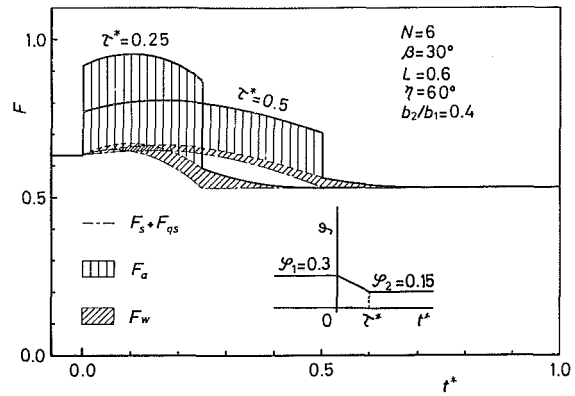

Fig. 9 Response of the torque coefficient F when the flow rate is decreased

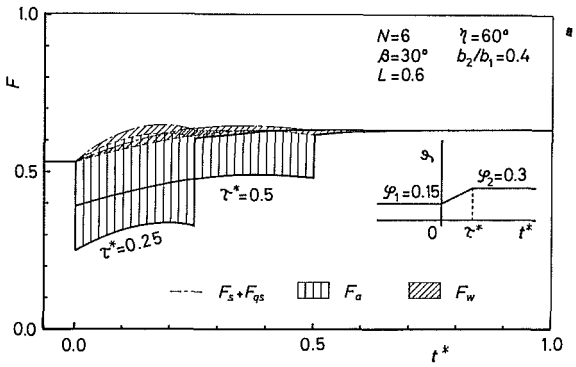

Fig. 10 Response of the torque coefficient F when the flow rate is increased

$b_2/b_1 = 0.4$. The flow is determined stepwise in time and the location of the shed vortices is corrected at each time step.

(i) The angular velocity $\Omega(t)$ is
(a) increased from Ω_1 to $\Omega_2 = 2.0\ \Omega_1$
(b) decreased from Ω_1 to $\Omega_2 = 0.5\ \Omega_1$
within a time interval τ keeping the flow rate Q_1 ($\varphi_1 = Q_1/2\pi r_2^2 b_2 \Omega_1 = 0.3$) constant.

(ii) The flow rate is
(a) decreased from $\varphi_1 = 0.3$ to $\varphi_2 = 0.15$
(b) increased from $\varphi_1 = 0.15$ to $\varphi_2 = 0.3$
within a time interval τ keeping the angular velocity Ω_1 constant.

In all of the present examples the flow rate or the angular velocity is changed linearly with time within the time interval τ and otherwise kept constant. The torque coefficient $F = T/(\rho r_2^4 b_2 \Omega_1^2)$ is shown as a function of nondimensional time $t^* = t/(2\pi/\Omega_1)$ in Figs. 7–10. The time step $\Delta t^* = 0.01$ is used in these calculations since further reduction in Δt^* does not change the results appreciably. The results show that

(1) Discontinuities appear at $t^* = 0$ and τ^*, which correspond to the sudden application and the removal of the acceleration. The size of the discontinuity agrees with the apparent mass component estimated by using C_a^Ω and C_a^φ.
(2) The wake component is larger in case (a), in which the load at $t^* = \tau^*$ is larger than that in case (b).
(3) The wake component is smaller than the other two components.

Conclusions

Unsteady flows through mixed flow impellers were analyzed on the assumption of a two-dimensional flow in a represen-

tative flow surface. Attention is paid to the unsteady torque due to small sinusoidal and/or large transient fluctuations of flow rate and/or angular velocity of the impeller. The unsteady torque is divided into quasisteady, apparent mass and wake components. Apparent mass torque coefficients are calculated for angular velocity and flow rate fluctuations. The major results are,

(1) The wake component is usually smaller than the other components and a rough estimation of the unsteady torque can be made by using the apparent mass coefficients and the steady head-capacity characteristic.
(2) The unsteady fluid dynamic torque has a stabilizing effect for torsional vibrations but the stability will be reduced if we reduce the flow rate.
(3) The stability for surging is mainly dependent on the slope of the steady head-capacity characteristics.
(4) The wake component has the effect of enhancing the stability of torsional vibration and surging.
(5) The unsteady torque and the apparent mass coefficients are calculated for impellers with various flow surface geometries, and their effects are discussed.

The authors are very grateful to Mr. K. Kim for his instinting support in the numerical calculations.

References

1 Katsanis, T., "Computer Program for Calculating Velocities and Streamlines on a Blade-to-Blade Stream Surface of a Turbomachine," NASA TN D-4525, Apr. 1968.

2 Senoo, Y., and Nakase, Y., "An Analysis of Flow Through a Mixed Flow Impeller," ASME *Journal of Engineering for Power*, Vol. 94, No. 1, Jan. 1972, pp. 43–50.

3 Denton, J. D., "A Time Marching Method for Two and Three-Dimensional Blade to Blade Flows," ARC R&M, 3775, 1975.

4 Daiguji, H., "Numerical Analysis of 3-D Potential Flow in Centrifugal Turbomachines," *Bull. of Japan Soc. Mech. Engrs.*, Vol. 26, No. 219, Sept. 1983, pp. 1495–1501.

5 Whitehead, D. S., "Force and Moment Coefficients for Vibrating Airfoils in Cascade," ARC R&M, 3254, Feb. 1960.

6 Shoji, H., Ohashi, H., and Kemp, N. H., "Forces on Staggered Airfoil Cascades in Unsteady In-Phase Motion," ASME JOURNAL OF FLUIDS ENGINEERING, Vol. 103, 1981, pp. 299–306.

7 Murata, S., and Tsujimoto, Y., "The Unsteady Forces on Flat-Plate Airfoils in Cascade Moving through Sinusoidal Gusts," *ZAMM*, Vol. 56, 1976, pp. 205–216.

8 Namba, M., "Three-Dimensional Analysis of Blade Force and Sound Generation for an Annular Cascade in Distorted Flows," *J. Sound & Vibr.*, Vol. 50, No. 4, 1977, pp. 479–508.

9 Tsukamoto, H., and Ohashi, H., "Transient Characteristics of Centrifugal Turbomachines," ASME JOURNAL OF FLUIDS ENGINEERING, Vol. 104, No. 1, 1982, pp. 6–14.

10 Nishioka, K., and Mitsunaka, Y., "On Unsteady Aerodynamic Forces and Moments of Radial Impeller Blades," *Bull. of Japan Soc. Mech. Engrs.*, Vol. 22, No. 173, 1979, pp. 1544–1551.

11 Shoji, H., and Ohashi, H., "Fluid Forces on Rotating Centrifugal Impeller with Whirling Motion," 1st Workshop on Rotodynamic Instability Problems in High Performance Turbomachinery, Texas A&M University, NASA Conf. Pub. 2133, 1980, pp. 317–328.

12 Erdos, J. I., Alzner, E., and McNally, "Numerical Solution of Periodic Transonic Flow through a Fan Stage," *AIAA Journal*, Vol. 15, No. 11, Nov. 1977, pp. 1559–1568.

13 Daiguji, H., and Shirahata, H., "A Finite Element Analysis of Unsteady Diagonal Cascade Flows," *Bull. of Japan Soc. Mech. Engrs.*, Vol. 23, No. 180, June 1980, pp. 888–894.

14 Hoffmeister, M., "Ein Beitrag zur Berechnung der incompressiblen reibungsfrien Strömung durch ein unendlich dünnes Scaufelgitter in einem Rotationshohlraum," *Maschinenbautechnik*, Vol. 10, No. 8, Aug. 1961, pp. 416–422.

15 Imaichi, K., Tsujimoto, Y., and Yoshida, Y., "An Analysis of Unsteady Torque on a Two-Dimensional Radial Impeller," ASME JOURNAL OF FLUIDS ENGINEERING, Vol. 104, No. 2, June 1982, pp. 228–234.

16 Tsujimoto, Y., Imaichi, K., Tomohiro, T., and Gotoo, M., "An Analysis of Unsteady Torque on a Quasi-Three-Dimensional Centrifugal Impeller," *Bull. of Japan Soc. Mech. Engrs.*, Vol. 27, No. 232, Oct. 1984, pp. 2166–2172.

17 Murata, S., Ogawa, T., and Gotoo, M., "On the Flow in a Centrifugal Impeller (2nd Rep. Effects of Change in Impeller Width)," *Bull. of Japan Soc. Mech. Engrs.*, Vol. 21, No. 151, Jan. 1978, pp. 90–97.

18 Weinig, F., *Die Strömung um die Schaufeln von Turbomaschinen*, Joh. A. Barth, Lipzig, 1935.

19 Sedov, L. I., *Two-Dimensional Problems in Hydrodynamics and Aerodynamics*, Interstate Publishers, N.Y., 1965.

20 Ohashi, H., "Unsteady Flow through a Cascade of Non-Staggered Flat Plates," *Journal of the Faculty of Engineering*, The University of Tokyo, Vol. 33, No. 2, 1975, pp. 123–148.

ERRATUM

T. Bulaty and H. Niessner "Calculation of 1-D Unsteady Flows in Pipe Systems of I.C. Engines," ASME **Journal of Fluids Engineering**, Vol. 107, Sept. 1985, pp. 407–412.

The following errors appeared in the above paper:

(a) $\frac{\partial}{\partial \mathcal{IC}}$ in equations (1) and (2) should read $\frac{\partial}{\partial t}$

(b) W^{D+1} in equation (3) should read W^{n+1}

(c) Equation (7) should read

$$\tilde{W}^{n+1} = W^{n+1} + D \cdot W^n$$

(d) Equation (9) should read

$$[C(\tilde{W}) \cdot \Phi(W)]_{j+1/2} = q \cdot \Phi_{j+1/2} \cdot \min\left\{\left(\frac{\tilde{W}_{j+2} - \tilde{W}_{j+1}}{\Phi_{j+1/2}}\right)_+, \frac{1}{q}, \left(\frac{\tilde{W}_j - \tilde{W}_{j-1}}{\Phi_{j+1/2}}\right)_+\right\}$$

(e) Equation (10) should read

$$[A(\tilde{W}) \cdot W]_j = -\{[C(\tilde{W}) \cdot \Phi(W)]_{j+1/2} - [C(\tilde{W}) \cdot \Phi(W)]_{j-1/2}\}$$

(f) Equation (12) should read

$$\tilde{W}^{n+1} = \tilde{W}^{n+1} + A(\tilde{W}^{n+1}) \cdot W^n$$

The address of both authors should read: Brown Boveri and Co., Ltd., CH-5401 Baden, Switzerland

The Use of the Dye-Layer Technique for Unsteady Flow Visualization

Mohamed Gad-el-Hak
Senior Research Scientist,
Flow Research Company,
Kent, WA 98032.
Mem. ASME

The unsteady flow around three-dimensional lifting surfaces undergoing a harmonic pitching motion was studied in a towing tank using the dye-layer technique. Different color fluorescent dyes were placed in the flow field by laying several thin, horizontal sheets prior to towing the lifting surface. The fluorescent dyes were excited using a sheet of laser light projected in the desired plane. The technique allowed the visualization of the flow in the separation zone on the low-pressure side of the lifting surface, the flow in the wake region, and the potential flow away from the surface. The complex unsteady flow structures were gleaned from observing the visualization results recorded on ciné films.

1 Introduction

Considerable experimental and theoretical research have been focused on studying the flow over two- and three-dimensional lifting surfaces for steady flow and time-independent boundary conditions [1]. At high angles of attack, the flow separates and the flow field is usually described by inviscid modeling of the vorticity shed from the wing edges [2, 3]. The separated flow on the lifting surface is complicated by a certain degree of unsteadiness. When the wing itself undergoes an unsteady motion, an unsteady, often three-dimensional, separated flow results. The understanding of such flows is of great practical interest in the design of fluid machinery, airplanes and other products. However, they represent a domain of fluid mechanics that is presently beyond the reach of definitive theoretical or numerical analyses.

Experimentally, the presence of reverse flow regions in the unsteady separated flow makes it difficult to use conventional velocity probes such as the hot-wire anemometer. Flow visualization techniques offer an attactive alternative to obtain qualitative, and sometimes quantitative information of the entire flow field. The dye-layer technique [4] was used in the present investigation to visualize the flow around seven wing configurations undergoing large amplitude, harmonic pitching motion. The models were towed in a water channel and several thin, horizontal sheets of fluorescent dye were excited with a sheet of laser light to visualize the complex, unsteady separated flow around each wing. In Sections 2 and 3 the experimental approach is described. Section 4 gives typical results of the visualization technique. Finally, Section 5 presents our concluding remarks.

2 Experimental Apparatus

Seven lifting surfaces undergoing a harmonic pitching motion were studied. The three-dimensional surfaces were: (1) a sharp leading edge rectangular wing having a chord length of $c = 12.5$ cm and an aspect ratio of $AR = 4$; (2) a similar rectangular wing but having a NACA 0012 cross-section; (3) a 25 deg swept wing with a sharp leading edge, a root chord of $c = 16.5$ cm and $AR = 4$; (4) a similar but swept forward wing; (5) a 60 deg delta wing with a sharp leading edge, $c = 25$ cm and $AR = 2.3$; (6) a 45 deg delta wing with a sharp leading edge, $c = 25$ cm and $AR = 4$; and (7) a similar 45 deg delta wing but having a NACA 0012 profile at each spanwise location.

The wings were towed in a water channel that is 18 m long, 1.2 m wide, and 0.9 m deep [4]. The four-bar mechanism shown in Fig. 1 was used to sting-mount and to pitch the wings

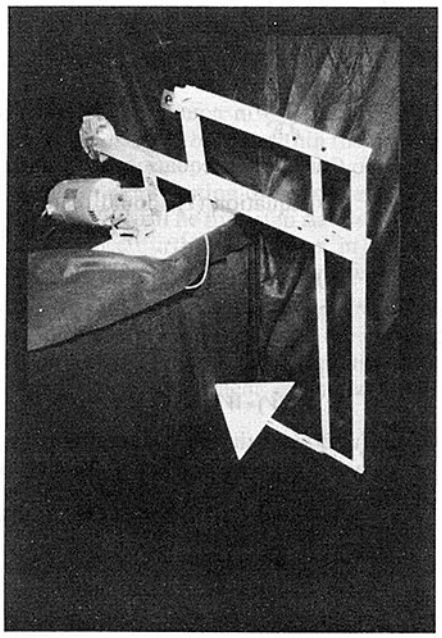

Fig. 1 Photograph of the four-bar pitching mechanism

Contributed by the Fluids Engineering Division of THE AMERICAN SOCIETY OF MECHANICAL ENGINEERS and presented at the Joint ASCE/ASME Mechanics Conference, Albuquerque, New Mexico, June 24-26, 1985, International Symposium on Physical and Numerical Flow Visualization.

around the desired position along the chord. In the experiments reported herein the wings were pitched around the 1/4 chord position. The mean angle of attack could be set from 0 to 45 deg. A Boston Ratiotrol motor derived the four-bar linkages to produce approximately sinusoidal oscillations of amplitude ± 5, ± 10 or ± 15 deg about a given mean angle of attack. The reduced frequency, $K \equiv \pi fc/U_\infty$, where f is the pitching frequency and U_∞ is the towing speed, was varied in the range of 0.2 to 3.0, and a digital readout displayed the instantaneous attack angle of the wing.

The pitching mechanism was rigidly mounted under a carriage that rides on two tracks mounted on top of the towing tank. During towing, the carriage was supported by an oil film which insured a vibrationless tow, having an equivalent freestream turbulence of about 0.1 percent. The carriage was towed with two cables driven through a reduction gear by a 1.5 h.p. Boston Ratiotrol motor. The towing speed was varied in the range of 5 to 140 cm/s ($R_c \equiv U_\infty c/\nu = 6.25 \times 10^3 - 3.50 \times 10^5$), and was regulated within an accuracy of 0.1 percent. The main frame supporting the tank could be tilted and levelled by adjusting four screw jacks. This feature was essential for smooth operation of the carriage, whose tracks are supported by the main frame. The towing tank was designed so that visualizations can be made from the top, sides, bottom and ends. The bottom and side walls are made of 19 mm thick plate glass with optical quality. The end walls are made of 38 mm thick Plexiglas.

3 Flow Visualization Technique

The complex, unsteady separated flows around the three-dimensional lifting surfaces were visualized using the dye-layer technique [4, 5]. Cotton strings, having a diameter of 1 mm, were stretched horizontally on a rake and painted with a concentrated solution of a fluorescent dye and alcohol. The alcohol was allowed to evaporate leaving the strings saturated with dye crystals. The rake was then placed in the water channel that has a weak, stable stratification, and towed at a relatively low speed (1 cm/s), so that the wakes behind the strings were laminar. As the dye was washed away from the strings, it formed several thin, horizontal sheets. These layers of dye remained thin, about 1 mm in thickness, due to the inhibition of vertical motion caused by the saline stratification in the tank. The density gradient in the tank was about 10^{-4} gm/cm^4, which yields a Brunt-Väisälä frequency of $N = 0.05$ Hz. This provided a time scale for gravity-driven motion which was far longer than a typical convection or pitching time period; hence the stratification should have negligible effect on the dynamics of the flow, at least that around the lifting surface and in the near-wake region. This conclusion was verified experimentally by conducting two runs using a conventional dye injection method, in the presence and in the absence of stratification in the tank. The visualization patterns in the two runs were indistinguishable.

The fluorescent dyes used in the present investigation were Fluorescein, Rhodamine-B, and Rhodamine-6G. These fluoresced green, dark red and yellow, respectively, when excited with an argon laser light. In a flood light, the first two dyes fluoresced green and dark red, while the Rhodamine-6G had a faint red color.

A sheet of laser light was used to excite the dye layers. A 5 watt argon laser (Spectra Physics, Model 164) was used in conjunction with an oscillating mirror to generate a sheet of light approximately 1 mm thick. The mirror was mounted on an optical scanner (General Scanning, Model G124) which was driven with a sine-wave signal generator set at a frequency equal to the inverse of the camera shutter speed. This yielded one scan per frame which was sufficient for the present purpose. It should be noted here that the quality of the light sheet resulting from the scanning mirror is far superior than that obtained with a cylindrical lense. The latter method results in nonuniform light intensity throughout the sheet due to the unavoidable impurities in glass lenses.

A vertical laser sheet parallel to the flow direction was used to visualize the three-dimensional flow field around the low-pressure side of each wing. The spanwise distance between the light sheet and the wing centerline, z, varied in the range of 40 to 70 percent of the wing's semispan. The visualization results were recorded using 35 mm photographs and 16 mm ciné films. The cameras were rigidly connected to the same carriage used to tow the wings, and were located outside the tank looking at right angle to the vertical sheet of laser light. Ciné films of the present investigation are available upon request (Flow Research Films No. 57 and 58).

The alternating horizontal sheets of different color dyes remained quiescent until disturbed by the moving lifting surface. Unlike conventional dye injection techniques [6–8], the dye layers marked the flow in the separation region, the flow in the wake region, and the potential flow away from the surface. This was particularly useful for observing the leading and trailing edge vortices associated with changing the angle of attack of the lifting surface.

4 Experimental Results

The dye-layer technique was used to visualize the unsteady flow around the seven lifting surfaces. The wings were pitched around the 1/4 chord position, at a reduced frequency that varied in the range of 0.2 to 3.0. The root chord Reynolds number, R_c, varied in the range of 6.25×10^3 to 3.50×10^5. An example of the visualization results is shown in Fig. 2. The sharp leading edge rectangular wing ($c = 12.5$ cm, $AR = 4$) was towed at a speed of $U_\infty = 6.9$ cm/s ($R_c = 8.63 \times 10^3$). The wing underwent the pitching motion $\alpha(t)^\circ = 15 + 15 \sin(3.3t)$, where $\alpha(t)$ is the time-dependent angle of attack, and t is time in seconds (reduced frequency $K = 3.0$). The sequence of photographs in Fig. 2 depicts the first complete cycle (0 to 30 to 0 deg) of the unsteady flow field in a vertical plane, parallel to the flow direction and located at $z = 10$ cm (40 percent of the semispan). Both the upward and downward motions of the wing are shown side by side for $\alpha = 0$, 5, 10, 15, 20, 25, and 30 deg.

The complex, unsteady flow field associated with a pitching, three-dimensional lifting surface can be mostly explained from the *mutual induction* between the leading edge separation vortex and the trailing edge shedding vortex. At large angles of attack, the flow separates at the leading edge and a clockwise vortex is formed and convected downstream (Fig. 2). This vortex is eventually shed from the trailing edge. When the wing is in the upstroke, the trailing edge moves downward and a shear layer is created at the upper surface. The shear layer rolls up into a counterclockwise vortex that is also shed from the trailing edge (Fig. 2). Conversely, a clockwise vortex

Nomenclature

AR = aspect ratio
c = root chord
f = pitching frequency
K = reduced frequency, $\pi fc/U_\infty$
N = Brunt-Väisälä frequency
R_c = chord Reynolds number, $U_\infty c/\nu$
s = wing semispan
t = time (s)
U_∞ = towing speed
x,y,z = Cartesian coordinates fixed with the wing
$\alpha(t)$ = angle of attack
ν = kinematic viscosity

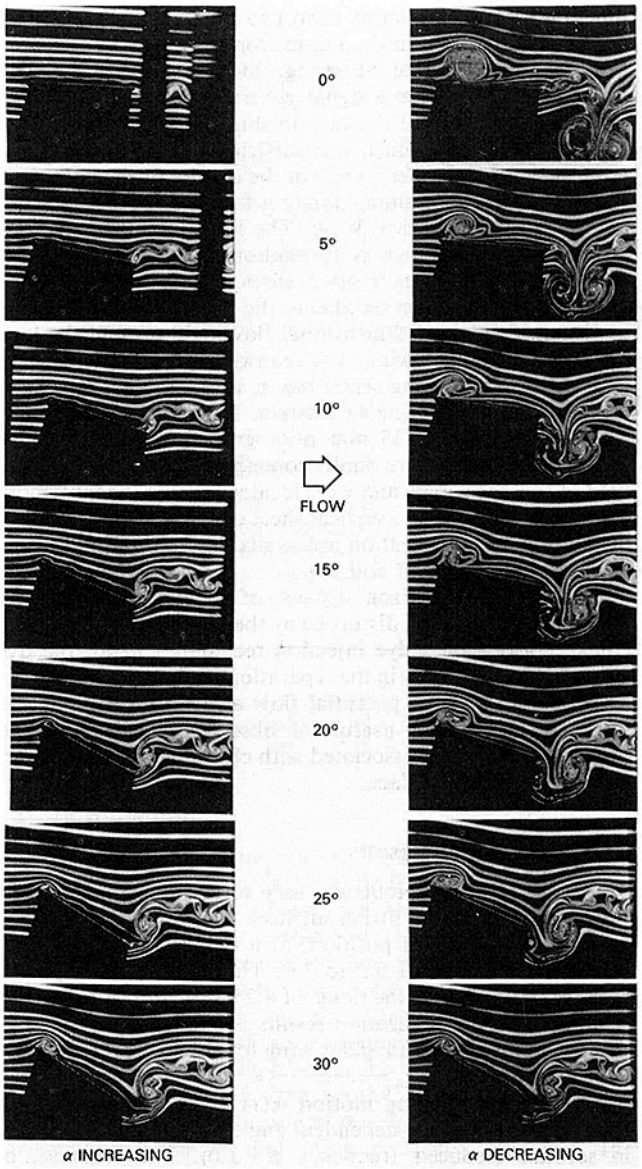

Fig. 2 Side view of a sharp leading edge rectangular wing undergoing a pitching motion. $AR = 4$, $R_c = 8.63 \times 10^3$, $K = 3.0$, $\alpha(t)$ deg = 15 + 15 sin (3.3t).

is formed during the downstroke (Fig. 2). These vortices enter the wake at different phases of the cycle and result in a particular wake pattern for a given reduced frequency. For the rectangular wing pitching at the reduced frequency of $K = 3$, the clockwise separation vortex from the leading edge is convected at a slow rate relative to the oscillation period. This vortex, at a particular cycle, convects downstream and leaves the trailing edge during the downstroke of the following cycle, at the same time as the clockwise trailing edge vortex. The combined vortex forms a vortex pair with the counterclockwise vortex produced in the previous upstroke. During the new upstroke, another counterclockwise vortex is formed and has a net effect of suppressing the thickness of the separation region.

4.1 Effects of Reduced Frequency. To investigate the effects of the reduced frequency on the flow field, the sharp leading edge rectangular wing was pitched at the reduced frequencies $K = 0.2$, 1.0 and 3.0. The root chord Reynolds number for all three runs was $R_c = 1.25 \times 10^4$, and the angle of attack was $\alpha(t) = 15 \pm 15$ deg. Figure 3 shows three photographs at the three different reduced frequencies taken when the angle of attack was $\alpha(t) = 20$ deg during the

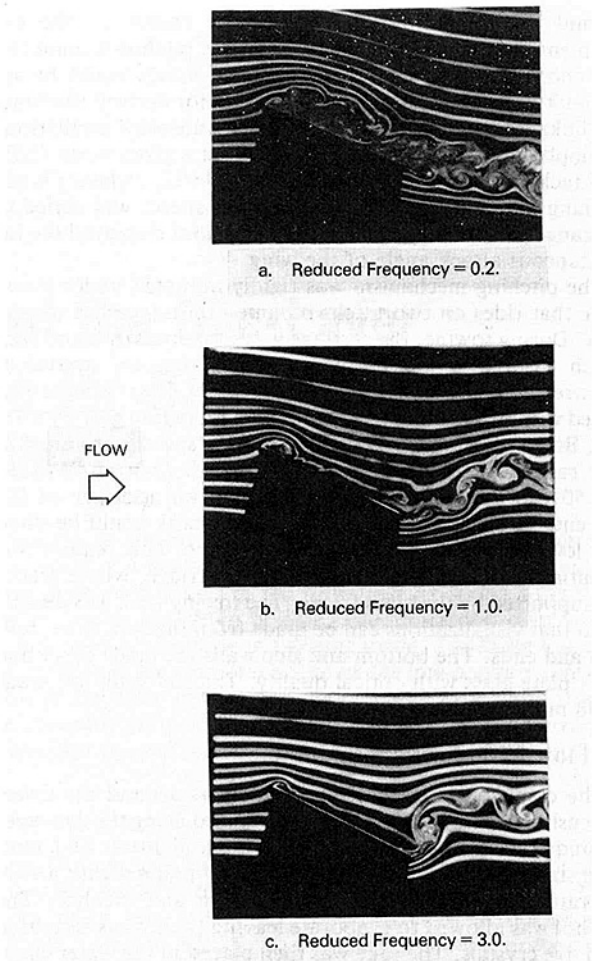

Fig. 3 Effects of reduced frequency. Sharp leading edge rectangular wing. $AR = 4$, $R_c = 1.25 \times 10^4$, $\alpha = 20$ deg (upstroke).

upstroke. The vertical laser light was parallel to the flow and was at a distance of 10 cm off the wing centerline, in all three cases.

At the lowest reduced frequency, $K = 0.2$, the trailing edge vortices are located inside the separated zone originating from the leading edge, as shown in Fig. 3(a). The mutual induction between the two vortical zones is less clear compared to higher reduced frequency runs. However, the general concept should still hold.

For $K = 1.0$ and 3.0, the effect of the mutual induction between the leading edge separation vortex and the trailing edge shedding vortex is more apparent, since the two types of vortices are separated in space. The difference between the $K = 1.0$ case and the $K = 3.0$ case is due to the vortex pattern in the wake. For $K = 1.0$, the clockwise leading edge separation vortex convects downstream and is shed from the trailing edge just before the wing starts the upstroke of the new cycle. During this upstroke, a counterclockwise vortex is generated at the trailing edge and forms a vortex pair with the leading edge vortex. This vortex pair tends to convect downstream and upward, so that the induced flow above the chord is more or less cancelled. During the downstroke, a clockwise vortex is generated at the trailing edge and its induced velocity tends to thicken the separation zone above the wing.

The situation is different at $K = 3.0$. The vortex from the leading edge is convected at a slower rate relative to an oscillation period and is shed at the downstroke, of the next cycle, with the clockwise trailing edge vortex. The combined vortex forms a vortex pair with the counterclockwise vortex produced

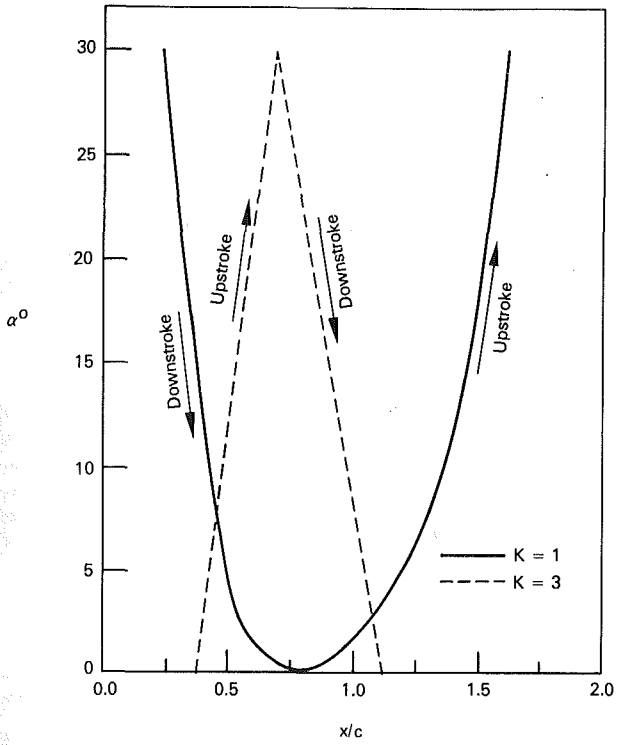

Fig. 4 Chordwise displacement of leading edge vortex core. Rectangular wing with a NACA 0012 cross-section. $R_c = 1.25 \times 10^4$.

in the previous upstroke. During the new upstroke, another counterclockwise vortex forms at the trailing edge and has a net effect of suppressing the thickness of the separation zone above the wing.

The chordwise displacement of the leading edge vortex core was determined from the ciné films. Figure 4 shows the core displacement for the NACA 0012 rectangular wing undergoing a pitching motion at the reduced frequencies $K = 1.0$ and $K = 3.0$. For the $K = 1.0$, the average convection speed of the leading edge vortex is approximately 45 percent of the towing speed. At the higher reduced frequency, this average convection speed is increased to approximately 65 percent of the freestream speed.

4.2 Effects of Leading Edge Shape. Two rectangular wings having the same chord ($c = 12.5$ cm) and aspect ratio ($AR = 4$) were tested to determine the effects of the leading edge shape. The first wing has a flat surface and a sharp leading edge, while the second wing has a NACA 0012 cross-section. The two wings were towed at a speed of $U_\infty = 10$ cm/s ($R_c = 1.25 \times 10^4$) and were harmonically pitched around the 1/4 chord point such that $\alpha(t)$ deg $= 15 + 15 \sin(1.6t)$; $K = 1.0$. Figure 5 shows the two wings during the upstroke when $\alpha(t) = 30$ deg. The distinct characteristics of the sharp leading edge wing is the existence of a counter-rotating vortex upstream of the leading edge separation vortex (Fig. 5(*a*)). The mutual induction of the vortex pair lifts itself away from the wall and results in a large intrusion into the inviscid region. The counter-rotating vortex is not observed on the blunt leading edge wing (Fig. 5(*b*)). In this case, the leading edge separation vortex rolls along the chord. The separated region is much thinner than that on the sharp leading edge wing. The fact that changing the leading edge shape leads to changes in the flow field implies that the aerodynamic characteristics of a wing could be changed with the proper passive control device. This may have important consequences on the ability to achieve high performance from a given lifting surface.

4.3 Effects of Wing Platform. Four sharp leading edge wings were tested to determine the effects of wing planform. A

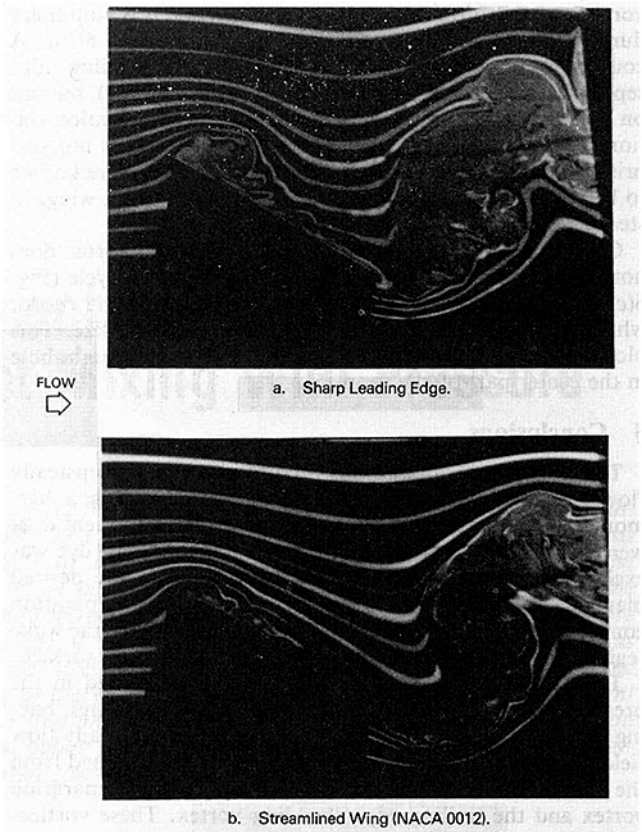

Fig. 5 Effects of leading edge shape. Rectangular wing. $AR = 4$, $R_c = 1.25 \times 10^4$, $K = 1.0$, $\alpha = 30$ deg (Upstroke).

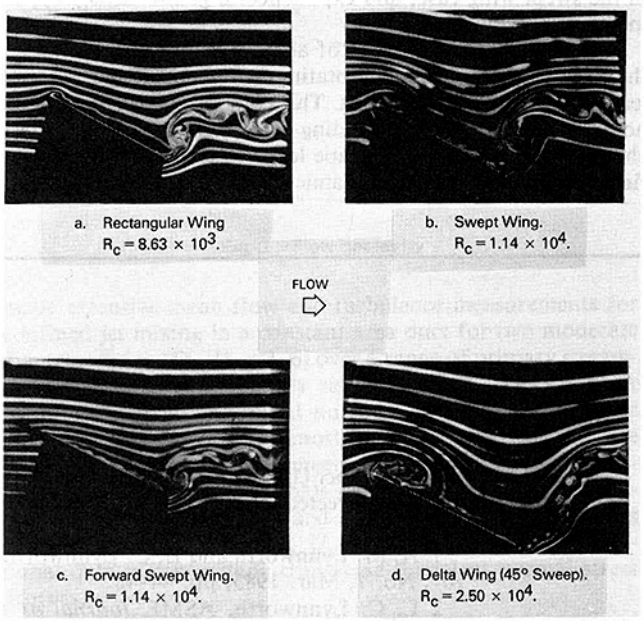

Fig. 6 Effects of wing planform. All wings have sharp leading edges. $AR = 4$, $K = 3.0$, $\alpha = 20$ deg (upstroke).

rectangular wing, a 25 deg swept wing, a forward swept wing and a 45 deg sweep delta wing, all having an aspect ratio of $AR = 4$, were pitched at angle of attack of α deg $= 15 \pm 15$ deg, and at a reduced frequency of $K = 3.0$. The four photographs in Fig. 6 depict the four wings during the upstroke at $\alpha(t) = 20$ deg. On the rectangular wing, the leading edge separation

vortex convects downstream (Fig. 6(*a*)), while it is stationary during part of the cycle on the swept wing (Fig. 6(*b*)). A counter-rotating vortex can be seen near the leading edge separation vortex on the forward swept wing (Fig. (*c*)), but not on the (backward) swept wing at the present visualization station ($z = 10$ cm, 40 percent of the semispan). This is not surprising since the separation patterns along the span are known to be very different on backward and forward swept wings in steady flight.

On the delta wing, the leading edge separation vortex does not convect, rather it experiences a growth-decay cycle (Fig. 6(*c*)). There exists a blob of dye that moves along the chord, while the leading edge vortex shrinks to minimum size. This blob of dye could be related to the possible separation bubble in the center part of the span [5].

5 Conclusions

The dye-layer technique was used to visualize the unsteady flow field around seven lifting surfaces undergoing a harmonic pitching motion. Horizontal sheets of fluorescent dyes were introduced in a towing tank prior to a run. The dye was excited using a sheet of laser light projected in the desired plane, to reveal details of the unsteady flow in the separation zone on the low-pressure side of the wing, the flow in the wake region, and the potential flow away from the lifting surface.

Three generic classes of lifting surfaces were used in the present investigation: rectangular, swept and delta wings, having sharp or blunt leading edges. The complex, unsteady flow field around the different wings can be mostly explained from the mutual induction between the leading edge separation vortex and the trailing edge shedding vortex. These vortices enter the wake at different phase of the pitching cycle dependent upon the reduced frequency.

The leading edge vortex convects downstream in the rectangular wing case, remains stationary during part of the cycle in the swept wing case, and experiences a growth-decay cycle in the delta wing case.

The distinct characteristics of a sharp leading edge wing is the existence of a counter-rotating vortex upstream of the leading edge separation vortex. This counter-rotating vortex is not observed in a blunt leading edge wing. The fact that changing the leading edge shape leads to changes in the flow field implies that the aerodynamic properties of a wing could be changed with the proper passive control device. This may have important consequences on the ability to achieve high performance from a given lifting surface.

The dye-layer technique is suited for visualizing complex flows around three-dimensional bodies undergoing unsteady motion. Classical dye injection methods are often difficult to implement in such flows. The extra degree of freedom provided by using fluorescent dye together with sheets of laser light is quite effective in revealing the complex vortical structures encountered in the present flow fields. More detailed visualizations using the present technique are to appear in a forthcoming article [9].

Acknowledgment

This work is supported by the U.S. Air Force Office of Scientific Research, under Contract No. F49620-82-C-0020, and monitored by Major M. S. Francis and Dr. J. D. Wilson. The author would like to acknowledge the valuable help of Dr. H.-T. Liu, who developed the dye-layer technique for visualizing internal waves, and Mr. R. Srnsky, who refined the art of photography into a science.

References

1 Hoeijmakers, H. W. M., Vaatstra, W., and Verhaagen, N. G., "On the Vortex Flow Over Delta and Double-Delta Wings," AIAA Paper No. 82-0949, 1982.

2 Legendre, R., "Ecoulement au Voisinage de la Pointe Avant D'une Aile à Forte Fleche aux Incidences Moyennes," *La Rech. Aèro.*, Vol. 30, 1952, pp. 3–8.

3 Smith, J. H. B., "Improved Calculations of Leading-Edge Separation from Slender, Thin, Delta Wings," *Proc. Roy. Soc. A.*, Vol. 306, 1968, pp. 69–90.

4 Gad-el-Hak, M., Blackwelder, R. F., and Riley, J. J., "On the Growth of Turbulent Regions in Laminar Boundary Layers," *J. Fluid Mech.*, Vol. 110, 1981, pp. 73–95.

5 Gad-el-Hak, M., and Ho, C.-M., "The Pitching Delta Wing," *AIAA J.*, Vol. 23, 1985, pp. 1660–1665.

6 Gad-el-Hak, M., Ho, C.-M., and Blackwelder, R. F., "A Visual Study of a Delta Wing in Steady and Unsteady Motion," in *Unsteady Separated Flows*, eds. M. S. Francis and M. W. Luttges, Univ. Colorado, 1983, pp. 45–51.

7 Gad-el-Hak, M., Blackwelder, R. F., and Riley, J. J., "Visualization Techniques for Studying Turbulent and Transitional Flows," in *Flow Visualization 3*, ed. W. J. Yang, Hemisphere, 1983, pp. 568–575.

8 Gad-el-Hak, M., and Blackwelder, R. F., "On the Discrete Vortices from a Delta Wing," *AIAA J. 23*, 1985, pp. 961–962.

9 Gad-el-Hak, M., and Ho, C.-M., "Unsteady Vortical Flow Around Three-Dimensional Lifting Surfaces," *AIAA J.*, Vol. 24, No. 5, 1986.

ERRATUM

In our paper [1], due to an error, several of the points in Fig. 3 are plotted a few percent too high. A corrected graph has been published as Fig. 5(*b*) on p. 72 in [2].

1 A. M. Lynnworth and L. C. Lynnworth, ASME **Journal of Fluids Engineering**, Vol. 107, No. 1, Mar. 1985, pp. 44–48.

2 L. C. Lynnworth, ASME *Journal of Vibration, Acoustics, Stress, and Reliability in Design*, Vol. 108, No. 1, Jan. 1986, pp. 69–81.

D. W. Choi
Graduate Student,
Department of Aeronautics
and Astronautics.

F. B. Gessner
Professor,
Department of Mechanical Engineering.
Mem. ASME

G. C. Oates
Professor,
Department of Aeronautics
and Astronautics.
Mem. ASME

University of Washington,
Seattle, Wash. 98195

Measurements of Confined, Coaxial Jet Mixing With Pressure Gradient

The mixing of a subsonic confined air jet with a coaxial secondary air stream is investigated experimentally. This work differs from previous studies in that emphasis is placed on the effects of an imposed adverse pressure gradient on mixing characteristics in the initial mixing (potential core) and transition regions. The results indicate that the presence of an adverse pressure gradient promotes more rapid mixing and spreading of the shear layer in the initial mixing region, as well as elevated turbulent normal stress and shear stress levels in the outer portion of the mixing layer after the primary and secondary streams have merged. Significant radial static pressure variations occur in both the initial mixing and transition regions as a result of turbulent normal stress gradients and streamline curvature effects induced by potential core entrainment.

Introduction

Confined jet mixing with a thin inlet boundary layer condition exhibits a combination of the characteristics of free-jet mixing, boundary layer flow, and potential core entrainment. In most cases of interest, mixing of this type is turbulent throughout the shear layer. For the general case of incompressible flow in a converging or diverging duct, the flowfield can be subdivided into two distinct regions with different characteristics (Fig. 1). The initial mixing region encompasses that portion of the flow in which the central (primary) stream and the outer (secondary) stream include distinct potential cores. In addition, a wall boundary layer exists, as does a shear layer region between the two cores. The transition region downstream is characterized by the absence of a potential core and by turbulent mixing across the entire duct cross section.

Previous investigations have focused primarily on coaxial jet mixing in constant area ducts within the transition region and in the region downstream where the flow approaches a fully-developed state. A number of these studies have concentrated on mixing behavior in configurations with large duct-to-nozzle diameter ratios, in which the potential core of the secondary stream extends well beyond the potential core limit of the primary stream. Curtet and his coworkers, for example, have made mean flow and turbulence measurements in a ducted jet with a relatively large diameter ratio ($D_d/D = 13.5$) in order to examine mixing characteristics with [1] and without [2] backflow present. Subsequently, Steward and Guruz [3] investigated confined jet mixing in a configuration having a much larger diameter ratio ($D_d/D = 38$) in order to examine the extent of similarity present in radial profiles of axial mean velocity, temperature, and concentration (of CO_2 tracer particles) in the mixing region. Razinsky and Brighton [4] have made extensive mean flow and turbulence measurements for confined jet mixing in a constant area duct for two moderate diameter ratios ($D_d/D = 3, 6$) over a range of primary stream-to-secondary stream velocity ratios ($0.5 \le U_j/U_e \le 9$). Their data extend from the initial mixing region to a streamwise location where the flow is almost fully developed, and include local wall pressure, axial mean velocity, longitudinal turbulence intensity, and Reynolds shear stress profiles. A subsequent study by Oosthuizen and Wu [5] for similar operating conditions ($D_d/D = 4$, $2 \le U_j/U_e \le 4$) has provided additional data which include transverse turbulent normal stress profiles.

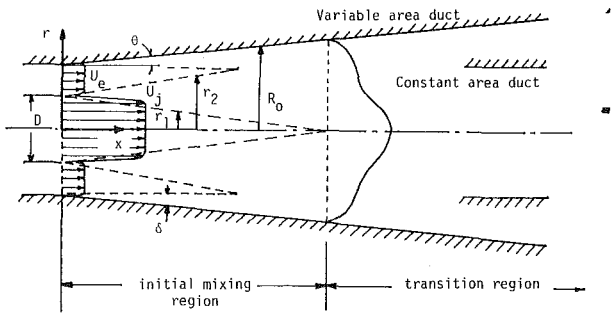

Fig. 1 Flow geometry

More recent studies have addressed the problem of confined jet mixing in a constant area duct in the presence of recirculation induced by a sudden expansion at the nozzle exit plane [6–8]. In all of these studies the primary and secondary streams were fully developed at the nozzle exit plane, and the average primary flow velocity was less than or equal to the average secondary stream velocity at this location. Under these conditions, Habib and Whitelaw have measured axial mean velocity and Reynolds stress profiles within a fixed configuration ($D_d/D = 2.8$, $D_0/D = 7.8$) for two different velocity ratios ($U_{j,m}/U_{e,m} = 0.33,1$) by means of hot-wire

Contributed by the Fluids Engineering Division for publication in the JOURNAL OF FLUIDS ENGINEERING. Manuscript received by the Fluids Engineering Division, September 23, 1983.

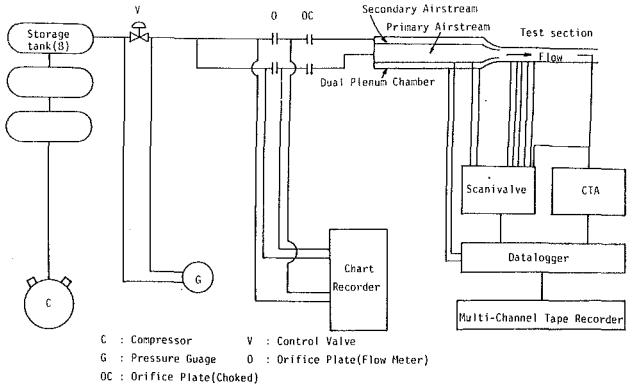

Fig. 2 Schematic flow diagram of flow facility

anemometry [6] and laser doppler anemometry [7]. Their results show that normal stress levels in the mixing region and in the region immediately downstream of the recirculation zone increase when mean shear rates are increased by operating at a velocity ratio different from unity. In a subsequent study of confined jet mixing downstream of a sudden expansion, Johnson and Bennett [8] examined the statistical properties of mass and momentum transport within and near the recirculation zone by means of laser velocimeter and laser induced fluorescence techniques. Their data are based on a fixed operating condition ($D_d/D \simeq 2$, $D_o/D \simeq 4$, $U_{j,a}/U_{e,a} \simeq 0.12$) and include probability density function profiles of axial mean velocity and concentration (of fluorescent dye particles) in the mixing region. Higher-order moment profiles (skewness and kurtosis) are also presented to form a relatively complete picture of statistical properties within the shear layer and recirculation zones.

All of these studies have increased our basic understanding of the mixing and transport processes which occur in a confined jet within a constant area duct, either with or without a sudden expansion at the nozzle exit. Additional mean flow data are available on the nature of confined jet mixing in a convergent-divergent duct for several inlet velocity ratios [9]. At the present time, however, there is little turbulence data available which describe local Reynolds stress behavior in confined jet flows which develop in the presence of streamwise pressure gradients induced by continuous duct divergence. Little experimental work has been done in the initial mixing region, primarily because of difficulties in obtaining valid data in the thin shear layer, although there is considerable motivation to understand the mixing processes in this region, because many mixing applications require the use of small length-to-diameter devices. The present study was undertaken, therefore, in order to develop a better understanding of local flow behavior in the initial mixing and transition regions of confined jet flows.

Experimental Apparatus

Figure 2 shows schematically the main parts of the flow facility and the instrumentation employed in this investigation. The air coming from eight high pressure storage tanks is divided into two streams and supplied to concentrically positioned plenum chambers. In the dual air supply lines, two aluminum orifice plates operate in a choked condition and are used to regulate the mass flow rate. In the dual plenum chamber, which is 2.286 m long with 0.762 m and 1.016 m inner and outer shell diameters, respectively, the air streams are dispersed by five "core busters," pass through two layers of fine mesh screen, three layers of honeycomb, and another four layers of fine mesh screen. An additional layer of honeycomb (3.175 mm cell diameter; $\ell/d = 50$) covered with a cloth screen was installed to clean the air and reduce turbulence intensities further ([10]). Flow passing through each cell of the honeycomb becomes nominally fully developed, which diminishes the lateral turbulence intensity as well as the longitudinal turbulence intensity until all scales of motion become dominated by viscous forces. The plenum chambers terminate in two concentric nozzles with exit diameters of 101.6 mm and 2.032 mm ($D_d/D = 2$). For corresponding nozzle contraction ratios of 56 and 15, the turbulence intensity based on the local mean velocity was reduced to less than 0.01 and 0.025 in the central and annular potential flows, respectively. The thickness of the inner nozzle lip was machined to

Nomenclature

d = wire or honeycomb diameter
D_d = duct diameter at nozzle exit
D = nozzle exit diameter
D_0 = outer duct diameter at nozzle exit
f = similarity parameter, defined as $f = (U - U_2)/(U_1 - U_2)$
I = local turbulence intensity, defined as $I = [(\overline{u'^2} + \overline{v'^2} + \overline{w'^2})/(3U^2)]^{1/2}$
k = tangential cooling factor for an inclined wire or turbulence kinetic energy
l = wire or honeycomb length
l_0 = normalizing length scale, defined as the radial position where $U = (U_1 + U_2)/2$
L_c = primary (central) jet potential core length
P = static pressure
R_0 = radius of the confining tube (Fig. 1)
r = radial position from the centerline
r_1 = radial position of the inner edge of the shear layer (Fig. 1)
r_2 = radial position of the outer edge of the shear layer (Fig. 1)
r_j = radius of the primary jet at the nozzle exit
U = axial mean velocity component
U_1 = axial velocity at the inner edge of the shear layer
U_2 = axial velocity at the outer edge of the shear layer
U_δ = axial velocity at the outer edge of the boundary layer
$U_{\delta,a}$ = axial velocity at the apparent edge of the boundary layer where normal stress levels are minimal
U_c = local axial centerline velocity
U_e = annular jet potential core velocity at nozzle exit (Fig. 1)
U_j = primary jet potential core velocity at nozzle exit (Fig. 1)
u' = axial fluctuating velocity component
$\overline{u'v'}$ = Reynolds shear stress
v' = radial fluctuating velocity component
w' = azimuthal fluctuating velocity component
x = axial position from the nozzle exit
α = wire inclination angle
δ = boundary layer thickness
θ = duct divergence angle (Fig. 1)
η = similarity coordinate, defined as $\eta = (r - r_1)/(r_2 - r_1)$
ρ = density

Subscripts

a = average value
c = centerline condition
e = annular jet condition at nozzle exit
i = initial condition
j = central jet condition at nozzle exit
m = maximum value
w = wall condition

0.254 mm to avoid significant wake-type velocity profiles in the initial mixing region. The boundary layer thickness was 1.524 mm, 2.032 mm and 2.54 mm for the primary jet stream, and the inner and the outer side of the secondary stream, respectively, at the nozzle exit. The initial core flow velocity for the primary jet was 29.87 m/sec and that for the annular stream was 11.35 m/sec ($U_j/U_e = 2.6$). Details of the nozzle configurations are described by Choi [11]. The two interchangeable test sections used were made of a 2.032 mm I.D. plexiglas tube (constant area mixing case) and a 3.175 mm thick aluminum sheet with a half divergence angle of 4 deg (variable area mixing case). Each test section was approximately 1.2 m long with 24 static pressure taps along the wall at 5.08 cm spacings.

The constancy of jet volume flow rates and temperature was checked by means of a total pressure tube and copper-constantan thermocouples installed inside the dual plenum chamber. The total pressure within the test section was measured with a hypodermic impact tube. The mean velocity and turbulence measurements were made by means of a Constant Temperature Anemometer (DISA 55M01), a Digital Voltmeter (Preston 723), an RMS Voltmeter (DISA 55D35), a Turbulence Processor (DISA 52B25), and a Standard Bridge (DISA 55M10). A normal wire probe ($\ell/d = 200$) was used for measuring the axial turbulent normal stress and the mean velocity profiles. An inclined wire probe ($\ell/d = 210$, $\alpha = 45$ deg) was used for measuring the Reynolds shear stress component and the remaining turbulence normal stress components.

In the present study, the maximum skewness angle of the flow was 4 deg. (for the variable area mixing case), and hence the simplified response equations developed by Hill and Sleicher [12] were used. In these response equations, the cooling law exponent was assigned a value of 0.45 and the tangential cooling factor k for the inclined wire was determined by comparing pipe flow Reynolds shear stress data with the theoretical relationship applicable to fully developed circular pipe flow. In the present investigation, the static pressure in the flow was determined indirectly through the use of Bernoulli's relationship with the stagnation pressure obtained from total probe measurements and the resultant mean velocity from hot-wire measurements. The stagnation pressure probe was made from a 0.5 mm hyperdermic needle with 1 in. probe length and a 1/8 in. O.D. supporting tube. The hot wire lengths normal to the flow were less than 0.5 mm.

Following the technique suggested by Kline and McClintock [13], uncertainty estimates were made at several representative points in the initial mixing and transition regions of both configurations (constant area and variable area mixing cases). On the basis of these calculations, it is estimated that the maximum uncertainty in measured values of U_c/U_j, U/U_j, $-\overline{u'v'}/U_c^2$, k/U_c^2, k/U^2, and $\overline{v'^2}/\overline{u'^2}$ is ± 1.0, ± 1.3, ± 4.6, ± 4.8, ± 6.1, and ± 12.6 percent, respectively, of the measured value itself. The maximum uncertainty in measured values of $(P-P_i)/(1/2\rho U_c^2)$, was found to be region dependent, varying from ± 0.028 in the initial mixing region to ± 0.057 in the transition region. The maximum uncertainty in normalized wall static pressure values, $(P_w - P_{w,i})/(1/2\rho U_c^2)$, is somewhat higher in the initial mixing region (± 7.5 percent) in comparison to the uncertainty associated with measurements in the transition region (± 4.3 percent). The maximum uncertainty in specifying the similarity coordinate position $(r-r_1)/(r_2-r_1)$ was estimated to be ± 3.0 percent for both cases. The corresponding uncertainty in the velocity ratio $(U-U_2)/(U_1-U_2)$ varied from ± 1.2 percent for the constant area mixing case to ± 2.5 percent for variable area mixing.

Results and Discussion

1. Mean Velocity Field. The axial variation of the centerline

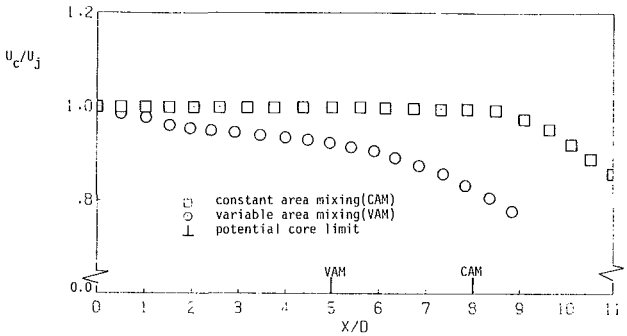

Fig. 3 Axial centerline velocity variation

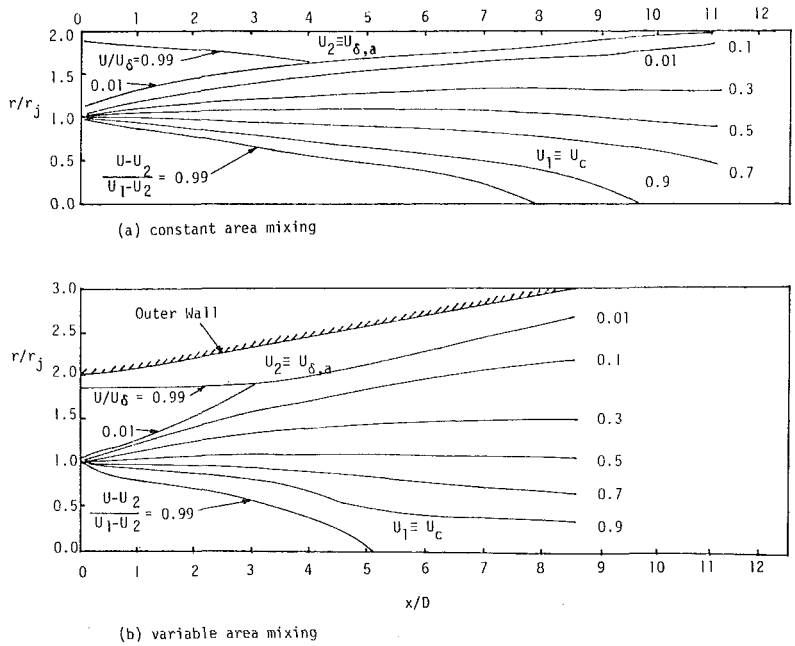

Fig. 4 Axial mean velocity contour maps. (*a*) constant area mixing; (*b*) variable area mixing

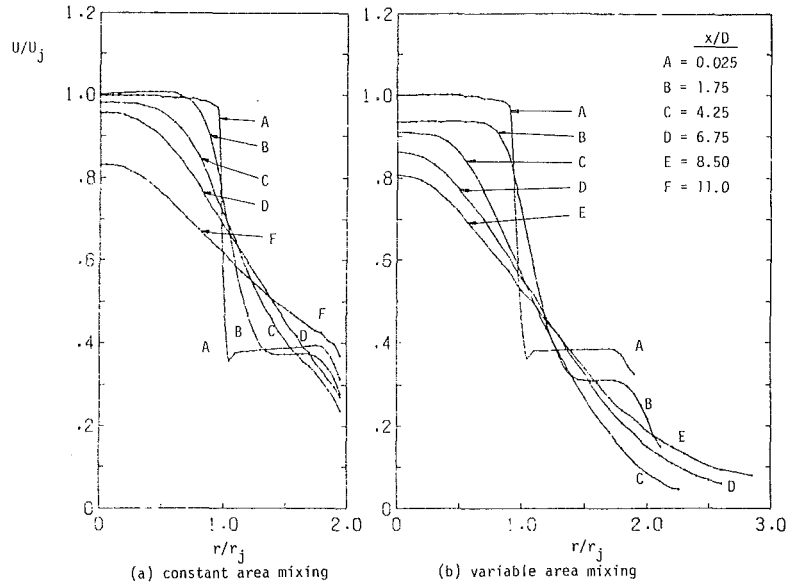

Fig. 5 Axial mean velocity profiles. (*a*) constant area mixing; (*b*) variable area mixing

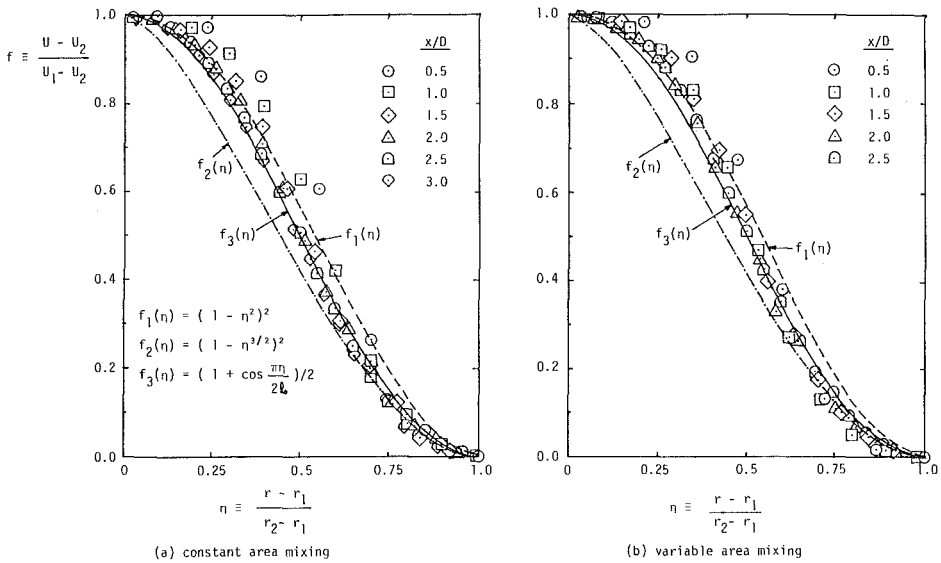

Fig. 6 Axial mean velocity profiles in terms of similarity coordinates; f_1 [15], f_2 [4], f_3 [14], (*a*) constant area mixing; (*b*) variable area mixing

velocity scaled with the initial jet velocity is shown in Fig. 3. For the constant area mixing case, the results indicate that the centerline velocity is essentially constant up to 8 diameters from the primary jet nozzle, whereas for the variable area mixing case, a slight, almost linear, decrease is followed by a rapidly steepening decrease after 5 diameters (the potential core limit of the primary flow). The results for the former case (constant area mixing) are indicative of nominally zero pressure gradient flow in the initial mixing region until the potential core of the primary flow becomes completely entrained (nominally at $x/D \simeq 8$).

Figure 4 is a mean velocity contour map for both cases which was constructed by interpolating the data to points with the prescribed numerical values shown for $(U-U_2)/(U_1-U_2)$ and U/U_δ. From the figure it can be seen that the wall boundary layer grows initially until it interacts with the mixing layer. Subsequently, the wall boundary layer merges with the mixing layer. In the region downstream there is no distinct division between the wall boundary layer and the mixing layer; the resultant effect on the flow is similar to that of a decreasing turbulent boundary layer thickness. For constant area mixing, predicted streamline patterns near the wall indicate that streamlines are curved slightly toward the wall [11], which implies that the near-wall flow is accelerated locally in the streamwise direction. This observation is supported by the measured velocity profiles in Fig. 5, which indicate that flow near the confining wall (at $r/r_j = 2$) is accelerated locally between $x/D = 4.25$ (profile C) and $x/D = 11.0$ (profile F) for the constant area mixing case.[1] For the variable area mixing case, the imposed adverse pressure gradient enhances the velocity difference between the primary and secondary streams at a given streamwise location. This velocity difference increase promotes more active momentum transfer and leads, in turn, to a more rapid spread of the mixing layer,

[1] In order to observe trends more clearly, symbols have not been used to identify experimental values in this figure and in the subsequent figures which show radial profiles of turbulence-related quantities. It should be noted, however, that the line distributions shown in these figures pass through each experimental value, so that local undulations in each distribution are indicative of excursions of the data from a smooth-line distribution.

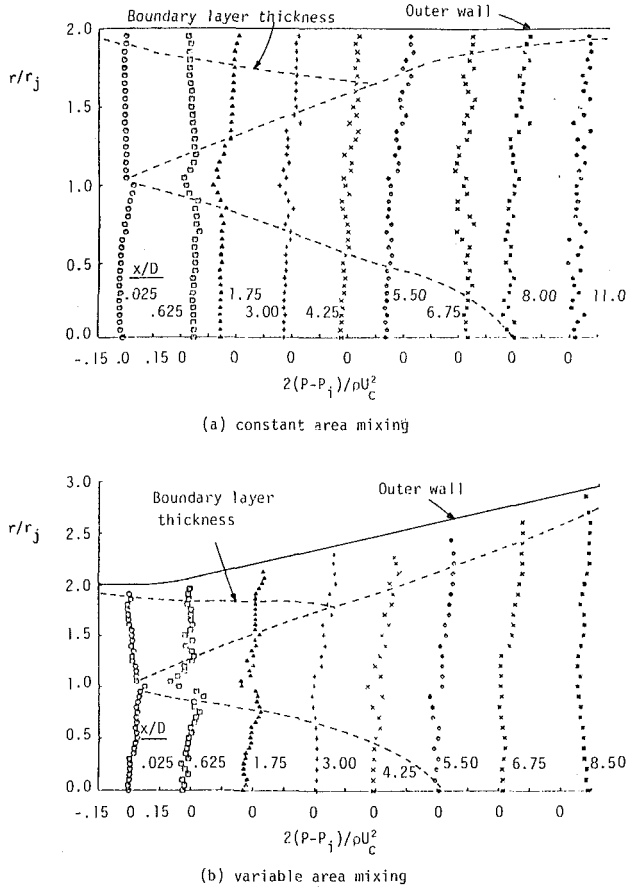

Fig. 7 Static pressure distributions. (*a*) constant area mixing; (*b*) variable area mixing

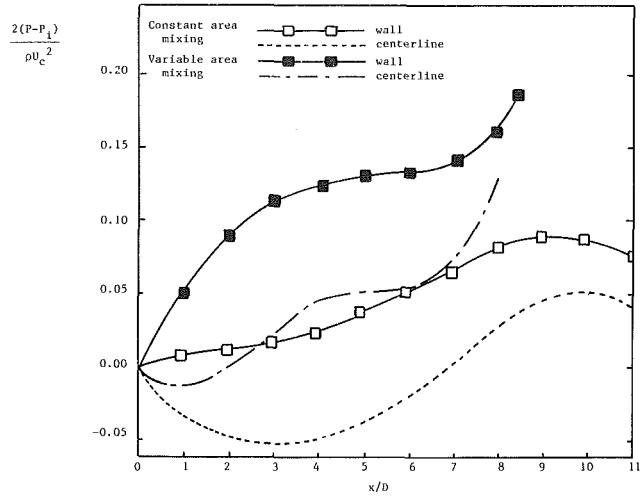

Fig. 8 Axial static pressure distributions

as shown in Fig. 4, and to reduced velocity levels near the confining wall (compare profiles C and D in Fig. 5(*a*) with those in Fig. 5(*b*)). For the variable area mixing case, the axial mean velocity profile near the wall approximately two diameters from the nozzle exit (profile B in Fig. 5(*b*)) resembles a typical turbulent boundary layer approaching separation under the influence of a strong adverse pressure gradient. Because of active momentum transfer toward the wall, however, separation did not occur within the duct further downstream.

In order to examine the extent of velocity profile similarity in the initial mixing region, axial mean velocity profiles in the shear layer were plotted in terms of similarity coordinates, as shown in Fig. 6. These profiles were measured between the nozzle exit plane and the potential core limit of the outer flow for each case (at $x/D \simeq 4$ for constant area mixing and at $x/D \simeq 3$ for variable area mixing; refer to Fig. 4). Also shown in Fig. 6 are the analytical forms for $f(\eta)$ proposed by Mikhail [14], Hill [15], and Razinsky and Brighton [4] for modeling velocity profile behavior in the initial mixing layer. The experimental profiles in this figure are indicative of a remarkable degree of similarity for each case if data taken in the immediate vicinity of the nozzle exit ($0 < x/D < 1.0$) are excluded. Within this initial region, velocity values in the inner portion of the shear layer ($0 \leq \eta \leq 0.5$) are elevated above values measured further downstream, an effect also observed by Razinsky and Brighton [4] in their experiments. A comparison of the proposed analytical forms for $f(\eta)$ with the data for each case appears to indicate best agreement between the data and the cosine function proposed by Mikhail [14]. This comparison is somewhat misleading, however, inasmuch as the analytical distribution shown is based on a fixed value of the normalizing length scale l_0, when, in reality, the present data show that l_0 actually decreases monotonically with streamwise position (e.g., l_0 decreases from its initial value at $x/D = 0.5$ to a value which is typically 15 percent less at $x/D = 2.5$). Close scrutiny of the results shown in Fig. 6 also reveals that although the cosine form for $f(\eta)$ provides a reasonable fit of the data for constant area mixing, the analytical function lies slightly below the data in the inner portion of the shear layer ($0 < \eta < 0.5$) for variable area mixing, and slightly above the data in the outer region of this layer ($0.5 < \eta < 1.0$). This subtle, but consistent, behavior demonstrates the difficulties of attempting to use similarity parameters to model velocity profile behavior in a mixing layer subjected to a varying streamwise pressure gradient.

2. Static Pressure Field. Measurement of the static pressure field showed noticeable pressure variations in the radial and axial directions throughout the flowfield. Figure 7 shows radial static pressure distributions measured at several axial positions for both test cases. These pressure variations result from mean field interactions and interactions between the mean field and the local turbulent field. The moderately large scatter which is evident in the downstream mixing zone ($x/D > 3$) for both test cases is attributable primarily to uncertainties associated with the indirect method of static pressure measurement. The mean field interactions in the initial mixing region correspond to wake-type mixing of the two streams and a jet entrainment effect. This type of interaction leads to a local peaking of the static pressure in the mixing layer at $x/D = 0.025$ (refer to Fig. 7). It would normally be anticipated that the transverse turbulent normal stresses, $\overline{v'^2}$ and $\overline{w'^2}$, would contribute to reducing the static pressure in the shear layer; however, the curvature effect of the streamlines in the near wake brought about by the well-known "negative displacement thickness effect" results in a higher static pressure than that which would be present without streamline curvature. Hence, it appears that any contribution of the transverse turbulent normal stresses is overshadowed by this curvature effect of the streamlines. In the early mixing region ($0.625 \leq x/D \leq 1.75$), the contribution of the transverse turbulent normal stresses to the static pressure within the mixing layer leads to a static pressure deficit in this layer. As the width of the mixing layer increases rapidly in the downstream region, gradients of the transverse turbulent normal stresses are diminished, and consequently pressure variations in the transverse direction are reduced. These results suggest that the radial momentum equation with $P = P(x, r)$ and an appropriate turbulence model which accounts for variations in the turbulent normal stresses (full Reynolds stress model, for example), should be considered to predict accurate flow properties in the initial mixing region.

Figure 8 shows the axial variation of measured centerline and wall static pressure distributions. The curves shown for the centerline cases represent a least squares polynomial fit to the fifty experimental values obtained. For the variable area mixing case (solid symbols), the vigorous entrainment process present in the near-wake region of the nozzle dominates the mixing process and masks the effects of turbulent boundary layer development along the outer wall. The resultant effect on the secondary stream leads to a moderately strong adverse pressure gradient initially along the wall in that region ($0 \leq x/D \leq 3$). A slight adverse pressure gradient is observed along the wall in the interval $3 \leq x/D \leq 6$ where the interaction between the turbulent boundary layer and shear layer occurs (compare Fig. 4 and Fig. 8), which implies that, through the interaction, growth of the turbulent boundary layer tends to suppress further spreading of the mixing layer and vice versa, resulting in a slight increase in effective flow area corresponding to the observed adverse pressure gradient. In the region further downstream of the interaction ($x/D > 6$), mixing behavior outweighs the effects of the turbulent boundary layer, resulting in more active momentum transfer toward the wall. Consequently, the effective flow area is increased, leading to a further increase in wall static pressure. For the case of constant area mixing, a similar pattern with a reduced adverse pressure gradient along the wall is observed; however, as the turbulent boundary layer starts to dominate the flow ($x/D > 10$), the wall static pressure decreases monotonically in the downstream region. The centerline static pressure distributions for both test cases show an evident departure from the corresponding wall static pressure distributions. The centerline static pressure variations are indicative of the fact that the central portion of the flow senses only the relative decrease in flow area for the primary stream as mixing starts to take place, and requires time to adjust to the surrounding flow conditions (entrainment process, growth of the wall boundary layer, etc.). The static pressure variations observed for the constant area mixing case follow the same patterns as those predicted numerically by Shavit [17]. Although his predictions apply for the laminar case, the effect of an induced pressure gradient should be qualitatively similar to that for the turbulent case.

The magnitude of the resultant adverse pressure gradient induced by the entrainment process depends on the initial velocity and area ratios of the two streams, which were fixed in the present study. A severe tail-up of the static pressure distributions in Fig. 8 for the variable area mixing case was found to be a typical effect of the exit condition.

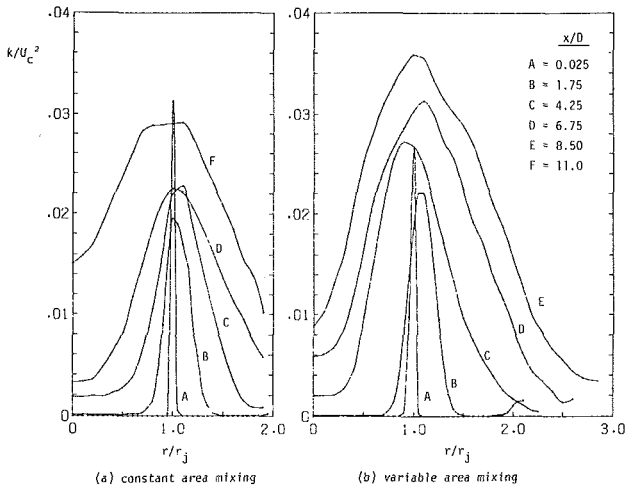

Fig. 9 Turbulence kinetic energy profiles. (*a*) constant area mixing; (*b*) variable area mixing

3. Turbulent Stresses. Turbulence kinetic energy profiles for both test cases are shown in Fig. 9. Similar distributions for the longitudinal and transverse turbulence intensities are reported by Choi [11]. In Fig. 9 the initial peaking of the turbulence kinetic energy at $x/D = 0.025$ corresponds to highly anisotropic turbulence in the thin wake region downstream of the nozzle exit, with the radial normal stress exceeding the axial normal stress. As turbulent jet mixing becomes more influential in the downstream direction, the axial normal stress becomes dominant and exceeds the radial normal stress. This phenomenon is illustrated in Fig. 10, which shows the axial variation of $\overline{v'^2}/\overline{u'^2}$ measured across the mixing layer. In the near-wake region of the flow ($x/D = 0.025$), it can be seen that the radial turbulent normal stress is higher by a factor of approximately 1.2 than the longitudinal normal stress. This unusual behavior can be explained as follows; The sudden disappearance of the confining inner nozzle wall induces a cur-

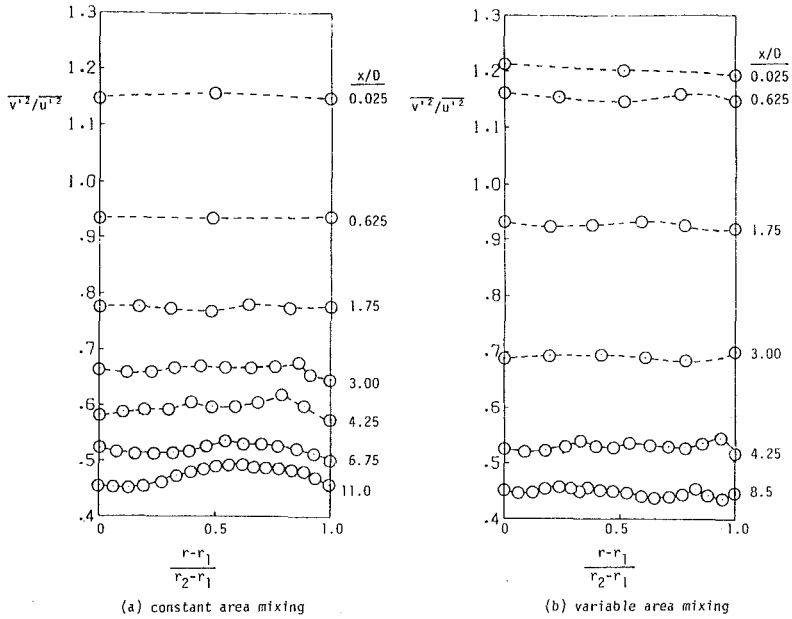

Fig. 10 $\overline{v'^2}/\overline{u'^2}$ distributions across the shear layer ($r_1 \leq r \leq r_2$) (*a*) constant area mixing; (*b*) variable area mixing

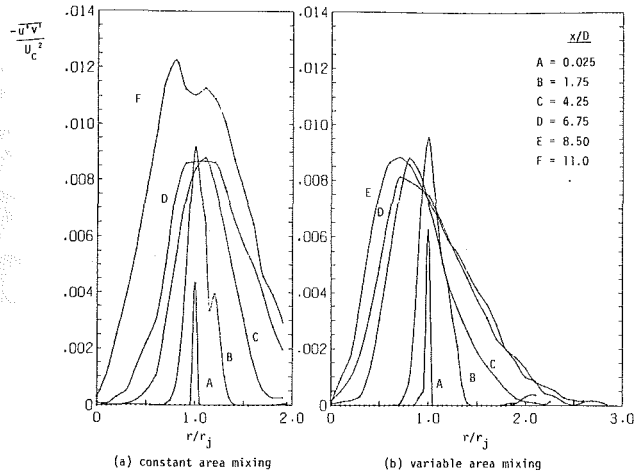

Fig. 11 Reynolds shear stress profiles. (*a*) constant area mixing; (*b*) variable area mixing

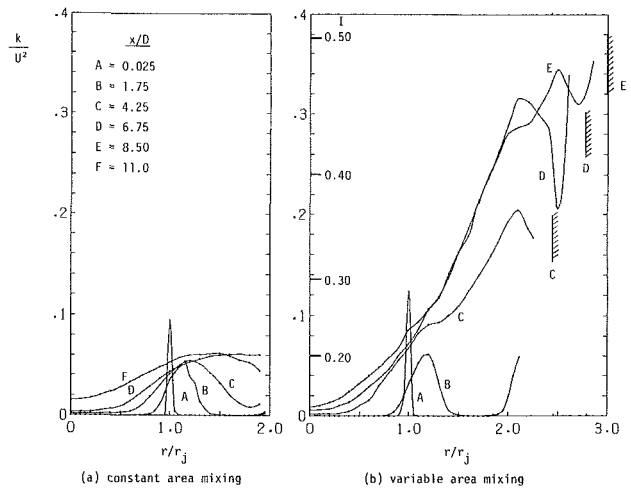

Fig. 12 Local turbulence kinetic energy profiles. (*a*) constant area mixing; (*b*) variable area mixing

vature effect of the streamlines (which converge toward the center of the wake) and creates a highly concentrated shear zone with high turbulence kinetic energy. Within the wake region where the streamlines are converging, vortex stretching takes place, resulting in an increase of the axial vorticity component and a decrease of the radial vorticity component. This vortex stretching mechanism leads to elevated values for $\overline{v'^2}$ in comparison to $\overline{u'^2}$ values. Similar behavior has been observed when grid flow turbulence is subjected to longitudinal strain induced by streamwise acceleration of the mean flow [18, 19]. In the region downstream of the near-wake region, an opposite argument based on diverging streamline behavior can be applied to explain the decay of the ratio $\overline{v'^2}/\overline{u'^2}$. For both test cases, it should be noted that the data in Fig. 10 indicate that the ratio of $\overline{v'^2}/\overline{u'^2}$ is approximately constant across the mixing layer at each streamwise location over the interval $0.025 \leq x/D \leq 11.0$. Additional data reported by Choi [11] indicate that the ratio of $\overline{w'^2}/\overline{u'^2}$ maintains an approximately constant value of 0.49 throughout the mixing layer.

Reynolds shear stress profiles are presented in Fig. 11. Maxima of the Reynolds shear stress are located close to the points where the mean velocity gradient is maximum. For constant area mixing, these points stay at about $r/r_j = 1.0$, whereas for variable area mixing, they migrate toward the centerline, which is readily verified by direct comparison with the mean velocity profiles shown in Fig. 5.

In order to examine the influence of an imposed streamwise pressure gradient on turbulence kinetic energy and Reynolds shear stress profiles more closely, the profiles shown in Figs. 9 and 11 were replotted by using the local axial mean velocity, U, as the normalizing factor. The resulting profiles for k/U^2 shown in Fig. 12 are indicative of trends similar to those observed for the $-\overline{u'v'}/U^2$ profiles. Figure 12 also includes a non-linear scale for the three-dimensional local turbulence intensity, I, which is equivalent to $[(2k)/(3U^2)]^{1/2}$. From the figure it can be seen that local turbulence kinetic energy and intensity levels in the initial mixing region ($x/D < 3$) are quite similar for the two cases (compare profiles A and B in Figs. 12(*a*) and 12(*b*)). Within the transition region, however, local turbulence kinetic energy and intensity levels in the inner portion of the mixing layer ($0 \leq r/r_j \lesssim 1$) for variable area mixing are greater than those for constant area mixing and, in the outer portion of this layer ($r/r_j \gtrsim 1$), these levels can exceed those for constant area mixing by an order of magnitude (compare profiles C and D in Figs. 12(*a*) and 12(*b*)). These results indicate that the presence of a streamwise adverse pressure gradient induced by duct divergence can amplify velocity fluctuations markedly in the outer portion of the mixing layer after the primary and secondary streams have managed. It is this amplification which enhances momentum transfer in the outer portion of the mixing layer and leads, in turn, to reduced axial mean velocity gradients in this region (compare profiles C and D in Figs. 5(*a*) and 5(*b*) for $r/r_j \gtrsim 1$).

Summary and Conclusions

The nature of confined jet mixing between two axisymmetric coaxial jets with potential cores has been investigated experimentally. For purposes of comparison, data were taken for confined jet mixing in a constant area duct and in a continuously diverging duct for the same prescribed inlet conditions ($D_d/D = 2.0$, $U_j/U_e = 2.6$). On the basis of the results, the following conclusions can be drawn:

1. The presence of an imposed streamwise adverse pressure gradient promotes more rapid mixing and spreading of the shear layer in the initial mixing region. Axial mean velocity profiles in this region are approximately self similar for a nominally fixed streamwise pressure gradient, but the profile shape is altered when the streamwise pressure gradient is changed. Within the initial mixing region, turbulent normal and shear stress profiles are not markedly altered by an imposed streamwise pressure gradient.
2. Within the transition region, an imposed streamwise adverse pressure gradient promotes much higher turbulence stress levels and more active momentum transfer in the outer portion of the mixing layer. These mechanisms lead to reduced axial mean velocity gradients in this region and tend to inhibit local flow separation along the confining wall.
3. Within both the initial mixing and transition regions, radial static pressure variations occur for both cases as a result of streamline curvature effects and transverse normal stress gradients in the flow. The former effect is most apparent in the initial mixing region where potential core entrainment causes streamlines to be curved toward the axial centerline. Downstream of this region transverse normal stress gradients dominate the static pressure field, which is characterized by reduced static pressure levels in the flow in comparison to wall pressure levels.

Acknowledgment

This work was sponsored by a grant from the Air Force Office of Scientific Research (AFOSR-80-0186). The authors would like to express their appreciation to AFOSR for their support of this study.

References

1 Barchilon, M., and Curtet, R., "Some Details of the Structure of an Axisymmetric Confined Jet with Backflow," ASME *Journal of Basic Engineering*, Vol. 86, 1964, pp. 777–787.

2 Curtet, R., and Ricou, F. P., "On the Tendency of Self-Preservation in Axisymmetric Ducted Jets," ASME *Journal of Basic Engineering*, Vol. 86, 1964, pp. 765–776.

3 Steward, F. R., and Guruz, A. G., "Aerodynamics of a Confined Jet with Variable Density," *Journal of Combustion Science and Technology*, Vol. 16, 1977, pp. 29–45.

4 Razinsky, E., and Brighton, J. A., "Confined Jet Mixing for Nonseparating Conditions," ASME *Journal of Basic Engineering*, Vol. 93, No. 2, 1971, pp. 333–349.

5 Oosthuizen, P. H., and Wu, M. C., "Experimental and Numerical Study of Constant Diameter Jet Mixing," *Proceedings, 1st Symposium on Turbulent Shear Flows*, Imperial College, Apr. 1977, pp. 10.1–10.7.

6 Habib, M. A., and Whitelaw, J. H., "Velocity Characteristics of a Confined Coaxial Jet," ASME JOURNAL OF FLUIDS ENGINEERING, Vol. 101, No. 4, 1979, pp. 521–529.

7 Habib, M. A., and Whitelaw, J. H., "Velocity Characteristics of Confined Coaxial Jets With and Without Swirl," ASME JOURNAL OF FLUIDS ENGINEERING, Vol. 102, No. 1, 1980, pp. 47–53.

8 Johnson, B. V., and Bennett, J. C., "Statistical Characteristics of Velocity, Concentration, Mass Transport, and Momentum Transport for Coaxial Jet Mixing in a Confined Duct," ASME *Journal of Engineering for Gas Turbines and Power*, Vol. 106, January, 1984, p. 121.

9 Helmbold, H. B., Luessen, G., and Heinrich, A. M., "An Experimental Comparison of Constant Pressure and Constant Diameter Jet Pumps," University of Wichita, School of Engineering, Engineering Report No. 147, 1954.

10 Lumley, J. L., "Passage of a Turbulent Stream through Honeycomb of Larger Length-to-Diameter Ratio," ASME *Journal of Basic Engineering*, June 1964, pp. 218–220.

11 Choi, D. W., "Investigation of Axisymmetric Confined Turbulent Jet Mixing in the Near region with Adverse Pressure Gradient," PhD thesis, University of Washington, 1983.

12 Hill, J. C., and Sleicher, C. A., "Equations for Errors in Turbulent Measurements with Inclined Hot-Wires," *Physics of Fluids*, Vol. 12, 1969, pp. 1126–1127.

13 Kline, S. J., and McClintock, F. A., "Describing Uncertainties in Single-Sample Experiments," *Mechanical Engineering*, Vol. 75, 1953, pp. 3 8.

14 Mikhail, S., "Mixing of Coaxial Streams inside a Closed Conduit," *Journal of Mechanical Engineering Science*, Vol. 2, No. 1, 1960, pp. 59–68.

15 Hill, P. G., "Incompressible Jet Mixing in Converging-Diverging Axisymmetric Ducts," ASME *Journal of Basic Engineering*, Vol. 89, No. 1, 1967, pp. 210–220.

16 Razinsky, E., and Brighton, J. A., "A Theoretical Model for Nonseparated Mixing of a Confined Jet," ASME *Journal of Basic Engineering*, Vol. 94, No. 3, 1972, pp. 551–558.

17 Shavit, G., "Analytical and Experimental Investigations of Laminar Mixing of Homogeneous and Heterogeneous Jets in a Confining Tube," Ph.D. thesis, Illinois Institute of Technology, June 1970.

18 Townsend, A. A., "The Uniform Distortion of Homogeneous Turbulence," *Journal of Mechanics and Applied Mathematics*, Vol. 7, Part 1, Mar. 1954, pp. 104–127.

19 Reynolds, A. J., *Turbulent Flows in Engineering*, Wiley, 1974, p. 25.

Impulsively Started Steady Flow About Rectangular Prisms: Experiments and Discrete Vortex Analysis

T. Sarpkaya
Naval Postgraduate School,
Monterey, CA 93943

C. J. Ihrig
USS Swordfish,
FPO,
San Francisco, CA 96678

Impulsively started steady flow about sharp-edged rectangular prisms has been investigated experimentally and numerically. The forces acting on the bodies have been determined at a Reynolds number of about 20,000 for various angles of incidence as a function of the relative displacement of the fluid. The results have shown that the shedding of the first few vortices has profound effects on both the lift and drag coefficients, often resulting in a large initial rise in drag. The surface-vorticity-distribution version of the discrete vortex model has shown that the strength of the vortex clusters varies from 80 to 90 percent of the vorticity generated in the shear layers. The Strouhal number is correctly predicted but the calculated forces are somewhat larger than those measured experimentally.

Introduction

The objectives of this study are to provide data on the forces acting on various rectangular prisms immersed in an impulsively started steady smooth flow at a Reynolds number of about 20,000 and to conduct numerical experiments through the use of the discrete vortex model for the purpose of simulating the kinematic and dynamic characteristics of the flow.

Aside from its intrinsic fluid mechanical interest, impulsively started flow about bluff bodies is of direct relevance to many practical applications. These include the loading of bodies immersed in the pressure suppression pool of boiling water nuclear reactors during a loss-of-coolant accident and the loading and subsequent response of bodies subjected to impulsive aerodynamic loads.

The body shapes and the ambient flow characteristics, although resulting in much simpler flows than those encountered in the practical applications cited, have been arranged to provide a basis for the improvement of the calculation methods and to acquire some insight into the role played by the shedding of the first few vortices.

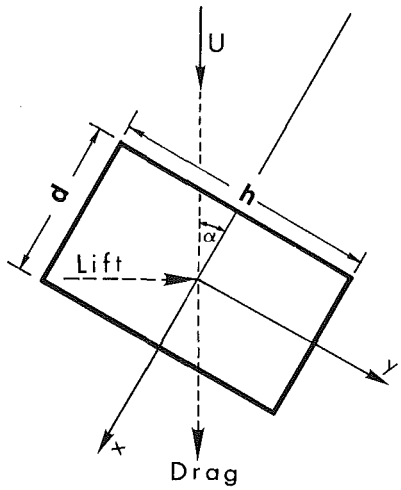

Fig. 1 Definition sketch and models used: $d/h = 0.62$ ($d = 0.85$ in., 2.16 cm); $d/h = 1$ ($d = 1$ in., 5.08 cm); $d/h = 1.62$ ($d = 2.75$ in., 7 cm)

Governing Parameters

The base pressure coefficient C_{pb} and the lift and drag coefficients, C_L and C_d, for a rectangular prism immersed in an impulsively started flow (see Fig. 1 for definitions) depend on the relative displacement s/h ($= Ut/h$), the cross sectional shape characterized by d/h, the Reynolds number Re ($= Uh/\nu$), the angle of incidence α, the ratio L/h, the geometric blockage ratio h/B, and the intensity ϵ and the scale λ/h of the free stream turbulence (FST). The end effects are not characterizable by a single parameter and depend in a complex manner on the type and shape of the two ends (e.g., a small gap, end plates), wall boundary layers, and on the parameters governing C_{pb}, C_L, and C_d.

Other than numerical experiments, there is no mechanical system which is capable of generating a truly impulsive flow. In fact, efforts to generate impulsive or uniformly accelerated flow at high Reynolds number or accelerations in a liquid medium may be hampered by the generation of compression and rarefaction waves and regions of intense cavitation. Because of this reason an acceleration parameter such as $a_p = h(dU/dt)/U^2$ will have to be added to the parameters cited above in order to account for the initial history of the fluid

Contributed by the Fluids Engineering Division for presentation in the JOURNAL OF FLUIDS ENGINEERING. Manuscript received by the Fluids Engineering Division, May 23, 1985.

motion. However, a systematic variation of such a parameter is extremely difficult. The best one can hope for is to maintain it as constant and as large as possible.[1]

The Strouhal number St ($=f_v h/U$), characterizing the vortex shedding frequency, is defined only for the later stages of the motion. Thus, it depends only on the time-invariant parameters d/h, Re, α, ϵ, λ/h, L/h, and h/B. These are the same parameters on which the lift and drag coefficients depend for t larger than about 1.5 $U/dU/dt$.

Background Studies

There is a large volume of literature which deals with fluctuating forces and the associated vortex shedding from bluff bodies subjected to steady ambient flow. The circular cylinder has attracted by far the greatest attention. Studies with rectangular prisms are relatively new. Most of the work done to date has been experimental, with the majority of it in wind tunnels in steady flows with low levels of FST (see e.g., Vickery, 1966; Nakaguchi et al., 1968; Graham, 1969; Bostock and Mair, 1972; Bearman and Trueman, 1972; Knauss, 1974; Lee, 1975; Obasaju, 1979 and 1983; Rockwell, 1977; Courchesne and Laneville, 1982; Bearman and Morel, 1983; Gartshore, 1984). A surprising feature of the steady flow experiments is that at a critical value of $d/h = 0.62$ the growing vortices are closest to the base of the body and the drag coefficient has a maximum value of nearly equal to 3, dropping off sharply on either side of $d/h = 0.62$. This is attributed to the fact that the prism with $d/h = 0.62$ has the minimum after body length needed to provide interference with the shear layers separating from the front of the prism (Gartshore, 1984).

Very little information exists regarding the impulsively started steady flow about bluff bodies and almost all of it has been restricted to circular cylinders (see e.g., Sarpkaya, 1975; Sarpkaya, 1978; Sarpkaya and Shoaff, 1979; Bouard and Coutanceau, 1980; Kline, 1981; Sarpkaya and Kline, 1982; Ihrig, 1983).

The pioneering work of Fromm and Harlow (1963) dealt with the evolution of an impulsively started flow about a rectangular cylinder at low Re. The numerical simulation was flawed by the use of central differencing at large cell Reynolds numbers which led to spatial oscillations ahead of the rectangle.

Davis and Moore (1982) presented numerical solutions for impulsively started flow about rectangular cylinders in an infinite domain through the use of special differencing schemes for time and convection. Davis et al. (1984) extended this study to include the effects of confining walls. The Reynolds number regime investigated was from 100 to 2800 although the successful simulations were confined to Re $<$ 1000. For a square prism in an infinite domain at $\alpha = 0$ and Re = 250, C_d and C_L exhibited a pure sinusoidal response as a function of s/h, C_d having a frequency twice the vortex shedding frequency. At Re = 1000, the effects of higher order harmonics on the force coefficients became quite prevalent. In contrast, C_d and C_L for $d/h = 1$, $\alpha = 15$ deg and Re = 1000 oscillated at the same frequency, indicating that only the leeside flow is separated. The behavior of C_d and C_L for $d/h = 1.7$ and $\alpha = 0$ was an initial rise in drag, followed by a C_d minimum (at about $s/h = 30$), and then a rapid rise to the steady state during which C_d oscillated at twice the vortex shedding frequency. In other words, C_d for the prisms at zero angle of incidence oscillated about a mean value at twice the vortex shedding frequency whereas C_d and C_L for angles of incidence larger than about 5 deg oscillated at the same frequency.

With the exception of the St data, obtained and used by Davis and Moore (1982) for purposes of comparison, no other data exist to substantiate the finer details of their numerical predictions.

Nagano et al. (1981) analyzed the two-dimensional flow past a rectangular prism through the use of an appropriate conformal mapping and the discrete vortex model. Suitable assumptions were made regarding the strength and position of the nascent vortices and the loss of vorticity due to turbulent dissipation. Their calculations have, in general, correctly predicted the trends in experimental results. However, the numerical model has failed to predict the large increase in C_d in the vicinity of $d/h = 0.62$.

Inamuro et al. (1983) used the surface-singularity distribution model to calculate the flow around a square prism. They found good agreement between the calculated and measured lift and drag coefficients and the Strouhal numbers. Their model does not satisfy the Kutta condition and the vortices are allowed to shed from the two front corners only.

Experimental Apparatus

Water Tunnel. The exploratory measurements (Ihrig, 1983) were carried out in a 12 ft (3.66 m) high, 2 ft by 2 ft (0.61 m $\times$ 0.61 m) cross-section vertical water tunnel (for additional details see Sarpkaya, 1978; Kline, 1981). Subsequently, the height of the tunnel was increased to 17 ft (5.2 m) to carry out the experiments reported herein.

The fluid motion was initiated and controlled by a quick-release valve, located at the base of the tunnel. The flow accelerated in about 0.1 seconds to a constant velocity of about 1 fps (0.3 m/s). For the data reported herein the acceleration parameter $a_p = h(dU/dt)/U^2$ was about 2.5. Repeated experiments with smaller values of a_p [$1 < a_p < 2.5$, $U = 1$ fps (0.3 m/s)], have shown that the effect of the duration of the initial acceleration on the subsequent evolution of the flow is confined to a time period about 1.5 times the acceleration

[1] As later discussion will show, the effect of a_p on the evolution of flow is confined to a time period of about $1.5t^*$ (corresponding to $Ut/h \approx 1$) where t^* is the acceleration period ($t^* = U/dU/dt$).

Nomenclature

a_p = acceleration parameter $[=h(dU/dt)/U^2]$
B = width of the test section
C_d = drag coefficient
$\bar{C}_d$ = mean drag coefficient
C_L = lift coefficient
$\bar{C}_L$ = mean lift coefficient
C_{pb} = base pressure coefficient
D = diameter
d = depth of the prism
$F(z)$ = complex function
f_v = vortex shedding frequency
h = height of the prism
i = complex number
L = length of the prism
N_c = number of control points
r = radial distance
r^* = vortex core radius
s = relative fluid displacement
t = time
t^* = acceleration period $(U/dU/dt)$
U = velocity of the ambient flow
X,Y = drag and lift forces
x,y = coordinate axes
z = complex variable
z_{bn} = position of boundary vortices
z_{jk} = position of shear layer vortices
α = angle of incidence
Γ = vortex strength
ϵ = turbulence intensity
θ = angle
$\kappa\chi$ = separation direction, ∓ 1
λ = turbulence length scale
ν = kinematic viscosity
ρ = density of fluid

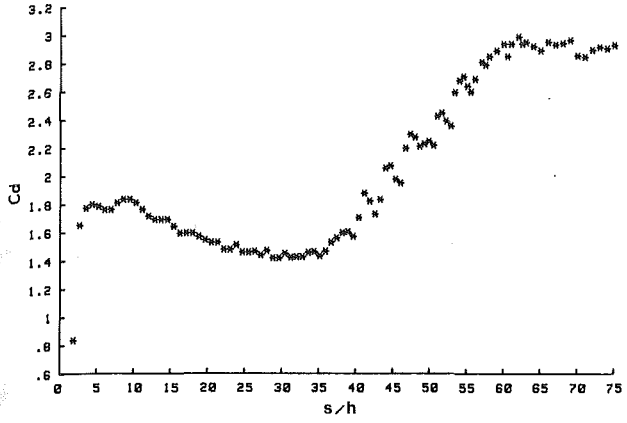

Fig. 2 Drag coefficient versus s/h for d/h = 0.62 and α = 1 deg

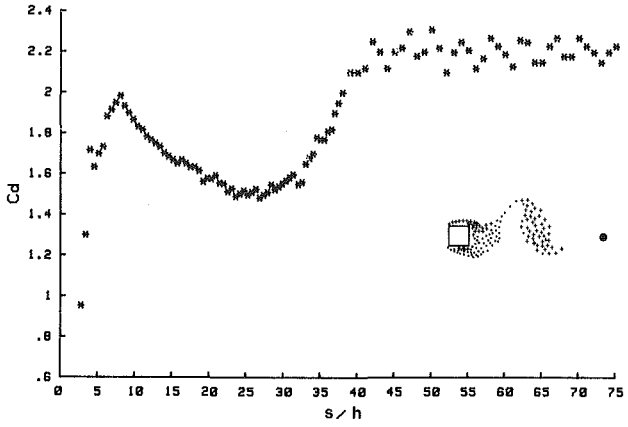

Inset: Vortex formation in the near wake at s/h = 22.4

Fig. 3 Drag coefficient versus s/h for d/h = 1 and α = 1 deg

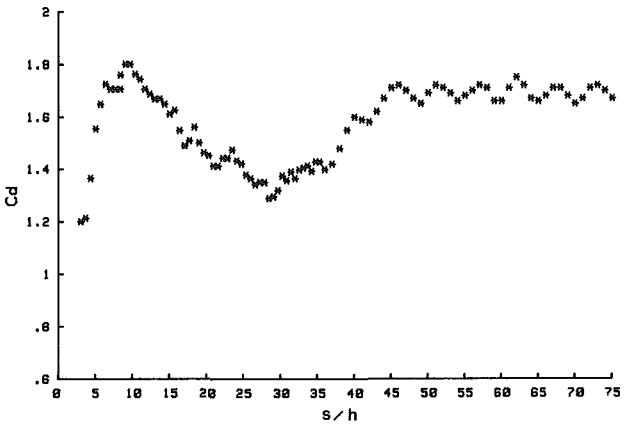

Fig. 4 Drag coefficient versus s/h for d/h = 1.62 and α = 1 deg

period (corresponding to $s/h \approx 1$) as evidenced by a comparison of the force traces for various values of a_p. In fact, the variations with a_p in either the lift or the drag force traces for $s/h > 1$ were no more than those encountered in tests with $a_p = 2.5$. This finding is in conformity with the measurements of Krause et al. (1985) and Sarpkaya and Kline (1982).

Measurement System and Test Bodies. Velocity was measured through the use of a variable resistance probe. A 13 feet (4 m) long platinum wire, placed vertically in the tunnel and mounted away from the walls, provided water-level indication to an amplifier-recorder assembly.

Three[2] prismatic two-dimensional bodies with d/h = 0.62, 1, and 1.62 were used (Fig. 1). The angle of incidence was varied from 0 to 45 degrees at 5 degree intervals.

Three force transducers were used to measure the instantaneous lift and drag forces and moment on the test bodies. Special housings were built for each gage so that they could be mounted on the tunnel wall at each end of the test body. The length of each prism was cut so that a gap of approximately 0.02 in. (0.5 mm) was present between the tunnel wall and each end. The gaps were filled with foam, glued to the ends of the prism. In addition, a special series of tests was carried out with a three piece prism (d/h = 1) to measure the forces acting on the middle one-third of the prism by fixing the two end segments on the tunnel walls and extending the force transducers into the ends of the middle segment. There was a gap about 0.02 in. (0.5 mm) at each end of the middle segment. The gaps were filled with heavy grease before each test. Numerous test runs have shown that the differences between the forces (per unit length) acting on the 24 in. (0.61 m) long prism and on the 8 in. (0.2 m) long middle segment are well within the experimental errors at the corresponding angles of incidence ($0 \leq \alpha \leq 45$), at least for the prism with d/h = 1. It is because of this reason that the questionable use of the end plates was disregarded.

Prior to testing a new body, calibration of the drag, lift and moment transducers was conducted. Furthermore, impulsive flow was initiated a number of times to verify that the velocity remained constant and the force signals were free from noise. Unfiltered raw digitized data were used to obtain the force-transfer coefficients.

The maximum possible error associated with the measurement of forces and moments was 5 percent. The variation of velocity during a given run was less than 0.5 percent for times larger than 0.1 second after the initiation of motion. None of the data presented herein has been corrected for blockage effects since absolute values are not as important as are the trends evident from the uncorrected values.

Results

An important observation made from the raw signals during the experiments was that the lift force amplitude (see Fig. 1) for all bodies at zero angle of incidence was very small, irregular and random, regardless of whether the force was measured on the full length of the prism or on its middle one-third segment. In some runs, C_L remained nearly zero for s/h as large as 50. In other runs, a small but irregular lift force developed for s/h larger than about 30. The lift force measurements were not repeatable even though everything else was kept essentially constant.[3] When the angle of incidence was set at α = 5 deg, both the lift and drag forces became very regular and repeatable (with a deviation less than 5 percent). It appears that in a perfectly uniform smooth flow (FST = 0) about a prism at zero angle of incidence the separation bubbles and vortices start out symmetrically and then develop an irregular behavior primarily because there is neither turbulence nor physical asymmetry to promote and reinforce an interaction between the separated shear layers, the afterbody and the near wake.

When the angle of incidence was decreased at 1 degree intervals from an initial value of α = 5 deg, an angle of incidence as small as α = 1 degree yielded perfectly regular and repeatable lift and drag forces for all test bodies. Evidently, either the freestream turbulence (Gartshore, 1984) and/or the asymmetry of the body relative to the direction of the ambient

[2] Two larger bodies were also used with d/h = 0.62 and d/h = 1. These results are not reported here because of space limitations and because of the larger geometric blockage.

[3] A similar observation was noted by Gartshore (1984) in steady flow (α = 0, d/h = 1/2, 2/3, and 1). The local instantaneous lift (not averaged along the span) was very irregular or unsteady *at low turbulence* but became very regular for higher intensities of turbulence.

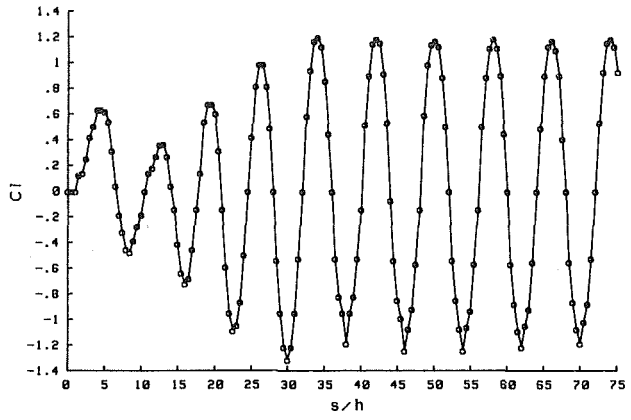

Fig. 5 Lift coefficient versus s/h for $d/h = 1$ and $\alpha = 1$ deg

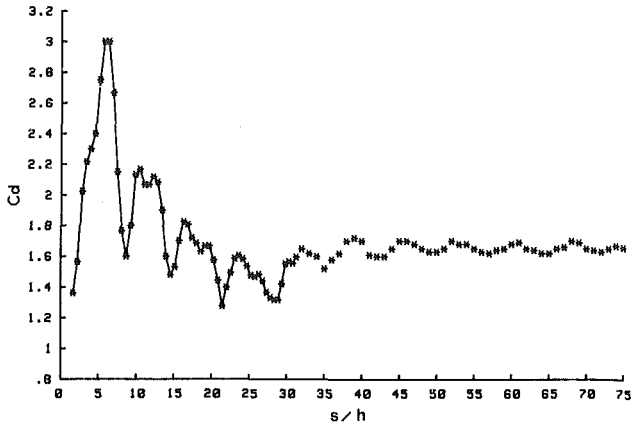

Fig. 7 Drag coefficient versus s/h for $d/h = 1$ and $\alpha = 10$ deg

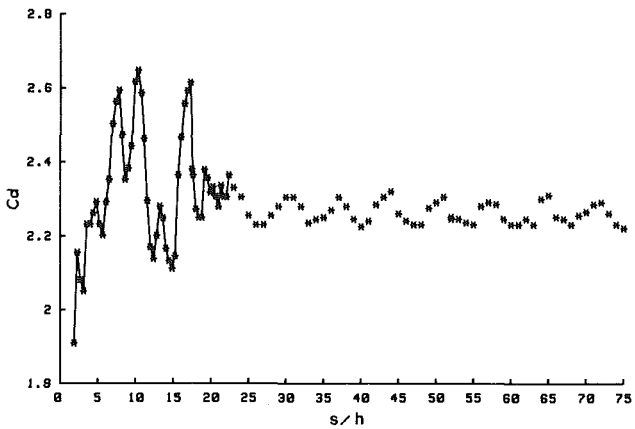

Fig. 6 Drag coefficient versus s/h for $d/h = 0.62$ and $\alpha = 10$ deg

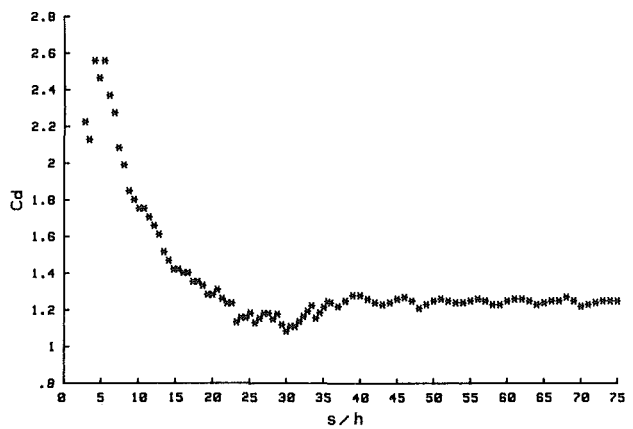

Fig. 8 Drag coefficient versus s/h for $d/h = 1.62$ and $\alpha = 10$ deg

flow regularize the lift force. However, only the asymmetry of the body, with or without FST, removes the randomness from the shedding of the first vortex and fixes the initial direction of the lift force.

Figures 2 and 4 show C_d as a function of s/h for $\alpha = 1$ deg, for prisms with $d/h = 0.62$, 1, and 1.62, respectively. All bodies exhibit an initial rise in C_d (between 1.8 and 2) near $s/h \approx 8$. Then C_d goes through a minimum (between 1.3 and 1.5) near $s/h \approx 27$. Subsequently, C_d rapidly approaches mean values dependent on the shape and the angle of attack of the body ($\bar{C}_d = 2.95$ for $d/h = 0.62$, $\bar{C}_d = 2.2$ for $d/h = 1$, and $\bar{C}_d = 1.70$ for $d/h = 1.62$, all for $\alpha = 1$ deg). These values are in good agreement with those obtained in steady flow (Nakaguchi et al., 1968; Bearman and Trueman, 1972; Courchesne and Laneville, 1982). Figures 2–4 also show that the ratio of C_d at $s/h = 8$ to the corresponding $\bar{C}_d$ at large s/h increases with increasing d/h [C_d $(s/h = 8)/\bar{C}_d \approx 0.63$ for $d/h \approx 0.62$, 0.90 for $d/h = 1$, and 1.06 for $d/h = 1.62$]. Thus, the larger the $\bar{C}_d$ the smaller is the relative magnitude of the initial rise in C_d. For a circular cylinder of diameter D, the initial rise in C_d occurs at $s/D \approx 2$ and the ratio C_d $(s/D = 2)/\bar{C}_d$ is about 1.35 at Re $\approx$ 20,000 (Sarpkaya and Shoaff, 1979).

The initial rise in C_d is a consequence of the growth and motion of the first few vortices following the initiation of the flow. At the start of the motion, the vortices grow rapidly and at a rate of growth such that the vorticity accumulates to an amount far in excess of that found in the later stages of the motion. This excess vorticity reduces the base pressure and gives rise to the said initial rise in C_d.

The amplitude of the lift coefficient for bodies with $d/h = 0.62$ and 1.62 for $\alpha = 1$ deg was quite small relative to that for the body with $d/h = 1$ (about 0.10 for $d/h = 0.62$ and 0.3 for $d/h = 1.62$). The evolution of the fluctuating lift for $d/h = 1$ is shown in Fig. 5 as a function of s/h. Following the shedding of the first five or six vortices, C_L acquires a nearly constant amplitude of about 1.2. This is smaller than the rms value of $C_L = 1.32$ reported by Vickery (1966) for reasons yet unclear.

The Strouhal number, determined from the later stages of the oscillations, is St = 0.126 for $d/h = 0.62$, St = 0.125 for $d/h = 1$, and St = 0.11 for $d/h = 1.62$. These values are nearly identical with those obtained in steady flow (Nakaguchi et al., 1968, Bearman and Trueman, 1972). The frequency of the drag fluctuations at large values of s/h is about twice the vortex shedding frequency, indicating that the flow separates at both the leeside and the windward side of the body.

The case of $\alpha = 10$ deg was chosen among the many test runs for the discussion of the effect of angle of incidence on C_d and C_L in impulsively started smooth flow. Figures 6 through 8 show C_d as a function of s/h for $\alpha = 10$ deg. The initial drag rise associated with the growth and motion of the first few vortices is more pronounced[4] than those shown in Figs. 2–4. In the later stages of motion, $\bar{C}_d$ is 2.25 for $d/h = 0.62$, 1.7 for $d/h = 1$, and 1.25 for $d/h = 1.62$. $\bar{C}_d$ for $d/h = 1$ agrees quite well with that obtained by Otsuki et al. (1974) and Lee (1975). There is no comparable data for $\bar{C}_d$ for $d/h = 0.62$ and 1.62 at an incidence of 10 degrees.

Figures 9 through 11 show C_L as a function of s/h for $\alpha = 10$ deg. For $d/h = 0.62$ and 1, the lift starts out as positive (see Fig. 1), showing that the first vortex is shed from the left side of the body, as seen from looking upstream. For $d/h = 1.62$, the lift force starts out as negative, indicating that the first

[4] In fact, the ratio of the initial rise in C_d to $\bar{C}_d$ is 1.18 for $d/h = 0.62$, 1.75 for $d/h = 1$, and 2.0 for $d/h = 1.62$, all for $\alpha = 10$ deg. Thus, the aerodynamic loads on prisms in the early stages of an impulsively started flow may be significantly larger than those in steady flow, depending on d/h and α.

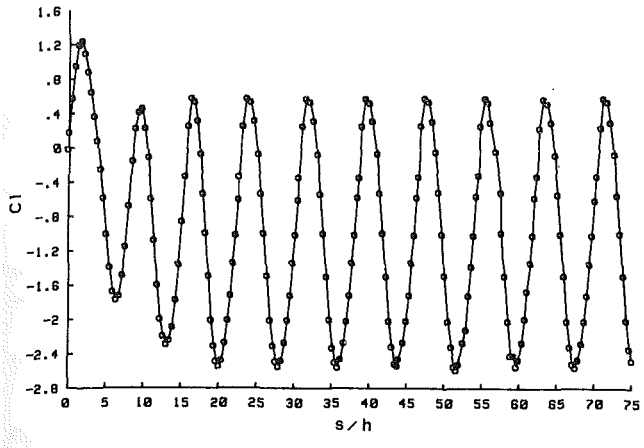

Fig. 9 Lift coefficient versus s/h for $d/h = 0.62$ and $\alpha = 10$ deg

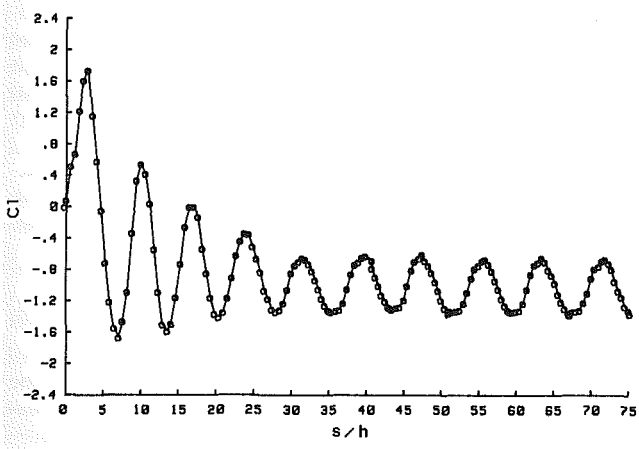

Fig. 10 Lift coefficient versus s/h for $d/h = 1$ and $\alpha = 10$ deg

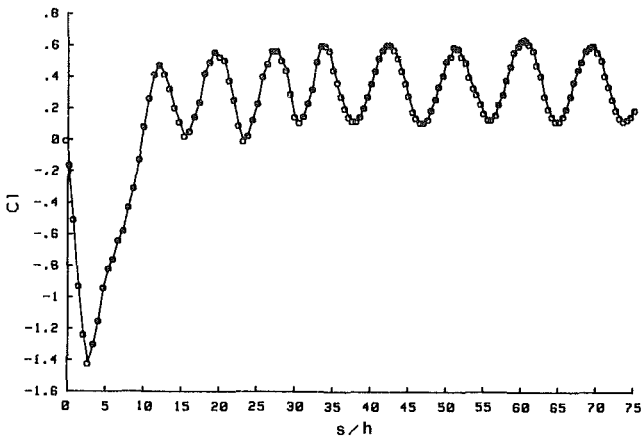

Fig. 11 Lift coefficient versus s/h for $d/h = 1.62$ and $\alpha = 10$ deg

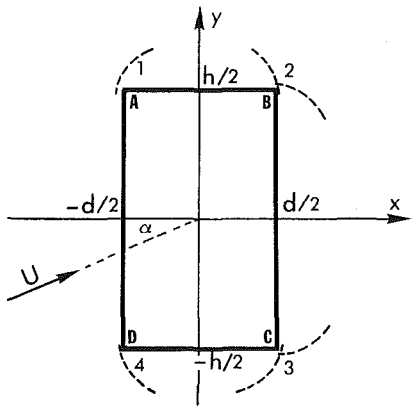

Fig. 12 Definition sketch for the numerical model

vortex is shed from the right side of the body. Clearly, the asymmetry of the body relative to the direction of the ambient flow removes the randomness from the shedding of the first vortex and fixes the initial direction of the lift force.

The Strouhal numbers calculated through the use of Figs. 9–11 yielded St = 0.127 for $d/h = 0.62$, St = 0.123 for $d/h = 1$ and St = 0.112 for $d/h = 1.62$. The same figures yielded a mean lift coefficient C_L (defined only in the later stages of motion) of -1.05 for $d/h = 0.62$, -0.8 for $d/h = 1$, and 0.4 for $d/h = 1.62$, all at $\alpha = 10$ deg. The negative lift slope is responsible for the galloping oscillations of certain prismatic shapes because the aerodynamic force reinforces the lateral motion (Parkinson and Santosham, 1967). Figures 6 through 11 also show C_d and C_L oscillate at about the *same frequency* since only the leeside flow is separated. This finding is in conformity with the numerical predictions of Davis and Moore (1982).

Flow visualization with polystyrene beads with bodies with $d/h = 0.62$ and 1 at $\alpha = 10$ deg has shown that the flow develops a separation bubble (separation, reattachment, and re-separation) on the left side of the body following the shedding of the first vortex from the left side of the body, as seen from looking upstream (see Fig. 1). The separation bubble results in a large negative pressure and gives rise to a negative C_L ind the later stages of the motion. For the prism with $d/h = 1.62$ at $\alpha = 10$ deg, the flow separates at both faces but the separation bubble at the left is larger at the start of the motion. This results in an initial negative side force. At $s/h \approx 10$, the separation bubble at the right grows larger and C_L becomes positive. When the angle of incidence is increased to 20 degrees, however, the separation bubble at the left remains and increases in size, but there is no separation bubble at the right, i.e., the flow does not reattach. This results in a mostly negative lift with $C_L = -0.5$.

Discrete Vortex Analysis

Certain separated time-dependent flows may be simulated through the use of the discrete vortex model (DVM) (see e.g., Sarpkaya, 1975; Sarpkaya and Shoaff, 1979). The free shear layers which emanate from the sides of the body are represented by an assembly of discrete vortices. It has not yet been proven that a continuous vortex sheet may be so discretized. Thus, attention is given here to large scale vortex structures rather than to small-scale instabilities resulting from the vortex interactions. Furthermore, only the most important features of the method, as it is applied to rectangular prisms, are described.

The body shape under consideration may be represented either through the use of a suitable conformal transformation (from rectangle to circle) or through the use of discrete surface singularities (Maskew, 1975). The distinguishing feature between the two methods is that the former is rather laborious (Nagano et al., 1978) even though the body shape is represented exactly whereas the latter is much simpler but the boundary condition (zero normal velocity) is satisfied only at a specified number of control points. The present analysis uses the surface singularity method (vortex-lattice method, as it is sometimes called) in spite of its shortcomings (Maskew, 1975).

Let there be N point vortices on the body contour and four separated shear layers, each represented by K_j (j = 1 through 4) point vortices (see Fig. 12). The vortex system must satisfy the zero normal velocity condition and Kelvin's theorem that the sum of all vortices must be zero at all times.

The complex potential may be written as,

$$F(z) = -Uze^{-i\alpha} + \sum_{1}^{N} (i\Gamma_{bn}/2\pi) Ln(z - z_{bn})$$

$$- \sum_{1}^{K_1} (i\Gamma_{1k}/2\pi) Ln(z - z_{1k})$$

$$+ (-1)\kappa b \sum_{1}^{K_2} (i\Gamma_{2k}/2\pi) Ln(z - z_{2k})$$

$$+ (-1)\kappa c \sum_{1}^{K_3} (i\Gamma_{3k}/2\pi) Ln(z - z_{3k})$$

$$+ \sum_{1}^{K_4} (i\Gamma_{4k}/2\pi) Ln(z - z_{4k}) \quad (1)$$

in which Γ_{bn} and z_{bn} represent the unknown strengths and the specified positions of the boundary vortices and Γ_{jk} and z_{jk}, the strengths and positions of the vortices on the jth shear layer. $\kappa b = 1$ if separation at B (see Fig. 12) is along AB and $\kappa b = 2$ if separation is along CB. Likewise, $\kappa c = 1$ if separation at C is along BC and $\kappa c = 2$ if separation is along DC, as determined from the direction of the velocities calculated along the extensions of BC and DC.

The total circulation may be written as,

$$\sum_{1}^{N} \Gamma_{bn} - \sum_{1}^{K_1} \Gamma_{1k} + (-1)\kappa b \sum_{1}^{K_2} \Gamma_{2k} + (-1)\kappa c \sum_{1}^{K_3} \Gamma_{3k} + \sum_{1}^{K_4} \Gamma_{4k} = 0 \quad (2)$$

where the counterclockwise rotation is assumed to be plus.

The condition of zero normal velocity on the boundary may be satisfied in a number of ways. The use of n control points (one control point midway between the vortices) leads to $(n+1)$ equations [including equation (2)] and n unknowns (Γ_{bn}). The ambiguity may be resolved, for example, by ignoring one of the control points. However, the fact remains that the zero normal velocity condition is satisfied only at the control points, i.e., the body is represented only approximately and the normal velocity at points other than the control points is not zero (i.e., there are holes on the body surface). The method used here is to minimize the error in normal velocity at as many control points as possible rather than making V_n exactly zero at a fewer number of points. For this purpose N_c control points (e.g., $N_c = 2n$, i.e., 2 control points between neighboring singularities) are chosen. On faces parallel to the x-axis $V_n = v = 0$ at each control point leads to

$$\mathrm{Im}(dF/dz) = 0 \quad (3)$$

On faces parallel to the y-axis, $V_n = u = 0$ leads to

$$\mathrm{Re}(dF/dz) = 0 \quad (4)$$

Solving for Γ_{bN} (the strength of the Nth boundary vortex) from equation (2), one has

$$\Gamma_{bN} = \sum_{1}^{K_1} \Gamma_{1k} - (-1)\kappa b \sum_{1}^{K_2} \Gamma_{2k} - (-1)\kappa c \sum_{1}^{K_3} \Gamma_{3k} - \sum_{1}^{K_4} \Gamma_{4k} - \sum_{1}^{N-1} \Gamma_{bn} \quad (5)$$

Inserting equation (5) into the normal velocity conditions given by equations (3) and (4), one has

$$R_j = \sum A_{jn}\Gamma_{bn} + B_j = V_n \quad (6)$$

where A_{jn} and B_j are known in terms of the position of Γ_{bn}, the position of the control points and the strength and position of the vortices on the free shear layers.

If V_n were exactly zero at each control point then $R_j = 0$. Assuming $R_j \neq 0$, the sum of the square of the errors at all control points is given by

$$E^2 = \sum R_j^2 \quad (7)$$

where R_j is a function of $(N-1)$ unknowns (Γ_{bn}, with $n = 1$ to $N-1$) only. The total error may be minimized through the use of the method of least squares by writing

$$\partial E^2/\partial \Gamma_{bn} = 0 \quad (8)$$

Performing the said analysis, one has

$$A^T A \Gamma_{bn} = A^T B \quad (9)$$

which represents a matrix of $(N-1) \times (N-1)$ linear equations for the $(N-1)$ unknowns. Once Γ_{b1} through $\Gamma_{b(N-1)}$ are determined, Γ_{bN} is obtained from equation (5). The Kelvin condition of zero total circulation is satisfied exactly. However, the normal velocity condition is satisfied only approximately at N_c control points. The zero-error points for the tangential velocity component are less well-known and difficult to determine since it requires the use of a conformal mapping.

The forces exerted on a stationary body by a time-dependent flow represented by the complex potential $F(z)$ can be calculated from the generalized Blasius theorem (Milne-Thomson, 1960) given by

$$\overline{X + iY} = \frac{1}{2} i\rho \oint (dF/dz)^2 dz + i\rho \frac{\partial}{\partial t} \oint F dz \quad (10)$$

in which X and Y represent the components of the force in the x and y directions (see Fig. 12). Inserting equation (1) in equation (10) and carrying out the indicated integrations, one finally has

$$X + iY = i\rho U e^{-i\alpha} \sum_{1}^{N} \Gamma_{bn} - \sum_{1}^{N} \sum_{1}^{K_1} \rho \frac{\Gamma_{bn}}{2\pi} \frac{\Gamma_{1k}}{z_{bn} - z_{1k}}$$

$$+ \sum_{1}^{N} \sum_{1}^{K_2} \rho \frac{\Gamma_{bn}}{2\pi} \frac{(-1)^{\kappa b}\Gamma_{2k}}{z_{bn} - z_{2k}}$$

$$+ \sum_{1}^{N} \sum_{1}^{K_3} \rho \frac{\Gamma_{bn}}{2\pi} \frac{(-1)^{\kappa c}\Gamma_{3k}}{z_{bn} - z_{3k}}$$

$$+ \sum_{1}^{N} \sum_{1}^{K_4} \rho \frac{\Gamma_{bn}}{2\pi} \frac{\Gamma_{4k}}{z_{bn} - z_{4k}}$$

$$- \sum_{1}^{N} i\rho \bar{z}_{bn} \frac{\partial \Gamma_{bn}}{\partial t} \quad (11)$$

Note that $\partial \Gamma_{jk}/\partial t = 0$.

The drag and lift coefficients are given by

$$\mathrm{Drag}/(0.5\rho h U^2) = 2(X\cos\alpha + Y\sin\alpha)/(\rho h U^2) \quad (12)$$

and

$$\mathrm{Lift}/(0.5\rho h U^2) = 2(-X\sin\alpha + Y\cos\alpha)/(\rho h U^2) \quad (13)$$

Specific Details of the Creation and Convection of the Vortices. The solution procedure employed was as follows:

(1) Calculate the velocity at any point $r < r^*$ using the exact solution of the Navier-Stokes equations for a single rectilinear viscous vortex (Lamb, 1954) i.e., $-u + iv = (\Gamma/2\pi r)$ [1 − Exp $(-r^2/4\pi\nu t)]e^{-i\theta}$ and at any point $r > r^*$ using the point vortex relation $(-u + iv = dF/dz)$. The radius r is measured

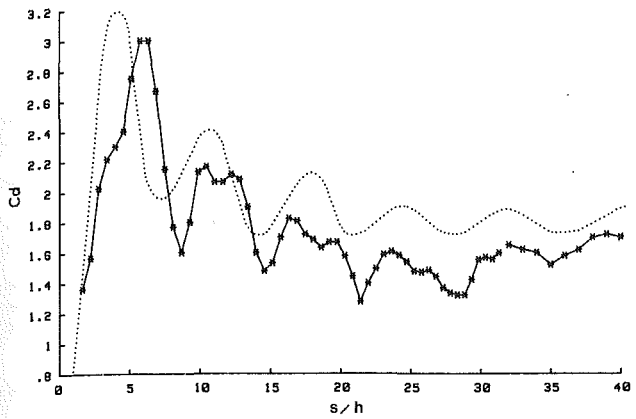

Fig. 13 Drag coefficient versus s/h for d/h = 1 and α = 10 deg, ****** data points, ... numerical analysis

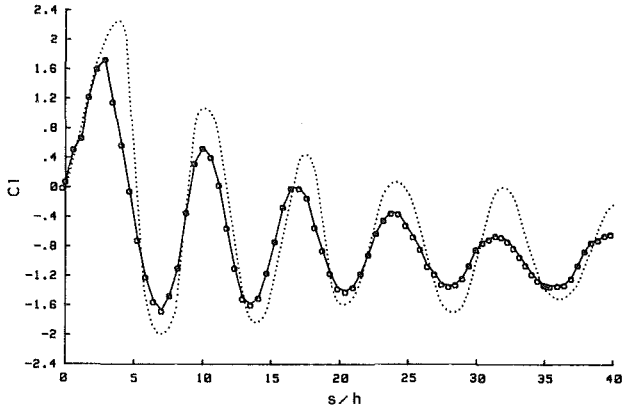

Fig. 14 Lift coefficient versus s/h for d/h = 1 and α = 10 deg, o o o o o o data points, ... numerical analysis

from the center of the vortex and θ is taken as plus in the CCW direction from the x-axis. The core radius r^* at which the tangential velocity is maximum is given by $r^* = 2.24(\nu t)^{1/2} = 2.24h\ (Ut/h)^{1/2}\ \mathrm{Re}^{-1/2}$ where t is the age of the vortex since its inception and $\mathrm{Re} = Uh/\nu$.

(2) Convect all free vortices (including the nascent vortices) twice for a time interval $\Delta t/2 = \delta t = 0.08h/U$ using the second order convection scheme given by

$$z_k(t+\delta t) = z_k(t) + 0.5[3(u_k + iv_k)_t - (u_k + iv_k)_{t-\delta t}]\delta t$$

Note that the nascent vortices are created every $\Delta t = 2\ \delta t$.

(3) Remove those vortices from the field whose cores touch the boundary.

(4) Combine two oppositely signed vortices when their cores touch.

(5) Calculate the lift and drag coefficients.

(6) Calculate the new values of the boundary vortices (placed at $\Delta s = h/20$ intervals along the boundary) using $N_c = 2n$ and the least squares procedure described previously.

(7) Calculate the tangential velocity V_{sj} at the two control points nearest the jth corner of the face along which the flow separates and denote the average V_{sj} as the outer flow velocity at the edge of the boundary layer.

(8) Find the strength of the jth nascent vortex from $\Gamma_{nj} = 0.5\ V_{sj}^2\ \Delta t$ (Sarpkaya, 1975).

(9) Introduce new nascent vortices at distances m_j away from the four corners: At $(-0.5\ d - m_1,\ h/2)$ for the corner A, at $(-0.5\ d - m_4,\ -h/2)$ for the corner D, at $[0.5\ d + m_2^{(\kappa b - 1)},\ 0.5\ h + m_2^{(2-\kappa b)}]$ for the corner B, and at $[0.5\ d + m_3^{(2-\kappa c)},\ -0.5\ h - m_3^{(\kappa c - 1)}]$ for the corner C. The Kutta condition is satisfied if $m_j = (2\pi)^{-1} V_{sj}\ \Delta t$ where $j = 1$ through 4 represents the corners A, B, C, and D, respectively.

(10) Repeat the above steps.

The numerical model has been supplied to the bodies with $d/h = 0.62$, 1, and 1.62 at various angles of incidence. Here only a representative case is discussed because of space limitations.

Figures 13 and 14 show the measured and calculated drag and lift coefficients as a function of s/h for $d/h = 1$, $\alpha = 10$ deg, and $\mathrm{Re} = 20{,}000$. The experimental data are replots (up to $s/h = 40$) of those already presented in Figs. 7 and 10. The Reynolds number enters into the numerical model only through the diffusion of the vortices. It does not account for the three-dimensional nature of the vorticity distribution, resulting from turbulence.

Comparisons of the predicted and measured normalized forces show reasonably good agreement with respect to the frequency of the oscillations, i.e., the Strouhal number is correctly predicted. However, the amplitudes of the predicted forces are somewhat larger.

The results obtained with other bodies at various angles of incidence yielded essentially the same conclusions. For the body with $d/h = 0.62$, it was not possible to ascertain as to whether $\bar{C}_d$ eventually reached a value close to 3 since the calculations were carried out up to $s/h = 40$ due to the limitations imposed on the computer time.

The results have shown that the strength of the vortex clusters varies from 80 to 90 percent of the vorticity generated in the shear layers, the 10 to 15 percent loss in vorticity arising from the removal of vorticity at the rear face of the body and a small amount of cancellation between elementary vortices of opposite sign which enter the same rolled-up vortex cluster. The corresponding experimental values for flat plates, cylinders and many other types of bluff bodies vary from 50 to 66 percent (Sarkpaya, 1975; Sarpkaya and Shoaff, 1979). Thus, the vortex clusters of the present model are about 50 percent stronger than those found in real flows under similar circumstances. The discrepancy between the magnitudes of the measured and calculated normalized forces is primarily due to the difference in the mechanisms whereby vorticity is lost. An additional loss in vorticity could have been introduced into the model in a manner similar to that used by Sarpkaya and Shoaff (1979) in order to bring the strengths of the shed vortex clusters, and thereby the magnitudes of C_d and C_L, into closer agreement with those obtained experimentally. However, it was decided to avoid a relatively subjective dissipation mechanism. It appears that the Strouhal number does not strongly depend on the strength of the shed vortex clusters. This is in conformity with the previous applications of the discrete vortex model (Sarpkaya and Shoaff, 1979).

Concluding Remarks

It has been shown that the impulsively started steady flow about a prism causes a rapid initial rise in C_d, often followed by a minimum, at s/h values dependent on d/h and α. Subsequently, both C_d and C_L approach their steady-state values at large s/h values. This is true whether the vortices develop symmetrically at first, as in the case of bodies at very small angles of incidence, or asymmetrically, as in the case of bodies at an angle of incidence larger than about 5 degrees. The asymmetric separation of flow, at different points and times, and the subsequent shedding of the first few vortex clusters result in relatively more complex oscillations in C_d and C_L (see Figs. 6–7). The development of separation bubbles and the subsequent reseparation of the flow at the two downstream corners reduce the wake size and the amplitude of the force oscillations due to the alternate shedding of the vortices (see Figs. 8 and 11). At angles of incidence larger than about 5 degrees, C_d and C_L oscillate with nearly identical frequencies since only the leeside flow is separated.

There are at present no reliable analytical techniques which accurately predict the behavior of the impulsively started flow about bluff bodies at relatively high Reynolds numbers. Most of the numerical models, however valuable, are restricted to small Reynolds numbers and relative displacements. The present model, unique in some ways (body representation, treatment of the number and position of the separation points, lift and drag calculations, etc.) and akin to previous ones in other ways (convection and diffusion of vortices), predicts the frequency of the lift and drag oscillations with reasonable accuracy. However, it is not free from deficiencies and requires some retrofitting to experimental results through the use of a suitable and somewhat subjective dissipation mechanism. The data presented herein should provide guidance and means of comparison for future analytical efforts.

Acknowledgments

This work is part of a basic/applied research on time-dependent flow about bluff bodies. The writers wish to acknowledge the generous support of the U. S. National Science Foundation. Special thanks are due Mr. Jack McKay for his skillful and industrious efforts which were essential to the experimental process described herein.

References

Bearman, P. W., and Morel, T., 1983, "Effect of Free Stream Turbulence on the Flow Around Bluff Bodies," *Progress in Aerospace Science*, Vol. 22, pp. 97–123.

Bearman, P. W., and Trueman, D. M., 1972, "An Investigation of the Flow Around Rectangular Cylinders," *Aeronautical Quarterly*, Vol. 23, pp. 229–237.

Bostock, B. R., and Mair, W. A., 1972, "Pressure Distributions and Forces on Rectangular and D-shaped Cylinders," *Aeronautical Quarterly*, Vol. 23, pp. 1–6.

Bouard, R., and Coutanceau, M., 1980, "The Early Stage of Development of the Wake Behind an Impulsively Started Cylinder for $40 < Re < 10{,}000$," *Journal of Fluid Mechanics*, Vol. 101, pp. 583–607.

Courchesne, J., and Laneville, A., 1982, "An Experimental Evaluation of Drag Coefficient for Rectangular Cylinders Exposed to Grid Turbulence," ASME Journal of Fluids Engineering, Vol. 104, pp. 523–528.

Davis, R. W., and Moore, E. F., 1982, "A Numerical Study of Vortex Shedding from Rectangles," *Journal of Fluid Mechanics*, Vol. 116, pp. 475–506.

Davis, R. W., Moore, E. F., and Purtell, L. P., 1984, "A Numerical Experimental Study of Confined Flow Around Rectangular Cylinders," *Physics of Fluids*, Vol. 27, pp. 46–59.

Fromm, J. E., and Harlow, F. H., 1963, "Numerical Solution of the Problem of Vortex Street Development," *Physics of Fluids*, Vol. 6, pp. 975–982.

Gartshore, I. S., 1984, "Some Effects of Upstream Turbulence on the Unsteady Forces Imposed on Prismatic Two-Dimensional Bodies," ASME Journal of Fluids Engineering, Vol. 106, pp. 418–424.

Graham, J. M. R., 1969, "The Effect of End-Plates on the Two-Dimensionality of a Vortex Wake," *Aeronautical Quarterly*, Vol. 20, pp. 237–247.

Ihrig, C. J., 1983, "Impulsively-Started Flow About Rectangular Cylinders," M.S. thesis, Naval Postgraduate School, Monterey, CA.

Inamuro, T., Adachi, T., and Sakata, H., 1983, "A Numerical Analysis of Unsteady Separated Flow by a Vortex Shedding Model," *Bulletin of the JSME*, Vol. 26, pp. 222–228.

Kline, H. K., 1981, "Impulsively-Started Flow About Submarine-Shaped Bodies," M.S. thesis, Naval Postgraduate School, Monterey, CA.

Knauss, D. T., 1974, "The Influence of Flow Orientation on the Vortex Frequencies of Bluff Cylinders at Low Reynolds Numbers," Ph.D. thesis, University of Maryland.

Krause, E., Ehrhardt, G., and Schweitzer, B., 1985, "Experiments on Unsteady Flows about Wing Sections," *Proc. of the Conference on Low Reynolds Number Airfoil Aerodynamics*, (Ed. T. J. Mueller), Univ. of Notre Dame, pp. 255–267.

Lamb, H., 1954, *Hydrodynamics*, (6th ed.), Dover Publications, N.Y.

Lee, B. E., 1975, "The Effect of Turbulence on the Surface Pressure Field of a Square Prism," *Journal of Fluid Mechanics*, Vol. 69, pp. 263–282.

Maskew, B., 1975, "A Subvortex Technique for the Close Approach to a Discretized Vortex Sheet," NASA Technical Memorandum, TM-X-62487.

Milne-Thomson, L. M., 1960, *Theoretical Hydrodynamics*, (4th ed.), The MacMillan Co., N.Y.

Nagano, S., Naito, M., and Takata, H., 1981, "A Numerical Analysis of Two-Dimensional Flow Past a Rectangular Prism by a Discrete Vortex Model," (in Japanese), *Trans. JSME*, Vol. 47, No. 413, pp. 32–47.

Nakaguchi, H., Hashimoto, K., and Muto, S., 1968, "An Experimental Study on Aerodynamic Drag of Rectangular Cylinders," *Journal of Japanese Society of Aeronautics and Space Sciences*, Vol. 16, pp. 1–5.

Obasaju, E. D., 1979, "On the Effect of End Plates on the Mean Forces on Square Sectional Cylinders," *Journal of Industrial Aerodynamics*, Vol. 5, pp. 179–188.

Obasaju, E. D., 1983, "An Investigation of the Effects of Incidence on the Flow Around a Square Section Cylinder," *Aeronautical Quarterly*, Vol. 34, pp. 243–259.

Otsuki, Y., Washizu, K., Tomizawa, H., and Ohya, A., 1974, "A Note on the Aeroelastic Instability of a Prismatic Bar with Square Section," *Journal of Sound and Vibration*, Vol. 34, pp. 233–245.

Parkinson, G. V., and Santosham, T. V., 1967, "Cylinders of Rectangular Section as Aeroelastic Nonlinear Oscillators," ASME Paper No. 67 Vib-50.

Rockwell, D. O., 1977, "Organized Fluctuations due to Flow Past a Square Cross Section Cylinder," ASME Journal of Fluids Engineering, Vol. 99, pp. 511–516.

Sarpkaya, T., 1975, "An Inviscid Model of Two-Dimensional Vortex Shedding for Transient and Asymptotically Steady Separated Flow Over an Included Flat Plate," *Journal of Fluid Mechanics*, Vol. 68, pp. 109–128.

Sarpkaya, T., 1978, "Impulsive Flow About a Circular Cylinder," Technical Report No. NPS-69SL78-008, Naval Postgraduate School, Monterey, CA.

Sarpkaya, T., and Kline, H. K., 1982, "Impulsively-Started Flow About Four Types of Bluff Body," ASME Journal of Fluids Engineering, Vol. 104, pp. 207–213.

Sarpkaya, T., and Shoaff, R. L., 1979, "Inviscid Model of Two-Dimensional Vortex Shedding by a Circular Cylinder," *AIAA Journal*, Vol. 17, No. 11, pp. 1193–1200.

Vickery, B. J., 1966, "Fluctuating Lift and Drag on a Long Cylinder of Square Cross-Section in a Smooth and in a Turbulent Stream," *Journal of Fluid Mechanics*, Vol. 25, pp. 481–494.

Measurements of Turbulence Generated by 60 Percent Solid Perforated Plates

M. D. Checkel
Department of Mechanical Engineering,
The University of Alberta,
Edmonton, Canada T6G 2G8

Combustion experiments simulating spark-ignition engine conditions require generation and measurement of high intensity, rapidly decaying turbulence in a combustion test cell. Turbulence is generated by drawing various perforated plates across the test cell and is measured by hot-wire anemometry in the test cell and behind the same perforated plates in a steadily flowing wind tunnel. To correlate test cell and wind tunnel turbulence measurements, a simple statistical model of hot-wire anemometer response in turbulence with negligible mean flow is used. Good agreement between the two measurements tends to confirm the model for this case and demonstrates the value of perforated plate turbulence generators in producing controllable, measurable turbulence for confined combustion research.

Introduction

The global requirement for more fuel-efficient and cleaner burning, yet inexpensive internal combustion engines has created an interest in lean burning engines due to their inherent efficiency and pollution advantages [1]. However, the slower burning of lean mixtures causes or amplifies several engine operating problems and has so far limited the penetration of very lean burning engines into a market dominated by engines burning near stoichiometric mixtures and using extensive pollution controls. To overcome the problems associated with low burning velocity, several researchers have demonstrated [2-5] that introduction of additional turbulence in the combustion chamber increases burning rate and decreases cycle-to-cycle burning rate variability. However, turbulence in engine cylinders is generated and decays over a very brief interval, is difficult to systematically control or measure, and influences all of the induction, mixture formation, and combustion processes. Also, the combustion takes place over a long period relative to the lifetime of the turbulence and it may or may not enhance the turbulence due to rapid compression, giving a combustion/turbulence interaction with two possible directions. As a result, it is difficult to obtain a thorough understanding of how individual engine processes interact with turbulence and to formulate strategies for optimizing turbulence generation in engines.

Combustion experiments in closed bombs have been undertaken to provide background information in aid of understanding engine combustion [e.g., 6-9]. Such experiments considerably reduce the number of variables to be controlled and provide for improved measurement and control of the turbulence so they can provide better fundamental information on mixture motion/flame growth interaction. The ideal bomb turbulence generating system would create turbulence of variable intensity and scale so that conditions similar to engines could be tested, would produce turbulence which decays in a similar manner to that in an engine, and would allow for easy and detailed measurement of the turbulence intensity, scale and structure. Various mechanisms for generating mixture motion in combustion bombs have been used, ranging from the laminar jet of Cole and Mirsky [6] to the high speed fans of Andrews et al. [7]. Studies by Ohigashi et al. [8] and by Checkel and Thomas [9] have used rapid motion of a perforated plate across the combustion chamber to generate turbulence and have demonstrated control of turbulence intensity and scale in the combustion chamber. Perforated plates have several advantages as turbulence generators for combustion experiments, chiefly:

1. Control of turbulence intensity, scale, and homogeneity is possible using variable plate speeds, plate hole sizes, and mixing/decay periods after plate motion.
2. Detailed measurements of turbulence production and decay can be performed downstream of the same plate in a wind tunnel air stream in a situation reasonably analogous to that in the bomb.
3. The turbulence is produced by jet mixing and decay processes which is similar to turbulence production in engines.

This paper explains how the turbulence measurements for reference [9] were made and the matching process between wind tunnel and bomb turbulence measurements.

The key to effectively using any turbulence generating system is to accurately assess the turbulence generated. However, the very transient nature of the turbulence produced and the lack of any directional mean velocity, while ideal for simulating engine chamber conditions, make turbulence analysis in the test cell difficult. Laser velocimetry systems with their capabilities of superimposing a high pseudo-velocity on the turbulence can eliminate the problem of no mean velocity but this advantage is offset by the complexity of the

Contributed by the Fluids Engineering Division of THE AMERICAN SOCIETY OF MECHANICAL ENGINEERS and presented at the Winter Annual Meeting, Miami Beach, Fla., November 17-21, 1985. Manuscript received by the Fluids Engineering Division, March 26, 1984. Paper No. 85-WA/FE-2.

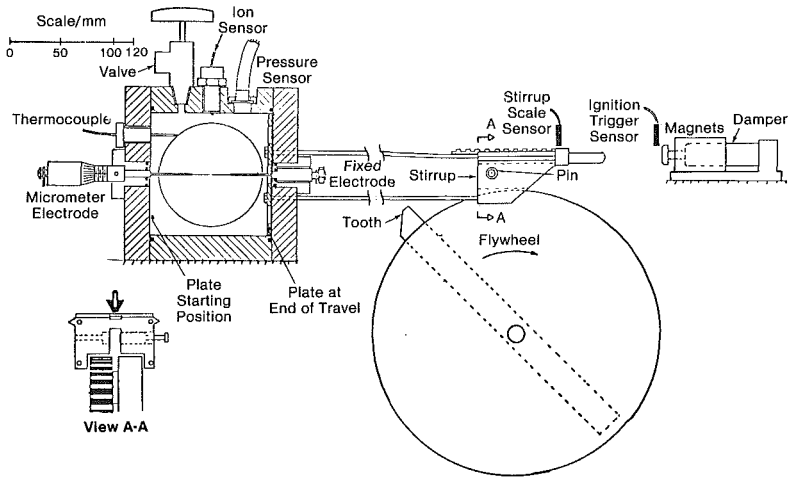

Fig. 1 Turbulent combustion bomb and plate moving mechanism

signal processing systems involved and the difficulties of using such systems for transient velocity measurements. For these reasons, a hot wire anemometer has been used both for characterization of turbulence produced by the perforated plates in the wind tunnel and for comparative measurements to confirm the similarity of turbulence production and decay in the combustion bomb.

To a first approximation, the hot-wire anemometer responds to the modulus of velocity in a plane perpendicular to its wire, so one is unable to resolve directional turbulence quantities unless there is a known directional mean velocity many times greater than the root-mean-square (rms) intensity. Indeed, as Bradbury [7] has shown, in a situation with significant turbulence intensity and negligible mean flow, conventional analysis of the hot-wire signal will indicate a false "mean velocity" and an erroneously low turbulence intensity.

This paper uses a simple model of hot-wire anemometer response and a Gaussian statistical model of nonisotropic turbulence to predict the relationship between anemometer output and root mean square velocity fluctuations of the nonflowing turbulence produced by perforated plate movement in the test cell. Using this model, the turbulence intensity-time history of the mixture motion in the combustion test cell is measured. Confirmation of the model and more detailed information on the turbulence structure is obtained by comparison with conventional analysis of hot-wire anemometer data obtained downstream of the same perforated plates in a steady-flow wind tunnel. The success of this turbulence analysis procedure demonstrates the use of the hot-wire anemometer in non-flowing turbulence and suggests perforated plate turbulence generators as a preferable alternative for producing turbulence of controlled scale and intensity for various closed cell experiments.

Experimental Arrangement

The turbulent combustion test cell referred to in this paper is shown schematically in Fig. 1. The cell is a 120 mm inside dimension cube with two electrodes formng a spark gap at the center of the chamber and opposing windows for flame observations. A movable perforated plate is installed in the chamber so that the central hole in the plate passes over the spark electrodes as it crosses the chamber. Geometrically similar plates with hole diameters of 2.5, 5, 10, and 20 mm arranged as shown in Fig. 2 were used in this study. (The 2.5 mm plate had one central 5 mm diameter hole to accommodate the spark electrodes and hot-wire anemometer located at the center of the bomb.)

The perforated plates are pulled across the chamber by rods running through O-ring seals to a mechanism outside the bomb. This mechanism contains a steadily rotating flywheel with a protruding tooth. On each revolution the tooth passes through a slot in a stirrup attached by four rods to the perforated plate inside the bomb. To initiate plate motion, a pin is fired across this slot, engaging the tooth and pulling the perforated plate across the chamber. As the flywheel tooth rotates clear of the pin, the stirrup mechanism carries on until it is arrested by a hydraulic shock absorber and two electromagnets which clamp the plate against the end of the chamber. Plate position and speed are monitored by optical sensors and proved repeatable within 4 percent. Plate speeds used in this study were V = 1, 5, 10, and 15 m/s.

For turbulence measurements in the test cell a hot-wire probe replaced one spark electrode, locating the sensor wire horizontal and perpendicular to the plate travel direction at the center of the chamber (Fig. 2). The single wire sensor used a 3 mm long, 5 μm diameter wire which gives an aspect ratio of 600. (This aspect ratio is important for the signal analysis since Champagne, Sleicher and Wehrmann [11] have reported that wires with aspect ratios of 600 or higher respond essentially to the component of velocity perpendicular to the wire with negligible effect of the parallel component.) The unlinearized output of the Disa 55M01 constant temperature bridge was recorded on a Racal Store 4 FM tape recorder with a 20 kHz low-pass filter. For analysis, the signal was digitized at 80 kHz

Nomenclature

D = perforated plate hole diameter
$k = \overline{u_y^2}/\overline{u_x^2}$ = degree of isotropy of turbulence
L = turbulence integral scale
n = decay exponent of turbulent fluctuations
$R_L = \sqrt{\overline{u_x^2}}*L/\nu$ = turbulence Reynold's number
U = mean velocity (generally in the x direction)
u_x, u_y, u_z = cartesian components of instantaneous fluctuating velocity
u_{xy} = instantaneous velocity in the $x-y$ plane
V = perforated plate speed in test cell
V = uniform approach velocity in wind tunnel
x = position downstream of perforated plate
$\sigma_x, \sigma_y = \sqrt{\overline{u_x^2}}\ \sqrt{\overline{u_y^2}}$ = rms of component fluctuating velocities
ν = kinematic viscosity

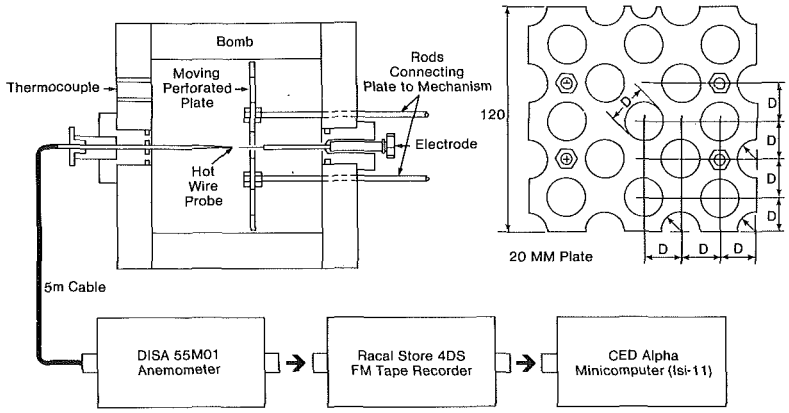

Fig. 2 Hot wire anemometry in the turbulent combustion bomb

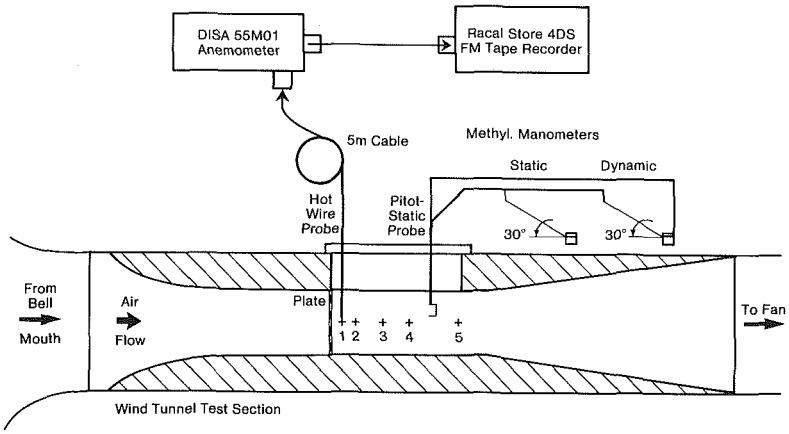

Fig. 3 Hot wire anemometry schematic for the wind tunnel

with a 12 bit analog/digital converter and calibration and signal processing were done on a small computer.

The turbulence generated by the same perforated plates in a 120 mm square wind tunnel test section was recorded and analyzed using the same anemometry system (Fig. 3). For each perforated plate scale and wind tunnel speed, turbulence was analyzed at points x = 25, 50, 100, 150, and 242 mm downstream of the perforated plates to match varying turbulence decay periods after plate passage in the test cell. Wind tunnel bulk velocities, (analogous to test cell plate speeds), in the range V = 1 to 12 m/s were tested.

In this constant area cross section wind tunnel, local bulk velocity gradually rises above approach velocity as boundary layer growth reduces the effective flow area of the test section. Because variable bulk flow and turbulence levels lead to variable boundary layer growth rates, it would have been difficult to compensate with an expanding cross-section tunnel since the tunnel would require adjustments and testing for each flow condition. As the predominant interest was in the high intensity turbulence close to the perforated plates, the effect of increasing bulk velocity on local mean velocity was ignored. The maximum increase in centerline mean velocity at the end of the wind tunnel test section was 8.7 percent.

The hot wire probes used in these studies were calibrated in a smooth flow wind tunnel against a pitot-static tube. For the 2 m/s to 20 m/s range an inclined methyl manometer was used. From 4 m/s down to 0.8 m/s this was supplemented by a micromanometer. The calibration data were fitted with a fourth order least-squares polynomial to use as a calibration function for the computer data processing system. (Recorded voltages were first corrected back to calibration conditions to account for air temperature and density changes, then the polynomial was used to convert this voltage to an air velocity.) This curve fit included the "zero velocity" point as a rough method of including sensitivity to the changing flow regime at very low velocity.

Note: The calibration range of wire Reynolds numbers was 0.24 to 6 and, according to the results of Collis and Williams [12] there is some justification for extrapolating the same heat transfer behavior down to less than 0.1 m/s where free convection starts to become significant. However, as the intent of this study was *not* to measure very low velocities, but rather to measure significant fluctuating velocities with very low mean, it was felt such a procedure would be cumbersome and also misleading. In turbulence with low mean velocity, the hot wire is seldom exposed to a truly near-zero velocity since it responds to all velocities in the plane perpendicular to its axis. When the velocity finally becomes truly near-zero, other effects such as the hot-wire wake recrossing the wire prevent significant measurements in any case. When this begins to occur on a regular basis, the indicated velocity decreases due to reduced heat transfer from the wire as discussed later.

In order to measure the full range of velocities present in the bomb and wind tunnel with one measurement system, some of the refinements available for wind tunnel anemometry were foregone, in particular the possibility of measuring mean voltage separately and amplifying the fluctuating voltage for better resolution of the fluctuating velocity component. This is obviously impractical in the bomb where the mean velocity decays rapidly. The limiting factor in the resolution available was the 48 dB signal to noise ratio of the FM tape recorder which translates into a velocity resolution of approximately 2

percent depending on the exact velocity and hot wire calibration. Background turbulence measurements in the wind tunnel with no perforated plate present indicated rms turbulence levels of 1.5 to 2.5 percent dependent of tunnel velocity. It was felt that this indicated turbulence was primarily random digitization noise rather than actual background turbulence, and thus would be uncorrelated with the measured turbulence with a plate in position. A correction procedure of subtracting the mean square of this "background level" at the same mean velocity from the indicated mean square turbulence level was introduced to eliminate the effects of this noise. While this correction generally changed rms intensity by less than 1 percent for significant turbulence levels, it rose to as much as 15 percent with the weak turbulence downstream of the smallest scale plate. For this reason the turbulence measurements at the last measurement station downstream of the 2.5 mm plate have been disregarded.

Turbulence Analysis

A first-order model for the response of a hot-wire anemometer in a turbulent fluid (with the wire parallel to and insensitive to the z component of velocity and the mean velocity parallel to the x axis) is given by the modulus of velocity in the $x-y$ plane;

$$\text{calibrated signal} = \sqrt{(U_x + u_x)^2 + u_y^2} \tag{1}$$

where calibrated signal means the velocity corresponding to the instantaneous voltage output. Provided that the mean flow, U_x, is greater than about ten times the rms turbulence intensity, only the effect of fluctuations in the x-direction is resolvable so equation (1) simplifies to:

$$\text{calibrated signal} = U_x + u_x \tag{2}$$

The direct evaluation of mean and fluctuating velocity components is thus a simple matter since the anemometer gives a directional velocity signal.

If, however, the mean flow is not much larger than the turbulence intensity, the output of the hot-wire anemometer will be significantly influenced by the velocity fluctuations perpendicular to both the mean flow and the hot-wire axis: u_y in this case. Since the anemometer signal may no longer be treated as a unidirectional velocity signal, analysis to derive mean velocity and turbulence intensity becomes much more difficult. Bradbury [10] has shown that it is possible, by assuming turbulence to be random, uncorrelated velocities with Gaussian distribution in each of the cartesian directions, to arrive at correction factors for hot-wire anemometer measurements in high-intensity turbulence. However, these correction factors become very unstable and dependent on turbulence structure for turbulence intensity greater than about 40 percent, particularly if the intensity perpendicular to the mean flow is greater than that parallel to the mean flow. While turbulence generated by perforated plates and grids is often assumed to be isotropic, previous studies such as those of Comte-Bellot & Corrsin [13] or Uberoi and Wallace [14] show that intensity perpendicular to the mean flow is less than that parallel to the flow and that this non-isotropy persists throughout the turbulence decay. Values for the degree of difference, k, where $\overline{u_y^2} = \overline{u_z^2} = k\,\overline{u_x^2}$, range from 0.65 to 0.95 depending on grid geometry, grid construction, blockage ratio, and downstream distance. In this study, where intensity normal to the flow was not independently measured, k was assumed to be 0.8, which corresponds to the median of measurements by Comte-Bellot and Corrsin [13]. Given indicated rms intensity as high as 35 percent of local mean velocity and the assumption that $\overline{u_y^2} = 0.8\,\overline{u_x^2}$, it is possible to correct the indicated mean velocity and rms intensity data for the wind tunnel using the factors derived by Bradbury [10]. The maximum corrections used in this case were 0.963 for mean velocity and 1.025 for turbulence intensity.

A more complex analysis of the anemometer signal is required to measure decaying turbulence in the combustion test cell where there exists turbulence intensity with negligible mean velocity. For a hot-wire sensor placed in such conditions, ($U_x = 0$), equation (1) will reduce to:

$$\text{calibrated signal} = \sqrt{u_x^2 + u_y^2} = \sqrt{u_{xy}^2} \tag{3}$$

As turbulence is generated by shear flows, turbulence with no mean flow will generally be decaying turbulence which was produced by some flow process occurring before the time or outside the region being considered. Since the turbulence in the test cell decays quite rapidly relative to the time scale of the turbulent velocity fluctuations involved, the only averaging process available is to take an ensemble average over several turbulence decay cycles. This gives a mean of the modulus of velocity in the $x-y$ plane:

$$\text{ensemble mean of signal} = \overline{|u_{xy}|} \tag{4}$$

For comparison with conventional turbulence descriptions and to promote accuate physical understanding, it is desirable to measure the 3 components of turbulence intensity, $\sqrt{\overline{u_x^2}}$, $\sqrt{\overline{u_y^2}}$, and $\sqrt{\overline{u_z^2}}$. This requires some prior knowledge of the statistical nature of the nonflowing turbulence which will be assumed to fit the following model during its later stages of decay:

1. the component velocities in the cartesian coordinate direction behave as three uncorrelated random variables with a Normal or Gaussian probability distribution of values, (i.e., $\overline{u_x u_y}, \overline{u_x u_z}, \overline{u_y u_z} \approx 0$).
2. the component velocities each have a zero mean,
3. the relationship between the variances of the component velocities, σ_x, σ_y, and σ_z is $\sigma_y^2 = \sigma_z^2 = 0.8\,\sigma_x^2$, and
4. the z component of flow has negligible effect on the hot-wire anemometer so all effects of z components may be ignored.

By combining this model of turbulence structure with the hot-wire response model already outlined it is possible to calculate component rms velocities from the ensemble-averaged output of a hot-wire anemometer in decaying turbulence with negligible mean flow.

The joint probability density function for two uncorrelated, normally distributed random variables, u_x and u_y, is

$$f(u_x,u_y) = \frac{1}{2\pi\,\sigma_x\sigma_y} \exp\left[-\frac{1}{2}\left(\frac{u_x^2}{\sigma_x^2} + \frac{u_y^2}{\sigma_y^2}\right)\right] \tag{5}$$

and the mean of any arbitrary function of u_x and u_y may be obtained by taking the first moment of this p.d.f. with respect to the arbitrary function. For this analysis, the function is

$$|u_{xy}| = \sqrt{u_x^2 + u_y^2} \tag{6}$$

so its mean is given by

$$\overline{|u_{xy}|} = \int_{-\infty}^{\infty}\int_{-\infty}^{\infty} \frac{\sqrt{u_x^2+u_y^2}}{2\pi\,\sigma_x\sigma_y} \exp\left[-\frac{1}{2}\left(\frac{u_x^2}{\sigma_x^2} + \frac{u_y^2}{\sigma_y^2}\right)\right] du_x du_y \tag{7}$$

As a first approximation, the integral of equation (7) may be easily solved if one assumes isotropic turbulence, i.e., $\sigma_y = \sigma_x$. In this case, the integral reduces (see Appendix) to:

$$\overline{|u_{xy}|} = \sqrt{\pi/2}\;\sigma_x = 1.253\;\sigma_x \tag{8}$$

implying that the average signal of a hot-wire anemometer in nonflowing, isotropic turbulence will be 1.253 times the rms turbulence intensity. Since, however, the turbulence field behind perforated plates is known to be nonisotropic, a more general solution is required. It is shown in the Appendix that equation (7) may be reduced to:

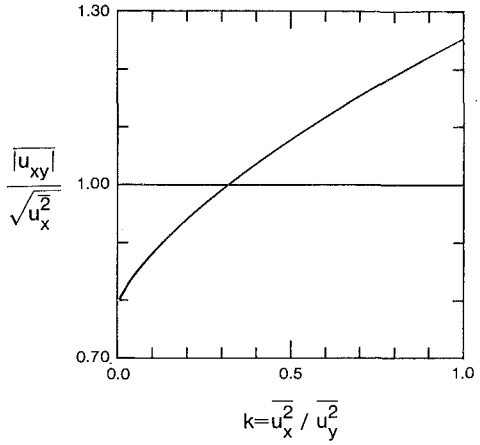

Fig. 4 Relationship between mean hot wire anemometer output $|\overline{u_{xy}}|$, and rms turbulence intensity, $\sqrt{u_x^2}$, for turbulence with no mean flow

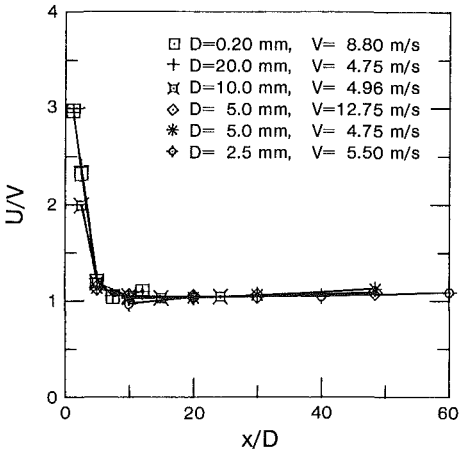

Fig. 5 Mean velocity downstream of perforated plates along a hole centreline. Note: V is the wind tunnel bulk velocity approaching the plate.

$$\overline{|u_{xy}|} = \frac{2\sqrt{\pi}\ \sigma_x^2\sigma_y^2}{(\sigma_x^2+\sigma_y^2)^{2/3}}\ F\left(.75,1.25;1;\left(\frac{\sigma_x^2-\sigma_y^2}{\sigma_x^2+\sigma_y^2}\right)^2\right)$$

and for the case of $\sigma_y^2 = k * \sigma_x^2$ with k varying from 0 to 1, this becomes

$$\overline{|u_{xy}|} = \sigma_x * \left[2\sqrt{\pi}\ \frac{k}{(1+k)^{3/2}}\ F\left(.75,1.25;1;\left[\frac{1-k}{1+k}\right]^2\right)\right] \quad (9)$$

An evaluation of equation (9) for various relative values of isotropy is given in Fig. 4. It is seen that for isotropic turbulence, mean hot-wire output is $\sqrt{\pi}/2$ times the rms intensity as expected and that for turbulence behind perforated plates or grids, where $\sigma_y^2 = 0.8 * \sigma_x^2$, mean hot-wire output is 1.19 times the rms intensity in the x direction.

Note: As discussed in the Appendix, this hypergeometric solution does not converge at the limit $k = 0$ which represents totally polarized or unidirectional turbulence. However, as k approaches 0, the solution approaches $\sqrt{2/\pi} = 0.798$ which is the constant expected for a normally distributed variable.

Measurements of Turbulence in the Wind Tunnel

Air flow through 60 percent solid perforated plates forms into discrete jets which penetrate the plate wake to create a high-shear turbulence generating zone. The jets break down rapidly and form a homogeneous, roughly isentropic turbulent bulk flow within 10 hole diameters of the plate. Whereas most researchers are interested in the homogeneous turbulence with low relative intensity far downstream of low blockage ratio grids, the intent of this study is to create and

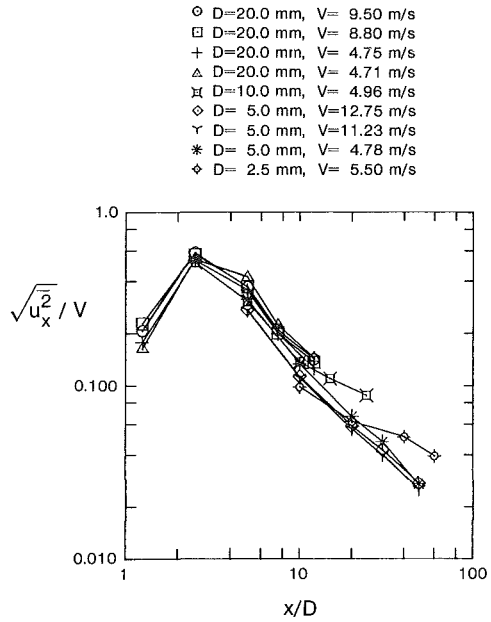

Fig. 6 Turbulence intensity downstream of perforated plates along a hole centreline. Note: V is the wind tunnel bulk velocity approaching the plate.

characterize very high intensity turbulence comparable to that in spark-ignition engines. Therefore, measurements have been made starting very close to the perforated plate. Figures 5 and 6 show the mean velocity and rms intensity behavior along a hole centerline downstream of perforated plates in the wind tunnel. Mean velocity in the vena contracta region close to the perforated plate is about three times the bulk approach velocity but drops rapidly as developing turbulence transports energy away from the jet centerline. Five diameters away from the plate, centerline mean velocity is only 15 percent above the bulk approach velocity and 10 D from the plate the centerline velocity is indistinguishable from the local bulk velocity. This smoothing out of the jet flows occurs more rapidly than is the case in most reported grid turbulence investigations, presumably due to the high turbulence levels produced by the 60 percent blockage ratio. Further downstream of the plate, local bulk velocity rises due to the constricting effects of boundary layer growth on the wind tunnel walls.

In Fig. 6, the behavior of rms velocity fluctuations is illustrated for a range of perforated plates and flow velocities. In the jet flow immediately downstream of the plate hole, velocity fluctuations are relatively small and occur at regular intervals due to eddy shedding around the perforated plate hole. At 2 1/2 D, where the jet core is entraining pockets of wake fluid, rms fluctuating velocity rises to a peak absolute value equal to about 50 percent of the bulk approach velocity, V. At 5D, where the excess mean velocity in the jet core is much smaller, the relative turbulence intensity rises to as high as 35 percent although its actual rms level is already dropping. At greater distances from the perforated plate, the turbulence decays rapidly. At high values of rms turbulent intensity ($R_L \simeq 500$), the decay exponent in the equation $\sqrt{\overline{u^2}} = (V x/D)^n$ appears to be $n = -1$ while for lower turbulence levels ($R_L \simeq 10$), the decay exponent reduces towards $n = -0.5$ as would be expected from a simple dimensional analysis such as given by Tennekes and Lumley [15].

It is notable that, while turbulence intensity levels produced by all perforated plates at a given number of diameters downstream are similar, the smaller scale plates (D = 2.5 mm, 5 mm) produce slightly lower levels. It is thought that this is a result of the difference in aspect ratio of smaller diameter holes. All perforated plates were 5 mm thick to withstand the acceleration stresses of plate movement in the bomb, so hole

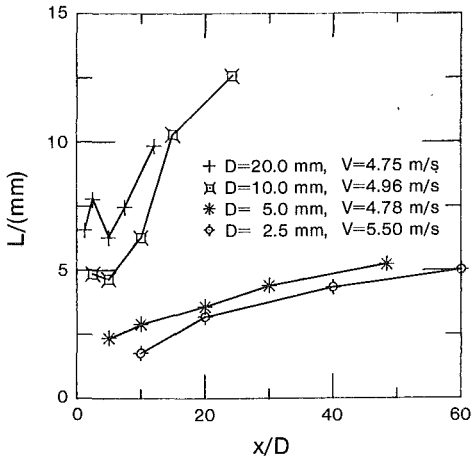

Fig. 7 Integral scale downstream of perforated plates along a hole centreline. $V \approx 5$ m/s.

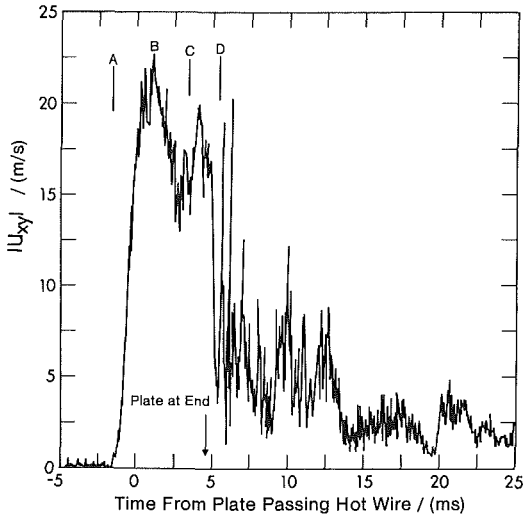

Fig. 8 Typical calibrated anemometer signal from the turbulent combustion bomb. D = 20 mm; V = 10.25 m/s

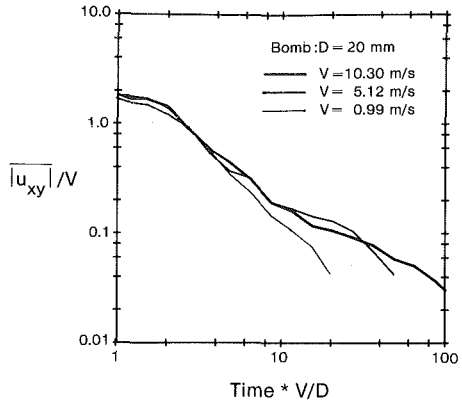

Fig. 9 Smoothed ensemble-averaged anemometer signals from the turbulent combustion bomb

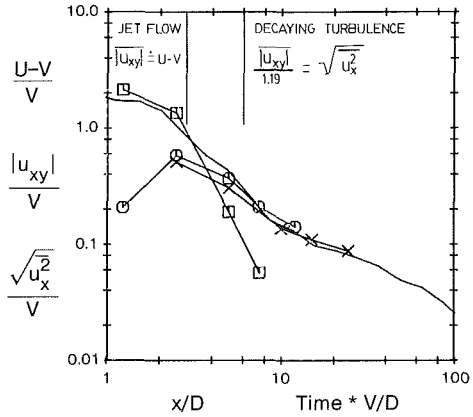

Fig. 10 Comparison of corrected bomb turbulence measurement and wind tunnel turbulence measurement

— $\overline{|u_{xy}|}/V$ from Bomb: $D = 20$ mm; $V = 10.30$ m/s

□ $(U-V)/V$ from Wind Tunnel: $D = 20$ mm; $V = 9.50$ m/s

○ $\sqrt{\overline{u_x^2}}/V$ from Wind Tunnel: $D = 20$ mm; $V = 9.50$ m/s

× $\sqrt{\overline{u_x^2}}/V$ from Wind Tunnel: $D = 10$ mm; $V = 4.96$ m/s

(Note: Beyond x/D = 5 the bomb measurement of $\overline{|u_{xy}|}$ has been divided by 1.19)

diameters greater than 5 mm appear as orifices to the flow while smaller diameter holes appear to have finite length and produce smaller scale turbulence resulting in lower turbulence energy levels in the downstream flows.

Measurement of turbulent scales is of strong interest for combustion research, but in the high intensity turbulence zone close to the plates it is difficult to make a meaningful measurement of scale due to the inhomogeneity of the turbulence. The initial jet flow field forms an ordered fluid motion with a scale set by plate hole spacing. Within each jet, turbulence fluctuations are initially dominated by eddy shedding from the perforated plates. In the zone beyond 10 D from the plate, where the excess jet velocity is negligible and turbulence intensity measurements become approximately homogeneous, the integral scale also rapidly tends to uniformity in planes parallel to the perforated plate. Figure 7 shows integral length scales taken along hole centerlines downstream of each perforated plate. In the early phase, (0 – 5 D), the integral scale on the jet centerline fluctuates as turbulence generation takes place. Then, as turbulence becomes homogeneous and starts to decay, the integral scale increases with greater distance downstream of the perforated plate. Integral scales measured on subsequent runs varied by as much as 20 percent, possibly due to scale inhomogeneities persisting further downstream of the initial jet flow than velocity inhomogeneities. Given this variability and the limited downstream range available, a precise measurement of the exponent of increase was not possible. However, the form of the curves indicates that beyond $x/D = 5$, integral scale increases at a rate corresponding roughly to $(x/D)^{1/2}$ as would be predicted from fundamental considerations for large Reynolds number turbulence.

When comparing integral scales produced by different perforated plates, it is seen that the 2.5 mm and 5 mm hole diameter plates produce significantly finer scale turbulence than the 10 mm and 20 mm plates. This would be expected if the primary turbulence generation for small diameter holes began in the confined space within the 5 mm perforated plate thickness rather than in the jet downstream of the perforated plate. The scales of turbulence produced would then be limited by actual hole diameter rather than by eddy shedding scale downstream of the hole.

Hot Wire Anemometer Measurements in the Test Cell

When a 60 percent solid perforated plate is pulled rapidly across the cubical test cell, the hot wire anemometer sensor will initially see negligible velocity as the plate approaches, then a strong unidirectional jet flow as the plate passes, followed by random turbulence with no significant mean flow once the plate is several hole diameters away. Figure 8 shows a typical anemometer signal from a single turbulence generation stroke in the bomb. When the plate is about to reach the

anemometer probe, (A), a rapidly rising gas velocity is detected as the air near the probe starts to pass through the plate hole. The velocity continues to rise, peaking when the probe is in the vena contracta region of the jet after plate passage (B). As the perforated plate moves on away from the probe, the jet begins to break down at the anemometer measuring point. The velocity signal generally exhibits a slight dip corresponding to eddy shedding (C), then breaks down to wildly fluctuating turbulence, (D). The mean value of the signal decreases rapidly as the turbulence energy is dissipated.

Because of the rapid transition and decay of fluid motions in the test cell and because of the directional insensitivity of the hot wire, a conventional signal analysis would be pointless. However, creating an ensemble-averaged mean signal from several turbulence production cycles gives a record of $\overline{|u_{xy}|}$, the mean of the effective cooling velocity in the plane perpendicular to the hot wire. For the initial jet flow within a few hole diameters of the plate, $\overline{|u_{xy}|}$ is equivalent to U_x, the mean velocity in the jet. Beyond the final jet breakdown point many hole diameters from the plate, $\overline{|u_{xy}|}$ may be related to $\sqrt{\overline{u_x^2}}$, the rms turbulence intensity, with the simple turbulence model given earlier. For the intervening period, however, there is no clear relationship.

In Fig. 9, ensemble average signals created from several turbulence generation cycles are shown for various perforated plate speeds. It is seen that these average signals scale with plate speed, V, and distance from plate in hole diameters, TIME*V/D, in the same manner as turbulence quantities measured in the wind tunnel. In the case of the lowest plate speed, (V = 1 m/s), however, the indicated mean effective cooling velocity, $\overline{|u_{xy}|}$, decreases more rapidly once the turbulence has decayed to less than 0.5 m/s. As discussed already, the hot wire calibration and sensitivity is suspect at the very low velocities involved in this case, particularly as there is no mean velocity to keep the heated wake of the hot wire from recrossing the wire and insufficient turbulence intensity to ensure that the wake temperature surplus is dissipated. The data thus indicates that accurate measurements of stationary turbulence below 0.5 m/s effective cooling velocity would require another method.

Figure 10 shows a typical comparison between turbulence measurements in the wind tunnel and in the bomb, with those in the bomb adjusted according to the methods outlined previously. (Beyond a value of TIME*V/D equal to five diameters, where the jet flows have broken down and mean flow is significantly less than turbulence intensity, the ensemble-averaged anemometer output has been divided by 1.188 to give rms velocity fluctuation in the x direction.)

During the jet flow regime, the hot wire in the bomb measures a velocity equivalent to ($U - V$) in the wind tunnel which is the jet flow velocity through the plate holes, less the plate velocity since the plate moves relative to the hot wire in the bomb. The agreement of $\overline{|u_{xy}|}$ (bomb measurement) with U_x (wind tunnel measurement) is fair at this point with the bomb velocities falling about 7 percent below wind tunnel measurements. As the excess mean velocity of the jet flow decreases and the turbulence level increases, $\overline{|u_{xy}|}$ begins to represent a significant amount of turbulence as well as the mean velocity. Thus, in the intermediate region the bomb turbulence measurement is comparable with neither mean velocity nor rms fluctuating velocity in the wind tunnel. After the mean jet velocity has become negligible, the bomb turbulence measurement, $\overline{|u_{xy}|}$ should be related to the rms fluctuating velocity measured in the wind tunnel by the model already outlined. Figure 10 indicates that the two quantities agree reasonably well from within ten diameters of the perforated plate out to about 25 diameters, the range for which matching data is available. Beyond the range for which comparable measurements are available, turbulence decay in the bomb continues at a rate slightly less than the -1 slope prevalent in the early turbulence decay. Evaluation of this slope shows it to be -0.724 which corresponds closely to the $-5/7$, (-0.714), decay rate measured by Baines and Peterson [16] downstream of grids and perforated plates in a wind tunnel. Comte-Bellot and Corrsin [13] measured somewhat slower decay rates, (-0.633 on average), and give several further references for measured decay rates between 0.60 and 0.65. During the initial period of turbulence decay, it would seem that the decay rate in the bomb should be quite accurately representative of homogeneous turbulence since there is no shear flow to generate additional turbulence as in a wind tunnel. However, during the final period of decay, when turbulent fluid motions below 1 m/s become important, the increasing inaccuracies of hot wire calibration and wake recrossing would tend to exaggerate the decay rate measured in the bomb.

Conclusions

This paper has been concerned with the analysis of turbulence produced behind 60 percent solid perforated plates for combustion experiments in a closed test cell. A comparison of measurements in the test cell and in an analogous wind tunnel system showed good agreement between the two, thus demonstrating the advantages of perforated plates for turbulence generation in such experiments; i.e. good control of turbulence characteristics is possible and thorough analysis of the turbulence is possible using an analogous wind tunnel experiment.

The response of a single wire hot wire anemometer probe in non-flowing, isotropic or nonisotropic turbulence has been considered and measurements indicate that the mean anemometer output can be successfully related to rms turbulence intensity values provided certain assumptions about the general structure of turbulence are made. This technique may prove useful to those who must measure high intensity turbulence with negligible mean velocity since the hot wire anemometry work involved is much less complex than laser anemometry techniques for comparable systems. In this case, the technique has been used only to compare test cell and wind tunnel turbulence production and decay. This comparison confirmed the feasibility of measuring turbulence in the analogous wind tunnel situation, thus avoiding further difficulties with analysis of non-flowing, very intense turbulence in the test cell itself.

References

1 "Fuel Economy and Emissions of Lean Burn Engines," The Institution of Mechanical Engineers, London, 1979.

2 Belaire, R. C., Davis, G. C., Kent, J. C., and Tabaczynski, R. J., "Combustion Chamber Effects on Burn Rates in a High Swirl Spark Ignition Engine," S.A.E. paper 830335, 1983.

3 Matsumoto, K., Inoue, T., Nakanishi, K., and Okamura, T., "The Effects of Combustion Chamber Design and Compression Ratio on Emissions, Fuel Economy, and Octane Number Requirement," S.A.E. paper 770117, 1977.

4 Nagayama, I., Araki, Y., and Ioka, Y., "Effects of Swirl and Squish on Spark Ignition Engine Combustion and Emission," S.A.E. paper 770117, 1977.

5 Lancaster, D. R., Kreiger, R. B., Sorenson, S. C., and Hull, W. L., "Effects of Turbulence on Spark-Ignition Engine Combustion," S.A.E. paper 760160, 1976.

6 Cole, D. E., and Mirsky, W., "Mixture Motion—Its Effect on Pressure Rise in a Combustion Bomb: A New Look at Cyclic Variation," SAE paper 680766, SAE Transactions, 1968, p. 2993.

7 Andrews, G. E., Bradley, D., and Lwakabamba, S. B., "Measurement of Turbulent Burning Velocity for Large Reynolds Numbers," Fifteenth Symposium (International) on Combustion, 1979, p. 655.

8 Ohigashi, S., Hamamoto, Y., and Klizima, A., "Effects of Turbulence on Flame Propagation in Closed Vessel," *Bulletin of the J.S.M.E.*, Vol. 14, No. 74, 1971, p. 849.

9 Checkel, M. D., and Thomas, A., "Turbulent Explosions in Closed Vessels," The Institution of Mechanical Engineers Conference on Combustion in Engineering, paper C57/83, 1983.

10 Bradbury, L. J. S., "Measurements with a Pulsed-wire and a Hot-wire Anemometer in the Highly Turbulent Wake of a Normal Flat Plate," *Journal of Fluid Mechanics*, Vol. 77, 1976, p. 473.

11 Champagne, F. H., Sleicher, C. A., and Wehrman, O. H., "Turbulence

Measurements with Inclined Hot-wires," *Journal of Fluid Mechanics*, Vol. 28, 1967, p. 153.

12 Collis, O. C., and Williams, M. J., "Two Dimensional Convection from Heated Wires at Low Reynolds Numbers," *J.F.M.*, Vol. 6, 1959, p. 357.

13 Comte-Bellot, G., and Corrsin, S., "The Use of a Contraction to Improve the Isotropy of Grid-generated Turbulence," *Journal of Fluid Mechanics*, Vol. 25, 1966, p. 657.

14 Uberoi, M. S., and Wallace, S., "Effect of Grid Geometry on Turbulence Decay," *The Physics of Fluids*, Vol. 10, No. 6, 1967, p. 1216.

15 Tennekes, H., and Lumley, J. L., *A First Course in Turbulence*, The MI Press, 1972, p. 73.

16 Baines, W. D., and Peterson, E. G., "An Investigation of Flow Through Screens," Trans. ASME, Vol. 73, 1951, p. 467.

17 Gradshteyn, I. S., and Ryzhik, I. M., *Table of Integrals, Series and Products*, formula 6.621, 1, Academic Press, London, 1980, p. 711.

APPENDIX

Solutions of Mean Hot Wire Anemometer Response Equation for Non-Flowing Turbulence

Given that one can measure $\overline{|u_{xy}|}$ with a hot wire anemometer in non-flowing turbulence by taking an ensemble average of the calibrated anemometer outputs, it is desirable to relate this to the conventional turbulence intensity descriptor, $\sqrt{\overline{u_x^2}}$. Assuming the x, y, and z components of velocity to be independent, random variables with a Gaussian probability distribution of values, and the z components to have negligible effect on the wire, one can write:

$$\overline{|u_{xy}|} = \int_{-\infty}^{\infty}\int_{-\infty}^{\infty} \frac{\sqrt{u_x^2+u_y^2}}{2\pi\sigma_x\sigma_y} \exp\left[-\frac{1}{2}\left(\frac{u_x^2}{\sigma_x^2}+\frac{u_y^2}{\sigma_y^2}\right)\right]dxdy \tag{A1}$$

where $\sigma_x^2 = \overline{u_x^2}$ and $\sigma_y^2 = \overline{u_y^2}$. This integral provides the desired relationship between $\overline{|u_{xy}|}$ and $\sqrt{\overline{u_x^2}}$ by taking the first moment of the joint probability density function of u_x and u_y with respect to $|u_{xy}|$. It may be solved for various conditions by assuming some relationship between $\overline{u_x^2}$ and $\overline{u_y^2}$.

For the simple case of $\sigma_y^2 = \sigma_x^2$, i.e., isotropic turbulence, the integral reduces to:

$$\overline{|u_{xy}|} = \int_{-\infty}^{\infty}\int_{-\infty}^{\infty} \frac{\sqrt{u_x^2+u_y^2}}{2\pi\sigma_x^2} \exp\left[-\left(\frac{u_x^2+u_y^2}{2\sigma_x^2}\right)\right]dxdy \tag{A2}$$

which may be solved by first introducing $u_x = r^*\cos\theta$, $u_y = r^*\sin\theta$ as variables and integrating over θ to give

$$\overline{|u_{xy}|} = \int_{-\infty}^{\infty} \frac{r^2}{\sigma_x^2} \exp\left(-\frac{r^2}{2\sigma_x^2}\right)dr \tag{A3}$$

On replacing r with a variable s such that $s = r^2/2\sigma^2$, this integral is converted to:

$$\overline{|u_{xy}|} = \sqrt{2}\,\sigma_x \int_0^{\infty} s^{1/2}\exp(-s)ds \tag{A4}$$

which is recognizable as a Gamma function.

$$\overline{|u_{xy}|} = \sqrt{2}\,\sigma_x\Gamma(3/2) = \sqrt{\frac{\pi}{2}}\,\sigma_x$$

or

$$\overline{|u_{xy}|} = \sqrt{\frac{\pi}{2}}\,\sqrt{\overline{u_x^2}} \tag{A5}$$

Thus, for the case of isotropic turbulence, the mean modulus of velocity perpendicular to the hot wire, $\overline{|u_{xy}|}$, is $\sqrt{\pi/2}$ or 1.253 times as great as the rms turbulence intensity.

Another special case of equation (A1) occurs for totally polarized turbulence, i.e., $\overline{u_y^2} << \overline{u_x^2}$. The result is an equation for the mean absolute value of a single Gaussian variable,

$$\overline{|u_{xy}|} = \int_{-\infty}^{\infty} \frac{|u_x|}{\sqrt{2\pi}\,\sigma_x} \exp\left[-\frac{u_x^2}{2\sigma_x^2}\right]dx = 2\int_0^{\infty} \frac{u_x}{\sqrt{2\pi}\,\sigma_x} \exp\left[-\frac{u_x^2}{2\sigma_x^2}\right]dx \tag{A6}$$

which may be easily integrated to give:

$$\overline{|u_{xy}|} = \sqrt{\frac{2}{\pi}}\,\sigma_x = \sqrt{\frac{2}{\pi}}\,\sqrt{\overline{u_x^2}} \tag{A7}$$

This is the standard result that for a normally distributed variable, the mean absolute value of the variable is $\sqrt{2/\pi}$ or 0.798 times its root mean square value.

Finally, we consider the general case of $\overline{u_y^2} = k\,\overline{u_x^2}$ with $0 < k < 1$, which covers non-isotropic turbulence with both components significant. Equation (A1) must now be solved without simplification. If radial coordinates $u_x = r\cos\theta$ and $u_y = r\sin\theta$ are made, equation (A1) becomes:

$$\overline{|u_{xy}|} = \int_{r=0}^{\infty} \frac{r^2}{2\pi\sqrt{k}\,\sigma_x^2}\left[\int_{\theta=0}^{2\pi} \exp\left[-\frac{1}{2}\left(\frac{r^2\sin^2\theta}{\sigma_x^2}+\frac{r^2\cos^2\theta}{k\,\sigma_x^2}\right)\right]d\theta\right]dr \tag{A8}$$

The inner integral in θ is first modified by using the half-angle formulas, $\cos^2\theta = 1/2(\cos2\theta + 1)$ and $\sin^2\theta = 1/2(1 - \cos2\theta)$ to become:

$$\text{integral} = \int_{\theta=0}^{2\pi} \exp\left[-\frac{r^2}{4k\,\sigma_x^2}\,(k+1+\cos2\theta(1-k))\right]d\theta \tag{A9}$$

Substituting $\phi = 2\theta$ and simplifying gives:

$$\text{integral} = 2\exp\left(\frac{-r^2(k+1)}{4k\,\sigma_x^2}\right)\int_{\phi=0}^{\pi} \exp\left[\left(\frac{(k-1)r^2}{4k\,\sigma_x^2}\right)\cos\phi\right]d\theta \tag{A10}$$

Now, $\int_{\phi=0}^{\pi} \exp(a\cos\phi)d\phi = \pi I_0(a)$ where I_0 is a modified Bessel function of the first kind of order 0 so the integral becomes:

$$\text{integral} = 2\pi\exp\left[-\left(\frac{k+1}{4k\,\sigma_x^2}\right)r^2\right]I_0\left[\left(\frac{k-1}{4k\,\sigma_x^2}\right)r^2\right] \tag{A11}$$

This solved integral may be substituted back into equation (A8) to give:

$$\overline{|u_{xy}|} = \frac{1}{\sqrt{k}\,\sigma_x^2}\int_{r=0}^{\infty} r^2\exp\left[-\left(\frac{k+1}{4k\,\sigma_x^2}\right)r^2\right]I_0\left[\left(\frac{k-1}{4k\,\sigma_x^2}\right)r^2\right]dr \tag{A12}$$

Equation (A12) may be transformed by replacing the variable r with a variable $s = r^2$ and by using $I_0(as) = J_0(ias)$ where J_0 is an unmodified Bessel function of the first kind and $i = \sqrt{-1}$. This gives:

$$\overline{|u_{xy}|} = \frac{1}{2\sqrt{k}\,\sigma_x^2}\int_{s=0}^{\infty} \sqrt{s}\exp\left[-\left(\frac{k+1}{4k\,\sigma_x^2}\right)s\right]J_0\left[i\left(\frac{k-1}{4k\,\sigma_x^2}\right)s\right]ds \tag{A13}$$

Fortunately, Gradshteyn and Ryzhik [17] give the integral of equation (A13) as:

$$\int_{s=0}^{\infty} s^{\mu-1}e^{-\alpha s}J_0(\beta s)ds = \frac{\Gamma(\mu)}{\alpha^{\mu}}\,F\left(\frac{\mu}{2}, \frac{\mu+1}{2}; 1; -\left(\frac{\beta}{\alpha}\right)^2\right)$$

where $\Gamma(a)$ is the Gamma function and $F(a, b; c; x)$ is the sum of the Gauss hypergeometric series defined as:

$$F(a,b;c;x) = 1+\frac{abx}{1!c}+\frac{a(a+1)b(b+1)x^2}{2!c(c+1)}+\ \ldots$$

The sum of this series coverges for $x < 1$ and equals 1 when $x = 0$. Equation (A13) may thus be rewritten as:

$$\overline{|u_{xy}|} = \frac{2\sqrt{\pi}\,k}{(k+1)^{3/2}} F\left(.75,1.25;1;\left[\frac{1-k}{1+k}\right]^2\right)\sqrt{\overline{u_x^2}} \qquad \text{(A14)}$$

This solution gives the relationship between rms turbulence in the x direction and mean hot-wire output caused by velocities in the $x-y$ plane for variable degree of isotropy, k. The hypergeometric series sum converges rapidly for any realistic values of k; for example for $k > 0.3$, less than 10 terms need be considered in order to reach a sum accurate to 5 significant figures. When $k = 1$, (isotropic turbulence), the hypergeometric series sum is 1 and the result is $\overline{|u_{xy}|} = 1.253\sqrt{\overline{u_x^2}}$ as calculated earlier with the simplified integral. At the limit $k = 0$, the hypergeometric function goes to ∞ so a solution cannot be calculated. However, as k approaches 0, the solution approaches 0.798, as previously calculated for one-dimensional turbulence.

Measurements of turbulence level in nonflowing situations are important for engine combustion research, vessel mixing studies, and for various fundamental turbulence theory tests. Using this solution and some knowledge of the degree of isotropy of the turbulence involved, one can measure these nonflowing turbulence levels with a simple hot wire anemometer system rather than the complex, expensive laser velocimetry equipment otherwise needed.

A Viscous-Inviscid Interaction Procedure—Part 1: Method for Computing Two-Dimensional Incompressible Separated Channel Flows

O. K. Kwon
Senior Project Engineer,
Allison Gas Turbine Division,
General Motors Corporation,
Indianapolis, Ind.

R. H. Pletcher
Professor,
Department of Mechanical Engineering
and Computational Fluids Dynamics Center,
Iowa State University,
Ames, Iowa
Mem. ASME

A viscous-inviscid interaction scheme has been developed for computing steady incompressible laminar and turbulent flows in two-dimensional duct expansions. The viscous flow solutions are obtained by solving the boundary-layer equations inversely in a coupled manner by a finite-difference scheme; the inviscid flow is computed by numerically solving the Laplace equation for streamfunction using an ADI finite-difference procedure. The viscous and inviscid solutions are matched iteratively along displacement surfaces. Details of the procedure are presented in the present paper (Part 1), along with example applications to separated flows. The results compare favorably with experimental data. Applications to turbulent flows over a rearward-facing step are described in a companion paper (Part 2).

Introduction

Flow separation, which occurs in many engineering applications, often leads to adverse influences on the performance of engineering devices. Thus, there has been considerable interest in developing methods of predicting flow fields containing separated regions. To date, the numerical solution of the full Navier-Stokes (or Reynolds) equations has been the most common practice for such flows. However, viscous-inviscid interaction procedures also have received a great deal of attention recently. Rather simple approaches such as spectral or integral relation methods [1, 2] and a further simplified approach using boundary-layer-type equations [3] have also been reported for analyzing internal separated flows, although these methods generally are limited in their applications.

Although significant progress has been made in the development of efficient computational methods for the Navier-Stokes (and Reynolds) equations, large amounts of computation time are still required, especially for turbulent flows. Generally, coarse and/or highly stretched grid systems are used for the solution of the Navier-Stokes equations in an attempt to reduce the computation time as well as to ease the virtual machine storage requirements at the price of large truncation errors. The deterioration in accuracy due to the large truncation errors can be partially compensated for by the use of higher order finite-difference formulas. The use of coarse grids for turbulent flows usually requires that additional empiricisms (wall functions) be used to treat the flow very near the wall. Such facts have provided motivation for considering the range of applicability of viscous-inviscid interaction methods based on more approximate forms of the governing equations.

Viscous-inviscid interaction techniques developed for predicting separated flows have been successful, in general, for both external and internal flows [4–12]. These techniques are based on the concept that the strong interaction between the viscous and inviscid flow is restricted to a zone near the separated flow region. Away from the region, the interaction is assumed to be weak. In the region where the interaction is relatively strong, the numerical solution is obtained by matching the viscous and inviscid flow solutions. Thus, the viscous flow solution is influenced by the flow both upstream and downstream through the pressure field established by the outer inviscid flow.

Most of the viscous-inviscid interaction procedures for internal flows reported in the literature [8–11] are based on an integral procedure for the viscous flow. Interaction methods based on finite-difference solutions to the boundary-layer equations in differential form have been demonstrated by several investigators [4–7]. These methods have been used for predicting external subsonic thin separation bubbles occurring on a smooth two-dimensional body.

In earlier work [7] the authors have applied viscous-inviscid interaction procedures for the calculation of separation bubbles on airfoils in subsonic flow using a small disturbance Hilbert integral formulation for the inviscid flow. An efficient procedure for matching the viscous and inviscid solutions was demonstrated in that study. In [3] a scheme was presented for computing fully developed channel flows undergoing sudden expansions. The scheme was based on solving the boundary-layer momentum and continuity equations in differential form

Contributed by the Fluids Engineering Division for publication in the JOURNAL OF FLUIDS ENGINEERING. Manuscript received by the Fluids Engineering Division, April 24, 1984.

in a coupled manner without viscous-inviscid iteraction. In the present paper, a viscous-inviscid interaction procedure is described for internal separated flows in a channel expansion. With this method the flow domain is divided into three subdomains, namely, two viscous regions near solid walls and one inviscid core region bounded by displacement surfaces on the upper and lower walls. In the viscous regions, the boundary-layer equations are solved by an inverse procedure using the coupling strategy described in [3] and making use of prescribed displacement thickness distributions as boundary conditions. In the inviscid flow region, the Laplace equation for streamfunction is solved to obtain the velocities on the displacement surfaces. The displacement thickness along both the upper and lower walls is updated iteratively following the procedure given in [7]. The feasibility of using this new interaction scheme for internal separated flow is demonstrated by comparisons with experimental data.

Analysis

Viscous Flow. The flow is assumed to be steady, incompressible, and two-dimensional; the boundary-layer form of the continuity and momentum equations is assumed to be an adequate model for the viscous flow. The usual boundary-layer coordinate system is employed with y being measured in the normal direction. It is important, however, where a step is present to employ the same reference axis (the step-side wall downstream of the step) in the computation of δ^* all along the step wall. In the separated flow region, the FLARE approximation [13] is used to permit marching the solution in the main flow (positive x) directions.

Earlier studies [3] indicated that unacceptable oscillations in wall shear stress may develop when large regions of reversed flow are present, unless the boundary-layer momentum and continuity equations are solved in a coupled manner. The boundary conditions are more conveniently applied in the inverse solution procedure for the coupled equations if the streamfunction, defined as follows, is introduced.

$$u = \frac{\partial \psi}{\partial y} \tag{1a}$$

$$v = -\frac{\partial \psi}{\partial x} \tag{1b}$$

The boundary-layer momentum equation now can be written in the form

$$Cu\frac{\partial u}{\partial x} - \frac{\partial \psi}{\partial x}\frac{\partial u}{\partial y} = -\frac{1}{\rho}\frac{dp}{dx} + \frac{1}{\rho}\frac{\partial}{\partial y}\left(\mu_{\text{eff}}\frac{\partial u}{\partial y}\right) \tag{2}$$

where

$C = 1$ when $u > 0$ and $C = 0$ when $u \leq 0$,
$\mu_{\text{eff}} = \mu$ for laminar flow,
$\mu_{\text{eff}} = \mu + \mu_T$ for turbulent flow

A separate x, y coordinate system is affixed to each of the upper and lower solid walls for the viscous flow calculation with y measured in the outward direction. The boundary conditions to these equations are

$$u(x,y_0) = v(x,y_0) = \psi(x,y_0) = 0 \tag{3a}$$

$$\lim_{y\to\infty} u(x,y) = u_e(x) \tag{3b}$$

where $y_0 = 0$ along surfaces having no steps and, for surfaces on which steps are present, $y_0 = h$ upstream of the step and $y_0 = 0$ downstream of the step. For the inverse solution scheme, the outer boundary condition, equation (3b), is replaced by

$$\delta^*(x) = \int_0^\infty \left(1 - \frac{u}{u_e}\right) dy \tag{4a}$$

or, as $y \to \infty$,

$$\psi(x,y) \to u_e(y - \delta^*) \tag{4b}$$

where $\delta^*(x)$ is a prescribed function. Since the reference axis for measuring y remains fixed along walls with steps, the δ^* given by equation (4a) defines the effective channel boundary (dispalcement body) for the inviscid flow. This δ^* distribution remains continuous in the neighborhood of the step.

An orthogonal Cartesian coordinate system was used in the present analysis. At the step, computational grid points were placed along the face of the rearward-facing step, and the no slip boundary condition was applied. No other special procedures were required to deal with the abrupt change in geometry, and no singular behavior was observed.

The system of equations solved numerically was composed of equations (1a) and (2). The equations were solved in a coupled manner for u and ψ giving rise to a 2×2 block tridiagonal system of algebraic equations for the unknowns. A fully implicit finite-difference scheme was used with Newton linearization employed for the coefficients of the convective terms. The numerical procedure used was very similar to that reported earlier [13], so details will not be repeated here. Only those points of the procedure that are different for the present study will be emphasized.

In [3], the boundary-layer equations were solved throughout the flow domain making use of the specified mass flow rate to determine the pressure gradient as part of the solution. However, the boundary conditions differ in the ap-

Nomenclature

C_D = empirical constant
c_f = skin-friction coefficient
h = rearward-facing step height
H_{in} = channel inlet height
k = turbulence kinetic energy
L = turbulent length scale
L_{REF} = reference length
l = mixing length
l_i = mixing length in the inner region
l_0 = mixing length in the outer region
Pr_k = turbulent Prandtl number for k
P = pressure
u = x component of velocity
u_e = edge velocity
v = y component of velocity
x = coordinate along the surface
y = coordinate normal to the surface
δ = boundary-layer thickness
δ^* = displacement thickness defined by equation (4a)
ϵ = convergence criteria
θ = momentum thickness
μ = molecular viscosity
ν = kinematic viscosity
ξ, η = transformed coordinates
ρ = density
τ = shear stress
ψ = streamfunction
ψ_T = total volume flow rate per unit width in a channel
ω = relaxation factor

Subscripts

BL = boundary-layer flow
e = exit of the computation domain
h = evaluated at the step
INV = inviscid flow
i = inlet of the computation domain
L = lower wall
max = maximum condition
n = iteration level
R = reattachment point
sw = switch point from inner to outer layer
U = upper wall
T = turbulent quantity
w = wall

Superscripts

$( )'$ = fluctuating quantity
$(\bar{\ })$ = time-averaged quantity

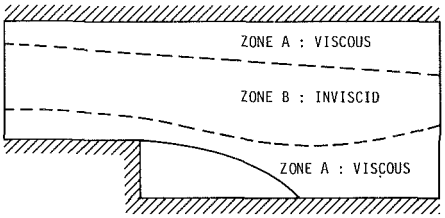

Fig. 1 Computational zones in a two-dimensional channel with a sudden expansion

plications presented in the present paper. When the boundary layer equations were solved in the inverse mode in the present study, the pressure gradient was also treated as an unknown but the displacement thickness, rather than the channel mass flow rate, was specified as a boundary condition. When the pressure gradient is unknown, standard procedures for solving 2×2 block tridiagonal systems of equations cannot be employed without using information contained in the outer boundary conditions to evaluate the pressure gradient prior to the back substitution step. This detail differs in the present study from that described in [3], although the methodology is similar. Further details on the solution procedure used in the present study can be found in [14].

Turbulence Modeling. The turbulent viscosity, μ_T, is evaluated using the turbulence kinetic energy-length scale equation (k-L) model, which was used successfully for predicting separated flows in [15]. This model employs a partial differential equation for the transport of turbulence kinetic energy and an ordinary differential equation for the transport of reference length scale for the outer region.

In the inner layer

$$\mu_T = \rho l_i^2 \left| \frac{\partial u}{\partial y} \right| \tag{5}$$

and in the outer layer

$$\mu_T = 0.548\, \rho k^{1/2}\, l_0 \tag{6}$$

In equation (6) the turbulence kinetic energy is calculated using the standard turbulence kinetic energy equation which can be written as

$$Cu \frac{\partial k}{\partial x} + v \frac{\partial k}{\partial y} = \frac{1}{\rho} \frac{\partial}{\partial y}\left[\left(\mu + \frac{\mu_T}{\mathrm{Pr}_k}\right)\frac{\partial k}{\partial y}\right] + \frac{\mu_T}{\rho}\left(\frac{\partial u}{\partial y}\right)^2 - C_D \frac{k^{3/2}}{l} \tag{7}$$

where $C_D = 0.164$, $\mathrm{Pr}_k = 1.0$, and C was treated in the same manner as for the momentum equation.

The boundary conditions for equation (7) are

$$k(x, y_{sw}) = -\overline{u'v'}\,(x, y_{sw})/C_D^{2/3} \tag{8a}$$

and

$$k(x, \infty) = k_\infty \tag{8b}$$

where k_∞ is the free-stream value of turbulence kinetic energy.

The inner boundary condition given by equation (8a) is specified at some distance from the wall (y_{sw}) where it is assumed that the generation and dissipation terms in equation (7) balance one another, and $\overline{u'v'}$ can thus be evaluated from Prandtl's mixing length formula

$$\overline{u'v'} = l^2 \left| \frac{\partial u}{\partial y} \right|^2 \tag{9}$$

This switch point normally corresponded to $y^+ \cong 60$. An initial distribution of k was determined by assuming that the turbulent viscosities given by equation (5) (with l_0 substituted for l_i) and by equation (6) were equal some distance upstream of the interaction zone where the calculation of k begins.

The mixing length in the inner region, l_i, is obtained from

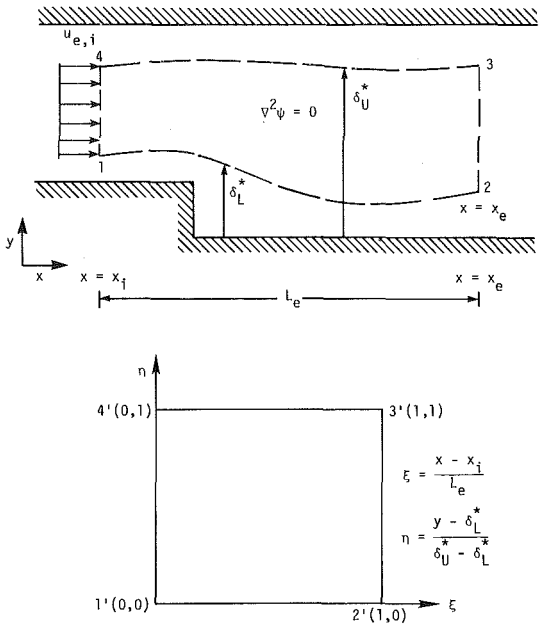

Fig. 2 Inviscid flow computational domain in physical and transformed coordinates

$$l_i = \kappa D y \sqrt{\frac{\tau_{\max}}{\tau_w}} \tag{10}$$

with

$$D = 1 - \exp\left[\left(\frac{1}{\nu}\left|\frac{\partial u}{\partial y}\right|_{\max}\right)^{1/2} \frac{y}{26}\right] \tag{11}$$

where $\kappa = 0.41$. The modification in equation (10) is based on the extension of the suggestion made by Reeves [16], and McD Galbraith and Head [17] on the mixing length in the near wall region. In the outer layer the mixing length is obtained from

$$l_0 = 0.12\, L \tag{12}$$

where L is given by the solution of the one-dimensional transport equation [15].

$$\frac{dL}{dx} = 1.25 \frac{|u_\tau|}{u_e}\left[\frac{L}{\delta} - \left(\frac{L}{\delta}\right)^2\right] \tag{13}$$

where the boundary layer thickness δ is defined as the normal distance from the wall at which the local u-velocity becomes 99.5 percent of the local boundary-layer edge velocity. The quantity $|u_\tau|$ is a representative velocity of turbulence taken to be $(|\tau_w|/\rho)^{1/2}$. The switch from inner to outer model is made at the y-location where l_i becomes equal to or greater than l_0.

Inviscid Flow. In the inviscid core region, zone B in Fig. 1, the flow is assumed to be two-dimensional, incompressible, and irrotational as indicated by the Laplace equation for streamfunction

$$\frac{\partial^2 \psi}{\partial x^2} + \frac{\partial^2 \psi}{\partial y^2} = 0 \tag{14}$$

Since the flow domain is irregular with respect to the Cartesian coordinate system in which equation (14) is written (see Fig. 2), it becomes advantageous to define new independent variables

$$\xi = \frac{x - x_i}{L_e}, \quad \eta = \frac{y - \delta_L^*}{\delta_U^* - \delta_L^*}$$

where L_e is a reference length taken as $x_e - x_i$, and thus to transform equation (14) to

$$\frac{\partial^2 \psi}{\partial \xi^2} - \frac{2}{\delta_{UL}^*}\left(\frac{d\delta_L^*}{d\xi} + \eta \frac{d\delta_{UL}^*}{d\xi}\right)\frac{\partial^2 \psi}{\partial \xi \partial \eta} + \frac{1}{\delta_{UL}^{*2}}\left\{L_e^2 + \left(\frac{d\delta_L^*}{d\xi}\right.\right.$$

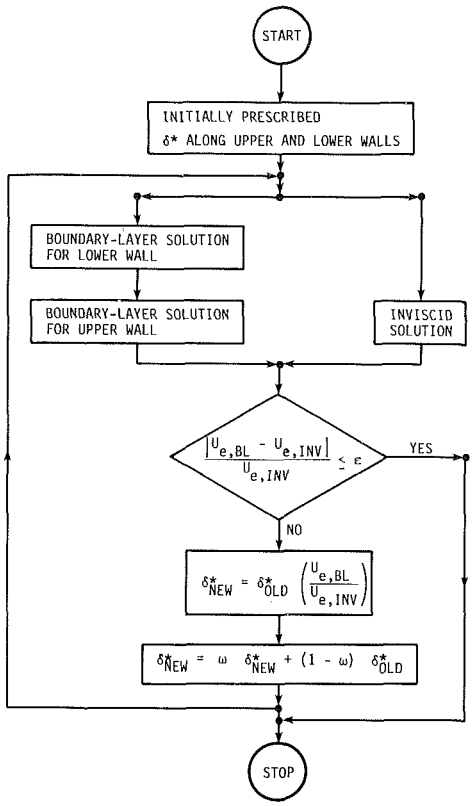

Fig 3 Skeleton flow chart for the viscous-inviscid interaction procedure

$$+\eta\frac{d\delta_{UL}^*}{d\xi}\Bigg)^2\Bigg\}\frac{\partial^2\psi}{\partial\eta^2}+\Bigg\{\frac{2}{\delta_{UL}^{*2}}\frac{d\delta_{UL}^*}{d\xi}\Bigg(\frac{d\delta_L^*}{d\xi}+\eta\frac{d\delta_{UL}^*}{d\xi}\Bigg)$$

$$-\frac{1}{\delta_{UL}^*}\Bigg(\frac{d^2\delta_L^*}{d\xi^2}+\eta\frac{d^2\delta_{UL}^*}{d\xi^2}\Bigg)\Bigg\}\frac{\partial\psi}{\partial\eta}=0 \tag{15}$$

where δ_{UL}^* is defined as $\delta_U^* - \delta_L^*$. The parameter δ_{UL}^* gives the height of the effective channel for the inviscid flow calculations. For the inviscid flow calculation the distances δ_U^* and δ_L^* must be measured from a common reference as indicated in Fig. 2. As seen there, the computational domain is regular in terms of the ξ, η coordinates.

The boundary conditions used for equation (15) are as follows:

upstream

$$\psi(0,\eta)=\psi_T\eta \tag{16a}$$

downstream

$$\left(\frac{\partial^2\psi}{\partial\eta^2}\right)_{(1,\eta)}=0 \tag{16b}$$

lower boundary

$$\psi(\xi,0)=0 \tag{16c}$$

and upper boundary

$$\psi(\xi,1)=\psi_T \tag{16d}$$

where ψ_T is the total volume flow rate per unit width in the channel.

After employing central differences to represent all terms in equation (15), the resulting system of algebraic equation was solved by an alternating direction implicit (ADI) scheme. The relaxation factor used was 1.5. The ADI method typically provided converged solutions in 10 to 15 iterations at the start of the viscous-inviscid interaction calculation. From the second iteration of the interaction calculation (or the global iteration), the number of iterations usually was reduced significantly by using the solutions at the previous global iteration level as the initially assumed values. The number of iterations required for the convergence was reduced steadily as the interaction solution converged. Finally, only 1 to 2 iterations were needed. The convergence criteria used for the inviscid flow solution in the present analysis was

$$\frac{|\psi_{i,j}^{n+1}-\psi_{i,j}^n|}{|\psi_{i,j}^n|}\le\epsilon_\psi$$

where ϵ_ψ was set equal to 0.5×10^{-4}.

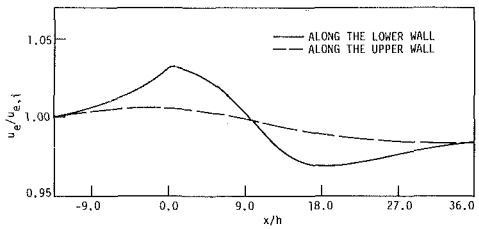

Fig. 4 Predicted edge velocity distributions for laminar flow in a sudden channel expansion, $hu_{max}/\nu = 412$, $h/H_{in} = 0.0664$

Viscous-Inviscid Interaction. The interaction calculation is initiated by prescribing a guessed distribution of $\delta^*(x)$ along the upper and lower solid walls in the interaction region. The viscous and inviscid solutions are obtained by the methods discussed above for the prescribed distributions of $\delta^*(x)$. Since these distributions are not, in general, correct, the viscous and inviscid solutions for $u_e(x)$ will not match on the displacement surfaces. The mismatch between the computed viscous and inviscid tangential velocities is used in a fixed-point iteration formula to improve the local $\delta^*(x)$, following Carter [6] and Kwon and Pletcher [7]. The equation used is written as

$$\delta_{n+1}^*=\delta_n^*(u_{e,BL}/u_{e,\mathrm{INV}})_n \tag{17}$$

Arguments supporting the form of equation (17) have been offered based on a local continuity concept in the boundary layer [7] and a simplifed integral momentum equation [6]. As indicated before, δ^* is defined in such a way as to be continuous across the step.

The present viscous-inviscid interaction procedure is outlined in Fig. 3. A relaxation step for equation (17) is indicated in the figure; however, ω was set equal to one for all the calculations to be reported in Part 1 of this paper. Convergence is assumed to occur when the following criterion is met throughout the interaction zone:

$$\frac{|u_{e,BL}-u_{e,\mathrm{INV}}|}{u_{e,\mathrm{INV}}}\le\epsilon \tag{18}$$

The numerical values of ϵ will be given for each case computed in the following section.

Results

Laminar Separating Flow. The viscous-inviscid interaction method was first applied to laminar sudden channel expansion flows in order to evaluate its capabilities without the additional uncertainties introduced through turbulence modeling. Comparisons were made with the measurements of Eriksen [18] (also reported by Goldstein et al. [19]). The interaction zone was established from $x/h = -13.5$ to $x/h = 36$. From the channel inlet to the start of the interaction zone, the flow was computed by the boundary-layer numerical scheme described in [3] in order to match the upstream conditions reported in [18]. In the computations, the value of δ^*/h was 1.335 on the lower (step) wall and 0.335 on the upper wall at the start of the interaction zone. The predicted boundary-layer edge velocities along the upper and lower walls are shown in Fig. 4 for a Reynolds number of 412 based on step height and maximum channel velocity. The ratio of step height to channel inlet height was 0.0664. The presence of the step is seen to induce a noticeable acceleration in the flow near the step (lower)

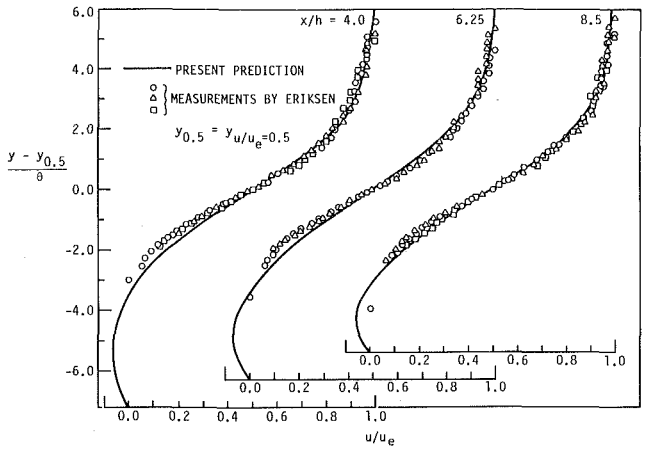

Fig. 5 Velocity profiles for a laminar flow in a sudden channel expansion. Predictions for $hu_{max}/\nu = 412$, $h/H_{in} = 0.0664$.

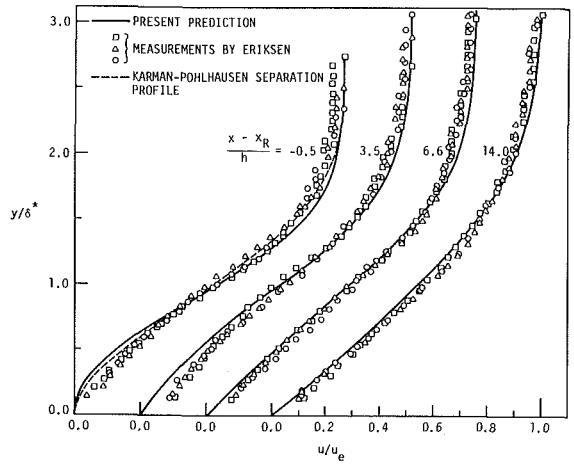

Fig. 6 Velocity profiles for a laminar flow in a sudden channel expansion. Predictions for $hu_{max}/\nu = 412$, $h/H_{in} = 0.0664$.

wall some distance upstream of the step. The predicted velocity profiles for the same flow conditions are compared with measurements in Figs. 5 and 6. The experimental data shown in these figures were obtained for h/H_{in} ranging from 0.0235 to 0.0664 and step height Reynolds numbers ranging from 100 to 500. Figure 5 presents profiles in the zone that includes the recirculating flow downstream of the step. The flow in the zone of reattachment and downstream are shown in Fig. 6. The computed reattaching velocity profile at $(x - x_R)/h = 0.5$ compares reasonably well with the measured data and with the Karman-Pohlhausen separation profile. The predicted velocity profile at 14 step heights downstream of reattachment agrees very well with the Blasius profile. The shape factor for the numerical solution at that point is 2.59, which is almost the same value as for the exact solution. Overall, the predicted results agree reasonably well with the measurements. The predicted reattachment length of 13.5 step heights is slightly longer than the 11 step heights observed experimentally.

A 56 × 45 grid was used for the inviscid solution. For the viscous flow calcualtions, about 150 grid points were used across the flow. The interaction zone was spanned by 174 streamwise steps. The interaction procedure converged to $\epsilon = 0.0007$ (see equation (19)) in 12 global iterations requiring approximately 10 seconds of CPU time per iteration on an NAS AS/6 computer.

Turbulent Separating Flow. The next case considered was the turbulent separating flow studied experimentally by Simpson at al. [20]. The measurements were obtained in a 4.9-m-long converging-diverging channel using hot-wires and a laser anemometer. The flow separation occurred on the flat bottom wall of the channel. Two-dimensionality in mean flow was promoted by suction and tangential injection control of the side and top wall boundary layers. The test section entrance was 0.91-m wide by 0.38-m high and the entrance velocity was 16.5 m/s. Free-stream turbulence intensity was 0.1 percent.

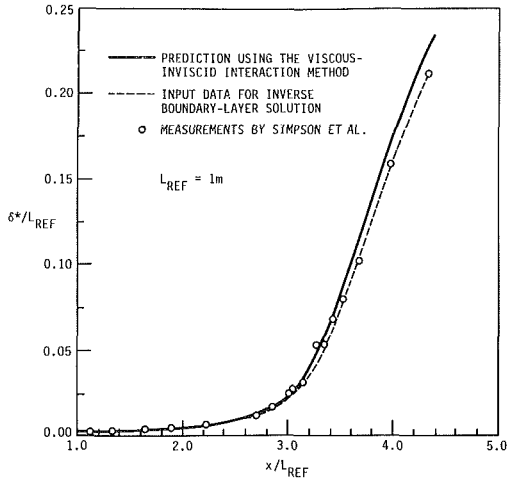

Fig. 7 Displacement thickness distribution for a turbulent separating flow in a two-dimensional channel

Both the inverse boundary-layer solution method and viscous-inviscid interaction method were used in the predictions. With the inverse boundary layer solution method, the boundary layer equations were solved inversely in a once-through fashion along the lower wall from $x = 0.607$ m to the end of the channel diverging section, $x = 4.35$ m, using the measured displacement thickness (see Fig. 7) as boundary conditions. The direct solution method was used initially from the channel inlet to the start of the inverse solution ($x = 0.607$ m). The measured edge velocities along the lower wall were used as the outer boundary condition in this region.

For the viscous-inviscid interaction solution, the interaction zone was assumed to range from $x = 0.805$ m to 4.386 m. In this region the boundary-layer equations were solved inversely along the lower wall.

To facilitate predictions, Simpson et al. [20] provided data on the location of a streamline in the inviscid flow near the upper channel wall. This streamline was used to establish upper boundary conditions for the inviscid flow solution in the present viscous-inviscid interaction procedure. The viscous-inviscid interaction calculation started with the measured displacement thickness distribution. Despite the fact that the flow was separated at the downstream computational boundary, the solution converged in 11 global iterations to $\epsilon = 0.005$. A 48 × 51 grid was used in the inviscid region. For the viscous flow calculations, about 100 unequally spaced grid points were used across the flow and 298 streamwise steps were used to span the interaction zone. The computation time per global iteration was about the same as reported for the laminar flow case.

The displacement thickness computed by the viscous-inviscid interaction procedure is compared with the measured data in Fig. 7. Although a slight overprediction is noticed in the diverging section of the channel, the overall agreement with the data is good.

The predicted edge velocity distribution and skin-friction distribution using both the inverse boundary-layer solution procedure and viscous-inviscid interaction method are compared with the measured data in Figs. 8 and 9. As can be seen from these figures, the viscous-inviscid interaction solutions agree better with the data than the inverse boundary layer solution. Separation was predicted at $x = 3.43$ m using the interaction method and at $x = 3.47$ m by using the inverse boundary-layer procedure. Both of these predicted values are

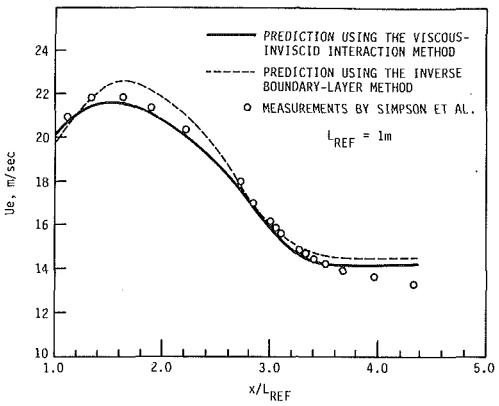

Fig. 8 Boundary-layer edge velocity distribution for a turbulent separating flow in a two-dimensional channel

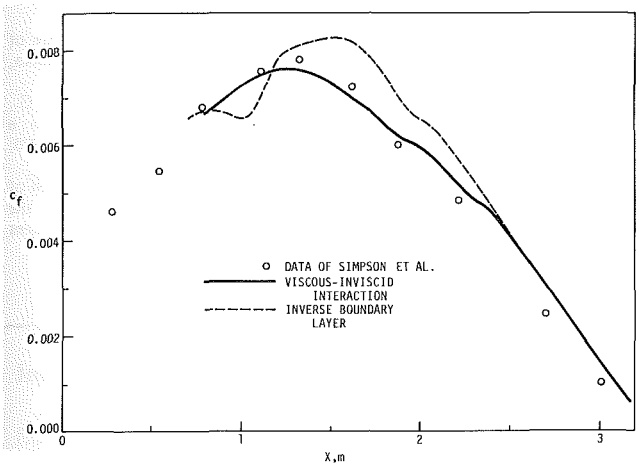

Fig. 9 Distribution of skin-friction coefficient for a turbulent separating flow in a two-dimensional channel

in good agreement with the measured value of 3.4 m. A comparison of predicted and measured velocity profiles is shown in Figs. 10 and 11. Although the negative velocities in the separated flow region are somewhat under-predicted, the overall agreement with the data is good.

The predicted Reynolds stresses for this flow are compared with measurements in Fig. 12. The Reynolds stresses predicted by the present turbulence modeling do not agree well with the measurements at $x = 3.972$ m. The predicted Reynolds stresses are observed to spread and decrease in magnitude from one streamwise station to the next. However, in contrast to this, the Reynolds stresses measured by Simpson et al. [20] are observed to grow. The measured time-average fluctuations of the streamwise mean velocity were very large even fairly far away from the wall; at $x = 4.43$ m, the maximum that occurred at $y = 0.6\delta$ was on the order of 23 percent of the outer edge velocity. Thus, some question might be raised as to whether the data measured by Simpson et al. [20] for the fluctuating quantities are completely isolated from the unsteadiness.

Conclusions

A viscous-inviscid interaction prediction method, which is very stable numerically and relatively economical, was described for internal separating flow where both viscous and inviscid flow regions exist throughout the computational domain. The present method was found not to require underrelaxation for a smooth channel expansion and a sudden expansion with a relatively small step height. The overall predictions of mean flow quantities for internal separating flow using the interaction method agreed reasonably well with measured data. However, for the laminar flow through a sudden channel expansion, the reattachment point was obseved to

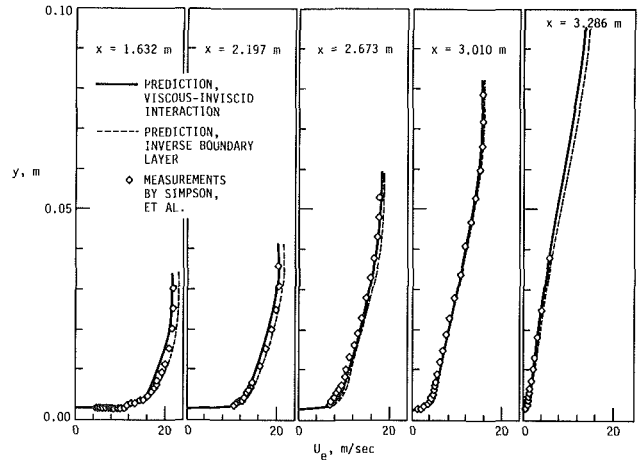

Fig. 10 Velocity profiles for a turbulent separating flow in a two-dimensional channel

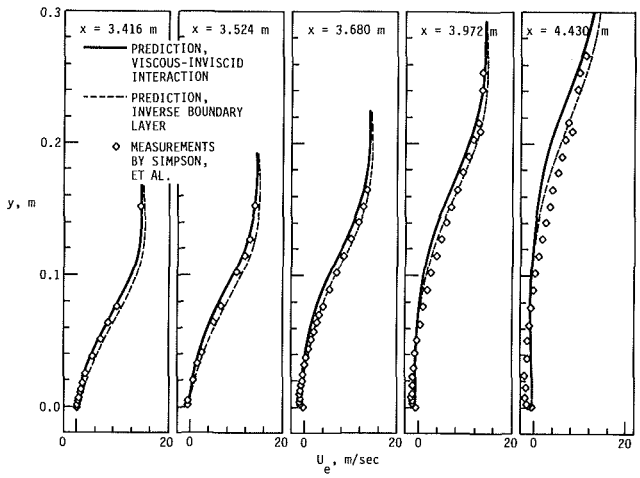

Fig. 11 Velocity profiles for a turbulent separating flow in a two-dimensional channel

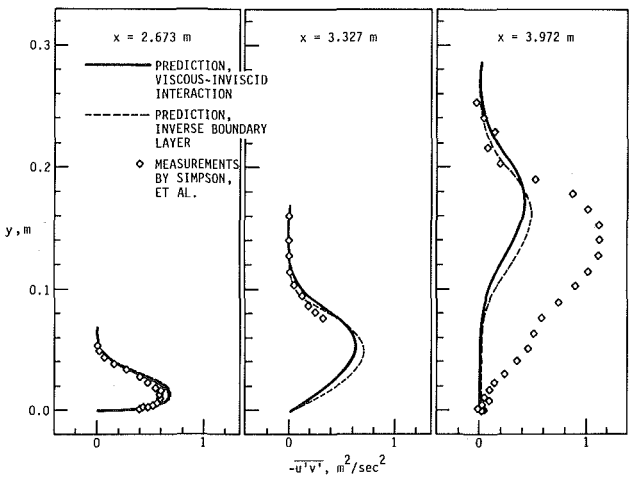

Fig. 12 Reynolds stress profiles for a turbulent separating flow in a two-dimensional channel

be overpredicted. The predictions using the inverse boundary-layer solution technique also compared reasonably well with the measured data for separating flows in a converging-diverging channel.

The turbulence model used in the present study was observed to be fairly successful in predicting mean flow quantities, although it failed to predict the Reynolds stresses accurately in the separated flow region.

Acknowledgments

The present work was supported by the National Science Foundation under Grants ENG-7812901 and MEA-8211713.

References

1 Plotkin, A., "Spectral Method Solutions for Some Laminar Channel Flows with Separation," *AIAA Journal*, Vol. 20, 1982, pp. 1713–1719.

2 Kumar, A., and Yajnik, K. S., "Internal Separated Flows at Large Reynolds Number," *Journal of Fluids Mechanics*, Vol. 97, 1980, pp. 27–51.

3 Kwon, O. K., Pletcher, R. H., and Lewis, J. P., "Prediction of Sudden Expansion Flows Using the Boundary-Layer Equations," ASME JOURNAL OF FLUIDS ENGINEERING, Vol. 106, 1984, pp. 285–291.

4 Briley, W. R., and McDonald, H., "Numerical Prediction of Incompressible Separation Bubbles," *Journal of Fluid Mechanics*, Vol. 69, 1975, pp 631–656.

5 Carter, J. E., and Wornom, S. F., "Solutions for Incompressible Separated Boundary Layers Including Viscous-Inviscid Interaction," NASA SP 347, 1975.

6 Carter, J. E., "A New Boundary-Layer Interaction Technique for Separated Flows," NASA TM 78690, 1978.

7 Kwon, O. K., and Pletcher, R. H., "Prediction of Incompressible Separated Boundary Layers Including Viscous-Inviscid Interaction," ASME JOURNAL OF FLUIDS ENGINEERING, Vol. 101, 1979, pp. 466–472.

8 Kim, J., Kline, S. J., and Johnson, J. P., "Investigation of Separation and Reattachment of a Turbulent Shear Layer: Flow Over a Backward-Facing Step," Thermoscience Div., Dept. of Mechanical Engineering, Stanford University, Report MD-37, 1978.

9 Le Balleur, J. C., and Mirande, J., "Experimental and Theoretical Study of Two-Dimensional Turbulent, Incompressible Reattachment," *AGARD Conference Proceedings*, No. 168, 1975, pp. 17.1–17.13.

10 Wooley, R. L., and Kline, S. J., "A Procedure for Computation of Fully Stalled Flows in Two-Dimensional Passages," ASME JOURNAL OF FLUIDS ENGINEERING, Vol. 100, 1978, pp. 180–186.

11 Moses, H. L., Jones, R. R. III, and Sparks, J. F., "An Integral Method for the Turbulent Boundary Layer with Separated Flows," Paper presented at the Joint ASME-CSME Applied Mechanics, Fluid Engineering and Bioengineering Conference, Niagara Falls, New York, June 18–20, 1979.

12 Le Balleur, J. C., "The Calculation of Flows with Strong Viscous Interactions by Means of Coupling Methods," Paper presented at AGARD Symposium on Computation of Viscous-Inviscid Interactions, Colorado Springs, Colorado, Sept. 29–Oct. 1, 1980.

13 Reyhner, T. A., and Flügge-Lotz, I., "The Interaction of a Shock Wave with a Laminar Boundary Layer," *International Journal of Nonlinear Mechanics*, Vol. 3, No. 2, 1968, pp. 173–199.

14 Kwon, O. K., and Pletcher, R. H., "Prediction of the Incompressible Flow over a Rearward-Facing Step," Technical Report HTL-26, CFD-4, ISU-ERI-Ames-82019, Engineering Research Institute, Iowa State University, 1981.

15 Pletcher, R. H., "Prediction of Incompressible Turbulent Separating Flow," ASME JOURNAL OF FLUIDS ENGINEERING, Vol. 100, 1978, pp. 427–433.

16 Reeves, B. L., "Two-Layer Model of Turbulent Boundary Layers," *AIAA Journal*, Vol. 12, 1974, pp. 932–939.

17 McD Galbraith, R. A., and Head, M. R., "Eddy Viscosity and Mixing Length from Measured Boundary-Layer Developments," *Aeronautical Quarterly*, Vol. 26, 1975, pp. 133–154.

18 Eriksen, V. L., "An Experimental Investigation of the Laminar Flow of Air over a Downstream – Facing Step," M.S. thesis, University of Minnesota, 1968.

19 Goldstein. R. J., Eriksen, V. L., Olson, R. M., and Eckert, E. R. G., "Laminar Separation, Reattachment, and Transition of the Flow over a Downstream-Facing Step," ASME *Journal of Basic Engineering*, Vol. 92, 1970, pp. 732–741.

20 Simpson, R. L., Chew, Y. T., and Shivaprasad, B. G., "Comparison of Computation and Experiment, Case No. 431," Data set prepared for the 1980–1981 AFOSR-HTTM-STANFORD Conference on Complex Turbulent Flows, Stanford University, 1981.

O. K. Kwon
Senior Project Engineer,
Allison Gas Turbine Division,
General Motors Corporation,
Indianapolis, Ind.
Assoc. Mem. ASME

R. H. Pletcher
Professor,
Department of Mechanical Engineering
and Computational Fluid Dynamics Center,
Iowa State University,
Ames, Iowa
Mem. ASME

A Viscous-Inviscid Interaction Procedure—Part 2: Application to Turbulent Flow Over a Rearward-Facing Step

The viscous-inviscid interaction numerical procedure described in Part 1 is used to predict steady, two-dimensional turbulent flow over a rearward-facing step. The accuracy of predictions is observed to be quite sensitive to the specification of length scale in the turbulence modeling. The best results are observed when the length scale is specified algebraically downstream of the step using parameters characteristic of the step geometry. Predictions of mean flow quantities and reattachment length are shown to be in generally good agreement with measurements obtained over a range of channel expansion ratios.

Introduction

A viscous-inviscid interaction calculation procedure for flows through two-dimensional channel expansions was described in Part 1 of this paper [1]. In the present part, applications of the scheme to turbulent flow over a rearward-facing step are considered. Aspects of turbulence modeling are discussed and predictions of the interaction scheme are compared with experimental measurements.

Computations of turbulent flows over a rearward-facing step have generally been carried out by solving the Reynolds-averaged Navier-Stokes equations. Recently, LeBalleur and Mirande [2] and Kim et al. [3] have employed viscous-inviscid interaction procedures for turbulent step flows. Both of these groups [2, 3] employed momentum integral methods for the viscous flow. The interaction schemes required much less computer time than those based on the full Reynolds-averaged Navier-Stokes equations. However, the accuracy of prediction schemes of all types was very sensitive to the choice of turbulence modeling. The model must adequately deal with regions of flow reversal, reattachment, and the redeveloping flow downstream of reattachment. The present viscous-inviscid interaction scheme (Part 1) employs finite-difference procedures for both the viscous and inviscid portions of the flow. All previous interaction schemes applied to turbulent step flows have utilized integral methods for the viscous portion of the flow. An evaluation of the available experimental data and an indication of the present state of the art in the prediction of turbulent flows over a rearward-facing step can be found in [4, 5].

The base-line turbulence model for this study utilizes a modeled form of the turbulence energy equation and a length scale transport equation [6]. This model has proven satisfactory for smooth surfaces on which separation occurs (see Part 1). For the rearward-facing step, however, improved predictions were observed when the length scale was specified algebraically downstream of the step using parameters characteristic of the step geometry.

Analysis

Viscous-Inviscid Interaction. The same finite-difference viscous-inviscid interaction procedure that was described in Part 1 [1] was used for the turbulent rearward-facing step calculations. An overrelaxation factor of 1.5 was employed in the ADI scheme used to obtain the inviscid solution. However, in some instances it was necessary to employ underrelaxation in the global matching procedure. To accommodate underrelaxation, equation (17) of Part 1 was modified to the form

$$\delta^*_{n+1} = \omega\delta^*_n\left(\frac{u_{e,\mathrm{BL}}}{u_{e,\mathrm{INV}}}\right)_n + (1-\omega)\delta^*_n \tag{1}$$

where ω is the relaxation factor.

Turbulence Modeling. The k-L turbulence model described in Part 1 has proven to be reasonably adequate for predicting mean flow characteristics for both attached and separated flows on smooth (step-free) surfaces. However, this k-L model was observed to perform poorly in the region downstream of the rearward-facing step. The length scale predicted by the transport equation for L appeared inappropriate in this region. Although some modifications to the length scale transport equation described in Part 1 showed promise, the best predictions were obtained by algebraically specifying the mixing length in the outer layer, l_0, downsteam of the step, instead of using the turbulence length scale obtained from the transport equation. In the present study, algebraic correlations for l_0 were developed using geometric parameters characteristic of the flow in the step geometry.

The correlations are

$$l_0 = 0.1\left(\frac{\delta}{\delta'}\right)\delta \tag{2}$$

Contributed by the Fluids Engineering Division for publication in the JOURNAL OF FLUIDS ENGINEERING. Manuscript received by the Fluids Engineering Division, April 24, 1984.

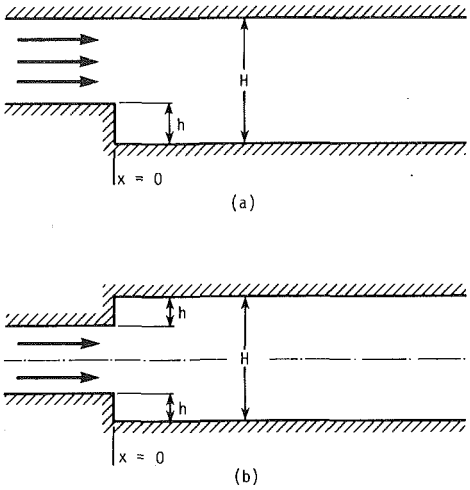

Fig. 1 Geometry and nomenclature for step flows; (a) single step, (b) symmetric expansion

$$l_0 = 0.08\left(1 + C_1 \frac{x}{\delta}\right)(\delta - y_D) \tag{3}$$

where

$$\delta' = \{0.5[y^2_{\tau_{max}} + (\delta - y_{\tau_{max}})^2]\}^{1/2} \tag{4}$$

and

$$C_1 = \begin{cases} 0.3 \text{ if } h/H \le 0.3 \\ h/H \text{ if } h/H > 0.3 \end{cases} \tag{5}$$

In the above, x is the distance downstream of the step; h is the step height; H is the channel height downstream of the step; y_D is the height of the dividing streamline downstream of the step; and $y_{\tau_{max}}$ is the height of maximum shear stress, with all heights measured from the wall on which the step occurs.

The parameter δ' is a characteristic width of the viscous layer. It is evaluated as the square root mean of the distance from the wall to the location of the maximum shear stress, $y_{\tau_{max}}$, and the distance from the point of maximum shear stress to the outer extent of the viscous region, δ-$y_{\tau_{max}}$. The parameter δ' can be considered as a mean distance for the propagation of turbulence quantities across the viscous layer, if the quantities are assumed to originate at the location of maximum shear stress. Thus, δ/δ' is the ratio of the actual boundary-layer thickness to a "mean travel distance" for the turbulence.

In the present analysis, the smaller value obtained from equations (2) and (3) was used for l_0 downstream of the step. That is, away from the step, equation (2) provides a smaller l_0 than equation (3) and, thus, is used. Immediately downstream of the step, use of equation (2) resulted in an abrupt change in l_0. Thus, equation (3) was used for a short distance (about one step height) downstream of the step to permit a smooth transition in values of l_0 used upstream and downstream of the step. The form of equations (2) and (3) evolved from studies in which models employing several different combinations of geometric parameters were evaluated. Further discussion on the development of the algebraic model for l_0 can be found in [7].

The evaluation of the mixing length in the inner layer, l_i, as specified by equations (9) and (10) of Part 1, appeared adequate for step flows. When recirculation was present, the criteria for switching from the inner to the outer model nearly always occurred within the region of reversed flow. Thus, l_0

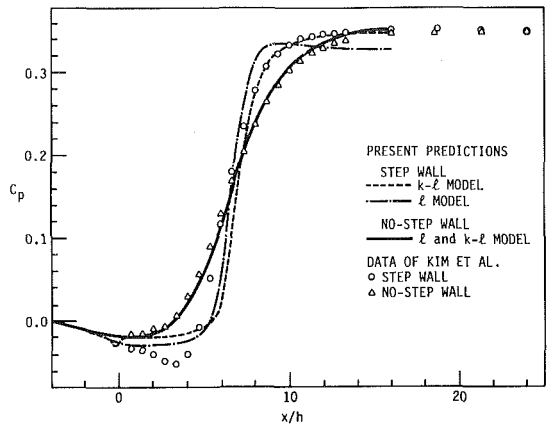

Fig. 2 Pressure coefficient distribution, reference flow

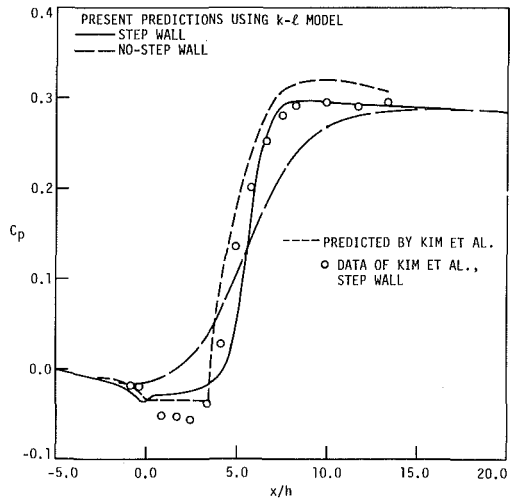

Fig. 3 Pressure coefficient distribution, step-1 flow

Nomenclature

C_1 = empirical constant
C_p = pressure coefficient
H = channel height downstream of the step
h = step height
k = turbulence kinetic energy
L = turbulence length scale
l = mixing length
l_i = mixing length in the inner region
l_0 = mixing length in the outer region
u = x component of velocity
u_e = edge velocity
x = coordinate along the surface measured from the step
y = coordinate normal to the surface
δ = boundary layer thickness
δ^* = displacement thickness
ϵ = convergence criteria, $|u_{e,BL} - u_{e,INV}|/u_{e,INV}$
μ_T = turbulent viscosity
ω = relaxation factor

Subscripts

BL = boundary layer flow
D = dividing streamline
INV = inviscid flow
i = inlet of the computation domain
n = iteration level
R = reattachment point
s = step
τ_{max} = maximum shear stress

Superscript

( )′ = fluctuating quantities
$\overline{(\ )}$ = time-averaged quantities

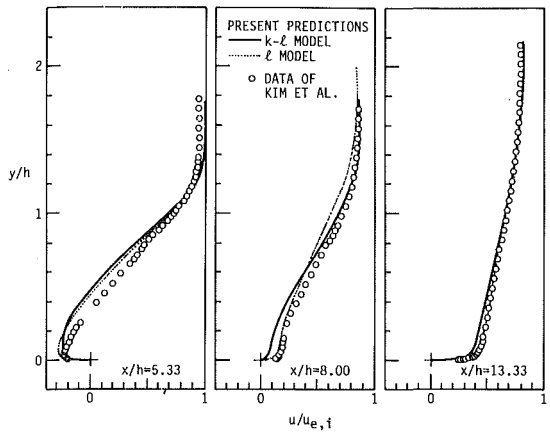

Fig. 4 Velocity profiles downstream of the step, reference flow

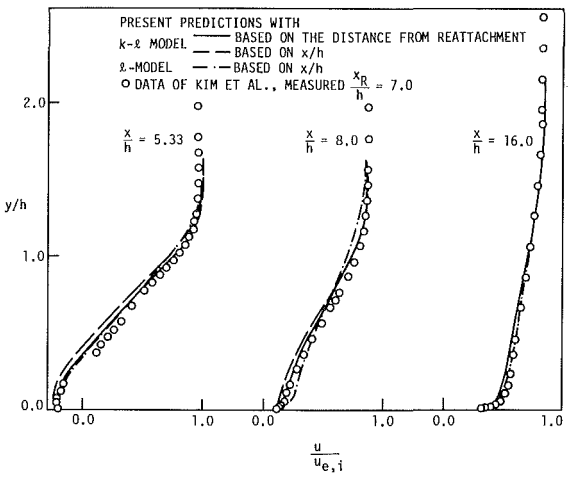

Fig. 5 Velocity profiles downstream of the step, step-1 flow

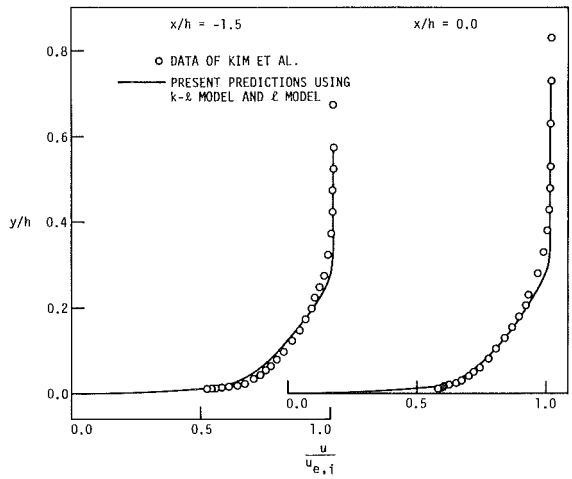

Fig. 6 Velocity profiles upstream of the step, step-1 flow

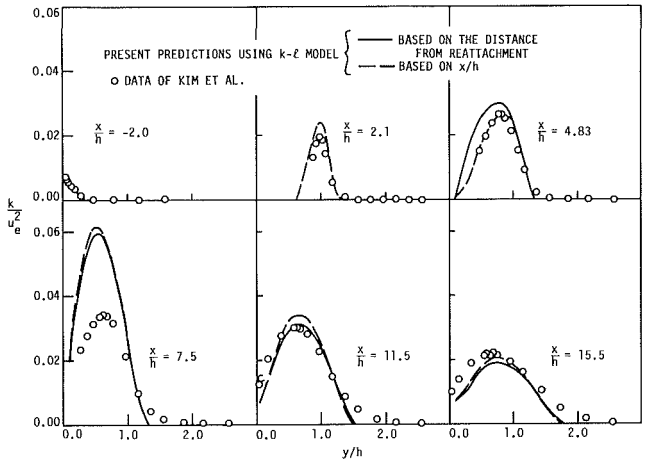

Fig. 7 Turbulence kinetic energy profiles, step-1 flow

was predominantly used to predict forward-going portions of the flow.

The results in the present paper were obtained from model combinations, which will be designated as *k-l* and *l*. The *k-l* model employed the *k-L* formulation of Part 1 everywhere except on the step wall downstream of the step where l_0 was evaluated as indicated by equations (2)–(5). In the *l* model, all length quantities were evaluated exactly as indicated above for the *k-l* model. The turbulence kinetic energy, however, was dropped as a model parameter, and the turbulent viscosity was evaluated from

$$\mu_T = \rho l^2 \left| \frac{\partial u}{\partial y} \right| \tag{6}$$

where

$l = l_i$ for the inner layer

$l = l_0$ for the outer layer

Results

The predictions of the present viscous-inviscid interaction scheme were first compared with the step flow measurements of Kim et al. [2]. The data were obtained in a wind tunnel using hot wire anemometry. The rearward-facing step was placed on the lower wall (see Fig. 1). The tunnel inlet section was 0.0762-m high, 0.6096-m wide, and 0.3048-m long. The test section of the tunnel behind the step was 2.3368-m long. The measurements were performed for a step height, *h*, of 0.0381 m (reference flow) and 0.0254 m (step-1 flow). The flows were designated "reference" and "step-1" by Kim et al. [2]. The typical reference velocity was 18.2 m/s with a variation of 0.15 m/s throughout the experiment. The boundary layer displacement thickness on the lower wall was approximately one step height at the step. The computation domain ranged from $x/h = -4$ to 16 for the reference flow and from $x/h = -5$ to 20 for the step-1 flow. Further computational details are given at the end of this section.

The predicted and measured pressure coefficients are compared in Figs. 2 and 3 for the two flows. The predictions obtained by Kim et al. [2] using a zonal viscous-inviscid interaction scheme based on an integral boundary-layer method are also shown on Fig. 3. The predictions of the present method agreed reasonably well with the measurements except very near the step. The wall pressure measurements indicated a short region of favorable streamwise pressure gradient just downstream of the step, which was not present in the predictions. In Fig. 2, the *k-l* model appears to perform slightly better than the *l* model on the step-side wall. The predictions of the two models are indistinguishable for the no-step wall for the reference flow. In Fig. 3, predictions by the present method using the *k-l* model are shown for both walls, although measurements were only reported for the step wall. The step-1 flow was also predicted using the *l* model, but the differences in pressure coefficient predicted by the two models were insignificant.

The velocity profiles in the separated and redeveloping regions downstream of the step are compared with the data measured for the reference flow in Fig. 4. Similar comparisons for the step-1 flow are shown in Fig. 5. The *l* model predicted slightly better mean velocity profiles and reattachment lengths

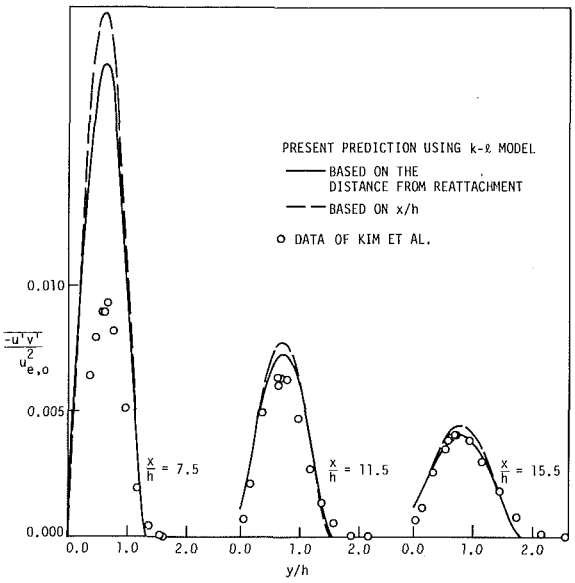

Fig. 8 Reynolds stress profiles, step-1 flow

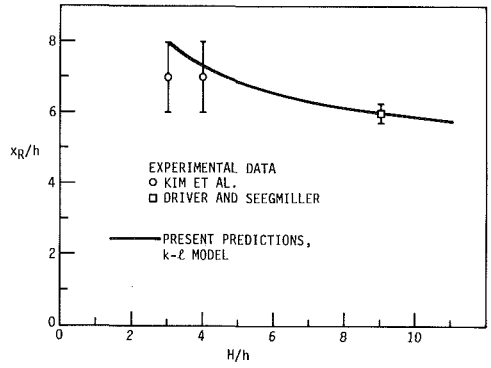

Fig. 9 Variation of reattachment length with expansion ratio

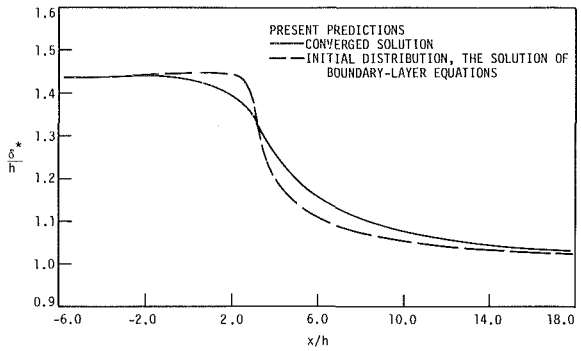

Fig. 10 Displacement body distribution, symmetric expansion, H/h = 10, Re_h = 9800

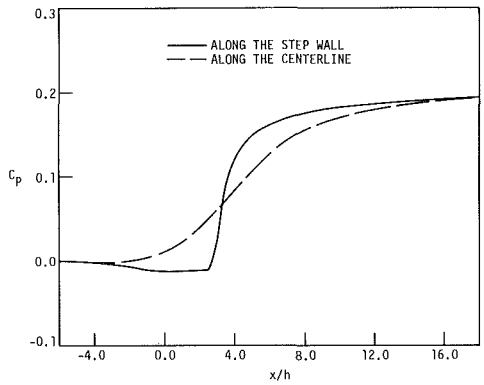

Fig. 11 Pressure coefficient distribution, symmetric expansion, H/h = 10, Re_h = 9800

than did the *k-l* model. The reattachment lengths calculated were $x/h = 7.95$ for the reference flow and 7.65 for the step-1 flow using the *k-l* model, and $x/h = 7.32$ for the reference flow and 7.2 for the step-1 flow using the *l* model. The measured reattachment length was $x/h = 7.0$ for both flows. The velocity profiles predicted using both the *k-l* and *l* models are indistinguishable upstream of the step (shown in Fig. 6 for the step-1 flow).

Predicted and measured values of turbulence kinetic energy for the step-1 flow are compared in Fig. 7. The turbulence kinetic energy is noticeably overpredicted near reattachment but can be seen to be in reasonably good agreement with the measurements elsewhere. The shear-stress is also overpredicted near reattachment, as can be seen in Fig. 8. This trend is characteristic of nearly all turbulence models evaluated by Eaton [4] for step flows.

The present interaction calculation scheme was used with the *k-l* turbulence model to compute flows for values of H/h ranging from 3 to 11. These calculations employed the same upstream flow conditions as used in the experiments of Kim et al. [2]. The predicted reattachment lengths are shown in Fig. 9, along with the available experimental data and the associated uncertainty intervals reported by the investigators [2, 8]. The data of Kim et al. [2] are for the reference and step-1 flows discussed previously. The predictions were made before the data of Driver and Seegmiller [8] et $H/h = 9$ became available. Although the inlet conditions for the Driver-Seegmiller experiment [8] were not identical to those employed by Kim et al. [2], in both cases the turbulent boundary layer was relatively thin at the step. In the Driver-Seegmiller experiment, $\delta_s/h \simeq 1.57$, whereas in the present predictions for $H/h = 9$, using the inlet conditions of Kim et al. [2], $\delta_s/h \simeq 1.21$. In all cases the predictions were within the uncertainty intervals associated with the measurements. The comparison tends to support the validity of the present prediction scheme and the *k-l* turbulence model over a range of step heights ($H/h \cong 3$–9), at least for inlet conditions similar to those reported by Kim et al. [2].

The present interaction scheme is also applicable to symmetric turbulent expansions in which an inviscid core is present. Results are given for a step height to channel inlet height ratio of 0.125 and a Reynolds number based on step height of 9800. The displacement surface (body) for this flow is shown in Fig. 10. The predicted reattachment occurred 4.32 step heights downstream of the step. The displacement surface obtained by a once-through solution of the boundary-layer equations using a total mass flow constraint [9] for fully developed symmetric expansion flow is also shown in the figure. The difference between the two displacement thickness distributions shown in Fig. 10 is a measure of the importance of elliptic effects for this flow. The calculated pressure coefficients are shown in Fig. 11. No accurate detailed profile measurements are available for this flow, but the present prediction for reattachment length was in good agreement with the prediction of Gosman et al. [10] and within the uncertainty interval for the data of Abbott and Kline [11] obtained under similar flow conditions. For this symmetric expansion, the reattachment length was somewhat shorter than the value of 5.85 which would be predicted (see Fig. 9 for $H/h = 10$) for a single step in a channel under similar inlet conditions.

One global iteration of the viscous-inviscid procedure typically required 9.7 seconds of CPU time for a rearward-facing step flow and 5.33 seconds for a symmetric channel expansion flow on an NAS AS/6 computer. Typically, 130 grid

points were used across each viscous layer and the interaction zone was divided into 104 streamwise increments for the inverse boundary-layer solution procedure. A 51 × 51 grid was used for the inviscid solution. The convergence rate was found to be dependent upon step height, the rate being faster for small step heights. The solution to the reference flow converged to $\epsilon = 0.0125$ [see equation (19) of Part 1] in 45 iterations using a relaxation factor of 0.1. The solution to the step-1 flow required 35 iterations to obtain $\epsilon = 0.0185$ using a relaxation factor of 0.2, while for the symmetric expansion flow, convergence to $\epsilon = 0.00095$ was achieved in 17 iterations using a relaxation factor of 0.5.

Conclusions

The viscous-inviscid interaction procedure employed in this study appears to provide a reasonable basis for the prediction of turbulent flows over a rearward-facing step. Although only a limited number of turbulence models were considered in this study, none of these appeared capable of accurately predicting the flow in the separated and reattaching regions without modifications which took into account geometric parameters characteristic of the step flow. The l and k-l models which made use of such characteristic parameters were seen to provide reasonably accurate predictions of mean flow parameters, including the reattachment length, for the turbulent step flows considered in this paper. Turbulence kinetic energy and shear stress were overpredicted near reattachment.

The interaction procedure also appears applicable to symmetric expansions. Less detailed experimental data are available for symmetric expansions containing inviscid flow regions, but in the case considered, the predicted reattachment length was found to be in agreement with measurements and the reattachment length predicted by another numerical scheme.

Acknowledgments

This material is based upon work supported by the National Science Foundation under Grants ENG-7812901 an MEA-8211713.

References

1 Kwon, O. K., and Pletcher, R. H., "A Viscous-Inviscid Interaction Procedure—Part 1: Method for Computing Two-Dimensional Incompressible Separated Channel Flows," ASME JOURNAL OF FLUIDS ENGINEERING, published in this issue pp. 64–70.

2 LeBalleur, J. C., and Mirande, J., "Experimental and Theoretical Study of Two-Dimensional Turbulent, Incompressible Reattachment," AGARD Conference Proceedings, No. 168, 1975, pp. 17.1–17.13.

3 Kim, J., Kline, S. J., and Johnston, J. P., "Investigation of Separation and Reattachment of Turbulent Shear Layer: Flow Over a Backward-Facing Step," Thermosciences Division, Mechanical Engineering Department, Stanford University, Report MD-37, 1978.

4 Eaton, J. K., and Johnston, J. P., "Backward-Facing Step Flow," 1980–1981 AFOSR-HTTM-STANFORD Conference on Complex Turbulent Flows: Comparison of Computation and Experiment, Mechanical Engineering Department, Stanford University, Vol. 1, 1982, pp. 275–286.

5 Eaton, J. K., "Incompressible Separated Flows—Internal Flows," 1980–1981 AFOSR-HTTM-STANFORD Conference on Complex Turbulent Flows: Comparison of Computation and Experiment, Mechanical Engineering Department, Stanford University, Vol. 2, 1982, pp. 886–904.

6 Pletcher, R. H., "Prediction of Incompressible Turbulent Separating Flow," ASME JOURNAL OF FLUIDS ENGINEERING, Vol. 100, 1978, pp. 427–433.

7 Kown, O. K., and Pletcher, R. H., "Prediction of the Incompressible Flow Over a Rearward-Facing Step," Technical Report HTL-26, CFD-4, ISU-ERI-Ames-82019, Engineering Research Institute, Iowa State University, 1981.

8 Driver, D. M., and Seegmiller, H. L., "Features of a Reattaching Turbulent Shear Layer Subject to an Adverse Pressure Gradient," AIAA Paper No. 82-1029, 1982.

9 Kwon, O. K., Pletcher, R. H., and Lewis, J. P., "Prediction of Sudden Expansion Flow Using the Boundary-Layer Equations," ASME JOURNAL OF FLUIDS ENGINEERING, Vol. 106, 1984, pp. 285–291.

10 Gosman, A. D., Khail, E. E., and Whitelaw, J. H., "The Calculation of Two-Dimensional Turbulent Recirculating Flows," *Proceedings of the Symposium on Turbulent Shear Flows*, Pennsylvania State University, 1977.

11 Abbott, D. E., and Kline, S. J., "Experimental Investigations of Subsonic Turbulent Flow over Single and Double Backward-Facing Steps," ASME *Journal of Basic Engineering*, Vol. 84, 1962, pp 317–325.

Computation of Gas Flowfields in Supersonic Particle Probes

L. J. Forney
School of Chemical Engineering,
Georgia Institute of Technology,
Atlanta, Ga. 30332

W. K. McGregor

D. B. Van Dyke

Sverdrup Technology, Incorporated,
Arnold AFS, Tenn. 37389

The results of computations to predict the properties of gas flowfields in supersonic particle probe inlets are presented. In particular, a supersonic gas impinging on a thin walled cylindrical probe aligned parallel to the freestream has been analyzed. Inviscid solutions are obtained by a slight variant to MacCormack's time-dependent finite difference method. Imposing outflow boundary conditions of fixed static pressure at the probe outlet, linear extrapolation of remaining gas properties, and a reflection technique on the probe wall including the tip, reasonable agreement is demonstrated for the shock detachment distance, stagnation pressure loss and gas ingestion rate. With some spacial smoothing and initial conditions characteristic of gas properties back of the shock, the numerical method converged in reasonable computation times, yielding a shock thickness of 2.5 grid spacings with no oscillations near the shock front.

1 Introduction

Liquid and solid particles are formed in combustion processes. Initially small submicron particles are formed by condensation of super-saturated vapor which may coagulate into larger liquid or solid particles. The knowledge of size distribution and chemical composition of combustion produced particles is important from the standpoint of system performance and reliable measurement techniques are necessary to evaluate these particle parameters.

Large concentrations of particles or their incandescence (e.g., conditions typical of solid propellant rocket exhausts) may preclude the use of nonintrusive optical methods to determine particle size distributions. In these cases, the insertion of a particle probe directly into the particle laden stream is necessary to extract a representative sample. Problems, however, are encountered when attempting to sample particles from the high speed exhaust plumes of solid propellant rocket motors, jet engines and some wind tunnels. In this case the gas flowfield around the probe inlet becomes complex particularly when the ambient flow is supersonic [1-3].

Probe designs for use in intrusive particle extraction within the exhaust plumes of solid propellant rocket motors must also be of rugged construction to withstand the high velocity and temperature environment. The dimension of test facilities may also prohibit the use of short sample lines. Thus, isokinetic sampling may be difficult to achieve and a condition of "choked flow" will exist in the sample probe. If the flow is choked, intrusive sampling from a supersonic stream will produce a detached shock in front of the particle collection probe. This shock front creates a velocity difference between the freestream and the gas entering the sampling probe, and a size-dependent preferential withdrawal of particles may take place [1].

The ideal cylindrical probe of Fig. 1 has many of the characteristics of external shock probes in general and allows the use of a relatively simple cylindrical grid system. The analysis of the simple cylindrical probe should provide insight into the sensitivity of various operating parameters and hence, aid in future probe design. The results presented here, however, are not expected to be directly applicable to any but the simplest of cylindrical particle collection probes.

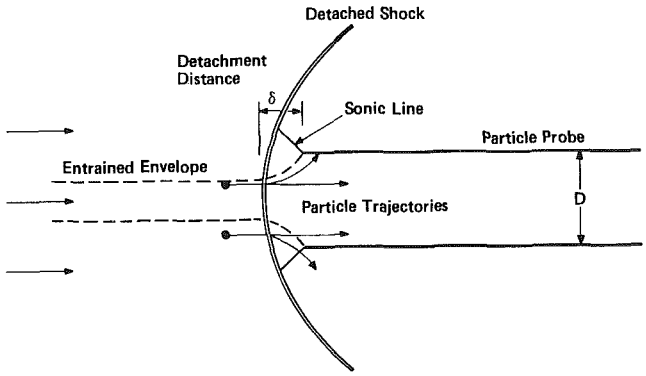

Fig. 1 Schematic of particle probe in supersonic stream

Since the gas Reynolds number based on the probe diameter for the geometry of Fig. 1 is sufficiently large ($\sim 10^4$) so that the boundary layers are very thin relative to the probe dimensions, it is permissible to approximate the flowfield near the probe inlet as an inviscid one [1]. The properties of the flowfield for this geometry are thus determined by the freestream Mach number M, the ratio of specific heats γ and the ratio of mass flowrate ingested to that geometrically incident on the frontal area of the probe q_s/q_m.

The purpose of the present paper is to document the results of numerical computations that predict the properties of the gas flowfield near the probe inlet including gas streamlines, ingestion rate and shock position. These results will be used in future work to determine the particle collection efficiencies for various probe designs.

Contributed by the Fluids Engineering Division for publication in the JOURNAL OF FLUIDS ENGINEERING. Manuscript received by the Fluids Engineering Division, October 18, 1984.

2 Numerical Methods

2.1 Conservation Expressions. The Euler equations for a two-dimensional, inviscid, flow of a perfect gas were solved. Steady-state solutions to the conservation expressions were obtained as asymptotic solutions for large times using a slight variant to the two-step time dependent method of MacCormack [4]. Normalizing the variables with respect to the probe radius r_0, freestream gas velocity u_1 and density ρ_1 such that

$$\tilde{\rho}=\rho/\rho_1,\ \tilde{u}=u/u_1,\ \tilde{v}=v/u_1,\quad \tilde{T}=\frac{RT}{u_1^2},$$

$$\tilde{t}=tu_1/r_0,\quad \tilde{r}=r/r_0$$

and $\tilde{x}=x/r_0$, the conservation expressions for an axisymmetric flow become:

$$\frac{\partial e}{\partial \tilde{t}}+\frac{\partial f(e)}{\partial \tilde{x}}+\frac{\partial g(e)}{\partial \tilde{r}}+\frac{h(e)}{\tilde{r}}=0 \tag{1}$$

where

$$e=\begin{Bmatrix}\tilde{\rho}\\ m\\ n\\ q\end{Bmatrix},\quad f(e)=\begin{Bmatrix}m\\ m^2/\tilde{\rho}+\tilde{\rho}\tilde{T}\\ mn/\tilde{\rho}\\ (q+\tilde{\rho}\tilde{T})(m/\tilde{\rho})\end{Bmatrix},$$

$$g(e)=\begin{Bmatrix}n\\ mn/\tilde{\rho}\\ n^2/\tilde{\rho}+\tilde{\rho}\tilde{T}\\ (q+\tilde{\rho}\tilde{T})(n/\tilde{\rho})\end{Bmatrix},\quad h(e)=\begin{Bmatrix}n\\ mn/\tilde{\rho}\\ n^2/\tilde{\rho}\\ (q+\tilde{\rho}\tilde{T})(n/\tilde{\rho})\end{Bmatrix}$$

and

$$m=\tilde{\rho}\tilde{u}$$
$$n=\tilde{\rho}\tilde{v}$$
$$q=\tilde{\rho}\left(\frac{\tilde{T}}{\gamma-1}+\frac{\tilde{u}^2+\tilde{v}^2}{2}\right).$$

In the present study the two-step finite difference scheme and boundary conditions adapted by Shina et al. [5] were employed with the following changes. A full time step was used for each step with forward differencing on the first and backward on the second. The term representing artificial viscosity was found to be unnecessary, however, but a spacial smoothing term e^* on the first time step was retained. The final result represents a slight variation to what is called MacCormack's method [4]. It should be noted that the numerical smoothing term e^* defined below may closely parallel the effects of artificial viscosity.

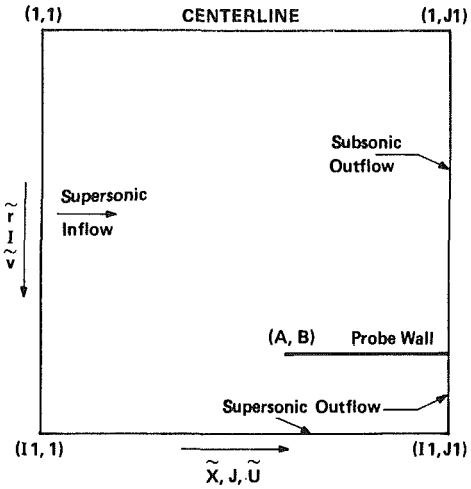

Fig. 2 Computational grid

Thus, the finite difference representation to equation (1) is

$$e'(\tilde{x},\tilde{r},\tilde{t}+\Delta\tilde{t})=e^*(\tilde{x},\tilde{r},\tilde{t})-\frac{\Delta\tilde{t}}{\Delta\tilde{x}}[f(\tilde{x}+\Delta\tilde{x},\tilde{r},\tilde{t})$$

$$-f(\tilde{x},\tilde{r},\tilde{t})]-\frac{\Delta\tilde{t}}{\Delta\tilde{r}}[g(\tilde{x},\tilde{r}+\Delta\tilde{r},\tilde{t})-g(\tilde{x},\tilde{r},\tilde{t})]$$

$$-\Delta\tilde{t}\frac{h(\tilde{x},\tilde{r},\tilde{t})}{\tilde{r}} \tag{2a}$$

and

$$e(\tilde{x},\tilde{r},\tilde{t}+\Delta\tilde{t})=\frac{1}{2}\{e(\tilde{x},\tilde{r},\tilde{t})+e'(\tilde{x},\tilde{r},\tilde{t}+\Delta\tilde{t})$$

Nomenclature

A = value of integer variable I at probe leading edge
B = value of integer variable J at probe leading edge
D = probe diameter (cm)
e = dimensionless density, momentum or energy
f = dimensionless axial flux of mass, momentum or energy
f_1 = ratio of stagnation pressures across shock
f_2 = ratio of stagnation pressure to static pressure upstream of shock
f_3 = ratio of temperatures across shock
g = dimensionless radial flux of mass, momentum or energy
h = dimensionless flux of mass, momentum or energy
I = integer variable in radial direction
$I1$ = maximum value of integer variable I
J = integer variable in axial direction
$J1$ = maximum value of integer variable J
M = gas Mach number
m = dimensionless mass flux in axial direction
n = dimensionless mass flux in radial direction
N = integer number of mesh points
P = static gas pressure (dynes-cm^{-2})
P_{0_1} = stagnation pressure upstream of shock (dynes-cm^{-2})
P_{0_2} = stagnation pressure downstream of shock (dynes-cm^{-2})
q = dimensionless energy
q_m = mass flow rate in mainstream in probe area (gm-s^{-1})
q_s = mass flow rate in probe sample line (gm-s^{-1})
r = radial coordinate (cm)
r_0 = probe radius (cm)
R = specific gas constant (cm^2-s^{-2}-K^{-1})
t = time
T = temperature (°K)
u = axial velocity (cm-s^{-1})
u_1 = axial velocity ahead of shock (cm-s^{-1})
v = radial velocity (cm-s^{-1})
x = axial coordinate (cm)
ρ = gas density (gm-cm^{-3})
ρ_1 = gas density ahead of shock (gm-cm^{-3})
γ = ratio of specific heats
α = ratio of static pressure at probe outlet to stagnation pressure
$\alpha_{\min}$ = minimum value of probe static pressure for maximum ingestion rate
ψ = stream function
δ = shock detachment distance (cm)

$$-\frac{\Delta\tilde{t}}{\Delta\tilde{x}}[f'(\tilde{x},\tilde{r},\tilde{t})-f'(\tilde{x}-\Delta\tilde{x},\tilde{r},\tilde{t})]$$

$$-\frac{\Delta\tilde{t}}{\Delta\tilde{x}}[g'(\tilde{x},\tilde{r},\tilde{t})-g'(\tilde{x},\tilde{r}-\Delta\tilde{r},\tilde{t})]$$

$$-\Delta\tilde{t}\frac{h'(\tilde{x},\tilde{r},\tilde{t})}{\tilde{r}}\Bigg\} \tag{2b}$$

where

$$f'(\tilde{x},\tilde{r},\tilde{t})=f(e'(\tilde{x},\tilde{r},\tilde{t}))$$

and

$$e^*(\tilde{x},\tilde{r},\tilde{t})=\frac{1}{4}[e(\tilde{x}+\Delta\tilde{x},\tilde{r},\tilde{t})+e(\tilde{x}-\Delta\tilde{x},\tilde{r},\tilde{t})$$
$$+e(\tilde{x},\tilde{r}+\Delta\tilde{r},\tilde{t})+e(\tilde{x},\tilde{r}-\Delta\tilde{r},\tilde{t})].$$

2.2 Computational Grid. For numerical calculations, the dimensions of the computational domain are $0\le\tilde{r}\le 1.25$, $0\le\tilde{x}\le 1.25$ with $\Delta\tilde{x}=\Delta\tilde{r}=1./(4N)$ and $N=10$. Although the numerical algorithm could be adjusted to arbitrary dimensions, the results were calculated with a square grid with 51 mesh points on a side. The computational grid used in the present paper is illustrated below. The probe wall located in Fig. 2 is aligned parallel to the centerline and its position is fixed by the leading edge located A-1 grid spaces below the centerline and B-1 spaces to the right where A-1 and B-1 are multiples of N.

2.3 Boundary Conditions:

2.3.1 Inflow and Outflow Conditions. The conditions imposed on the inflow, outflow and wall boundaries are discussed below.

supersonic inflow:

$$\begin{aligned}\tilde{\rho}&=1. & 0\le\tilde{r}\le 1.25\\ \tilde{u}&=1. & \tilde{x}=0.\\ \tilde{v}&=0. & \tilde{t}\ge 0.\\ \tilde{T}&=1./(\gamma M^2)\end{aligned}$$

subsonic outflow:

$$\tilde{T}=\frac{\alpha\tilde{P}_{0_2}}{\tilde{\rho}} \qquad \begin{aligned}&0\le\tilde{r}\le 1.0\\ &\tilde{x}=1.25\\ &\tilde{t}\ge 0.\end{aligned} \tag{3}$$

for $\alpha\le 1$, where $\tilde{P}_{0_2}$ is the normalized stagnation pressure back of the shock front. This fixes the static pressure on the subsonic outflow within the probe. The value of $\tilde{P}_{0_2}$ in equation (3) can be written in the form [6]

$$\tilde{P}_{0_2}=\left(\frac{\tilde{P}_{0_2}}{\tilde{P}_{0_1}}\right)\left(\frac{\tilde{P}_{0_1}}{\tilde{P}(\tilde{x}=0)}\right)\tilde{P}(\tilde{x}=0)$$

or

$$\tilde{P}_{0_2}=f_1(M)f_2(M)\tilde{P}(\tilde{x}=0)$$

where

$$\tilde{P}(\tilde{x}=0)=1/(\gamma M^2)$$

$$f_1(M)=\left(1+\left(\frac{2\gamma}{\gamma+1}\right)(M^2-1)\right)^{-\frac{1}{\gamma-1}}\left(\frac{(\gamma+1)M^2}{[(\gamma-1)M^2+2]}\right)^{\frac{\gamma}{\gamma-1}}$$

and

$$f_2(M)=\left[1+\left(\frac{\gamma-1}{2}\right)M^2\right]^{\frac{\gamma}{\gamma-1}}$$

centerline:

$$\begin{aligned}\partial\tilde{\rho}/\partial\tilde{r}&=0. & \tilde{r}&=0.\\ \partial\tilde{u}/\partial\tilde{r}&=0. & 0\le\tilde{x}&\le 1.25\\ \tilde{v}&=0. & \tilde{t}&\ge 0.\\ \partial\tilde{T}/\partial\tilde{r}&=0.\end{aligned}$$

probe wall (upper and lower surfaces):

$$\begin{aligned}\partial\tilde{\rho}/\partial\tilde{r}&=0. & \tilde{r}&=\tilde{r}_p\\ \partial\tilde{u}/\partial\tilde{r}&=0. & \tilde{x}_p&\le\tilde{x}\le 1.25\\ \tilde{v}&=0. & \tilde{t}&\ge 0.\\ \partial\tilde{T}/\partial\tilde{r}&=0.\end{aligned}$$

The values of $\tilde{x}_p$ and $\tilde{r}_p$ above designate the leading edge of the probe tip. The boundary conditions on the probe wall represent the reflection technique [5]. The reflection technique was also applied in a simple manner to the probe tip. This implies that numerically at the leading edge of the probe:

$$\tilde{\rho}(\tilde{x}_p-\tilde{\Delta}x,\tilde{r}_p,\tilde{t})=\tilde{\rho}(\tilde{x}_p,\tilde{r}_p,\tilde{t})$$
$$\tilde{u}(\tilde{x}_p,\tilde{r}_p,\tilde{t})=0.$$
$$\tilde{v}(\tilde{x}_p-\Delta\tilde{x},\tilde{r}_p,\tilde{t})=\tilde{v}(\tilde{x}_p,\tilde{r}_p,\tilde{t})$$
$$\tilde{T}(\tilde{x}_p-\Delta\tilde{x},\tilde{r}_p,\tilde{t})=\tilde{T}(\tilde{x}_p,\tilde{r}_p,\tilde{t}).$$

It should be noted that these boundary conditions create an apparent thickness to the probe wall of approximately one grid spacing $\Delta\tilde{r}$. This is not a problem, however, since the uncertainty in wall thickness is less than the shock thickness imposed by the finite difference scheme. The boundary condition on the probe tip was the only one of a number of averaging schemes that provided a stable solution.

The remaining gas properties on the subsonic and supersonic outflows are determined by linear extrapolation from two adjacent interior grid points. For example.

$$\tilde{p}(\tilde{x},\tilde{r},\tilde{t})=2\tilde{\rho}(\tilde{x}-\Delta\tilde{x},\tilde{r},\tilde{t})-\tilde{\rho}(\tilde{x}-2\Delta\tilde{x},\tilde{r},\tilde{t})$$

2.3.2 Initial Conditions. Initial conditions were imposed on all interior grid points. Values of gas properties were chosen that were characteristic of conditions in the subsonic region back of the shock.

$$\tilde{\rho}=1.0$$
$$\tilde{u}=1.0$$
$$\tilde{v}=0.$$
$$\tilde{T}=(1./\gamma M^2)f_3(M)$$

where

$$f_3(M)=1+\frac{2(\gamma-1)}{(\gamma+1)^2}\left(\frac{\gamma M^2+1)}{M^2}\right)(M^2-1)$$

represents the ratio of temperatures across the shock. Values of the density listed above were chosen to be smaller than expected back of the shock front which was found to increase the rate of convergence.

2.3.3 Time Step. The time step was established according to the Courant, Friedrichs and Lewy [7] criteria where

$$\Delta t=\min\left\{c\frac{\Delta x}{|u+a|},\ c\frac{\Delta r}{|v+a|}\right\}$$

and $0\le c\le 1$. In the present work the discussion is restricted to the x coordinate. Normalizing Δt with r_0/u_1 and the local value of the gas velocity with u_1, one obtains

$$\frac{\Delta\tilde{t}}{\Delta\tilde{x}}=\frac{cu_1}{u+a}=\frac{c\left(\frac{u_1}{a_1}\right)\left(\frac{a_1}{a}\right)}{\frac{u}{a}+1}.$$

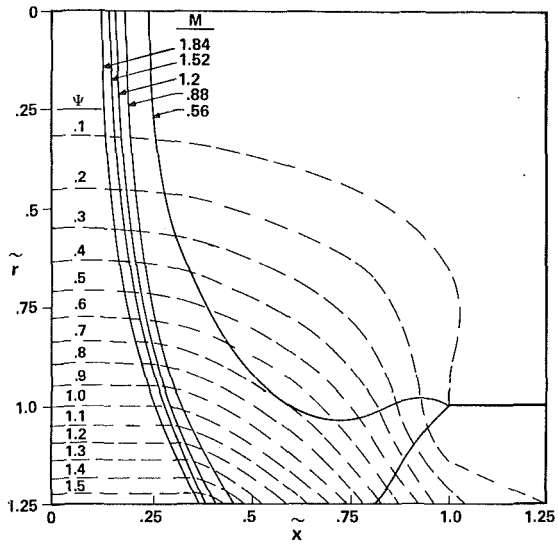

Fig. 3 Computed flowfields; M = 2, $\gamma = 1.4$ and $\alpha = 0.95$. Solid lines are lines of constant Mach number. Dashed lines are streamlines.

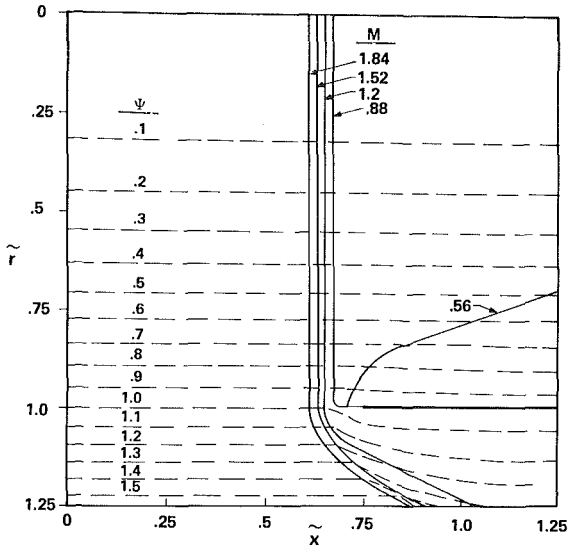

Fig. 5 Computed flowfield; M = 2, $\gamma = 1.4$ and $\alpha = 0.8$. Solid lines are lines of constant Mach number. Dashed lines are streamlines.

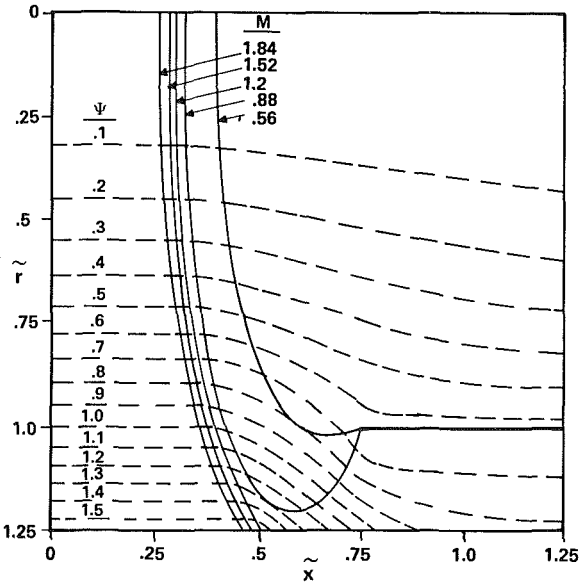

Fig. 4 Computed flowfield; M = 2, $\gamma = 1.4$ and $\alpha = 0.9$. Solid lines are lines of constant Mach number. Dashed lines are streamlines.

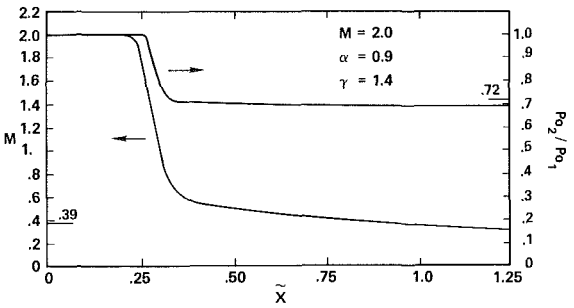

Fig. 6 Gas Mach number and stagnation pressure distribution on axis of symmetry

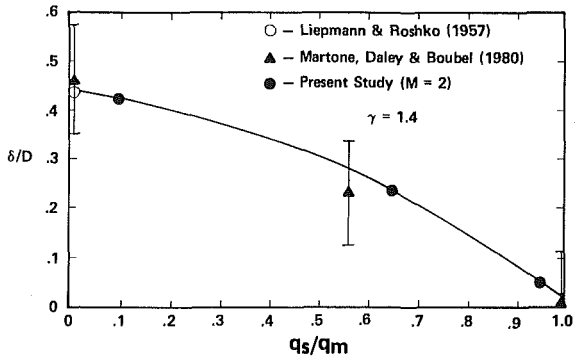

Fig. 7 Shock detachment distance as a function of mass flowrate in probe for M = 2. Data of Martone et al. are estimated for M = 1.47.

where M_1, T_1 designate gas properties ahead of the shock. Denoting gas properties back of the shock as M_2 and T_2, one can show for both sides of the shock front

$$\frac{M_1}{M_1+1} < \frac{M_1}{M_2+1}\left(\frac{T_1}{T_2}\right)^{1/2}.$$

Therefore, a value of the time step was chosen in the present study such that

$$\frac{\Delta \tilde{t}}{\Delta \tilde{x}} = c\left(\frac{M_1}{M_1+1}\right)$$

where $.45 < c < .75$. Here, the smaller values were necessary for smaller probe ingestion rates.

3 Results

3.1 Flowfields. Several numerical solutions were sought for the probe inlet flowfield. For a fixed value of the freestream Mach number M = 2, several values of the probe outlet static pressure were chosen corresponding to values of $\alpha = 0.95$, 0.9, and 0.8. The streamlines and lines of constant Mach number for each of these cases are illustrated in Figs. 3-5. In all three cases 2400 iterations were made corresponding to a computation time of $t \sim 36 r_0/u_1$. This is approximately twice the computation time recommended for convergence to a steady-state solution [5]. In the present computations the flowfield was nearly convergent in a computation time of $t \sim 20\, r_0/u_1$, but some oscillations were still present in the third significant figure for gas properties near the center of the probe inlet.

Since a condition of equal static and stagnation pressures at the probe outlet ($\alpha = 1.$) corresponds to a case of no flow within the probe or $q_s/q_m = 0.$, the shock detachment distance in Fig. 3 for $\alpha = 0.95$ is nearly equal to that for a solid body of revolution as discussed in Sec. 3.2 below. Decreasing the pressure or reducing α as shown in Figs. 4 and 5 shifts the

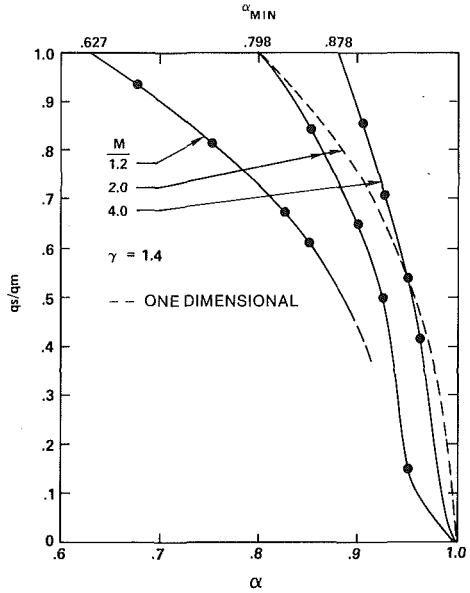

Fig. 8 Probe mass flowrate as a function of the static pressure at probe outlet

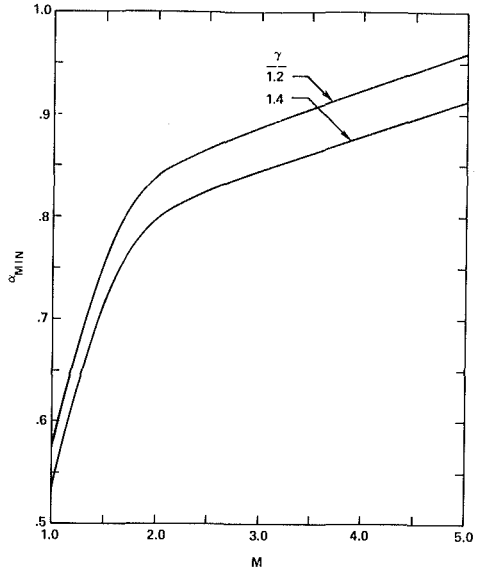

Fig. 9 Ratio of static to stagnation pressure for maximum probe ingestion rates

shock front closer to the probe. In addition, there is a larger mass flux into the probe inlet with decreasing back pressure and the streamlines demonstrate less curvature for smaller α.

3.2 Shock Detachment Distance. The distance from the shock front to the entrance plane of the particle probe was determined from Figs. 3–5. Since the shock thickness in these types of calculations is scaled by the grid spacing, the midpoint of the shock front was determined as that point for which the value of the Mach number is midway between its expected values immediately ahead and behind the shock.

A plot of the magnitude of the gas Mach number on the axis of symmetry ($\bar{r}=0$) of the flowfield for Fig. 4 is shown in Fig. 6 for the indicated conditions. In this case the shock thickness is approximately 2.5 grid spaces and the center of the shock is that point for which $M=1.42$. Also plotted in Fig. 6 is the stagnation pressure distribution on the probe axis. The indicated limit of $P_{0_2}/P_{0_1}=.72$ corresponds to the theoretical value for the stagnation pressure loss across a normal shock of $M=2$. The theoretical limit in the local gas Mach number of .39 shown on Fig. 6 is predicted for a pressure ratio $\alpha=.9$.

A plot of the normalized shock detachment distance δ/D is shown in Fig. 7. Also included in Fig. 7 are data for the detachment distance corresponding to a solid body of revolution and estimates of δ/D from the photographs of Martone, Daley, and Boubel [8]. These data suggest that the present calculations predict large scale features of the flowfield correctly.

3.3 Probe Mass Flowrates. A natural constraint in the use of particle probes with long sample lines is the mass flowrate. Provided the back pressure on the sample line is sufficiently low, the mass flowrate in the probe is determined by the probe inlet pressure, heat transfer and friction losses within the line.

Figure 8 represents the ratio of the probe inlet mass flowrate to the freestream value incident on the probe frontal area q_s/q_m as a function of the pressure ratio $\alpha=P/P_{0_2}$ at the probe outlet of the computational grid. The stream function and q_s/q_m were established by using the trapezoidal rule to integrate the mass flowrate per unit area across the probe exit. Thus the ingestion rate of the probe becomes

$$q_s/q_m = 2\int_0^1 \rho(\bar{x},\bar{r})u(\bar{x},\bar{r})\bar{r}d\bar{r}.$$

The results of numerical computations are presented in Fig. 8 for three Mach numbers. The upper limit of $q_s/q_m \to 1.0$ or the minimum in α represents the maximum ingestion rate for the probe for each Mach number. These limits are predicted by matching the static pressure within the probe with the pressure back of the shock for each Mach number or

$$\alpha_{\min} = P_2/P_{0_2}$$

where P_2 is the static pressure back of the shock now located at the probe entrance. Values for $\alpha_{\min}$ are plotted in Fig. 9 for two values of the ratio of specific heats.

Also shown for comparison on Fig. 8 are the one-dimensional calculations for $M=2$. Since one-dimensional calculations ignore the shock curvature which becomes more pronounced in the limit $q_s/q_m \to 0$, the one-dimensional results do not correlate the present calculations very well for small q_s/q_m.

3.4 Numerical Error. The present numerical code yielded a shock thickness of ~2.5 grid spacings. This represents 3.1 percent of the probe diameter since $\Delta\bar{x}=\Delta\bar{r}=.025$. The use of the reflection technique on the probe walls, although simple to implement and numerically stable, produced an uncertainty in the wall thickness of one radical grid spacing $\Delta\bar{r}$. This reduced the apparent probe diameter by 1.2 percent from the thin wall assumption. These values represent uncertainty in streamline position. In addition, MacCormack's method is 2nd order accurate in the grid spacing or the truncation error is $<<1$ percent for the present problem.

The numerical computation of stagnation pressure back of the bow shock and within the probe was 4.5 percent less than the theoretical limit for a normal shock as indicated on the right of Fig. 6. One can show analytically that a 4.5 percent difference in stagnation pressure would yield a 15 percent difference in the local gas Mach number or probe ingestion rate. The latter figure is compatible with the indicated difference in probe ingestion rates between simple one-dimensional calculations and the present numerical results for $M=2$ and $\alpha=.9$ in Fig. 8.

Clearly, as demonstrated in Fig. 8, the present numerical results approach the correct limit in the probe pressure ratio $\alpha_{\min}$ as the shock moves closer to the probe inlet. In other words, when the effects of shock curvature are eliminated the one-dimensional calculations agree well with the present two-dimensional numerical results. Thus, one is lead to believe that the physics of shock curvature is primarily responsible for these discrepancies and not the numerical methods.

3.5 Computation Time. The source code for the finite difference method used in the present study was written in Fortran and occupied approximately 460 lines. The source file was compiled with the IBM professional Fortran language and the compiled version occupied ~150 K bytes of radom access memory. The program was executed on a desktop IBM PC AT computer with an 80287 math co-processor, 512 KB of memory and a 1.2 MB disk drive.

The run time varied between 7 and 17 hrs for each set of boundary conditions on the 51×51 grid with the longer times corresponding to smaller ingestion rates into the probe. This compares with a run time on a large modern CDC 170 mainframe of 30 to 67 mins. It is interesting to note that Shina et al. [5] required 3½ to 7 hr on a 60×90 grid with a CDC 6600 mainframe in 1970 with a two-step Lax-Wendroff technique to analyze an underexpanded jet. Thus, improvements in numerical methods and computer hardware will now allow the accurate numerical treatment of mixed subsonic/supersonic flows economically on some desktop personal computers.

4 Conclusions

The numerical procedure outlined provides stable solutions to the inviscid Euler equations. Using MacCormack's iterative scheme, a reflection technique on the probe walls and tip, and introducing some numerical smoothing on the first time step, it was possible to achieve realistic solutions free of oscillations near the shock front. In the steady-state solutions, the shock thickness is approximately 2.5 grid spaces which represents 3.1 percent of the probe diameter. Using a 51×51 mesh with 40 grid spaces across the radius of the probe inlet, it was possible to run the numerical code on some desktop microcomputers.

Large scale features of the flowfield such as the shock detachment distance, probe ingestion rate and stagnation pressure loss were determined. The data suggest that the present solutions are realistic representations of the gas flowfield and that the results approach simple one-dimensional calculations for probe boundary conditions that reduce shock curvature.

Additional work is now in progress to determine particle collection efficiencies for the straight-walled cylindrical design.

Acknowledgment

The present study was supported by the Air Force Rocket Propulsion Laboratory, Edwards Air Force Base, California. Partial support was also provided by Sverdrup Technology Incorporated, Arnold AFS, Tennessee under subcontract A-84-EL-024. The authors would also like to thank the reviewers of the present manuscript for many helpful comments.

References

1 Forney, L. J., McGregor, W. K., and Girata, P. T. Jr., "Particle Sampling with Supersonic Probes: Similitude and Particle Breakup," AEDC-TR-83-26, Arnold Air Force Station, Tennessee, 1983.

2 Forney, L. J., and McGregor, W. K., "Scaling Laws for Particle Breakup in Nozzle Generated Shocks," *Particulate Science and Technology*, Vol. 4, 1984.

3 Forney, L. J., Walker, A. E., and McGregor, W. K., "Effect of the Basset Term on Particle Relaxation Behind Normal Shock Waves," Final Report AFOSR-83-0182, AFOSR, Bolling Air Force Base, Washington, D.C., 1984.

4 MacCormack, R. W., "The Effect of Viscosity in Hypervelocity Impact Cratering," AIAA Hypervelocity Impact Conference, April 1969, AIAA paper no. 69-354.

5 Shina, R., Zakkay, V., and Erdos, J., "Flowfield Analysis of Plumes of Two-Dimensional Underexpanded Jets by a Time-Dependent Method," *AIAA 9*, 1971, p. 2363.

6 Liepmann, H. W., and Roshko, A., *Elements of Gas Dynamics*, J. Wiley, N.Y. 1957.

7 Courant, Friedrichs, and Lewy, *Math. Ann. 100*, Vol. 32, 1928.

8 Martone, J. A., Daley, P. S., and Boubel, R. W., "Sampling Submicrometer Particles Suspended in Near Sonic and Supersonic Free Jets," *J. APCA 30*, 1980, p. 898.

Mean Flow Characteristics of a Turbulent Offset Jet

J. R. R. Pelfrey

J. A. Liburdy

Thermal Fluids Laboratory,
Mechanical Engineering Department,
Clemson University,
Clemson, SC 29631

A detailed study of the mean flow characteristics of a turbulent offset jet is presented. The flow is characterized by a longitudinal variation of curvature, skewed impingement onto a flat surface, a recirculating region, and the development of a wall jet region. Flow structure is described in the preimpingement, recirculation and impingement regions. An interdependence is shown among the pressure differential across the jet, jet curvature and entrainment. The magnitude of the curvature strain rate is found to be significant and implies that this flow cannot be accurately modelled as a thin shear layer. The jet decay and spread rates are similar to those of a plane jet if appropriate curved coordinates are used. The extent of the impingement region is approximately 20 nozzle widths downstream, in agreement with previous studies.

Introduction

The offset jet consists of several flow complexities which to date preclude a complete analysis. The general flow field is shown in Fig. 1 where the main features and regions of interest are depicted. A plane, incompressible, turbulent air jet is discharged into quiescent ambient surroundings above a plate offset from, and parallel to, the axis of the jet discharge. Entrainment of the fluid below the jet and above the plate causes a reduced pressure in this region forcing the jet to deflect towards the boundary and eventually attach to it. Previous investigators have characterized this flow by the exit Reynolds number (based on the nozzle width and exit velocity) and offset ratio (the height of the nozzle centerline above the plate per nozzle width). Offset jets occur in many engineering applications such as environment discharge, heat exchangers, fluid injection systems, combustion chambers and others.

The most detailed experimental study of offset jets was reported by Sawyer [1 and 2] who followed an earlier work by Bourque and Newman [3]. These studies and others have examined the effect of offset height on the wall pressure distribution and attachment location. Early analyses have assumed a uniform pressure within the recirculation region which leads to a constant radius of curvature of the jet centerline. Measurements by Rajaratnam and Subramanya [4] and Bourque [5] have shown this to be erroneous. Other models have assumed a prescribed variation of curvature, [6] and [8]. Detailed analyses have required assumptions for the jet velocity profile [1, 3, 7, 8, and 9] and entrainment rates [2 and 8]. In general these investigators have assumed conditions to be similar to, or slightly modified from, plane free jets. Several studies have measured the velocity profiles using pitot-static tubes [1, 4, 10 and others] and hot wires [6]. The data on the wall static pressure variation along the offset plate have been used to identify the center of recirculation [10] and the impingement location [11], which have been assumed to coincide with the minimum and maximum pressure locations respectively. For large nozzle Reynolds numbers (generally agreed to be larger than 10^4) the impingement distance becomes solely a function of offset ratio.

Several studies have addressed the downstream development of the wall jet region. Rajaratnam and Subramanya [4] have found that, beyond a developing region, the velocity profiles scale similarly to a classical wall jet with no dependence on offset ratio. This has been confirmed by other investigators [6, 10, and 12]. The wall stress, downstream of impingement, can be scaled in such a way as to eliminate the offset ratio dependence. Rajaratnam and Subramanya [4] show that the appropriate scales are the maximum shear stress and distance from impingement to where the wall shear stress has decayed to one-half of its maximum. The maximum wall shear stress occurs slightly downstream of impingement. In general, the maximum wall shear stress per exit nozzle dynamic pressure decreases with increasing offset ratio. Further details concerning previous investigations have been reported by Pelfrey [12].

The results of the present work provide a detailed description of the mean flow characteristics primarily in the preattachment and impingement regions. Some discussion is provided on the effects of curvature strain rate and impingement on parameters such as the jet spread, decay rate, entrainment, and wall shear stress. These results should aid in the understanding and modelling of curvature and impingement effects in complex jet flows.

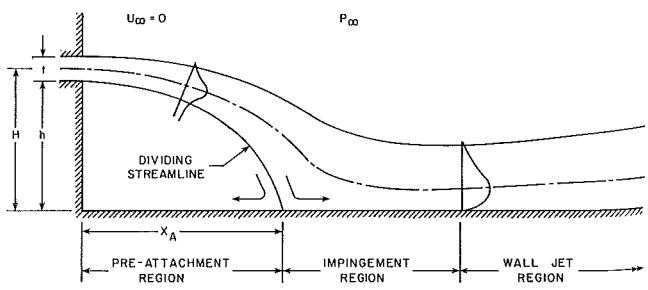

Fig. 1 Offset jet flow geometry

Contributed by the Fluids Engineering Division for publication in the JOURNAL OF FLUIDS ENGINEERING. Manuscript received by the Fluids Engineering Division, February 11, 1985.

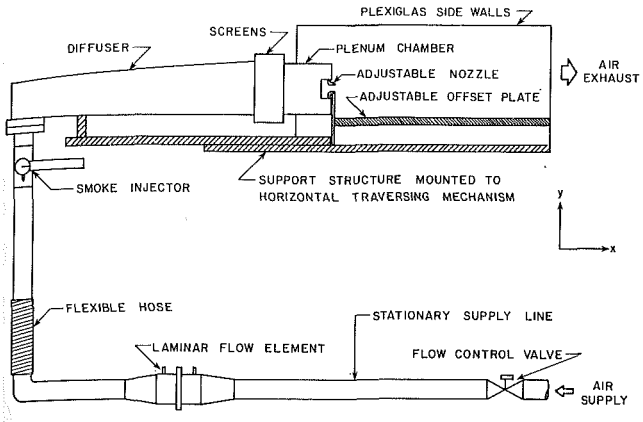

Fig. 2 Schematic of flow arrangement

Experimental Facility

A schematic representation of the flow system is shown in Fig. 2. Oil-free compressed air was supplied by a compressor (4.3 m^3/min at 7.0×10^5 N/m^2) through a series of three surge tanks which were used to throttle the air to the desired pressure and to eliminate any line pressure fluctuations. From the last surge tank the flow was filtered and a flow control valve used to adjust the air flow rate. The flow rate was measured using a laminar flow element which is accurate to ± 0.5 percent over the flow rate range desired. The air then passed through a smoke injector where particles generated by the vaporization of a light oil were entrained into the flow. (Details of the smoke injector operation and its use are given later.) The flow then passed through a 7 deg diffuser opening through a series of five screens before entering the plenum chamber (.15m × .13m × .13m long). The size of the plenum chamber was selected based upon ASME flow standards. An adjustable width, two-dimensional nozzle was at the downstream exit of the plenum chamber. The nozzle width was fixed at 12.5 mm and the span at 150 mm (aspect ratio of 12). The aluminum nozzle was machined according to specifications for ASME flow nozzles with the inner surface finely polished to minimize any flow disturbances.

The flow exiting the nozzle discharged above a horizontal flat copper plate and was contained by two Plexiglas sidewalls, in the flow direction, spaced .15 m apart. The sidewalls began at the entrance to the plenum chamber and continued through the chamber and flow nozzle to the end of the offset plate which was .61 m downstream of the nozzle exit. By using continuous sidewalls through the plenum chamber, nozzle, and discharge section, flow disturbances were kept to a minimum. The offset plate contained 1.5mm OD flush mounted pressure taps used to measure the static pressure distribution. The taps were connected via flexible tubing to a water micromanometer. The uncertainty of the wall pressure distribution was calculated to be ±4 percent. Water manometers were also used to measure the pressure within the plenum chamber and the pressures at the laminar flow element for flow adjustment.

The air flow velocity over the offset plate was measured using a laser Doppler anemometer (LDA), set up in the dual frequency shifted, forward scatter mode. The probe volume was .5 mm × .5 mm at the e^{-2} points by 1.9 mm long. Seed particles were introduced into the flow by means of an injector located in the flow just prior to the diffuser, as shown in Fig. 2. The injector consisted of 1.5mm stainless steel tube coiled around a 300 W cartridge heater. A light oil premixed with a cool air supply was passed through the tubing around the heater where the oil was vaporized and entrained into the air flow stream. The amount of particles injected was controlled by varying the oil flow rate, air flow, and the voltage applied to the heater (i.e., heater temperature). Extensive testing of this technique has led to accurate velocity measurements throughout the flow with validated data rates of at least 50,000 samples per second.

The experimental set-up allowed traversing of the flow field over the entire .61 m of offset plate length in the flow direction and from approximately .15m above the nozzle down to the plate surface. In addition, provision was made for checking the two-dimensionality of the flow at any downstream location and elevation. The LDA system was supported by a steel plate mounted onto horizontal and vertical adjustable supports. The LDA probe volume was positioned to within ±0.5 mm accuracy over the entire flow field.

The LDA data analysis sequence consisted of a fixed fringe mode output of a counter processor recorded on magnetic tape and then analyzed with a PDP 11/03 microcomputer using software we have developed. Velocity data were obtained in a sequence of two runs at a particular test condition. The LDA was used to traverse the field measuring one velocity component; the optics were then rotated and the second velocity component measured.

The use of laser Doppler anemometry has significant advantages over other techniques in many flow situations, see Whitelaw [13]. However, one of the problems still in debate is the mean velocity bias error. This bias is a result of the dependence of the individual realizations, as detected, on the seed velocity. This error can become significant when the turbulence intensity is high, and when the mean velocity is large. In the offset jet flow one would expect the largest bias error to occur in the region of high shear near the dividing streamline and half-width position of the jet.

Nomenclature

E = entrainment parameter
h = distance from the offset plate to the lower nozzle edge
H = distance from the offset plate to the nozzle centerline
J = normalized jet volumetric flow parameter
l = characteristic length
P = static pressure
P_∞ = ambient pressure
Q = jet volumetric flow rate per unit span
R = radius of curvature
t = nozzle width
U = mean velocity component in the x direction
U_o = mean velocity at the nozzle exit
V = mean velocity component in the y direction
$\bar{V}$ = mean velocity vector magnitude
$\bar{V}_{max}$ = maximum mean velocity at a given streamwise position
x = coordinate in the direction of the jet exit velocity measured from the jet exit plane
x_A = distance, along the offset plate, to attachment
y = coordinate normal to the jet exit velocity measured from the offset plate
δ = jet half-width
δ_m = distance from the wall to the maximum velocity position downstream of impingement
ζ = coordinate normal to the maximum velocity vector at a given streamwise position
η = coordinate parallel with the maximum velocity vector at a given streamwise position measured from the jet exit
ρ = fluid density
τ_{max} = maximum wall shear stress downstream of impingement
τ_o = wall shear stress

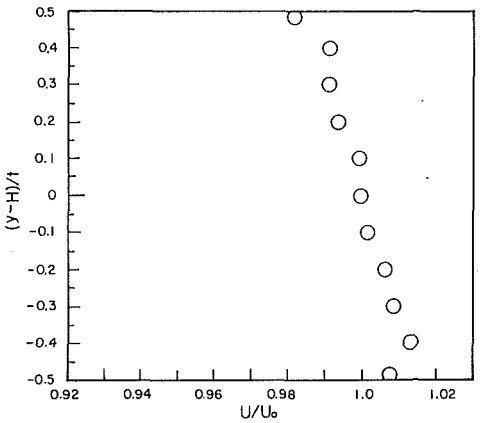

Fig. 3 Nozzle exit velocity profile

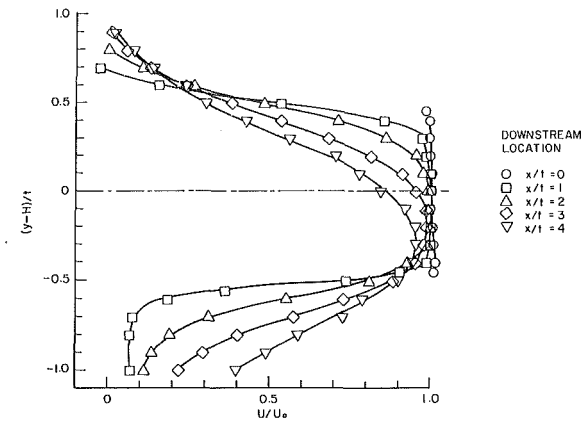

Fig. 4 Jet development profiles

Various techniques have been proposed to correct for this mean velocity bias. We have utilized two techniques which can reduce the bias to an acceptable level. By employing appropriate frequency shifting the bias towards higher velocities can be reduced. Meyers and Clemmons [14] have developed a relationship for a bias correction which addresses the arrival rate of seed particles with frequency shifting. The parameters are the optical system configuration, counter reset time between samples, individual velocity measurement and finge shift velocity. It can be shown that as the individual seed particle velocity increases (assuming the fringe velocity is of the same orientation) the required correction becomes increasingly small. The magnitude of the fringe velocity can be adjusted to reduce the dependence of the correction term on the seed particle velocity. Based on the analysis of Meyers and Clemmons [14], the mean velocity bias correction for our data is less than 1 percent.

The data from the counter was recorded on magnetic tape with a low pass filter of 10 kHz. All the analyses were then performed on the microcomputer which sampled the analog tape signal at a uniform rate. This procedure, along with the optical system and counter settings, assured no significant mean bias error.

Wall shear stress measurements were made with a flattened Preston tube with inside tube dimensions of .28 mm high by .65 mm wide and a .15 mm wall thickness. The tube was calibrated in fully developed pipe flow; the results agree to within ±1 percent of the calibration suggested by Patel [15]. The wall stress data presented here are based on our calibration. The uncertainty of the wall stress distribution was calculated to be ±5 percent. This technique has been used by several investigators in impinging flows but does lose validity near impingement where the velocity and pressure distributions are rapidly changing.

Results

In order to determine the mean flow characteristics two components of the velocity vectors were measured in the entire flow field. In addition, the wall pressure distribution and the wall shear stress (downstream of impingement) were also measured. All data presented are for an offset ratio of seven and nozzle Reynolds number of 15000.

At the nozzle exit the velocity profile was essentially flat. However, a slight skewness was found. Near the lower lip the velocity was slightly greater than in the center of the nozzle; near the upper lip the velocity was slightly lower than in the center of the nozzle. Figure 3 shows, on an exaggerated scale, the nozzle exit velocity profile. This result was reproducable and is similar to the acceleraiton observed by Yi [16] in flow near the edge of a bluff body prior to separation. Nevertheless, the profile was flat within ±1.4 percent over 87 percent of the nozzle width and within ±1.8 percent over 92 percent of the nozzle width. The velocity profile was numerically integrated resulting in a flow rate within 1 percent of the flow rate indicated by the laminar flow element. The exit velocity profile was measured using several different sampling rates (500 to 10,000 Hz) and averaging times (.25 to 4.0 sec.) to determine any low frequency oscillations. Oscillations were not detectable and results were repeatable. The turbulence intensity at the nozzle exit was uniform at 1 percent except very near the nozzle lips.

Figure 4 shows the jet development from the nozzle exit to four nozzle widths (t) downstream. It is obvious that the flow is immediately affected by the recirculation region below the exit. In a study of the near field of a plane turbulent jet, Persen [17] suggests an expression for jet spread in the region beyond the extinction of the potential core but prior to fully developed conditions. Everitt and Robins [18] show the influence of the nozzle aspect ratio on the downstream distance required to achieve fully developed conditions. We have found the length of the potential core to be $4.0t$. This agrees with Persen [17] for a rounded edge orifice but is slightly less than those studies reported by Everitt and Robins [18]. With η the longitudinal jet coordinate and δ the half-width the near field spread suggested by Persen [17] is

$$\frac{(\delta)^2}{(\delta^\circ)^2} = \frac{(\eta - \eta_0)^2}{l^2} + 1 \qquad (1)$$

where δ° is the jet half-width at the end of the potential core, at η_0, and l is a characteristic length dependent on the orifice geometry. Persen found l to be equal to $5.82t$ for a rounded edge orifice. An attempt to correlate the near field data for the offset jet according to equation (1) was unsuccessful. We show later that this near field spread is not appropriate for the offset jet.

The U and V velocity component distributions are shown in Figs. 5 and 6, respectively. Evidence of a secondary recirculation in the lower left corner is seen in each figure. The flow is rotating counterclockwise within a region approximately 1 nozzle width square. Further details of this were not pursued.

The U and V components were combined to determine the mean velocity vectors, as shown in Fig. 7. The center of rotation is seen to occur at seven nozzle widths downstream and two and one-half nozzle widths above the wall. This corresponds to the location of minimum wall pressure, which was measured to be within six and seven nozzle widths downstream. The maximum velocity of the backward flow along the wall was .41 of the nozzle exit velocity. This large velocity is approximately twice that measured in backstep flow recirculation by Etheridge and Kemp [19] for a rearward facing step flow. This would imply a large loss of jet momentum required to drive the recirculating flow.

Superimposed on Fig. 7 are the positions of the dividing streamline, maximum jet velocity and jet half-width. The loca-

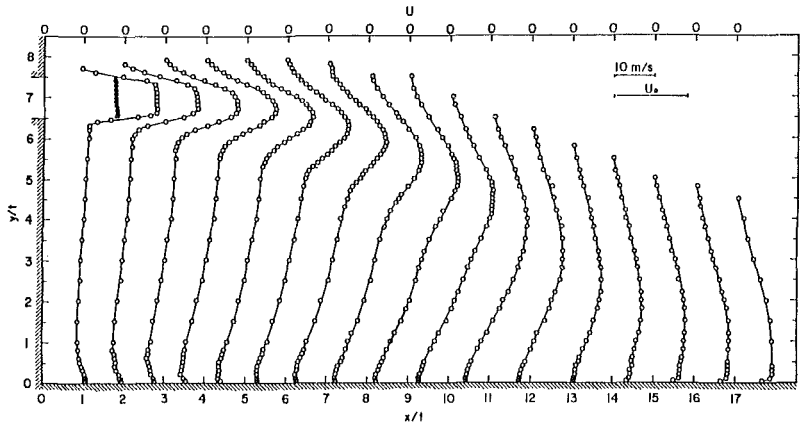

Fig. 5 U component mean velocity profiles

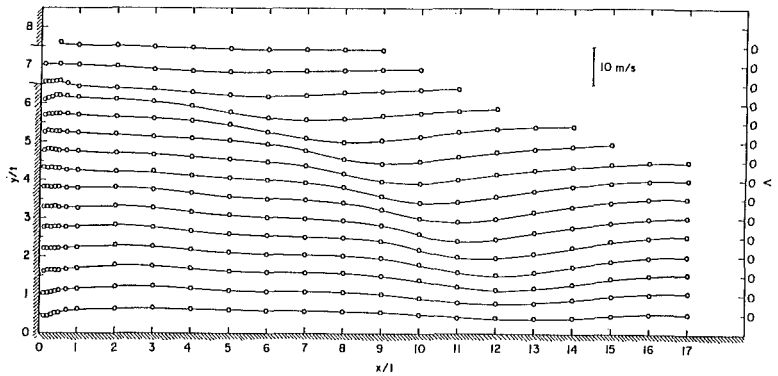

Fig. 6 V. component mean velocity profiles

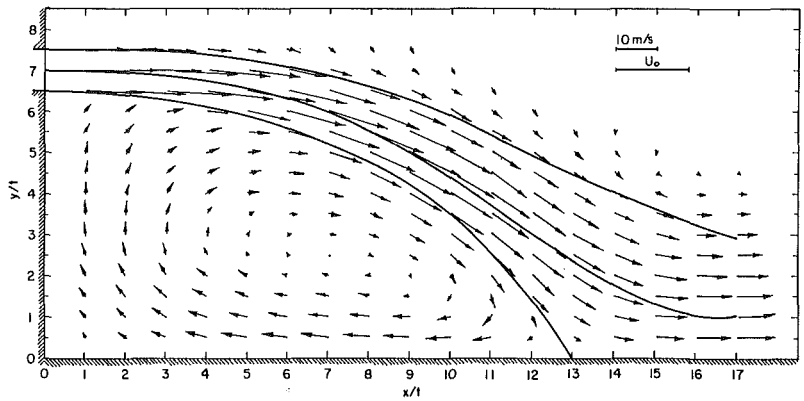

Fig. 7 Mean velocity vectors

tion of the dividing streamline was determined from numerical integration of the velocity profiles at each downstream location. The integration was carried out along a vertical plane from the wall until the mass flux was zero. A fourth order polynomial fit was used to construct the curve shown in Fig. 7 (higher order fits were were less satisfactory). This dividing streamline, on average, separates the primary jet flow from the recirculation region. The position of maximum velocity was determined by interpolation of the velocity vectors at each downstream location and then a fifth order polynomial was used to curve fit the points. This curve then was used to identify a curved coordinate, η, which measures the distance from the nozzle exit along the locus of maximum velocity. This coordinate was then used to find the half-width positions by projecting normal to η toward the outer edge of the jet (ζ direction) until the velocity was one-half the local maximum. These points were found by interpolation.

The maximum velocity decay and spread rates (determined from the half-width variation along the flow direction) are shown in Fig. 8. Also shown are the corresponding slopes for a plane jet. It should be noted that impingement occurs prior to the required distance for fully developed flow in a plane jet. Despite the curvature strain rate it is seen that the curved jet, when using the curved coordinates η and ζ, behaves similarly to the plane jet. Only very near impingement, where there is an increased rate of maximum velocity decay, do deviations from the plane jet occur. Slightly downstream of impingement the maximum velocity rapidly increases as the jet is compressed in the cross stream direction.

For self-preserving flows a local parameter J (defined as the volumetric flow rate per span of flow, Q, normalized by the local maximum velocity times the half-width, $\bar{V}_{\max}\,\delta$) is constant along the flow direction. We have calculated J based on both the volumetric flow above the maximum velocity loca-

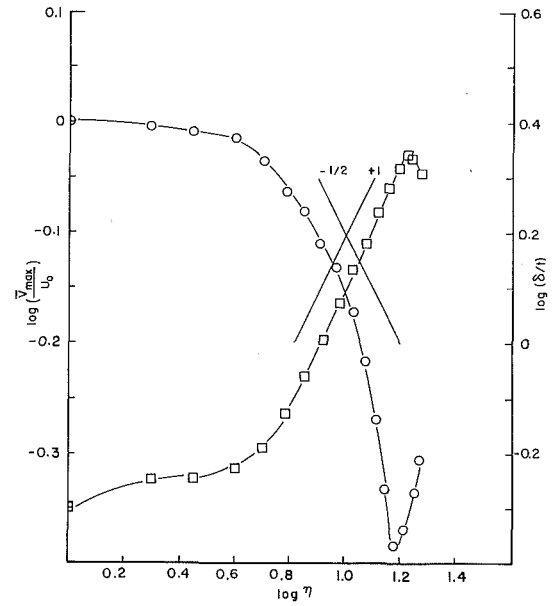

Fig. 8 Maximum velocity decay and upper jet spread

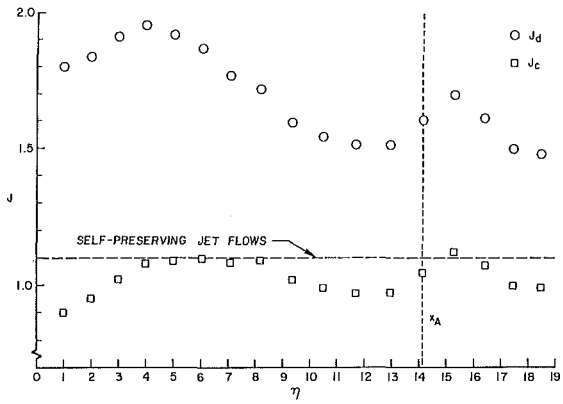

Fig. 9 Nondimensional jet volumetric flow parameter, J

tion, J_c, and the volumetric flow above the dividing streamline, J_d. The downstream variation is shown in Fig. 9 along with the value for developed plane jets. J_c is seen to be identical to the self-preserving plane jet value until $\eta > 8$. As is shown later, for $\eta > 8$ the relative curvature becomes large and results in a reduced local volumetric flow rate.

The entrainment parameter, E, defined as

$$E = \frac{dQ/d\eta}{\bar{V}_{\max}} \tag{2}$$

is shown in Fig. 10 along with fully developed wall jet and plane jet values. For $\eta > 8$ the entrainment parameter is significantly reduced, which is consistent with the decrease in J shown in Fig. 9. The entrainment is seen to approach zero just prior to impingement. This is also where the pressure differential across the jet is approximately zero. (A detailed pressure distribution is shown in Fig. 13.)

Shear flows with streamline curvature experience an additional rate of strain, $\bar{V}/R$, which can either have a stabilizing or destabilizing effect on the turbulence, depending on the sign of the velocity gradient which determines the local shear rate of strain. Such flows can be classified according to the relative magnitude of the curvature-to-shear strain rate ratio, Bradshaw [20]. Figure 11 shows the magnitude of the relative curvature, δ/R where δ is the half-width of the upper side of the jet and R the radius of curvature of the maximum velocity position. In Fig. 12 the curvature strain rate variation is shown

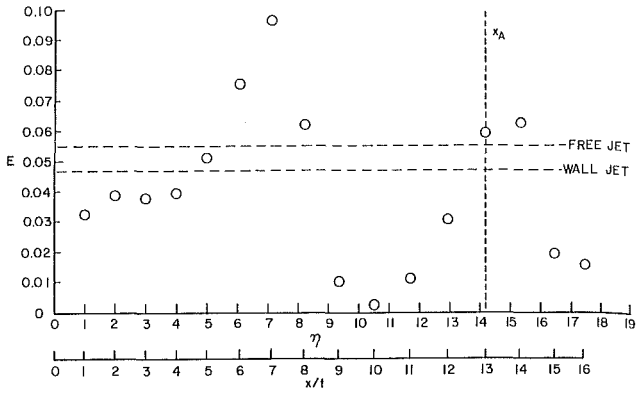

Fig. 10 Entrainment parameter, E

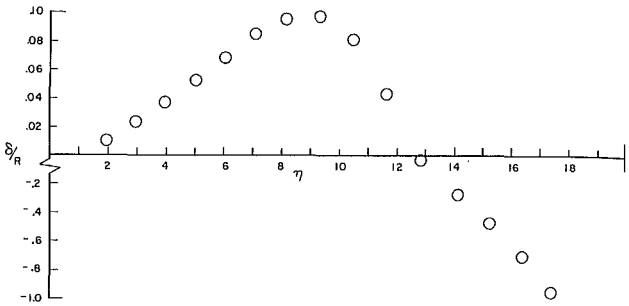

Fig. 11 Jet width to radius of curvature ratio

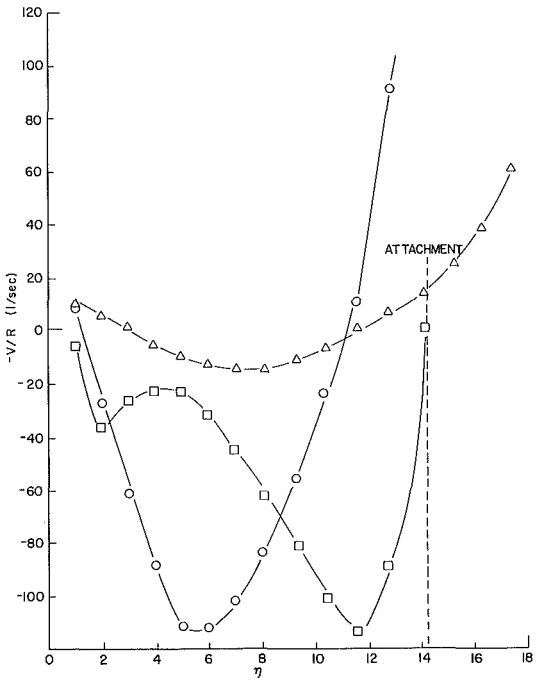

Fig. 12 Curvature strain rate

along the dividing streamline, maximum velocity and half-width positions. This ratio can be interpreted as a ratio of length scales associated with the shear layer and curvature. As this ratio becomes large curvature effects are reduced. It is obvious from Figs. 11 and 12 that (i) the influence of curvature should be a rapidly changing function of position along the jet flow direction and (ii) this flow cannot be treated as a thin shear layer. The effects of curvature on some of the turbulence structure parameters have been reported by Pelfrey and Liburdy [21].

We have used the detailed velocity profiles to estimate the pressure distribution along the dividing streamline. Briefly,

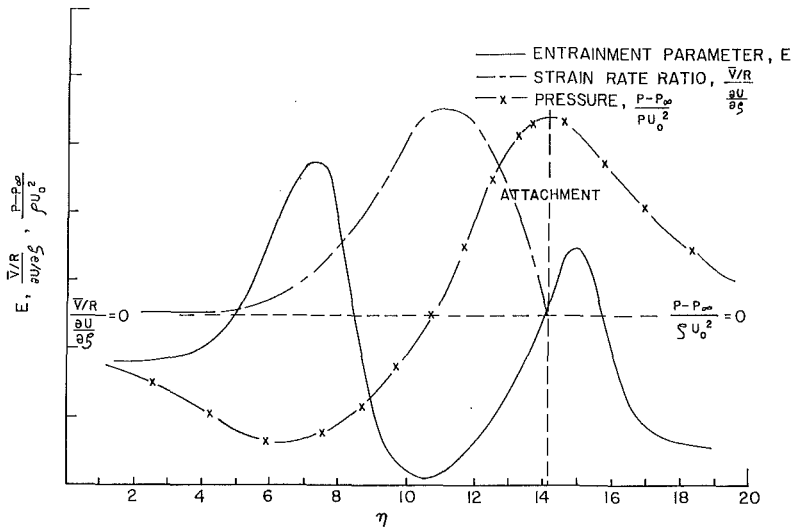

Fig. 13 Entrainment parameter, cross-jet pressure difference, and curvature-to-shear strain rate ratio

the procedure used is as follows. A momentum-force balance was applied to small increments along the flow direction beginning at the nozzle exit. The incremental volumes were defined from the dividing streamline vertically outward beyond the jet. The change of momentum was balanced by the shearing force along the dividing streamline, pressure at the dividing streamline, and jet pressure variation along the flow. Based on these calculations the pressure distribution and the local shear stress along the dividing streamline were determined. Further details of the calculations can be found in [12]. The integrated shearing force, per spanwise distance, along the dividing streamline was found to be $.497(\rho U_0{}^2 x_A)$, where x_A is the distance along the plate to impingement normalized by the nozzle width. This integrated force is within 4 percent of the overall momentum loss determined by using the integrated velocity and pressure profiles at the nozzle exit and the vertical plane at impingement, which is $.519\ (\rho U_0{}^2 x_A)$. This consistency adds validity to the calculated dividing streamline pressure distribution which is discussed below in terms of the pressure differential across the jet.

An analytical study by Williams et al. [22] examined the effects of curvature on the entrainment and the existing pressure distribution of an abrupt separating flow. They assumed a constant eddy viscosity turbulence model to arrive at a similarly solution. Their results show a very slightly decreasing entrainment with increasing pressure difference across the shear layer, while, simultaneously, the curvature increases. We have plotted the downstrem variation of the entrainment parameter, E, normalized pressure differential across the jet, $(P-P_\infty)/\rho U_0{}^2$, and the relative curvature strain rate to shear strain rate, $(-\bar{V}/R)/(\partial U/\partial \zeta)$, along the dividing streamline in Fig. 13. The strain rate ratio can be interpretted as the inverse ratio of curvature to integral time scales. Here, the correlation among pressure differential, entrainment, and relative curvature strain rate is seen. Very slightly downstream of the minimum pressure the curvature strain rate is a maximum which coincides with a peak entrainment. Further downstream, as the pressure difference reverses sign (prior to impingement) the entrainment reaches a minimum (near zero for this case). As the pressure difference reverses sign the entrainment increases reaching a second local maximum at impingement nearly coinciding with the maximum pressure difference. The curvature-to-shear strain rate ratio along the dividing streamline reaches a maximum where the pressure difference is zero and the entrainment rate is a minimum. The strain rate ratio is a rapidly changing function of position with the maximum (.32) representing a significant extra strain rate.

Details near the impingement region of the x component

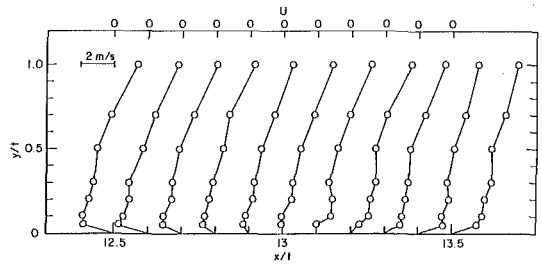

Fig. 14 Detailed velocity profiles near impingement

velocity are shown in Fig. 14 where measurements were made to within 1.2 mm of the wall. The attachment distance along the plate, normalized by the nozzle width, was found to be 13.0 ± 0.05. This position is defined as the point where $(\partial U/\partial y)=0$. This attachment distance is within the uncertainty of previous investigators [3, 4, and 10] who have used other techniques such as tufts, wall pressure measurements, and dye injection.

The characteristics of impingement are significant in determining both the downstream development and the recirculating flow. As the jet flow experiences skewed impingement, the lower shear layer of the jet is separated into forward and reversed flow. We have found that the incipient impingement causes a low pass filtering of the turbulent kinetic energy [23]. Thus, the relative strength of the larger eddies increases prior to impingement. The turbulent structure then goes through a rapid and devastating distortion of impingement. The redevelopment of the turbulent structure is thus expected to influence the immediate downstream shear stress distribution. It was necessary to increase the averaging time of the mean velocity downstream of impingement until approximately 20 nozzle widths downstream. This implies an increase of the integral time scales however, we did not detect any extremely low frequency oscillations of the impingement location at this offset ratio. The r.m.s. values of the x and y components of velocity were measured in the impingement region and are reported in [21]. Further investigations of the effect of offset ratio on the occurrence of low frequency oscillations are planned.

Downstream measurements of velocity profiles and wall shear stress were made. The goal was to reproduce the downstream results of others and to establish the extent of the influence of impingement before the wall jet region. Velocity and wall stress data have been presented by [5 and 11]. We have found that the velocity profiles collapse to the classical wall jet distribution beyond 20 nozzle widths downstream of

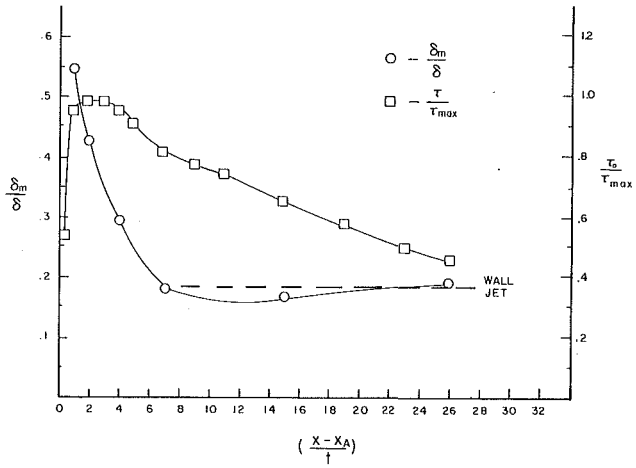

Fig. 15 Relative jet spread and wall shear stress development downstream of impingement

the jet exit. Prior to this the wall flow is still experiencing a mild acceleration with the positions of maximum velocity and half-width moving closer to the wall. These results are in good agreement with [4 and 10]. Figure 15 shows the downstream development of the inner and outer layer of the wall jet, where δ_m is the distance from the wall to the maximum velocity and δ is the outer layer half-width. Also shown is the scaled wall shear stress distribution where τ_{max} is the maximum wall shear stress downstream of impingement. Within seven slot widths downstream of impingement the inner-to-outer layer thickness ratio attains the wall jet value. The wall shear stress distribution agrees very well with that reported by Rajaratnam and Subramanya [4].

Conclusion

A detailed description of the mean flow characteristics of a turbulent offset jet is provided in the preattachment and impingement regions. This data is meant to improve our understanding of the flow structure in this complex flow field and aide in modelling attempts. The streamline curvature, brought about by the pressure differential across the jet, significantly alters the entrainment rate. However, in streamline coordinates defined by the jet maximum velocity locus, the velocity decay and upper jet spread rates are similar to plane jets. The magnitudes of the curvature strain rate to shear strain rate (relative inverse time scale) and ratio of jet width to radius of curvature (relative length scale) are significant in this flow indicating that it cannot be approximated as a thin shear layer. The recirculation region is fed by a relatively strong backflow for the reported offset ratio of seven. We did not observe very low frequency oscillations of the attachment location. Since we did detect an increase in the integral time scale near impingement, further study of the effect of offset ratio on the impingement region is recommended.

Acknowledgments

Partial funding in support of this work was provided by the National Science Foundation Grant No. ISP-8011451 and is gratefully appreciated.

References

1 Sawyer, R. A., "The Flow Due to a Two-Dimensional Jet Issuing Parallel to a Flat Plate," *J. of Fluid Mech.*, Vol. 9, 1960, pp. 543–560.

2 Sawyer, R. A., "Two-Dimensional Reattachment Jet Flows Including the Effects of Curvature on Entrainment," *J. of Fluid Mech.*, Vol. 17, 1963, pp. 481–498.

3 Bourque, C., and Newman, B. G., "Reattachment of a Two-Dimensional Incompressible Jet to an Adjacent Flat Plate," *Aerion. Quar.*, Vol. 11, Aug. 1960, pp. 201–232.

4 Rajaratnam, N. and Subramanya, N., "Plane Turbulent Reattached Wall Jets," *ASCE J. of Hydraulics Div.*, Vol. 94, HY1, 1968, pp. 95–112.

5 Bourque, C., "Reattachment of a Two-Dimensional Jet to an Adjacent Flat Plate," *Advances in Fluidics*, ed. by F. T. Brown, ASME, New York, 1967, pp. 192–204.

6 Hock, J., and Jiji, L. M., "Two-Dimensional Turbulent Offset Jet-Boundary Interaction," ASME *J. of Fluids Engr.*, Vol. 103, Mar. 1981, pp. 154–161.

7 Perry, C. C., "Two-Dimensional Jet Attachment," *Advances in Fluidics*, ed. by F. T. Brown, ASME, New York, 1967, pp. 205–217.

8 Ayukawa, K., and Shakouchi, T., "Analysis of a Jet Attaching to an Offset Parallel Plate," *Bull. of JSME*, Vol. 19, 1976, pp. 395–401.

9 Nozaki, T., Hatta, K., Sato, N., and Matsumura, H., "Reattchment Flow Issuing from a Finite Width Nozzle (Report 2. Effects of Initial Turbulence Intensity)," *Bull. of JSME*, Vol. 24, No. 188, Feb. 1981, pp. 363–369.

10 Parameswaran, V., and Alpay, S. A., "Studies on Re-attaching Wall Jets," *Trans. of Canadian Society of Mech. Engr.*, Vol. 3, 1975, pp. 83–89.

11 Kumada, M., Mabuchi, I., and Oyakawa, K., "Studies in Heat Transfer to Turbulent Jets with Adjacent Boundaries (3rd Report, Mass Transfer to Plane Turbulent Jet Reattachment on an Offset Parallel Plate)," *Bull. of JSME*, Vol. 16, 1973, pp. 1712–1722.

12 Pelfrey, J. R. R., "Characteristics of a Turbulent Plane Offset Jet," Ph.D. dissertation, Mechanical Engineering Department, Clemson University, Clemson, S.C., 1984.

13 Whitelaw, J. H., "Laser Velocimetry: Problems and Opportunities," *Engineering Applications of Laser Velocity*, ed. H. W. Coleman and P. A. Pfund, ASME Pub., New York, 1982.

14 Meyers, J. F., and Clemmons, J. I., Jr., "Processing Laser Velocimeter High Speed Burst Counter Data," *Laser Velocimetry and Particle Sizing*, ed. H. D. Thompson and W. H. Stevenson, Hemisphere, New York, 1978.

15 Patel, V. C., "Calibration of the Preston Tube and Limitations on its Use in Pressure Gradients," *J. Fluid Mech.*, Vol. 23, 1965, pp. 185–208.

16 Yi, C. H., "Incompressible Turbulent Separations From an Axisymmetric Curved Afterbody," Ph.D. thesis, Mechanical and Aerospace Engineering Dept. Rutgers, The State University, June, 1972.

17 Persen, L. N., "The Near Field of a Plane Turbulent Jet," Fluid Dynamics of Jets with Applications of V/STOL, *AGARD Conference Proceedings*," No. 308, 1981.

18 Everitt, K. W., and Robins, A. G., "The Development and Structure of Turbulent Plane Jets," *J. of Fluid Mech.*, Vol. 88, Part 3, 1978, pp. 563–583.

19 Etheridge, D. W., and Kemp, D. H., "Measurements of Turbulent Flow Downstream of a Rearward-Facing Step," *J. of Fluid Mech.*, Vol. 86, Part 3, 1978, pp. 545–566.

20 Bradshaw, P., "Effects of Streamline Curvature on Turbulent Flow," AGAR Dograph No. 169, 1973.

21 Pelfrey, J. R. R., and Liburdy, J. A., "Effect of Curvature on the Turbulence of a Two-Dimensional Jet," Accepted for Publication, *Experiments in Fluids*, 1985.

22 Williams, J. C. III, Chenc, E. H., and Kim, K. H., "Curvature Effects in the Laminar and Turbulent Freejet Boundary," *AIAA J.*, Vol. 9, No. 4, 1971, pp. 733–736.

23 Pelfrey, J. R. R., and Liburdy, J. A., "Turbulence Characteristics of an Offset Jet," Second International Symposium on Applications of Laser Anemometry to Fluid Mechanics, Lisbon, July 2–5, 1984.

24 Paizis, S. T., and Schwarz, W. H., "Entrainment Rates in Turbulent Shear Flows," *J. of Fluid Mech.*, Vol. 68, 1975, pp. 297–308.

C. K. Shyh
Graduate Student.

B. R. Munson
Professor.

Department of Engineering Science and Mechanics, Iowa State University, Ames, Iowa 50011

Interfacial Instability of an Oscillating Shear Layer

The oscillating interface between a very viscous fluid layer (which oscillates as a nearly rigid body with the bounding container) and a relatively inviscid layer becomes unstable under certain conditions. The dimensionless experimental stability results are correlated by a modified form of the classical Kelvin-Helmholtz shear layer instability result.

Introduction

It has long been known that the interface between two fluid layers moving with different velocities can become unstable [1]. In many situations it is important to know whether the interface will remain smooth and stable or whether interfacial waves will develop. Although numerous theoretical and experimental results have been obtained for such Kelvin-Helmholtz type instabilities, most have been concerned with fluids of relatively low viscosity or flows with constant velocity.

In this paper we present experimental results concerning the stability of the interface between two liquids in a circular container, as shown in Fig. 1. The relative motion between the two fluids is caused by sinusoidal oscillation of the container. The viscosity of one layer is considerably greater than that of the other layer. The greater viscosity layer has a motion that is essentially rigid body oscillation, while the less viscous layer remains relatively motionless. Thus, an oscillatory shear layer is formed at the interface. The purpose of this investigation is to determine the conditions under which the interface becomes unstable.

The standard Kelvin-Helmholtz instability concerns two inviscid fluid layers of densities ρ_1 and ρ_2, moving with uniform speeds, U_1 and U_2. The interfacial surface tension, T, and gravity, g, act as stabilizing forces, while inertia is a destabilizing force. According to linear stability theory [2], the critical velocity difference needed to initiate interfacial waves is given by

$$(U_1 - U_2)^2 = \frac{2}{\alpha_1 \alpha_2}\sqrt{\frac{Tg(\alpha_1 - \alpha_2)}{\rho_1 + \rho_2}} \tag{1}$$

where $\alpha_1 = \rho_1/(\rho_1 + \rho_2)$ and $\alpha_2 = \rho_2/(\rho_1 + \rho_2)$. If one of the fluids is a viscous fluid, the results are similar [3]. For example, the critical velocity difference for the case with a viscous lower layer is smaller than that given by equation (1) by a factor of $\alpha_2^{1/2}$. Stability of the interface in the oscillating shear layer flow described in this paper is related to this classical result, although there are some differences.

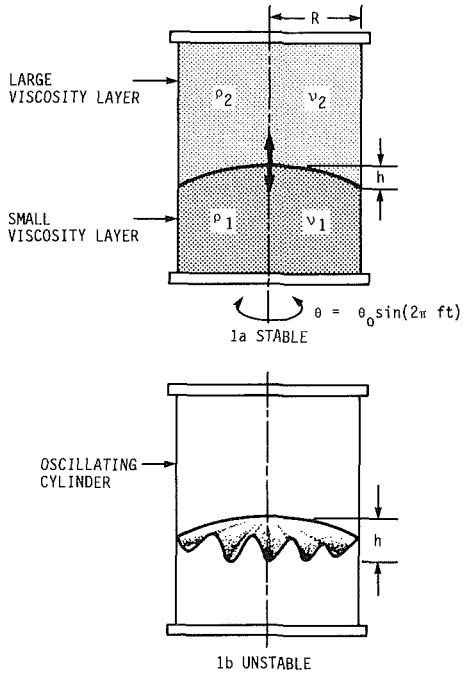

Fig. 1 Flow geometry

Experimental Apparatus

The experimental apparatus used in this study consists of a clear, open-topped plexiglass cylinder of radius R, which was oscillated sinusoidally about its centerline with amplitude θ_0 and frequency f, as shown in Fig. 1. The oscillation of the cylinder was produced by an electric stepping motor that was controlled by a Rockwell Aim 65 computer. Thus, the frequency and amplitude of oscillation could be controlled as desired. Three different cylinders of radii $R = 3.49$ cm, 6.03 cm, and 9.84 cm were used.

A layer of very viscous silicone oil (density ρ_2, kinematic viscosity ν_2) was floated on a layer of relatively small viscosity fluid (density ρ_1, viscosity $\nu_1 << \nu_2$). The viscosity of the silicone oils used ranged from $\nu_2 = 2{,}000$ cs to 60,000 cs. (The viscosity of water is approximately 1 cs.)

A variety of relatively inviscid fluids was used for the lower layer in order to produce a wide range in density and surface

Contributed by the Fluids Engineering Division for publication in the JOURNAL OF FLUIDS ENGINEERING. Manuscript received by the Fluids Engineering Division, March 20, 1985.

Table 1 Characteristics of the various liquids used

Liquid	Specific Gravity s.g.	Surface Tension σ (dyne/cm)
Silicone oil (2,500 cs)	0.973	21.3
Silicone oil (3,000 cs)	0.973	21.3
Silicone oil (5,000 cs)	0.973	21.3
Silicone oil (10,000 cs)	0.975	21.3
Silicone oil (30,000 cs)	0.975	21.5
Silicone oil (60,000 cs)	0.976	21.5
Calcium chloride solution	1.40	56.4
Calcium chloride solution	1.20	59.0
Calcium chloride solution	1.75	56.3
Calcium chloride solution	1.10	59.8
Water	1.00	62.2
Meriam manometer oil (blue)	1.75	24.0
Meriam manometer oil (yellow)	1.20	25.3
Meriam manometer oil (red)	2.95	32.1
Ethylene glycol	1.113	39.9
Propylene glycol	1.036	32.5

tension differences between the two fluids. The specific gravities and surface tensions, σ(liquid-to-air interface), of the various liquids were measured at the temperatures used. These values are listed in Table 1. For two immiscible liquids, the interfacial surface tension is given, to a good approximation, as the difference in surface tensions of the two liquids with respect to air [4]. Thus, $T=\sigma_1-\sigma_2$.

The following experimental procedure was used. The cylinder was cleaned and filled with the two liquids being tested (for example, (1) aqueous calcium chloride solution of specific gravity 1.2 and viscosity 6 cs and (2) 10,000 cs silicone oil of specific gravity 0.975).

The cylinder was then oscillated at the desired frequency and amplitude. If the parameters used were below the critical values, the interface remained smooth, without interfacial waves. The frequency and/or amplitude were increased until interfacial waves were first observed – the critical conditions. The amplitude of the resulting interfacial deformation was determined from photographs of the surface.

By repeating the above procedure for numerous combinations of fluids and cylinder sizes, it was possible to obtain a better understanding of the interfacial instability.

Results

The investigated flow contains a very viscous upper layer that oscillates with the bounding cylinder very nearly as a rigid body. On the other hand, the lower layer has low viscosity, so that its motion is essentially confined to thin boundary layers on the bottom and sides of the cylinder and at the interface with the viscous fluid. Thus, an oscillating shear layer motion is generated between the two fluids.

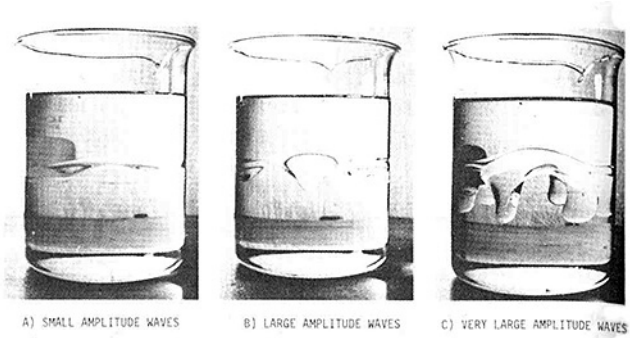

Fig. 2 Photographs of the unstable interface

It is expected that the stability of the interface is a function of the fluid properties (viscosity, density, and surface tension) and the flow geometry (cylinder size, frequency and amplitude of oscillation, and fluid depth). The dependence on these parameters is discussed below.

If the cylinder motion is not too great (low frequency and amplitude of oscillation), the interface remains smooth, although it is not flat. Because of the oscillation of the cylinder, the interface oscillates up and down in phase with the motion of the cylinder, as shown in Fig. 1(*a*). This motion is caused by the imbalance between centrifugal and gravitational forces (and to a lesser degree, surface tension), because of the acceleration (oscillation) of the viscous layer. This effect is similar to that investigated by Berman et al. for the motion of two fluid layers in spin-up of a centrifuge in which the interface shape is different during spin-up (acceleration) than during steady state rotation [5].

If the amplitude or frequency of the cylinder oscillation exceeds a critical value, interfacial waves will develop, as shown in Fig. 1(*b*). These waves (instability) are superposed upon the smooth, oscillating interface (basic flow) discussed above. The photographs in Fig. 2 show such waves for a simple demonstration consisting of two fluid layers (10,000 cs oil over water) in an oscillating laboratory beaker (not the apparatus used in this study).

Typical results showing the magnitude of the distortion of the interface, h (defined in Fig. 1), as a function of the amplitude of oscillation, θ_o, are shown in Fig. 3. In this case, the frequency of oscillation if $f=1$ cycle/s, and the upper fluid is $\nu_2=10{,}000$ cs silicone oil. The lower fluid is calcium chloride solution of specific gravities 1.2 or 1.4. The amplitude at which the instability begins is shown by the "break" in the curve as indicated by the arrow. For flows with θ_o less than this critical value, the nonzero values of h are due to the oscillatory motion of the smooth, stable interface. For flows with θ_o greater than the critical value, the change in slope of the curve corresponds to the growth of interfacial waves – the instability.

Nomenclature

c = constant in dimensionless stability representation
f = frequency of oscillation
F_G = gravity force
F_I = inertia force
F_{IC} = convective inertia force
F_{IU} = unsteady inertia force
F_T = surface tension force
g = acceleration of gravity
h = amplitude of distortion of interface
H = depth of viscous layer
R = radius of cylinder
t = time
T = $\sigma_1-\sigma_2$ = interfacial surface tension
u = fluid velocity
U_1, U_2 = shear layer velocities
x = space coordinate
α = fR^2/ν = kinetic Reynolds number
α_1 = $\rho_1/(\rho_1+\rho_2)$
α_2 = $\rho_2/(\rho_1+\rho_2)$
θ_o = amplitude of oscillation
ν_2 = kinematic viscosity of viscous layer
ν_1 = kinematic viscosity of low viscosity layer
ρ_2 = density of viscous layer
ρ_1 = density of low viscosity layer
σ_2 = surface tension of air-viscous fluid interface
σ_1 = surface tension of air-low-viscosity fluid interface

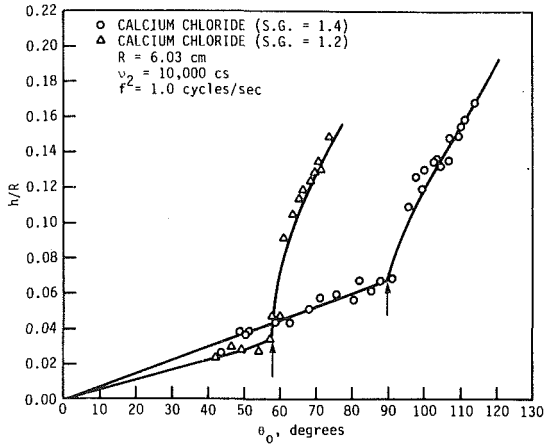

Fig. 3 Amplitude of interface distortion as a function of amplitude of rotation (uncertainty estimates: $h/R \pm 10$ percent, $\theta_o \pm 3$ percent)

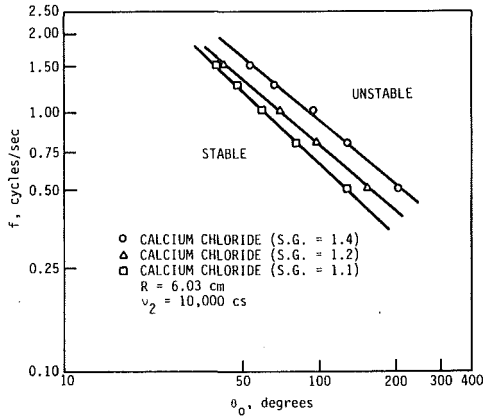

Fig. 4 Amplitude-frequency stability boundary for different density ratios (uncertainty estimates: $f \pm 3$ percent, $\theta_o \pm 8$ percent)

Thus, for a given frequency, f, the flow becomes unstable at a certain amplitude, θ_o. Similarly, for a given amplitude, the flow becomes unstable at a certain frequency. Results showing the critical frequency and amplitude are presented in Fig. 4 for various specific gravities of the lower fluid. As the amplitude increases, the interface becomes unstable at a smaller frequency. At the critical condition, the amplitude and frequency of oscillation are related by $f\theta_o^{3/4} = \text{constant}$. Also, an increase in the density of the lower fluid makes the layer become more stable.

To cover a wide range of density ratios and surface tensions, other liquid combinations were used. For example, three types of Meriam manometer fluids ("red oil, blue oil, and yellow oil") were used as the lower fluid. The results presented in Fig. 5 for these cases are similar to those of Fig. 4.

A set of tests was run to determine the effect of the viscosity of the upper fluid on the stability conditions. The stability criteria (amplitude and frequency of oscillation) were independent of the viscosity, provided the upper layer oscillated with the cylinder as a rigid body. That is, no difference was observed for silicone oils with viscosities of $\nu_2 = 60{,}000$ cs, 30,000 cs, or 10,000 cs. However, for smaller viscosities it was necessary to oscillate the cylinder faster (larger f and/or θ_o) to produce the instability. For $\nu_2 \lesssim 2{,}000$ cs, it was not possible to produce the instability, because the viscous layer did not oscillate as a rigid body.

A measure of whether the viscous layer will oscillate as a rigid body can be obtained by considering the kinetic Reynolds number appropriate for oscillatory flows, $\alpha = R^2 f/\nu$. If α is small ($\alpha < 1$), the flow acts as though it were quasi-steady, and

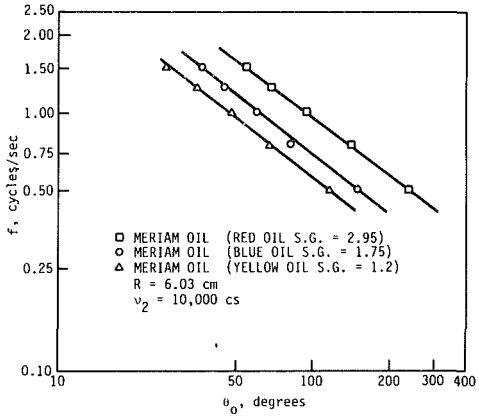

Fig. 5 Amplitude-frequency stability boundary for different fluids (uncertainty estimates: $f \pm 3$ percent, $\theta_o \pm 8$ percent)

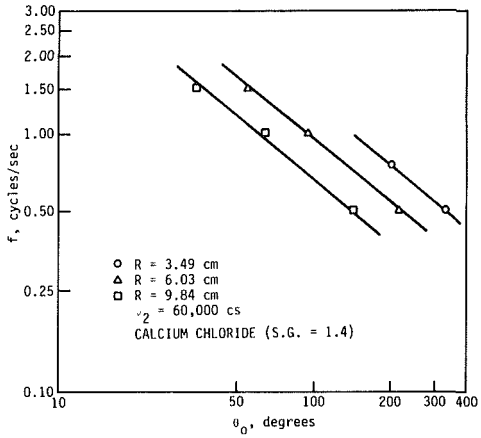

Fig. 6 Amplitude-frequency stability boundary for different cylinder radii (uncertainty estimates: $f \pm 3$ percent, $\theta_o \pm 8$ percent)

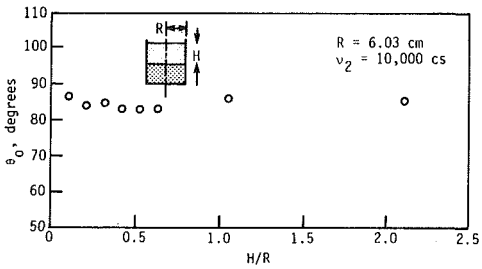

Fig. 7 Amplitude of oscillation for instability as a function of viscous layer depth (uncertainty estimates: $\theta_o \pm 8$ percent, $H/R \pm 5$ percent)

the viscous layer oscillates essentially as a rigid body. If α is large ($\alpha >> 1$), the motion is confined to a relatively thin oscillating Stokes layer near the cylinder. For this experiment with $R = 3.49$ cm, $f = 3.14$ rad/s, and $\nu_2 = 2{,}000$ cs, we obtain $\alpha = 1.9$. Thus, it was necessary to have $\nu_2 \gtrsim 2{,}000$ cs to maintain the viscous layer as a nearly rigid body rotation as needed to produce the unsteady shear layer.

The results of Fig. 6 show that the stability conditions are a function of the size of the cylinder. For a given frequency, an increase in the cylinder radius causes the instability to occur at a smaller amplitude of oscillation. This occurs because for given f and θ_o the velocity difference between the two fluid layers increases as the radius increases.

On the other hand, the depth of the fluid layers has essentially no effect on the interfacial instability. As seen in Fig. 7, with other parameters held constant, the amplitude of rotation for the onset of instability is essentially independent of the depth of the viscous layer.

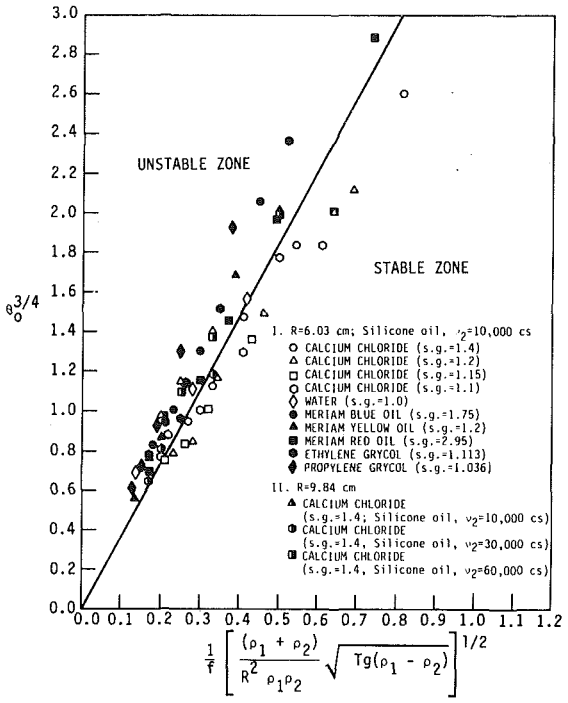

Fig. 8 Dimensionless form of stability criteria (uncertainty estimates: $\theta_o \pm 8$ percent, $[((\rho_1 . \rho_2)/R^2\rho_1\rho_2)\sqrt{Tg(\rho_1-\rho_2)}]^{1/2}/f \pm 8$ percent)

As with any stability consideration, the results should be presented in dimensionless form. For the flow considered, the stabilizing forces are surface tension, F_T, and gravity, F_G, while the destabilizing force is inertia, F_I. Thus, one would expect instability when the dimensionless force ratio, F_I^2/F_TF_G, becomes large enough.

Characteristic values of the surface tension and gravity forces can be written as $F_T \sim TR$ and $F_G \sim g(\rho_1-\rho_2)R^3$. On the other hand, characteristic values of the inertia force depend on whether the inertia is caused by convective acceleration, $F_{IC} \sim \rho u\partial u/\partial x \sim \rho_1(f\theta_o R)(f\theta_o R/R) = \rho_1 f^2\theta_o^2 R$, or by unsteady effects, $F_{IU} \sim \rho\partial u/\partial t \sim \rho_1 f^2\theta_o R$.

If we use the steady (convective) inertia term, F_{IC}, in the ratio F_I^2/F_TF_G, we obtain the result that for given fluids and cylinder size, instability should occur for $f\theta_o = \text{constant}$. This corresponds to the classical Kelvin-Helmholtz criteria of equation (1) (i.e., $U_2 - U_1 = \text{constant}$ with $U_1 = 0$ and $U_2 = f\theta_o R$). However, if we use the unsteady inertia term, F_{IU}, we obtain $f\theta_o^{1/2} = \text{constant}$.

As mentioned previously, the experimental results indicate that instability occurs with $f\theta_o^{3/4} = \text{constant}$. Thus, we conclude that both types of inertia forces are important destabilizing mechanisms, because if we form the ratio $F_{IC}F_{IU}/F_TF_G$, we obtain $f\theta_o^{3/4} = \text{constant}$, in agreement with the experiment.

Therefore, we propose that the stability criteria for the oscillating shear layer flow is a modified form of the Kelvin-Helmholtz result and can be given by

$$\theta_o^{3/4} = c \times \frac{1}{f}\left[\frac{(\rho_1+\rho_2)}{R^2\rho_1\rho_2}\sqrt{Tg(\rho_1-\rho_2)}\right]^{1/2} \tag{2}$$

where c is a constant.

The results of all the experiments performed are presented in this dimensionless form in Fig. 8. All the data condense and are distributed along a narrow region dividing the stable and unstable zones. The value of c in equation (2) was found to be $c = 3.7$. Note that the units of f and θ_o used in equation (2) and Fig. 8 are expressed in rad/sec and radians.

Conclusions

The interface separating two liquids can become unstable under certain conditions. In the case presented here, the velocity difference between two layers is caused by the oscillatory motion of the bounding container. The viscosity of one layer is so great that its motion is essentially that of an oscillating rigid body, while the low viscosity of the other layer ensures that it is nearly motionless. By driving the viscous layer at a great enough amplitude and frequency, the velocity difference between the two fluid layers is considerable enough to produce a Kelvin-Helmholtz type instability. The stabilizing forces are gravity and surface tension, while the destabilizing forces are inertia effects caused by both steady and unsteady components. The boundary between the stable and unstable conditions is given quite well by a modified Kelvin-Helmholtz stability criterion (equation (2)).

The results presented are valid only if the viscous layer moves as a nearly rigid body. If the viscosity is not great enough, the motion produced by the oscillating cylinder will be that of an oscillating Stokes layer (not rigid body motion), and the interfacial stability characteristics will be different from those presented here.

Acknowledgment

The support of NSF Grant MEA-8204148 and the Engineering Research Institute at Iowa State University is greatly appreciated.

References

1 Helmholtz, H., "Ueber discontinuirliche Flussigkeitsbewegungen," *Wissenschaftliche Abhandlungen*, 1882, pp. 146-57.

2 Chandrasekhar, S., *Hydrodynamic and Hydromagnetic Stability*, Oxford University Press, 1961, Chapter XI.

3 Lindsay, K. A., "The Kelvin-Helmholtz Instability for a Viscous Interface," *Acta Mech.*, Vol. 52, 1984, pp. 51-61.

4 Davies, J. T., *Interfacial Phenomena*, Academic Press, 1961.

5 Berman, A. S., Bradford, J., and Lundgren, T. S., "Two-Fluid Spin-Up in a Centrifuge," *J. Fluid Mech.*, Vol. 84, Part 3, 1978, pp. 411-431.

The Functional Role of Wing Corrugations in Living Systems

R. H. Buckholz
Department of Mechanical Engineering,
Columbia University,
New York, NY 10027

Questions concerning the functional role of spanwise wing corrugation in living systems are experimentally investigated. Attention was initially directed to this problem by observation of the irregular shape of many insect wings as well as other studies indicating higher lift on these wings. First, a flow visualization scheme was used to observe and photograph streamlines around two different wing sections. One of these, a sheet metal model with geometry matching that of a butterfly wing, was studied at a chord Reynolds number of 1500 and at a Reynolds number of 80 based on corrugation depth. A steady-state recirculation region near the model leading edge was found, and the separated flow region above this recirculation zone formed a laminar reattachment to the model. A second thicker wing was corrugated on the upper surface. Closed streamlines inside these upper surface corrugations were photographed at Reynolds numbers of 8000 and 3800 based on chord length, and 200 and 90 based on corrugation depth. Reductions in pressures on the corrugated upper wing surface relative to a smooth upper wing surface were then measured.

I Introduction

Studies of insect flight mechanics have elucidated some novel and unique fluid dynamic phenomena. Insect wings, and butterfly wings in particular, do not exhibit the nominal smooth wing section profile associated with modern aircraft. Their wing section profiles have irregularities and corrugations; photographs of these wing corrugations show peak-to-peak amplitudes of up to 10 percent of the chord length. Furthermore, additional smaller scale wing surface irregularities amounting to a lesser fraction of the chord length become clear at higher magnification. The precise role of these larger irregularities, in the Reynolds number range 10^2 to 10^3, is studied in this paper.

The sustained glide of many seconds, for some butterflies, does not occur in nature (Rainey, 1975). This is an obvious case where wing surface geometry is important. Gliding ability, for these nearly straight and level flights, over substantial periods of time depends largely upon the steady state aerodynamic properties of the wing. This steady-state aerodynamic performance can be extended to include quasi-steady flight.

The present study is an experiment which combines flow visualization and pressure distribution measurements both on a smooth and on a corrugated wing section. The experimental flow pattern results are presented first. Pressure distribution results for a smooth versus a corrugated wing section are then presented. Previous studies have not reported equivalent measurements at these aerodynamically low Reynolds numbers. It is not the intention here to tailor a particular airfoil section for these Reynolds number applications, but rather to illustrate trends associated with wing surface irregularities that occur in nature. A design methodology for low Reynolds number airfoil sections is given by McMasters et al. (1979, 1981).

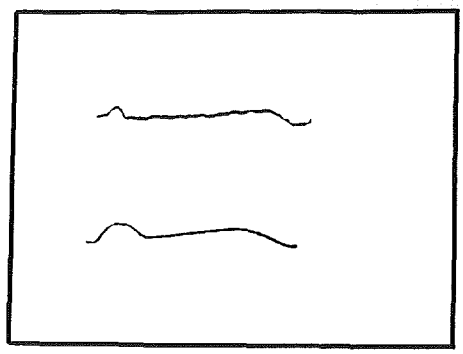

Fig. 1 Upper wing section profile taken from the Malaysia butterfly, Prothol Calydonia; lower profile is from the sheet metal model tested. The leading edge is on the right, and flow direction is from right to left. The leading edge to trailing edge distance is 1.5 inch.

Other experiments on the effects of wing corrugations under steady flow conditions have also been reported. Lift and drag of a noctuid moth (Catoealer) were measured by Nachtigall (1974). His measurements were made on the entire insect with wings spread in the gliding position. Measurements were made at 1.5 m/s, which corresponds to an estimated wing chord Reynolds number of 4000. (Nachtigall did not report the Reynolds number.) The measured lift was unexpectedly sensitive to the presence of wing surface scales. Lift as a function of the angle-of- attack was larger for the wing with scales. The nominal increase in lift was 15 percent. It is also significant that no measurable change in drag could be detected between the insect wing with scales and the insect wing without scales. Rees (1975) tested smooth and corrugated wings, using a twenty-two times life size model of a hover fly wing. Lift and drag were measured in a water tunnel at Reynolds numbers

Contributed by the Fluids Engineering Division for publication in the JOURNAL OF FLUIDS ENGINEERING. Manuscript received by the Fluids Engineering Division, October 18, 1983.

450, 800, and 900. He found little difference between the smooth and corrugated model. However, it is possible that the characteristic surface irregularity dimensions for Nachtigall's (1974) moth wing scales and for Rees' hover fly wing were different, since neither reported these dimensions. Further work by Neuman et al. (1977) drew attention to the effect of wing corrugations on insect wing at a Reynolds number 10^4. He suggests that corrugated wings with closed separation bubbles, which maintain low pressure inside, may produce higher lift. Newman also visualized trapped regions of air recirculating inside the wing corrugations. He observed a turbulent reattachment of the separated streamline. Rudolph (1978) tested models of dragon fly wings in a water tunnel. He used a two component force balance and flow visualization methods at Reynolds numbers between 150 and 1200. His visualization results indicate regions of "swirling flow" inside the folds of the corrugations. Rudolph concludes that wing corrugations delayed stall, and flow separation.

Further knowledge of the influence of spanwise corrugations on the flow and pressure fields at aerodynamically small Reynolds numbers is sought in this study. Recent work shows regions of recirculation inside the folds of the corrugations and suggests a possible increase in lift due to surface corrugations. Actual butterfly wings have aspect ratios which can be as low as three. Therefore, three-dimensional effects, such as wing tip leakage, are certain to play a role in overall aerodynamic performance. It is important in this experiment to isolate the role of wing surface irregularities. Thus, wing section models used here emphasize the two-dimensional flow fields.

II Methods

A low speed, low turbulence, wind tunnel was specially built to operate over a speed range of up to 20 ft/s. The contraction section was designed using a matched pair of cubic curves, according to the method described by Morel (1975, 1977). Test section wind speeds were measured using a pitot-static tube connected to a Datametric Barocel Electronic Manometer. Pressure differences down to .0001 in H_2O could then be measured. Turbulent velocity data and mean speeds were also measured by using a constant temperature hot-wire anemometer. The flow visualization results were obtained by using a smoke-wire method. This visualization method has been used by many investigators (e.g., Corke et al., 1977). Drops of oil (Life-Lite smoke oil) were gravity fed from a reservoir onto the smoke-wire through a 1mm hole. As the drop fell along the wire a regular pattern of smaller droplets was left behind. Each droplet of oil acts as a streakline source as the oil is slowly vaporized by a current through the wire; the smoke-wire was operated manually. The scheme was to observe and photograph streaklines of smoke which passed over the airfoil midsection. Typical tests were done at wind speeds of 2m/s and .6m/s, and corresponding Reynolds numbers based on smoke-wire diameter were 21 and 6. These values were below the reported minimum Reynolds number of 40 for the onset of the Karman-Benard vortex street (Kovasznay, 1949). Two different wing sections were used; and flow visualization data were obtained for each wing section tested.

A butterfly wing section profile was obtained from the Prothol Calydonia, a Malaysia butterfly. Photographs of wing section contours were taken under a microscope. A distinct crimp near the leading edge of the wing, Fig. 1, was observed to persist along the spanwise direction for the major portion of the lifting surface. Typical chordwise sections were traced and details were used to make a two-dimensional sheet metal model of the butterfly wing section. Only the larger scale wing irregularities were modeled. A 35-mm Nikon camera was used for flow visualization photography. Smoke in the test section

Table 1 Location, from the leading edge, of pressure taps on the model NACA 4415 wing section; distance is normalized by the chord length. (Uncertainty in $X/C = .02$.)

Upper surface	.05	.15	.20	.30	.40	.50	.56	.60	.70	.80	.84
Lower surface	.10	.20	.30	.40	.50	.56	.60	.65	.75	—	—

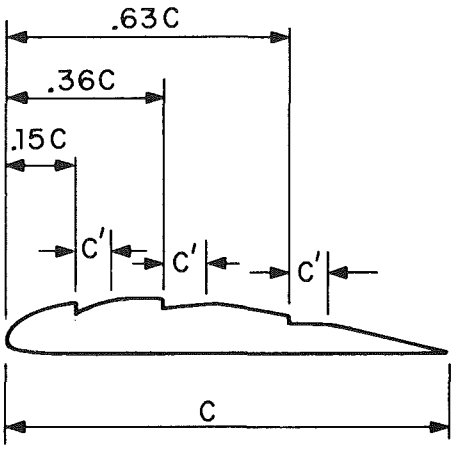

Fig. 2 Profile of the corrugated plexiglass wing section tested; groove distance from the leading edge is normalized by the chord length. Groove length, c, is .1 c.

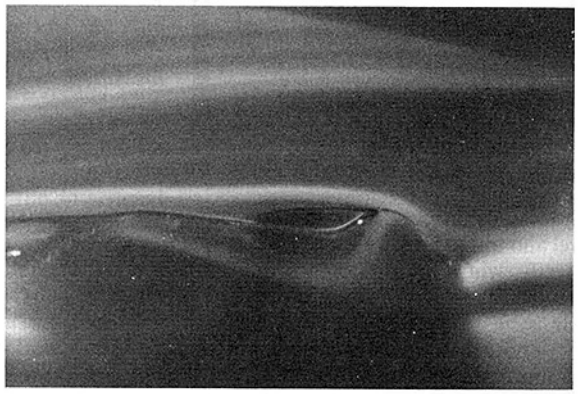

Fig. 3 Flow pattern over the model butterfly wing section, wind speed .6m/s, Reynolds number 1,500 based on the chord and 80 based on the leading edge bump height. Flow direction is from right to left.

was illuminated through a slit which ran along the length of the section. The camera shutter was manually released. A wing section model 10cm in span and 3.8cm in chord was built. One typical Reynolds number based on this wing chord and on a wind speed of .6m/s, was 1,500.

To study in further depth the effect of wing corrugation, a second airfoil section was made from plexiglass. It was the principal concern of this study to qualitatively determine the effect of transverse airfoil corrugations on flow characteristic and on wing pressure distribution. Therefore, the choice of this second wing was somewhat arbitrary. Flow around this smooth second wing section was photographed and used as a standard to compare against a similar corrugated wing section. This model wing section had a 10cm span and a 6.7cm chord. Chordwise pressure measurements were made via twenty static pressure taps, each .3mm in diameter-eleven on the upper surface and nine on the lower. Test speeds were 0.6m/s, 2.0m/s and 5.6m/s; corresponding Reynolds numbers based on chord length were 3,800, 8,500 and 23,000, respectively. Static pressure along the wing section was sequentially measured using a Datametrics Electronic Manometer. Pressure differences could be read to .0001in of water. Pressure tap locations are given in Table 1.

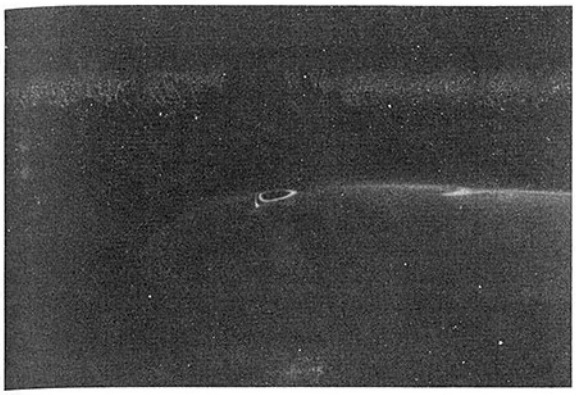

Fig. 4 Trapped vortex in the wing section corrugation closest to the leading edge; Reynolds number 8300 based on chord length and 200 based on corrugation height. Angle of attack was 0 deg.

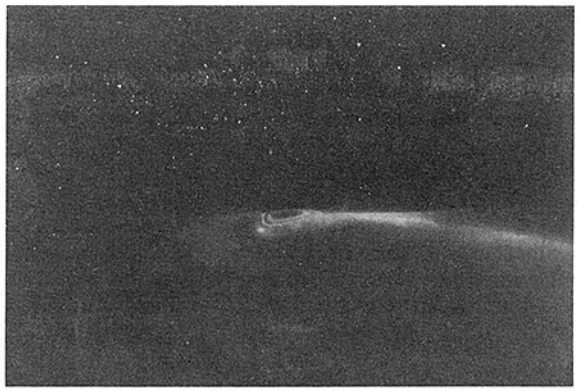

Fig. 5 Trapped vortex in the wing section corrugation closest to the leading edge; several closed streamlines are visible. Angle of attack was 10 deg, Reynolds number was 8,300.

Pressure decreases which may accrue from spanwise corrugations on this NACA 4415 model were studied by grooving the upper surface of the wing section. Flow visualization and pressure measurement limitations lead to the present simplification of three grooves on the upper surface, Fig. 2.

Each groove was .17cm deep and .64cm in length. Their locations were selected so that effects on the neighboring pressure field could be measured. Variations of chordwise pressure over the corrugated wing section were then measured. To repeat measurements on the smooth section, three removable slats were made which could be fitted onto the grooved surface. The smooth and corrugated wing section were subjected to the same flow at identical angles of attack. Measured pressure differences are assumed to track the influence of wing corrugations. The removable slats were inserted, without changing the angle of attack or wind speed. Chordwise pressure was measured at Reynolds numbers of 3800, 8500 and 23,000 and at angles of attack from -5 to 15 deg.

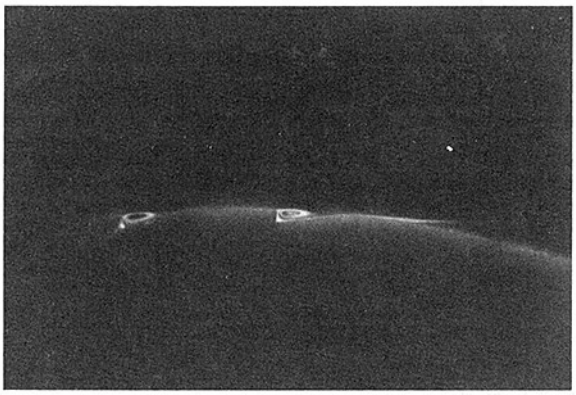

Fig. 6 Trapped vortices in the two corrugations closest to the leading edge; Reynolds number 8300 based on chord length and 200 based on corrugation depth. Angle of attack was 5 deg.

III Results and Discussion

The flow visualization results are presented first; then the pressure profiles for the smooth and corrugated wing section are given.

(*a*) Flow Visualization Experiments. Flow visualization on the butterfly airfoil model shows a large laminar recirculation bubble in the wing corrugation fold just behind the leading edge, Fig. 3. Results qualitatively show that the size of the recirculation zone depends on the angle of attack of the wing section. This visualization result shows a smooth free streamline separating from the leading edge; and then reattaching downstream. This results in a different effective wing shape which is somewhat dependent on the angle of attack. The change in size of this recirculation zone – with Reynolds number and angle-of-attack – adds further change to the apparent contour. However, replacing the corrugated wing section and the separated flow region by a similarly smooth wing section is not likely to produce similar pressure or flow fields along the closed streamline surface. The streamline surface would be the same, but the boundary conditions on the separated free streamline and on the solid surface would be different.

It is well known that flow reattachment, following leading edge separation, may be attributed to turbulent diffusion of momentum. However, this does not appear to be the case here. The work of Newman et al. (1977) shows the turbulent flow reattachment behind the leading edge corrugation of a dragonfly wing for a Reynolds number about 10^4 based on chord length. In this experiment the viscous diffusion of momentum from the free stream (Reynolds number about 100 based on corrugation height) may help to promote flow reattachment. Velocity profiles on the free stream side of the recirculation zone would tend to flatten out, due to momentum diffusion from the free stream. At these low Reynolds numbers the performance of most wing sections tends to deteriorate with decreasing Reynolds numbers. It appears that for an insect like wing section, the lift coefficients can be maintained by reattaching the separated flow.

Flow over the second wing section was then studied first using the smoke-wire method. The wing profile has been altered by the three grooves shown in Fig. 2. Streamlines near the leading edge passed smoothly over the wing section. The flow is from left to right in Fig. 4; a trapped vortex is shown inside the corrugation that is closest to the leading edge. The Reynolds number based on corrugation depth is 200, and this is near the recirculation Reynolds number for Fig. 3. Direct evidence of the trapped vortices in the leading edge corrugation is displayed again in Fig. 5. Here two closed streaklines, one inside the other, are shown. Reynolds numbers are the same as those in Fig. 4. In figure 6 trapped vortices inside the first and second upper surface corrugations are shown. Flow over the corrugations shown in Figs. 4, 5, and 6 appear to be laminar. The corresponding Reynolds numbers based on corrugation depth have been matched with the recirculation region Reynolds number shown on the model butterfly wing section, Fig. 3.

(*b*) Static Pressure Measurements. Pressure distribution data for Reynolds numbers in the range 10^2 to 10^3 are relatively scarce. To establish credence to test section flow conditions and the method of measurement, a .95cm diameter circular cylinder was placed in the test section, and pressure distribu-

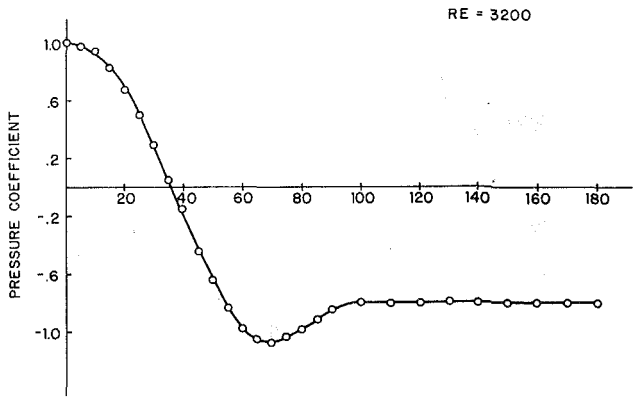

Fig. 7 Pressure coefficient on a circular cylinder, Reynolds number 3200 (Uncertainty in $\alpha = \pm 2$, and $C_p = \pm 0.15$).

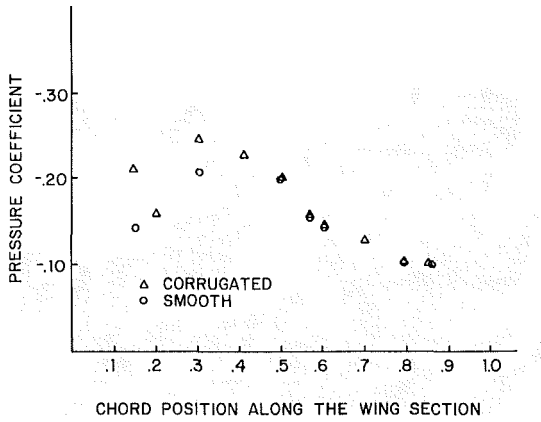

Fig. 8 Pressure distribution on the top surface of the plexiglass airfoil at Reynolds number 8300 at 0 deg angle of attack; Reynolds number based on corrugation depth was 200. (Uncertainty in $X/C = \pm .02$, $\alpha = \pm .3$ deg, and $C_p = \pm .015$.)

tions for Reynolds number 3200 were measured. These results compare well with the steady flow pressure distribution result given by Linke (1964) for Reynolds number 2800.

It was then desired to see what effect the three spanwise grooves have on the wing section static pressure distribution. For the data presented here, the difference in pressure between the smooth and corrugated wing sections is emphasized. Results presented are expressed in terms of the pressure coefficient; where ρ = air density, U is the undisturbed wind tunnel velocity, and ΔP is the pressure difference between the uniform flow static pressure and airfoil static pressure.

$$C_P = \Delta P / \frac{1}{2}\rho U^2$$

Measurements were made at conditions near those used to obtain the previous flow visualization results. Reynolds numbers were 8500 and 3800 based on chord length, and 200 and 90 based on corrugation depth. Figures 8, 9, 10, and 11 show pressure coefficient distributions on the upper surface for the 0 and 5 deg angles of attack. On the lower surface the pressure distributions remained the same for both the smooth and grooved upper wing surface.

Streamline patterns show some flow separation near the trailing edge, and this accounts for the flat pressure distribution on the upper surface (near the trailing edge) of the wing section, Figs. 9 and 11. It was typical for the pressure profile in this separation region (near the trailing edge) to be flat for both the smooth and the corrugated wing sections.

At zero deg angle of attack the region of augmented negative pressure for the corrugated section extended farther in the chordwise direction (Figs. 8 and 10). This is probably a

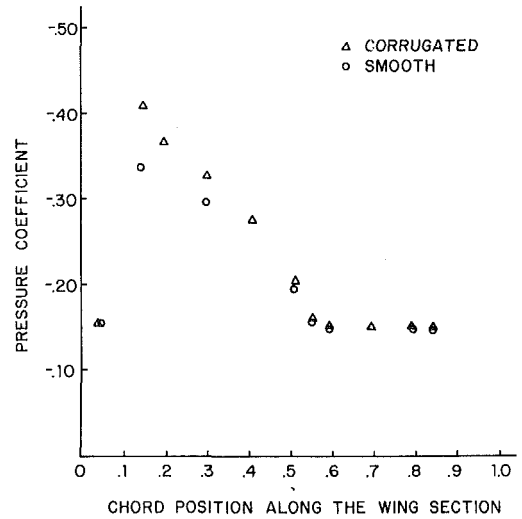

Fig. 9 Pressure distribution on the top surface of the plexiglass airfoil at Reynolds number 8300 at 5 angle of attack; Reynolds number based on corrugation depth was 200. (Uncertainty in $X/C = \pm .02$, $\alpha = \pm .3$ deg, and $C_p = \pm .015$.)

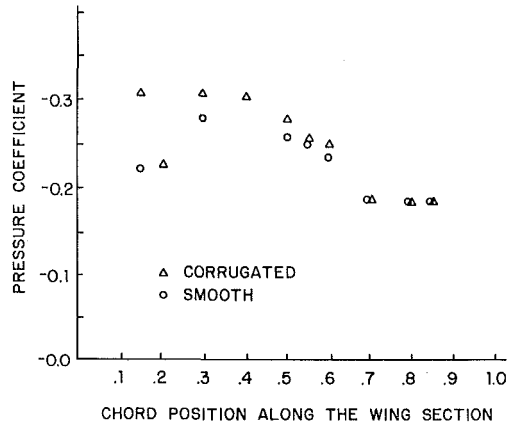

Fig. 10 Pressure distribution on the top surface of the plexiglass airfoil at Reynolds number 3800, angle of attack 0 deg; Reynolds number based on corrugation depth was 90. (Uncertainty in $X/C = \pm .02$, $\alpha = \pm .3$ deg, and $C_p = \pm .015$.)

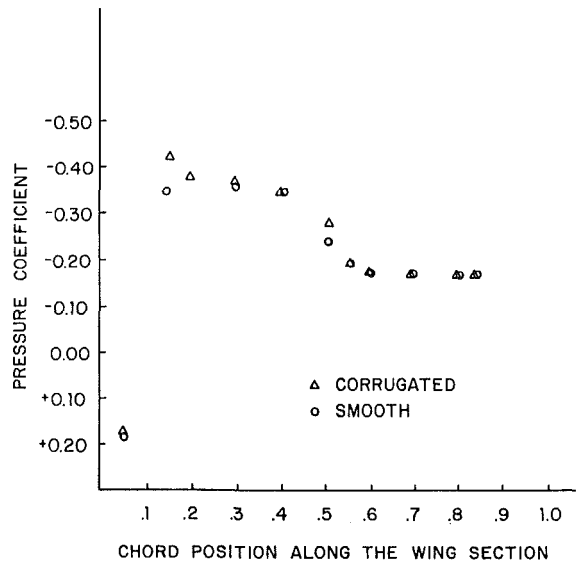

Fig. 11 Pressure distribution on the top surface of a NACA 4415 airfoil at Reynolds number 3800 at 5 deg angle of attack; Reynolds number based on corrugation depth was 90. (Uncertainty in $X/C = \pm .02$, $\alpha = \pm .3$ deg, and $C_p = \pm .015$.)

Table 2 Values of the pressure coefficient, Cp, at $x = .15c$. Variation of Cp with Reynolds number and angle of attack, for the smooth and corrugated section, are shown. (Uncertainty in $C_p = \pm .015$.)

Reynolds Number (chord)	Reynolds Number (corrugation)	Wing Section	Cp $= -5^\circ$	Cp $= 0^\circ$	Cp $= 5^\circ$	Cp $= 10^\circ$	Cp $= 15^\circ$
3,800	-	smooth	+.09	-.23	-.37	-.19	-.17
3,800	90	corrugated	-.17	-.30	-.45	-.19	-.17
8,500	-	smooth	+.01	-.14	-.35	-.34	-
8,500	200	corrugated	-.05	-.21	-.42	-.34	-
23,000	-	smooth	+.02	-.14	-.32	-.33	-
23,000	560	corrugated	-.07	-.18	-.38	-.59	-

result of reduced separation occurring at the small and negative angles of attack.

The pressure in the corrugation closest to the leading edge was consistently more negative in relation to the measurement taken from the same pressure tap on the smooth section; this behaviour is also encountered in Figs. 8, 9, 10, and 11. The groove nearest the leading edge was machined on the surface so that it cut across the second static pressure tap from the leading edge. During the course of the experiment it was possible to measure pressure on the smooth airfoil by inserting the smooth-surface contour slat, and pressure at the bottom of this first corrugation was measured by removing the slat. This pressure top was located at. 15c. Surface geometry of the slat and pressure tap was checked under a 20x microscope. Results are shown in Table 2.

Table 2 shows that the pressure at $x = .15c$ decreased by roughly 20 percent. However, the magnitude of this decrease varies with Reynolds number and with angle of attack.

IV Summary

At a Reynolds number of 150 (based on corrugation height) trapped standing vortices in the irregularity fold on the upper surface of the model butterfly wing were photographed. Laminar reattachment occurred after the separation bubble. The presence of separated flow and the flow reattachment leads to a modification of the effective wing shape. The appearance of a trapped vortex on the wing surface is consistent with results from other studies where the Reynolds numbers were higher.

Photographs of streaklines near the corrugations on the upper surface of the thicker airfoil show trapped vortices inside these wing surface irregularities. Flow separation was observed to occur over the latter portion of this wing section model. No standing vorticies were observed in the third wing surface corrugation, the one closest to the trailing edge. Also, no direct evidence of stall delay due to wing surface corrugations was observed in this experiment.

At the one corrugation near the leading edge a trend to slightly reduce the negative pressures was measured. This suggests a lift increase but an increase not as pronounced as that Nachtigall (1977) reported. it is conceivable that more corrugations on the upper surface would tend to decrease the pressure even more. However, a parametric study of corrugation size was not within the scope of this experiment. A full explanation must await more detailed studies, but it does not seem unreasonable to suggest the possibility of some optimal corrugation geometry to further augment the lift.

Acknowledgment

The author is grateful to the reviewers for their constructive comments. He also wishes to thank Mr. G. Ordonez for his help with the flow visualization.

References

1 Corke, T., Koga, D., Drubka, R., and Nagib, H., 1977, "A New Technique for Introducing Controlled Sheets of Smoke Streamlines in Wing Tunnels," ICIASF 77 Record.

2 Kovasznay, L. S. G., 1949, "Hot-Wire Investigation of the Wake Behind Cylinders at Low Reynolds Numbers," *Proceedings of the Royal Society*, Series A, Vol. 198.

3 Linke, plot taken from M. V. Morrkovin, "Flow Around a Circular Cylinder – a Kaleidoscope of Challenging Fluid Phenomena," ASME Symposium on Fully Separated Flows, 1964, p. 104.

4 Maxworthy, T., 1981, "The Fluid Dynamics of Insect Flight," *Ann. Rev. Fluid Mech.*, Vol. 13, pp. 329–350.

5 McMasters, J. H., and Henderson, M. L., 1979, "Low-Speed Single-Element Airfoil Synthesis," *Tech. Soaring*, Vol. VI, No. 2. pp. 1–21.

6 McMasters, J. H., Nordvik, R. H., Henderson, M. L., and Sandvig, J. H., 1981, "Two Airfoil Sections Designed for Low Reynolds Number," *Tech. Soaring*, Vol. VI, No. 4, pp. 2–24.

7 Morel, T., 1975, "Comprehensive Design of Axisymmetric Wind Tunnel Contraction," ASME JOURNAL OF FLUIDS ENGINEERING, June, pp. 225–233.

8 Morel, T., 1977, "Design of Two-Dimensional Wind Tunnel Contractions, ASME JOURNAL OF FLUIDS ENGINEERING," June, pp. 371–378.

9 Nachtigall, W., 1974, *Insects in Flight*, New York, McGraw-Hill, pp. 26–29.

10 Newman, B. G., Savage, S. B., Schouella, D., 1977, "Model Tests on a Wing Section of an Aeschnu Dragonfly; Scale Effects in Animal Locomotives" Pedley, T. Academic Press, pp. 445–477.

11 Rainey, R. C., 1976, *Insect Flight*, Oxford, Blackwell Scientific Publications.

12 Rees, C., 1975, "Aerodynamic Properties of an Insect Wing Section and a Smooth Aerofoil Compared," *Nature*, Vol. 258, pp. 141–142.

13 Rudolph, R., 1978, "Aerodynamic Properties of Libellulia Quadrimaculata L. (ANISOPTERA: LIBELLULIDE), and the Flow Around Smooth and Corrugated Wing Section Models During Gliding Flight," *Odonatologica*, Vol. 7, No. 7, pp. 49–58.

14 Savage, S. B., Newman, B. G., Wony, D. F. M., 1979, "The Role of Vortices and Unsteady Effects During the Hovering Flight of Dragonflies," *J. Exp. Biol.*, Vol. 83, pp. 59–77.

Terukazu Ota[1]
Professor.

Hideya Nishiyama
Research Assistant.

Department of Mechanical and Production Engineering,
Akita University,
Akita 010, Japan

Flow Around Two Elliptic Cylinders in Tandem Arrangement

Flow around two elliptic cylinders in tandem arrangement was experimentally investigated through measurements of the surface static pressure distribution and estimations of the flow parameters such as the drag, lift and moment coefficients. The elliptic cylinders examined had an axis ratio of 1:3 and they were aranged in tandem with an identical angle of attack. The angle of attack ranged from 0 to 90 deg and the nondimensional cylinder spacing l/c from 1.03 to 4.0, where l denotes the distance between the cylinder centers and c is the major axis. It has been found that the flow characteristics vary drastically with the angle of attack and also the cylinder spacing.

Introduction

Flow interaction between bluff bodies has been long investigated for practical and fluid mechanical aspects. Two circular cylinder are the most typical shapes among others and numerous efforts have been devoted to clarify complex character of the flow associated with separation. Zdravkovich [1] has reviewed investigations upto 1977. Since then, many papers have discussed the flow interaction between two circular cylinders [2–7]. Flow in tube banks and flow-induced vibration of tubes therein are the important problems to be considered for design and manufacture of heat exchangers [8–13].

The flow interactions between noncircular bluff bodies also have been investigated by numerous investigators. The drag force on groups of normal flat plates was measured by Ball, et al. [14], Hayashi, et al. [16] and Kamemoto, et al. [16]. Reference [16] reported vortex shedding behavior. The flow interaction between two rectangular cylinders was investigated by Kobayashi [17] and Sykes [18]. Three-dimensional flow over buildings and structures was examined by Lee, et al. [19] and Azuma, et al. [20] among others. Interference drag of two bluff bodies is cited in a book by Hoerner [21]. In spite of these numerous efforts, the flow interaction between two bluff bodies (especially noncircular bodies) still remains one of the very important fluid-mechanical problems to be understood, because of the complicated nature of the separated flow.

In the present paper, the flow aroud two elliptic cylinders in tandem arrangement is described based on measurements of the static pressure distribution and the corresponding fluid-dynamic coefficients. Flow around an elliptic cylinder has been investigated by numerous authors [21–29]. It is well known that the drag coefficient of an elliptic cylinder at small angles of attack is less than that of a circular cylinder, and the heat transfer capability of the former is higher than or comparable to that of the latter [30, 31]. Knowledge of the flow and heat transfer characteristics of an elliptic cylinder may be useful in developing high performance heat exchangers. For such a purpose, however, it is basically necessary to clarify the flow interference among a group of elliptic cylinders. Unfortunately, there is very little information available in this area.

The purpose of the present study is to investigate the flow interference between two elliptic cylinders in tandem arrangement in a uniform flow of air. The elliptic cylinders examined have an axis ratio of 1:3. Although an infinite number of relative positions between the two elliptic cylinders are possible, in the present study they are arranged in the following way: The line through the centers of the elliptic cylinders is aligned with the flow direction and their angle of attack is the same (Fig. 1).

Experimental Apparatus and Technique

The experiments were conducted in a low speed open circuit wind tunnel. Its closed test section is 150 mm wide, 500 mm high, and 800 mm long. The free stream velocity U_∞ was varied from about 8 m/s to 37 m/s with the corresonding Reynolds number based on the major axis of the cylinder varying from about 27000 to 120000. The free stream turbulence intensity ranged from 0.2 to 0.8 percent [32].

The two elliptic cylinders examined have an axis ratio of 1:3, the major axis being 50 mm and the spanwise length 150 mm, which gives an aspect ratio 3. The two cylinders were made of Fiber-Reinforced-Plastic (F.R.P.) by the following procedure. A basic ellipitic cylindner was first constructed of a thin balsa plate, ribbed with other balsa plates, on which thirty copper pipes of 3 mm outer diameter were put side by side. Next the F.R.P. was applied to that cylinder and its surface was manually finished. Finally thirty pressure holes of 0.3 mm diameter were drilled. The pressure taps were arranged spirally

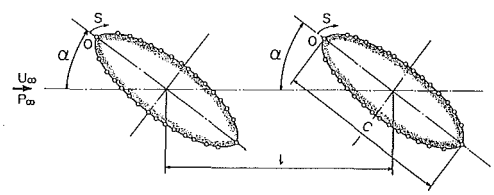

Fig. 1 Arrangement of two elliptic cylinders and coordinate system

[1] Presently, Professor, Department of Mechanical Engineering, Faculty of Engineering, Tohoku University, Sendai 980, Japan.

Contributed by the Fluids Engineering Division for publication in the JOURNAL OF FLUIDS ENGINEERING. Manuscript received by the Fluids Engineering Division, August 8, 1984.

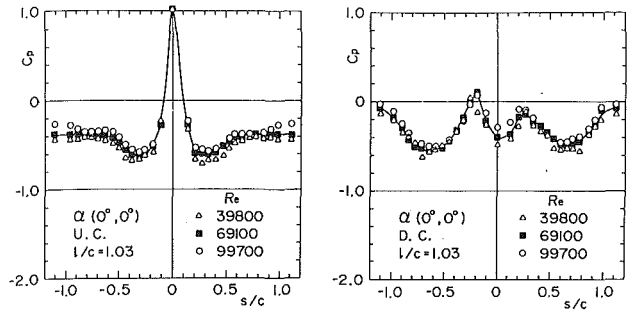

Fig. 2 Pressure distribution

on the surface in order to reduce their mutual interference. The pressure distribution was measured with two water-multimanometers. The drag, lift, and moment coefficients, C_D, C_L, and C_M, based on the major axis of the elliptic cylinder were evaluated from the pressure distribution by numerical integrations. The moment coefficient around the cylinder center is defined positive in the counterclockwise direction. The drag coefficient does not account for the surface skin friction. The position of zero angle of attack was carefully determined by comparing the pressure distributions on two sides of the cylinder. Furthermore, comparisons of the present results for each single cylinder with previous data confirm a reasonable accuracy of the present elliptic cylinders. The cylinder spacing l defining the distance between centers of the cylinders was varied from 1.03 to 4.0 times the major axis c and the angle of attack α (described (α,α) in the figures) was changed from 0 to 90 deg at 15 deg interval, though some additional experiments were conducted at $\alpha = 5$, 10 and 20 deg.

Uncertainty of the present data depends upon several factors: manufacturing accuracy of the elliptic cylinder, reading error of the manometer and accuracy of the arrangement of the elliptic cylinders. The accuracy of the pressure coefficient is estimated to be about ± 3 to ± 5 percent with the corresponding uncertainty of the fluid-dynamic coefficients of C_D, C_L, and C_M at about ± 5 to ± 8 percent. Their uncertainty may exceed ± 10 percent in the critical Reynolds number regime, where the flow around two cylinders is very unstable. In the present paper, the critical Reynolds number is defined as the value of Re, at which the pressure distribution varies drastically. Furthermore, uncertainty of the results for the downstream cylinder may exceed ± 10 percent in the neighborhood of the critical spacing, at which the so-called jumping phenomenon occurs and the flow is unstable. The accuracy of the angle of attack is about ± 0.25 deg, and that of the cylinder spacing about ± 3 percent. The pressure coefficients and the corresponding fluid-dynamic coefficients are uncorrected for the tunnel wall effects. The blockage ratio varies from 0.03 at $\alpha = 0$ deg to 0.10 at $\alpha = 90$ deg.

Experimental Results and Discussion

Pressure Distribution. Figure 2 shows representative examples of the pressure distribution for $\alpha = 0$ deg and $l/c = 1.03$ at several Reynolds numbers. In general, the pressure distribution exhibits no essential dependency upon the

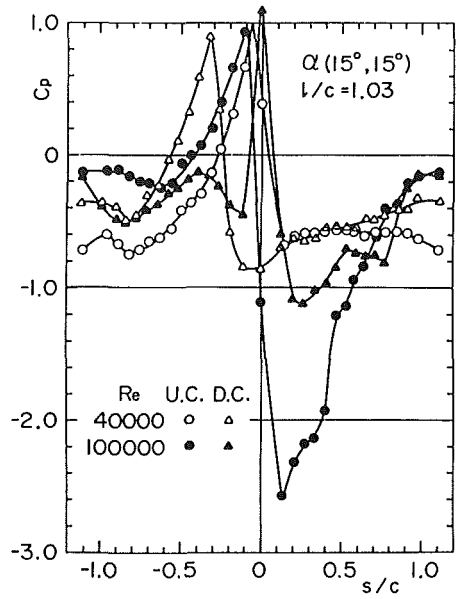

Fig. 3 Pressure distribution

Reynolds number in the present experimental range, though the critical Reynolds number regime is an exception as shown later. C_p of the upstream cylinder (*UC* for brevity hereafter) for $\alpha = 0$ deg and $l/c = 1.03$ (smallest spacing in the study) is almost equal to that of the single cylinder in spite of an existence of the downstream cylinder. The flow separates near the minor axis and C_p is essentially constant in the separated flow region. At Re = 99700, C_p increases slightly in the neighborhood of the trailing edge. It suggests that the flow around the cylinder reaches an initial state of the critical flow. Such a supposition may be reasonable since Schubauer [25] reported previously that the flow around an axis ratio of 1:2.96 at $\alpha = 0$ deg reaches the critical state at Re = 85000 to 312000.

On the other hand, C_p of the downstream cylinder (DC hereafter) is quite different from that of the single cylinder or UC. Two shear layers separated from UC attach onto DC at about $s/c = \pm 0.2$ where C_p attains its maxima. The flow between two cylinders is relatively slow moving because of the very small spacing and then C_p reaches a mimimum at the leading edge. C_p downstream of the attachment point decreases with the surface distance, reaches a minimum near the minor axis and subsequently increases to the trailing edge. It is well known that the separated shear layer is very unstable and immediately transits to a turbulent layer. Therefore, the flow attached onto DC may be highly turbulent and be able to move along the surface against an unfavorable pressure gradient. It results in a downstream shift of the separation point as forming a small wake behind DC.

Figure 3 represents the pressure distribution for $\alpha = 15$ deg and $l/c = 1.03$. It shows a great difference of C_p at Re = 40,000 and 100,000. It has been reported by the present authors [33] that the flow around an elliptic cylinder of axis ratio 1:3 reaches the critical state at about Re = 80,000 for

Nomenclature

c = major axis of elliptic cylinder
C_D, C_L, C_M = drag, lift and moment coefficents = $D/\frac{1}{2}\rho U_\infty^2 c, L/\frac{1}{2}\rho U_\infty^2 c, M/\frac{1}{2}\rho U_\infty^2 c^2$
C_p = pressure coefficient = $(P-P_\infty)/\frac{1}{2}\rho U_\infty^2$
D,L,M = drag, lift and moment
l = distance between two cylinder centers
P_∞, U_∞ = static pressure and velocity of upstream uniform flow, respectively
Re = Reynolds number = $U_\infty c/\nu$
s = surface distance from leading edge, taken positive along suction side
α = angle of attack
ρ,ν = density and kinematic viscosity of air

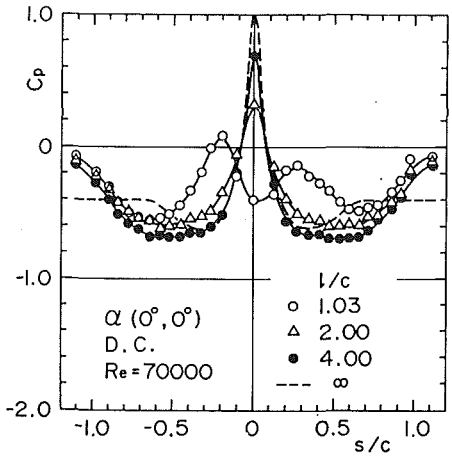

Fig. 4 Effects of *l/c* on pressure distribution

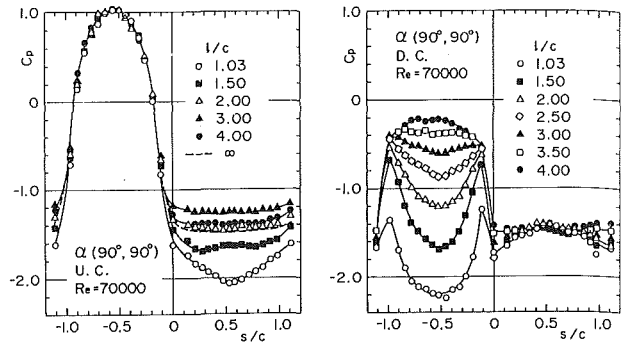

Fig. 5 Effects of *l/c* on pressure distribution

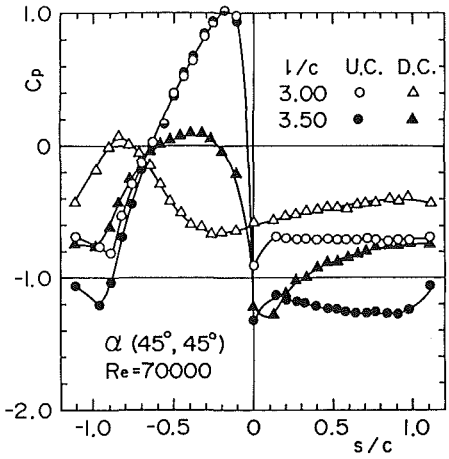

Fig. 6 Pressure distribution

α = 15 deg and that the critical Reynolds number depends strongly upon the angle of attack. The results for UC show that the critical flow state is reached at Re = 100,000 even though DC exists.

At Re = 40,000, the flow aound UC separates at about s/c = 0.2 and −1.0, and the separated shear layer from the pressure side attaches onto DC at about s/c = −0.3. However it seems that the shear layer separated from the suction side does not attach onto DC but rolls up behind it. Then C_p on the suction side of DC increases on the downstream side, suggesting a downstream shift of the separation point. On the pressure side of DC, the flow separates at about s/c = −0.9, whose location is almost equal to that on UC. At this subcritical Reynolds number, the flow between two cylinders may be relatively slow moving as at α = 0 deg shown in Fig. 2.

On the other hand, at Re = 100,000 the flow around UC is clearly the critical state. The flow on the suction side separates in a laminar state at about s/c = 0.3. The separated shear layer transits to the turbulent one immediately downstream of the separation point and reattaches to the surface at about s/c = 0.5 as forming a so-called separation bubble, whose existence is confirmed with a surface oil flow pattern on the present study. Subsequently, a turbulent boundary layer develops downstream and separates finally in the neighborhood of the trailing edge. The flow on the pressure side seems to separate laminarly at about s/c = −0.9. Such a drastic change of the flow around UC brings about a complicated flow around DC. That is, an oncoming flow to DC is accelerated near the leading edge of UC and approaches the leading edge of DC as it attains a narrow high peak of C_p there. On the suction side of DC, C_p decreases steeply from a maximum at the leading edge to a minimum around s/c = 0.25, increases downstream and then shows no essential variation between about s/c = 0.5 to 0.75. Subsequently, C_p again increases steeply toward the trailing edge. Such a profile of C_p suggests an existence of a separation bubble even on the suction side of DC. It may be reasonable to suppose that the flow separates near s/c = 0.5 and reattaches to the surface at about s/c = 0.75, forming a separation bubble which is confirmed with a surface oil flow pattern. The separated shear layer from the suction side of UC attaches onto DC at about s/c = −0.4 where C_p attains a maximum. However, the shear layer separated from the pressure side of UC seems not to attach onto DC but to roll up behind DC forming a vortex street. As found later, the critical flow is reached at small angles of attack ($\alpha \leqq$ 15 deg) in the present range of Re. In general, the pressure distribution shows no essential dependency upon Re except in the critical Reynolds number regime at $\alpha \leqq$ 15 deg.

Figures 4 and 5 represent examples of effects of the cylinder spacing upon the pressure distribution. Figure 4 shows a case of DC at α = 0 deg and Re = 70,000. The cylinder spacing has no any effect upon the pressure distribution on UC at α = 0 deg. Thus, the results are omitted in this paper. At a spacing as small as l/c = 1.03, two separated shear layers from UC attach onto DC and C_p reaches two peaks at about s/c = ±0.2. As l/c increases, the separated shear layers from UC roll up in front of DC and C_p attains a maximum at the leading edge, though its values is quite lower than unity even at l/c = 4.0. DC locates in a wake of UC which is highly turbulent. Accordingly the flow around DC attaches along the surface and resulting in a very narrow wake behind it. These flow features are examined with a flow visualization using aluminum powders floating on an open water channel.

Figure 5 shows a case of α = 90 deg. C_p on the upstream surface of UC is independent of l/c but not the case on the downstream one as demonstrated in the figure. The base pressure coefficient of UC varies greatly with l/c and C_p inside the separated flow region is relatively uniform at $l/c > 1.5$. However, at l/c = 1.03, the flow between the cylinders is relatively slow moving and the main flow is scarcely entrained into the separated flow region. This results in a minimum pressure at the downstream stagnation point. On the contrary, the flow around DC varies with l/c, especially on the upstream surface. At smaller spacing of $l/c \leqq$ 3.0, two shear layers separate from UC, attach onto DC and its locations seem not to move with l/c. C_p at the attachment points, however, decreases as decreasing l/c. It may be due to the fact that at α = 90 deg, the wake produced behind UC is very large. Consequently, as l/c decreases, the inner part of the separated shear layer attaches onto DC and the main flow is scarcely entrained into the separated flow region between the two cylinders. At l/c = 3.5, C_p on the upstream surface becomes fairly uniform. It suggests that two separated shear layers from UC roll up in front of DC and wash out there. Results at l/c = 4.0 represent clearly such the flow feature. The oncoming flow to DC may become a relatively uniform one and C_p attains a

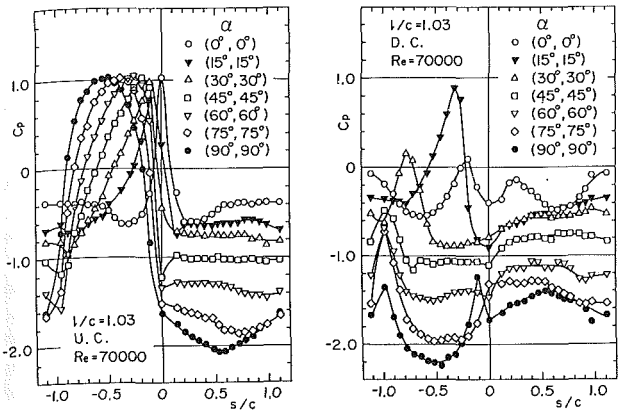

Fig. 7 Effects of α on pressure distribution

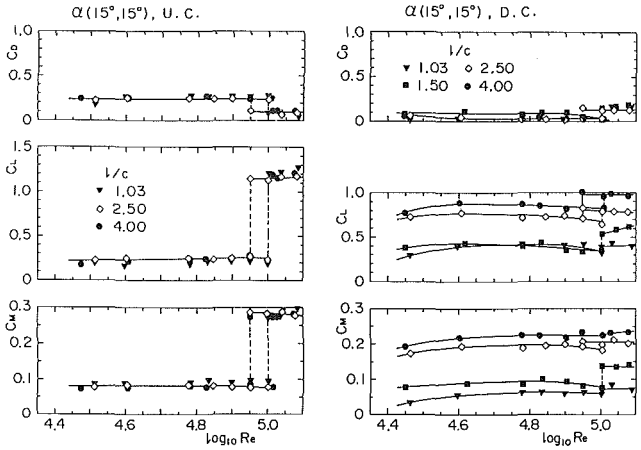

Fig. 8 Variations of C_D, C_L, and C_M with Re

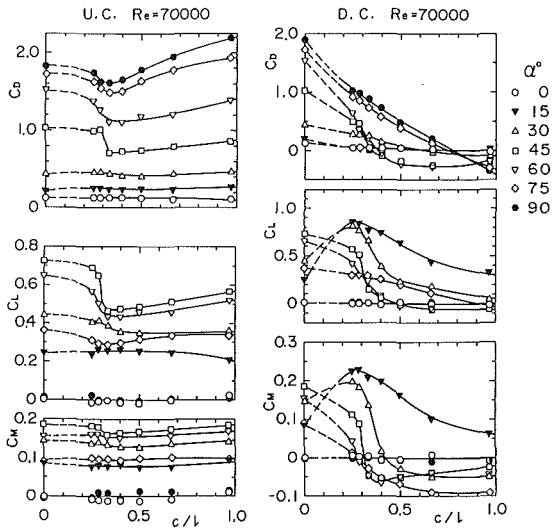

Fig. 9 Variations of C_D, C_L, and C_M with *l/c*

maximum at the upstream stagnation point ($s/c = -0.55$). On the downstream surface of DC at small spacings, C_p reaches a maximum at the downstream stagnation point, since two separated shear layers from UC roll up behind DC. But at $l/c = 3.5$ and 4.0, C_p in the separated flow region is essentially constant, because the flow on it separates near the major axis points.

It is well known for two circular cylinders in tandem arrangement that there exists a critical spacing, say about $l/d = 3.8$, at which the flow around two circular cylinders changes discontinuously, d being the cylinder diameter [1]. Figure 6 represents a comparison of the results at $l/c = 3.0$ and 3.5 both for UC and DC. The angle of attack selected is 45 deg, since a discontinuous variation of the fluid-dynamic coefficient at the critical spacing is the largest, as shown later. It describes that the flow around two elliptic cylinders in tandem arrangement varies drastically between $l/c = 3.0$ and 3.5 in a similar way for two circular cylinders. At $l/c = 3.0$, the shear layer separated from UC near the trailing edge attaches onto DC at about $s/c = -0.8$ where C_p becomes a maximum, but a variation of C_p on the suction side of DC is very small. The shear layer separated from UC near the leading edge seems not to attach onto DC but to roll up behind it.

On the other hand, at $l/c = 3.5$, the base pressure of UC decreases greatly, though C_p on the pressure side change very little. Furthermore, the pressure distribution around DC varies in a quite different manner from that at $l/c = 3.0$. C_p attains a maximum upstream of the minor axis on the pressure side. This suggests that two separated shear layers from UC roll up ahead of DC. C_p on the suction side is much lower than at $l/c = 3.0$ and increases to the downstream as suggesting a downstream shift of the separation point. It has been found that at this critical spacing, the flow around DC is severely unstable. The flow around the cylinder fluctuates intermittently with time from the flow found just before the fluctuation to that just after. This results in a very large fluctuation of the fluid-dynamic coefficients, though the resusts are omitted in this paper.

Shown in Fig. 7 are typical examples of effects of the angle of attack upon the pressure distribution at a subcritical Reynolds number, where the Reynolds number has no essential effects upon it. The pressure distribution on the pressure side of UC shows no essential variation with the cylinder spacing even at a very narrow one such as $l/c = 1.03$. It is clear that the upstream stagnation point shifts from the leading edge at $\alpha = 0$ deg to the minor axis at $\alpha = 90$ deg and C_p in the separated flow region decreases as α increases. Furthermore, at larger angles of attack, C_p in the separated flow region is not uniform and reaches a minimum at some point depending on α.

On the other hand, the C_p-distribution on DC shows a complicated profile. At $\alpha = 0$ deg, two separated shear layers from UC attach onto DC at about $s/c = \pm 0.2$ and C_p becomes a maximum there. However, with increasing α, one of the separated shear layers does not attach onto DC but rolls up behind it. That from the pressure side of UC attaches onto DC and its location moves downstream as α increases. However, at larger angles of attack than 30 deg, its location seems to be indepedent of α, say about $s/c = -1.0$. On the suction side of DC, C_p varies complicatedly with α and is not uniform except at $\alpha = 45$ deg. This may originate from a rolling-up of the separated shear layer from UC near the suction surface of DC. At $\alpha = 90$ deg, the inner parts of two separated shear layers from UC attach onto DC at about $s/c = -0.1$ and -1.0 and values of C_p at the attachment points are quite lower than at other angles of attack. In general, C_p in the separated flow region decreases with an increase of α. This may be due to the fact that as α increases, the wake behind UC increases its width and then inner parts of the separated shear layers approach DC and roll up behind it.

Drag, Lift, and Moment Coefficients. Shown in Fig.8 are representative examples of the drag, lift and moment coefficients for $\alpha = 15$ deg at various cylinder spacings. As previously described for the pressure distribution in Fig. 3, the critical Reynolds number exists at $\alpha = 15$ deg and the pressure distribution varies drastically. In accordance with such a variation, C_D, C_L, and C_M change discontinuously from about Re = 90,000 to 100,000 both for UC and DC. C_D decreases discontinuously for UC but increases for DC. C_L and C_M increase both for UC and DC. It may be detected in

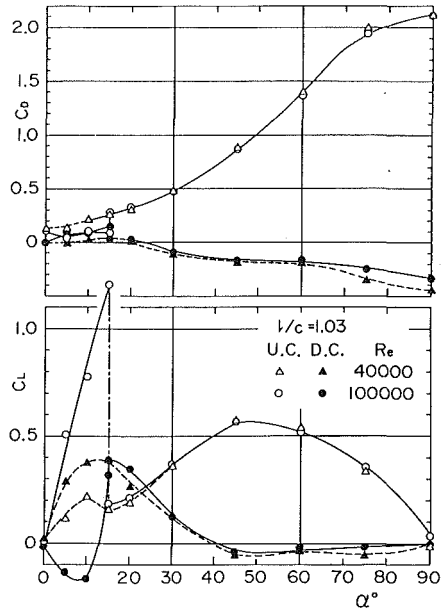

Fig. 10 Variations of C_D and C_L with α

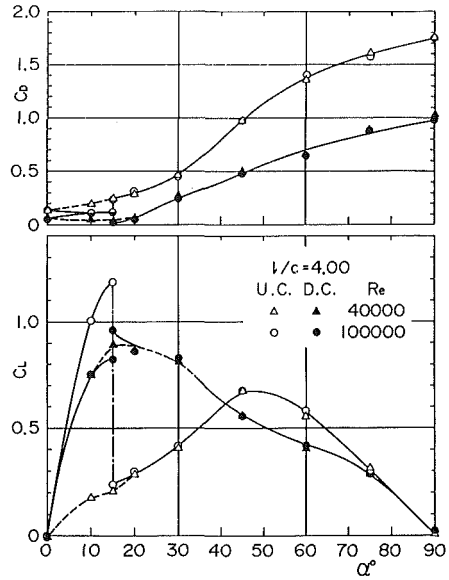

Fig. 11 Variations of C_D and C_L with α

the figure that a magnitude of sudden variations of C_D, C_L, and C_M at the critical Reynolds number is larger for UC compared to DC. At the subcritical Reynolds number, the fluid-dynamic coefficients for UC show no dependency upon the cylinder spacing. However as to DC, they are strongly dependent upon the cylinder spacing. For both cylinders, variations of C_D, C_L, and C_M with Re are, in essence, small at the subcritical Reynolds number.

Figure 9 represents variations of C_D, C_L, and C_M with the cylinder spacing l/c at Re = 70,000, which is the subcritical Reynolds number for UC at all the angles of attack. As far as UC is concerned, at α = 0 deg and 15 deg, C_D, C_L, and C_M show no essential variation with l/c. However, at larger angles of attack, as l/c increases from 1.03, they decrease slightly, reach minimums at about l/c = 3.0 and subsequently increase steeply beyond l/c = 3.0. Its increasing rate is largest for α = 45 deg. Such a discontinuous variaton is originated from the so-called jumping phenomenon, where two separated shear layers from UC roll up in front of DC. Accordingly UC sheds a vortex pair from both sides of the cylinder. The critical spacing for the present two elliptic cylinders having an axis ratio of 1:3 is, in an exact sense, dependent on α. That is, it generally increases with α. However, in a region from α = 30 to 75 deg, its dependency upon α is very weak and is approximately equal to 3.0. Its value is, in appearance, smaller than l/d = 3.8 for two circular cylinders in tandem arrangement [1]. However, when the cylinder spacing is normalized with a diameter d of a circular cylinder whose circumferential length is equal to that of the present elliptic cylinder of axis ratio 1:3, the critical spacing becomes l/d = 4.2, which is fairly close to 3.8 for two circular cylinders. As l/c increases beyond 3.5, the fluid-dynamic coefficients for UC are nearly equal to those for the single cylinder.

On the other hand, for DC, characteristic variations of C_D, C_L, and C_M with l/c are very complicated compared to those for UC and represent a strong dependency upon α. It is clear that the drastic variation of the flow around UC brings about a similar steep change of the flow around DC. In general, as l/c increases, C_D, C_L, and C_M first increase gradually, then increase steeply at the critical spacing but their values beyond that spacing are smaller than those for the single cylinder, though several exceptional cases are detected clearly . That is, C_D at α = 45 and 60 deg shows no essential variation for $l/c \leqq$ 2.0 and its value is negative. Furthermore, C_M at α = 45 and 60 deg decreases with increasing l/c in a region of $l/c \leqq$ 2.5. The most distinguished cases are the resuslts of C_L and C_M at α = 15 and 30 deg. They reach maxima beyond the critical spacing and their values are much higher than those for the single cylinder. The oncoming flow to DC is highly turbulent and then the critical flow may be attained even at Re = 70,000, resulting in higher values of C_L and C_M at α = 15 and 30 deg. Near the critical spacing, say at l/c = 3.0 and 3.5, the flow around DC is very unstable. The shear layers separated from UC roll up intermittently upstream of DC and the pressure fluctuation around it is very severe. Accordingly, the corresponding fluid-dynamic coefficients also fluctuate severely and their values of l/c = 3.0 and 3.5 shown in Fig. 9 are mean values.

Figures 10 and 11 demonstate variations of C_D and C_L with α at Re = 40,000 and 100,000. The later Reynolds number brings about the critical flow both around UC and DC at 0 deg $< \alpha \leqq$ 15 deg as previously described in relation to the pressure distribution. At the small spacing of l/c = 1.03, the characteristic variations of C_D and C_L are quite different for UC an DC. At the subcritical Reynolds number, Re = 40,000, C_D of UC increases monotonically with α from 0.1 at α = 0 deg to 2.1 at α = 90 deg. On the contrary, C_D of DC rather decreases with α and becomes negative at α = 30 deg. It says that the flow around DC originates a thrust force, whose value increases with α since the wake width behind UC increases with it. On the other hand, C_L for UC at Re = 40,000 first increases, reaches a maximum around α = 45 deg and subsequently decreases, though a small hump is found around α = 10 deg. C_L for DC first increases, reaches a maximum around α = 15 deg and then decreases. C_L at larger angles of attack, $\alpha \leqq$ 45 deg, is negative. It may be due to the fact that at higher angles of attack, the shear layer separated from UC near the leading edge rolls up on the suction surface of DC and brings on a high pressure there.

At Re = 100,000, the flow around UC for small angles of attack, $\alpha \leqq$ 15 deg, attains the critical state and a small separation bubble is formed on the suction side of the cylinder [33]. This results in a great movement of the turbulent separation point to the downstream. Such a drastic change of the flow brings about a slight decrease of C_D and is a large increase of C_L with α in a region of $\alpha \leqq$ 15 deg. The maximum value of C_L reaches about 1.2 at α = 15 deg. At higher angles of attack, $\alpha >$ 15 deg, both values of C_D and C_L are almost equal to those at the subcritical Reynolds number, Re = 40,000. As far as DC is concerned, the complicated flow is originated from the sudden change of the flow around UC. As

α increases from 0 deg, C_D first shows a slight increase, decreases suddenly at $\alpha = 15$ deg and subsequently becomes almost equal to that for the subcritical Reynolds number beyond $\alpha = 15$ deg. C_L, on the other hand, first decreases from 0 at $\alpha = 0$ deg to -0.15 at $\alpha = 10$ deg, increases steeply to 0.3 at $\alpha = 15$ deg and subsequently becomes equal to that at Re = 40,000 beyond $\alpha = 15$ deg.

At a larger spacing such as $l/c = 4.0$ shown in Fig. 11, the results for UC both at Re = 40,000 and 100,000 show a trend which is essentially the same as at $l/c = 1.03$ shown in Fig 10. However, the results for DC are quite different. The separated shear layers from UC roll up in front of DC. Consequently the oncoming flow to DC becomes relatively uniform but is highly turbulent. It may result in a flow around DC which resembles the critical flow even at a low Reynolds number of 40,000 in a region of $\alpha \leqq 30$ deg. Accordingly, the results for DC at Re = 40,000 are in good agreement with those at Re = 100,000, where the critical flow occurs both around UC and DC. The results of C_M show very similar features to C_L, and they are omitted in the present paper.

Concluding Remarks

Flow around two elliptic cylinders having an axis ratio of 1:3 in tandem arrangement is experimentally examined. In general, effects of the Reynolds number are found to be small in the experimental range, though at small angles of attack, $\alpha \leqq 15$ deg, the critical flow is attained at higher Reynolds number and a great influence of Re upon the flow around UC and also DC is observed.

The flow around UC shows generally a weak dependency upon the cylinder spacing l/c except at large angles of attack, in which a very large wake is formed behind UC. On the other hand, the flow around DC exhibits a very complicated variation with l/c. The strong dependency upon l/c originates from the fact that, at small spacings, the separated shear layers from UC attach onto DC and the flow between two cylinders is relatively slow moving, and at large spacings, two shear layers roll up in front of DC. It is found that the so-called jumping phenomenon of the flow occurs at the critical spacing, whose dependency upon α is relatively weak.

Acknowledgments

The present authors express their sincere thanks to Mr. N. Kon and our former students Messrs. Y. Taoka, K. Miyoshi, and T. Toba for their assistance in the experiments.

References

1 Zdravkovich, M. M., "Review of Flow Interference Between Two Circular Cylinders in Various Arrangements," ASME JOURNAL OF FLUIDS ENGINEERING, Vol. 99, 1977, pp. 618-633.

2 Okajima, A., "Flows Around Two Tandem Circular Cylindrs at High Reynolds Numbers," *Trans. JSME*, Vol. 44, 1978, pp. 2663-2671.

3 Kiya, M., Arie, M., Tamura, H., and Mori, H., "Vortex Shedding From Two Circular Cylinders in Staggered Arrangement," ASME JOURNAL OF FLUIDS ENGINEERING, Vol. 102, 1980, pp. 166-173.

4 Igarashi, T., "Flow Characteristics Around Two Circular Cylinders in Cross Flow (1st Report)," *Trans. JSME*, Vol. 46, 1980, pp. 1026-1036.

5 Arie, M., Kiya, M., Moriya, M., and Mori, H., "Pressure Fluctuations on the Surface of Two Circular Cylinders in Tandem Arrangement," ASME JOURNAL OF FLUIDS ENGINEERING, Vol. 105, 1983, pp. 161-167.

6 Quadflieg, H., "Wirbelinduzierte Belastungen eines Zylinderpaares in inkompressibler Strömung bei grossen Reynoldszahlen," *Forsch. Ing. Wes.*, Vol. 43, 1977, pp. 9-18.

7 El-Taher, R. M., "Experimental Study of Interaction Between a Pair of Circular Cylinders Normal to a Uniform Shear Flow," *J. Wind Eng. Ind. Aerodyn.*, Vol. 17, 1984, pp. 117-132.

8 Ishigai, S. Nishikawa, E., Nishimura, K., and Cho, K., "Experimental Study of Structure of Gas Flow From in Tube Banks With Tube Axis Normal to Flow (Part 1)," *Trans. JSME*, Vol. 37, 1971, pp. 2319-2326.

9 Nishikawa, E., and Ishigai, S., "Structure of Gas Flow and Its Pressure Loss in Tube Banks With Tube Axes Normal to Flow," *Trans. JSME*, Vol. 43, 1977, pp. 3310-3317.

10 Chen, S. S., "Dynamics of Heat Exchanger Tube Banks," ASME JOURNAL OF FLUIDS ENGINEERING, Vol. 99, 1977, pp. 462-469.

11 Savkar, S. D., "A Brief Review of Flow Induced Vibrations of Tube Arrays in Cross-Flow," ASME JOURNAL OF FLUIDS ENGINEERING, Vol. 99, 1977, pp. 517-519.

12 Fitzpatrick, J. A., and Donaldson, I. S., "A Preliminary Study of Flow and Acoustic Phenomena in Tube Banks," ASME JOURNAL OF FLUIDS ENGINEERING, Vol. 99, 1977, pp. 681-686.

13 Ball, D. J., and Hall, C. D., "Drag of Yawed Pile Groups at Low Reynolds Numbers," *ASCE J. Waterway, Port, Coastal and Ocean Division*, Vol. 106, 1980, pp. 229-238.

14 Ball, D. J., and Cox, N. J., "Hydrodynamic Drag Forces on Groups of Flat Plates," *ASCE J. Waterway, Port, Coastal and Ocean Division*, Vol. 104, 1978, pp. 163-173.

15 Hayashi, M., Sakurai, A., and Ohya, Y., "Wake Interference of a Row of Normal Flat Plates Arranged Side by Side in a Uniform Flow," *Trans. Japan Soc. Aero. Space Sci.*, Vol. 26, 1983, pp. 22-36.

16 Kamemoto, K., Ozawa, N., and Suzuki, R., "Numerical Experiments on an Unsteady Separated Flow Behind Two Flat Plates in a Side-by-Side Arrangement Using the Discrete Vortex Method (Part 1)," *Trans. JSME*, Vol. 49, 1983, pp. 1619-1629.

17 Kobayahi, T., "Characteristics of Fluid-Dynamic Forces Acting on Circular or Square Cylinders in Close Proximity," *Trans. JSME*, Vol. 42, 1976, pp. 1452-1461.

18 Sykes, D. M., "Interference Effects on the Response of a Tall Building Model," *J. Wind Eng. Ind. Aerodyn.*, Vol. 11, 1983, pp. 365-380.

19 Lee, B. E., and Soliman, B.F., "An Investigation of the Forces on Three Dimensional Bluff Bodies in Rough Wall Turbulent Boundary Layers," ASME JOURNAL OF FLUIDS ENGINEERING, Vol. 99, 1977, pp. 503-510.

20 Azuma, A., Iuchi, M., Watanabe, I., et al., "Wind Tunnel Investigations on Buildings and Structures," *J. Japan Soc. Aero. Space Sci.*, Vol. 22, 1974, pp. 290-295.

21 Hoerner, S. F., *Fluid-Dynamic Drag*, Published by the Author, 1958.

22 Zahm, A. F., Smith, R. H., and Louden, F. A., "Forces on Elliptic Cylinders in Uniform Air Stream" NACA Tech. Rep. No. 289, 1928.

23 Warden, R., "Resistance of Certain Strut Forms," ARC R&M, No. 1599, 1934.

24 Schubauer, G. B., "Air Flow in a Separating Laminar Boundary Layer," NACA Tech. Rep. No. 527, 1935.

25 Schubauer, G. B., "Air Flow in the Boundary Layer of an Elliptic Cylinder," NACA Tech. Rep. No. 652, 1939.

26 Williams, D. H., and Brown, A. F., "Experiments on an Elliptic Cylinder in the Compressed Air Tunnel," ARC R&M, No. 1817, 1937.

27 Modi, V. J., and Wiland, E., "Unsteady Aerodynamics of Stationary Elliptic Cylinders in Subcritical Flow," *AIAA J.*, Vol. 8, 1970, pp. 1814-1821.

28 Modi, V. J., and Dikshit, A. K., "Near Wakes of Elliptic Cylinders in Subcritical Flow," *AIAA J.*, Vol. 13, 1975, pp. 490-497.

29 Modi, V. J., and Ieong, L., "On Some Aspects of Unsteady Aerodynamics and Vortex Induced Oscillations of Elliptic Cylinders at Subcritical Reynolds Number," ASME *Journal of Mechanical Design*, Vol. 100, 1978, pp. 354-362.

30 Ota, T., Aiba, S., Tsuruta, T., and Kaga, M., "Forced Convection Heat Transfer From an Elliptic Cylinder of Axis Ratio 1:2," *Bull. JSME*, Vol. 26, 1983, pp. 262-267.

31 Ota, T., Nishiyama, H., and Taoka, Y., "Heat Transfer and Flow Around an Elliptic Cylinder," *Int. J. Heat Mass Transfer*, Vol. 27, 1984, pp. 1771-1779.

32 Ota, T., and Itasaka, M., "A Separated and Reattached Flow on a Blunt Flat Plate," ASME JOURNAL OF FLUIDS ENGINEERING, Vol. 98, 1976, pp. 79-86.

33 Ota, T., and Taoka, Y., "Flow Around Two Elliptic Cylinders," Preprint of JSME Meeting, No. 820-10, 1982, pp. 1-3.

Mean Flow Effects on the Low-Wavenumber Pressure Spectrum on a Flexible Surface

A. P. Dowling
The University Engineering Department,
Cambridge CB2 1PZ, England

The Lighthill theory is extended so that it may be used to determine the flow noise induced by a turbulent boundary layer over a plane homogeneous flexible surface. The influence of the surface properties and the mean flow on the sound generation is brought out explicitly through the use of a Green function. The form of the low-wavenumber wall-pressure spectrum on a rigid surface with an arbitrary mean flow profile is determined. The effect of a coating layer is investigated.

1 Introduction

The sound generated by a turbulent boundary layer is influenced by surface flexibility and by the mean flow. We derive an expression for the low-wavenumber wall pressure spectrum in terms of a Green function and nonlinear sources. The Green function brings out explicitly the influence of both the mean flow profile and surface flexibility. Chase and Noiseux [1] investigated the influence of a mean flow profile on the hard wall pressure spectrum. We extend that work to include surface compliance and investigate singularities in the surface pressure spectrum.

In underwater problems the Mach number of the mean flow is very small, and for low wavenumbers the flow only has an appreciable effect for spectral components whose surface phase speeds are nearly equal to the speed of sound. When the flow profile over a hard surface is neglected Ffowcs Williams [2] found that the pressure spectrum for these modes had a nonintegrable singularity. Bergeron [3] analyzed this singularity in more detail and showed that it arose from a two-dimensional form of Olbers' paradox because the turbulent source region is considered to be of infinite extent and the sound field from each source element does not decrease rapidly enough for the intergrated effect to be finite. In this paper we include the effect of an arbitrary mean boundary layer profile. It is found that this eliminates the singularity for all upstream propagating elements but enhances it for downstream propagating elements. For these downstream propagating components the singularity in the pressure spectrum is a double pole, and is stronger than the single pole found for uniform flow by Ffowcs Williams. This singularity is due to a "trapped" mode, which propagates downstream supersonically in the boundary layer and subsonically in the flow outside it. The energy in this mode therefore remains trapped near the surface and only decays slowly with distance from the source. The influence of the boundary layer on these sonic elements is found to depend only on the free stream velocity and the displacement thickness of the boundary layer and to be independent of the details of the mean flow profile.

Dowling [4] modelled the effect of the flow profile for long wavelength modes by a vortex sheet positioned at a height h above the surface. Consideration of an arbitrary mean flow profile shows that the vortex sheet result always describes the effect of a mean flow profile on the spectral elements with sonic phase speeds (the only elements much influenced by the mean flow), even when the boundary layer height is not small compared with the surface wavelength. This is because modes with sonic surface wave speeds have infinite wavelengths normal to the surface. In particular, by solving the problem for an arbitrary mean flow profile, we find where the equivalent vortex sheet should be positioned; at a height h above the surface equal to the boundary layer displacement thickness.

The influence of a coating layer over a hard surface is investigated. It is found that if the sound speed in the coating is greater than that in the fluid it is possible for the coating to eliminate the singularity for downstream propagating modes. A coating with a low sound speed has an adverse effect on the surface pressure and can even introduce new singularities into the wall pressure spectrum.

2 The Surface Pressure on a Flexible Wall

Consider a turbulent boundary layer flow over a plane, homogeneous, flexible wall. In our problem the flexible wall is assumed to be only linearly disturbed from it rest position

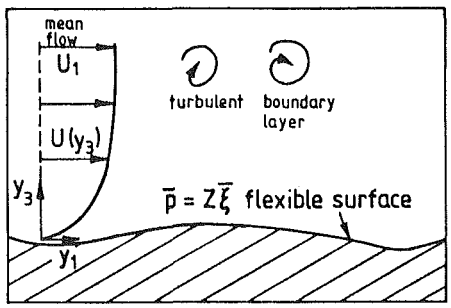

Fig. 1 The geometry of the flexible surface and turbulent boundary layer

Contributed by the Fluids Engineering Division for publication in the JOURNAL OF FLUIDS ENGINEERING. Manuscripts received by the Fluids Engineering Division, August 8, 1984.

$y_3 = 0$, and the mean flow $U(y_3)$ is assumed to be a function of y_3 only, as shown in Fig. 1. Far from the surface $U(y_3)$ tends to the free-stream velocity U_1 and $U(0) = 0$. The impedance is uniform over the whole surface and the relationship between surface pressure perturbation p' and displacement ξ can be conveniently expressed in terms of their Fourier transforms:

$$\bar{p}(0,\mathbf{k},\omega) = Z(\mathbf{k},\omega)\bar{\xi}(\mathbf{k},\omega) \tag{1}$$

where $\bar{p}(y_3,\mathbf{k},\omega) = \int p'(\mathbf{y},\tau)e^{-i(\omega t + k_1 y_1 + k_2 y_2)}dy_1 dy_2 dt$.

We write the instantaneous particle velocity as $\{U(y_3),0,0\} + \mathbf{u}'$. Then by differentiating the equation of mass conservation with respect to time and subtracting from it the divergence of the momentum equation we obtain:

$$\frac{\partial^2\rho}{\partial\tau^2} - U^2\frac{\partial^2\rho}{\partial y_1^2} - 2U\frac{\partial^2(\rho u_i')}{\partial y_1 \partial y_i} - 2\frac{dU}{dy_3}\frac{\partial}{\partial y_1}(\rho u_3') - c_1^2\nabla^2\rho = \frac{\partial^2 T_{ij}}{\partial y_i \partial y_j} \tag{2}$$

$T_{ij} = \rho u_i' u_j' + (p' - c_1^2\rho')\delta_{ij} - \sigma_{ij}$, σ_{ij} is the viscous stress tensor and c_1 is the unperturbed value of the sound speed in the fluid. Finally the mass equation and 3-component of momentum equation can be used to eliminate $\mathrm{div}(\rho\mathbf{u}')$ and $\partial(\rho u_3')/\partial y_1$, respectively, to show that:

$$\frac{1}{c_1^2}\left(\frac{\partial}{\partial\tau} + U\frac{\partial}{\partial y_1}\right)^3\rho + 2\frac{dU}{dy_3}\frac{\partial^2\rho}{\partial y_1 \partial y_3} - \left(\frac{\partial}{\partial\tau} + U\frac{\partial}{\partial y_1}\right)\nabla^2\rho = \frac{1}{c_1^2}\left\{\left(\frac{\partial}{\partial\tau} + U\frac{\partial}{\partial y_1}\right)\frac{\partial^2 T_{ij}}{\partial y_i \partial y_j} - 2\frac{dU}{dy_3}\frac{\partial^2 T_{3j}}{\partial y_1 \partial y_j}\right\} \tag{3}$$

We solve this by introducing $\bar{\rho}(y_3,\mathbf{k},\omega)$ and $\bar{T}_{ij}$ the Fourier transforms of the density perturbation and T_{ij}, respectively. For convenience we take $\bar{\rho} + \bar{T}_{33}/c_1^2$ as our variable. The equation for $\bar{\rho} + \bar{T}_{33}/c_1^2$ can be written in self-adjoint form as:

$$\frac{\partial^2}{\partial y_3^2}\left(\frac{\bar{\rho} + \bar{T}_{33}/c_1^2}{\omega + Uk_1}\right) + f\frac{\bar{\rho} + \bar{T}_{33}/c_1^2}{\omega + Uk_1} = \frac{1}{c_1^2}\left\{\frac{k_\alpha k_\beta \bar{T}_{\alpha\beta} + \gamma^2\bar{T}_{33}}{\omega + Uk_1} - 2ik_\alpha\frac{\partial}{\partial y_3}\left(\frac{\bar{T}_{\alpha 3}}{\omega + Uk_1}\right)\right\} \tag{4}$$

where α and β are summed over 1 and 2,

$$f(y_3,\mathbf{k},\omega) = \frac{(\omega + Uk_1)^2}{c_1^2} - k_1^2 - k_2^2 + \frac{d^2U}{dy_3^2}\frac{k_1}{\omega + Uk_1} - 2\left(\frac{dU}{dy_3}\right)^2\frac{k_1^2}{(\omega + Uk_1)^2}$$

and $\gamma = \{(\omega + Uk_1)^2/c_1^2 - k_1^2 - k_2^2\}^{1/2}$ with the sign of the square root chosen so that γ has the same sign as ω when γ is real and $Im\gamma$ is negative when γ is purely imaginary.

Outside the boundary layer the flow is only linearly disturbed from the free stream velocity $(U_1,0,0)$ and $\bar{T}_{ij} = 0$. Since the disturbances must either decay at large y_3 or be outward propagating sound waves,

$$\frac{\partial\bar{\rho}}{\partial y_3} = -i\gamma_1\bar{\rho} \text{ for large positive } y_3 \tag{5}$$

γ_1, $= \{(\omega + U_1k_1)^2/c_1^2 - k_1^2 - k_1^2\}^{1/2}$, is the limit of γ as y_3 tends to infinity. Very near the surface $y_3 = 0$ the flow is only linearly disturbed and $p' = c_1^2\rho'$. The linearized 3-component of the momentum equation and the surface condition (1) then give:

$$\rho_1\omega^2\bar{\rho} = Z\partial\bar{\rho}/\partial y_3 \tag{6}$$

since $U(0)$ is zero. ρ_1 is the mean value of density in the fluid.

We solve for $\bar{\rho}$ in equation (4) by introducing a Green function $G(y_3,x_3,\mathbf{k},\omega)$ which satisfies:

$$\frac{\partial^2 G}{\partial y_3^2} + fG = \delta(y_3 - x_3) \tag{7}$$

Multiplying equation (7) by $(\bar{\rho} + \bar{T}_{33}/c_1^2)/(\omega + Uk_1)$ and subtracting from it the product of G and equation (4) we obtain:

$$\frac{\bar{\rho} + \bar{T}_{33}/c_1^2}{\omega + Uk_1}(x_3,\mathbf{k},\omega) = \frac{1}{c_1^2}\int\left\{G\frac{k_\alpha k_\beta \bar{T}_{\alpha\beta} + \gamma^2\bar{T}_{33}}{\omega + Uk_1} + \frac{2ik_\alpha}{\omega + Uk_1}\frac{\partial G}{\partial y_3}\bar{T}_{\alpha 3}\right\}dy_3 + \left[\frac{\bar{\rho} + \bar{T}_{33}/c_1^2}{\omega + Uk_1}\frac{\partial G}{\partial y_3} - G\frac{\partial}{\partial y_3}\left(\frac{\bar{\rho} + \bar{T}_{33}/c_1^2}{\omega + Uk_1}\right)\right]_0^\infty \tag{8}$$

The term at $y_3 = \infty$ is zero if we choose a Green function G such that,

$$\partial G/\partial y_3 \to -i\gamma_1 G \quad \text{as} \quad y_3 \to \infty \tag{9}$$

Similary insisting that G satisfies the surface boundary condition:

$$\frac{\partial G}{\partial y_3} = G\left\{-\frac{U'(0)k_1}{\omega} + \frac{\rho_1\omega^2}{Z}\right\} \text{ on } y_3 = 0 \tag{10}$$

($U'(0) = dU/dy_3$ evaluated at $y_3 = 0$) eliminates the contribution to (8) from $y_3 = 0$. These two boundary conditions together with equation (7) completely determine the Green function.

With this particular Green function, equation (8) gives the Fourier transform of the surface pressure perturbation as:

$$\bar{p}(0,\mathbf{k},\omega) = \omega\int\left\{G\frac{k_\alpha k_\beta \bar{T}_{\alpha\beta} + \gamma^2\bar{T}_{33}}{\omega + Uk_1} + \frac{2ik_\alpha}{\omega + Uk_1}\frac{\partial G}{\partial y_3}\bar{T}_{\alpha 3}\right\}dy_3 \tag{11}$$

We now have the surface pressure given explicitly in terms of a Green function and nonlinear sources. It remains to calculate the Green function which we do by the method used by Chase and Noiseux [1].

3 Calculation of the Green Function

$G(y_3,x_3,\mathbf{k},\omega)$ can be expressed in terms of two solutions $E(y_3)$ and $F(y_3)$ of the homogeneous equation:

$$\frac{\partial^2 E}{\partial y_3^2} + fE = 0 \tag{12}$$

where E satisfies the boundary condition at infinity (9),

$$\frac{\partial E}{\partial y_3} = -i\gamma_1 E \quad \text{for large } y_3 \tag{13}$$

and F the surface boundary condition (10):

$$\frac{\partial F}{\partial y_3} = F\left\{-\frac{U'(0)k_1}{\omega} + \frac{\rho_1\omega^2}{Z}\right\} \text{ on } y_3 = 0. \tag{14}$$

Since E and F are only defined to within an arbitrary constant we will choose,

$$E(0) = F(0) = 1 \tag{15}$$

Then $G(y_3,x_3,\mathbf{k},\omega)$ is given by (see for example Morse and Feshbach [5]):

$$G(y_3,x_3,\mathbf{k},\omega) = \begin{cases} F(x_3)E(y_3)/W & y_3 \geq x_3 \\ E(x_3)F(y_3)/W & y_3 \leq x_3 \end{cases} \tag{16}$$

where W is the Wronskian, $F\,\partial E/\partial y_3 - E\,\partial F/\partial y_3$, and is independent of y_3. We will therefore evaluate W on $y_3 = 0$, where the boundary conditions (14) and (15) show that:

$$W = E'(0) + U'(0)k_1/\omega - \rho_1\omega^2/Z \tag{17}$$

$E'(0)$ denotes the value of the derivative $\partial E/\partial y_3$ at $y_3 = 0$. Substitution for W in (16) shows in particular that

$$G(y_3,0,\mathbf{k},\omega) = \frac{E(y_3)}{E'(0) + U'(0)k_1/\omega - \rho_1\omega^2/Z} \tag{18}$$

and the representation (11) becomes:

$$\tilde{p}(0,\mathbf{k},\omega)=\frac{\omega}{E'(0)+U'(0)k_1/\omega-\rho_1\omega^2/Z}$$

$$\times\int\left\{E(y_3)\,\frac{k_\alpha k_\beta\tilde{T}_{\alpha\beta}+\gamma^2\tilde{T}_{33}}{\omega+Uk_1}+\frac{\partial E}{\partial y_3}\,\frac{2ik_\alpha\tilde{T}_{\alpha 3}}{\omega+Uk_1}\right\}dy_3 \qquad (19)$$

This is equivalent to Chase and Noiseux's equation (28) (see reference [1]), extended to take into account surface flexibility. A similar expression has recently been derived by Chase in reference [6], equation (42), by an indirect method. We will now go on to use equation (19) to investigate the consequences of surface compliance. It is in a particularly convenient form because the influence of surface flexibility is displayed explicitly in the term Z. $E(y_3)$, the solution to equation (12) with boundary conditions (13) and (15), depends only on the mean flow profile and not in any way on the surface properties. The effect of a change in surface properties can be investigated by considering the function $[E'(0)+U'(0)k_1/\omega-\rho_1\omega^2/Z]^{-1}$ for different surface impedances. It remains for us to calculate $E(y_3)$.

E satisfies a linear second order differential equation (12) with the boundary conditions (13) and (15). This can easily be solved numerically for a particular mean flow profile. The results in Section 4 were obtained for a tanh-velocity profile $U(y_3) = U_1\tanh(y_3/\delta)$, where δ is a measure of the boundary layer height. To aid numerical integration the problem for $E(y_3)$ was cast into the form of a non-linear first order differential equation for $\phi(y_3)$. This technique was used by Michalke [7] when investigating flow stability. $\phi(y_3)$ is defined by:

$$E(y_3)=\exp\left[\int_0^{y_3}\phi(y_3')dy_3'\right] \qquad (20)$$

Then $\phi, = E^{-1}dE/dy_3$, satisfies

$$\frac{d\phi}{dy_3}=-\phi^2-f \qquad (21)$$

with boundary condition $\phi(\infty) = -i\gamma_1$. Rather than integrate over an infinite range the spatial variable was changed to $z = \tanh(y_3/\delta)$. Then the resulting equation was integrated from $z = 1$, where ϕ is $-i\gamma_1$, to $z = 0$, using a Runge-Kutta-Merson method, thus determining $\phi(0) = E'(0)$ as required in (19). These values of $E'(0,\mathbf{k},\omega)$ are used in Section 4.

In fact the dominant flow effect does not depend on the details of the boundary layer profile. In order to see that and to interpret the results in Section 4 we will derive an asymptotic form for $E(y_3)$ valid for low values of the flow Mach number $M = U_1/c_1$. In underwater applications M is of the order of 0.01 and this limit is justified. We write $\eta = y_3/\delta$, $U(y_3) = U_1V(\eta)$, $s_1 = k_1c_1/\omega$ and $s_2 = k_2c_1/\omega$. For sonic and supersonic phase elements $(s_1^2+s_2^2)^{1/2}$ takes values of order unity. δ is of the order of the boundary layer height. We will not assume that $\omega\delta/c_1$ is small as in Chase and Noiseux's detailed calculations [1]. For a boundary layer of height 5 cm in water and a frequency of 5 kHz, $\omega\delta/c_1$ is about unity. When cast in terms of nondimensional variables the problem for E is:

$$\frac{d^2E}{d\eta^2}+\delta^2\gamma_1^2E=E\left[\left(\frac{\omega\delta}{c_1}\right)^2\{2Ms_1(1-V)+M^2s_1^2(1-V^2)\}\right.$$

$$\left.+\frac{2M^2s_1^2}{(1+MVs_1)^2}\left(\frac{dV}{d\eta}\right)^2-\frac{Ms_1}{1+MVs_1}\,\frac{d^2V}{d\eta^2}\right] \qquad (22)$$

We seek a solution for E as a power series in the Mach number M; $E(\eta) = E_0(\eta) + ME_1(\eta) + \ldots$. Then

$$\frac{d^2E_0}{d\eta^2}+(\delta\gamma_1)^2E_0=0 \qquad (23a)$$

$$\frac{d^2E_1}{d\eta^2}+(\delta\gamma_1)^2E_1=\left[\left(\frac{\omega\delta}{c_1}\right)^2 2(1-V)-\frac{d^2V}{d\eta^2}\right]s_1E_0. \qquad (23b)$$

The solution for E_0, satisfying the boundary condition at infinity, is:

$$E_0(\eta)=Ae^{-i\delta\gamma_1\eta}, \text{ where } A \text{ is a constant.} \qquad (24)$$

$E_1(\eta)$ is then the solution of an inhomogeneous second order differential equation with constant coefficients and can be found in a straightforward way to give:

$$E_1(\eta)=As_1e^{i\delta\gamma_1\eta}\int_\eta^\infty\left\{\frac{dV}{dS}\right.$$

$$\left.+2\left(\frac{\omega\delta}{c_1}\right)^2X(S)\right\}e^{-2i\delta\gamma_1S}\,dS \qquad (25)$$

where $X(\eta) = \int_\eta^\infty (1-V(S))dS$.

A can be calculated from the boundary condition (15), $E(0) = 1$, and then $E(\eta)$ is determined to order M. In particular this gives:

$$\frac{dE}{d\eta}(0)=-i\delta\gamma_1(1+MB)-s_1\mathrm{M}\left\{\frac{dV}{d\eta}(0)\right.$$

$$\left.+2\left(\frac{\omega\delta}{c_1}\right)^2X(0)\right\} \qquad (26)$$

where

$$B=-2s_1\int_0^\infty\left\{\frac{dV}{dS}+2\left(\frac{\omega\delta}{c_1}\right)^2X(S)\right\}e^{-2i\delta\gamma_1S}dS.$$

Returning to dimensional variables we have:

$$\frac{dE}{dy_3}(0)=-i\gamma_1(1+MB)-U'(0)\frac{k_1}{\omega}-2k_1\omega\mathrm{M}\,\frac{\delta_1}{c_1} \qquad (27)$$

correct to order M. δ_1 is the boundary layer displacement thickness defined by $\delta_1 = \int_0^\infty(1-U(y_3)/U_1)dy_3$. We have retained the order M terms in this expression because it is possible for the leading term, $-i\gamma_1$, to vanish.

To lowest order in M $E(y_3) = e^{-i\gamma_1y_3}$ and the representation (19) gives:

$$\tilde{p}(0,\mathbf{k},\omega)=\frac{D_iD_j}{E'(0)+U'(0)k_1/\omega-\rho_1\omega^2/Z}$$

$$\times\int e^{-i\gamma_1y_3}\tilde{T}_{ij}(y_3,\mathbf{k},\omega)dy_3 \qquad (28)$$

for modes with sonic and supersonic phase speeds. $D_\alpha = k_\alpha$ for $\alpha = 1, 2$ and $D_3 = \gamma_1$. The terms in the numerator cannot all vanish simultaneously and so we have only kept the lowest order terms there. But in the denominator the leading order term can vanish and so terms of order M must be retained.

The wall pressure spectrum can be derived from the Fourier transform of the surface pressure in the usual way (see, for example, Dowling [4] for the details) and is given by:

$$P(\mathbf{k},\omega)=\frac{D_i^+D_j^+D_kD_l}{|E'(0)+U'(0)k_1/\omega-\rho_1\omega^2/Z|^2}$$

$$\times\int e^{i\gamma_1^+y_3-i\gamma_1y_3'}T_{ijkl}(y_3,y_3',\mathbf{k},\omega)dy_3dy_3' \qquad (29)$$

where the dagger denotes the complex conjugate and T_{ijkl} is the cross-correlation of the turbulent sources:

$$T_{ijkl}(y_3,y_3',\mathbf{k},\omega)$$

$$=\int\overline{T_{ij}(\mathbf{y},\tau)T_{kl}(y_1+\Delta_1,y_2+\Delta_2,y_3',\tau+\tau_0)}$$

$$\times e^{-ik_\alpha\Delta_\alpha-i\omega\tau_0}d^2\Delta d\tau_0 \qquad (30)$$

If the acoustic analogy has been successful in extracting the essential field structure T_{ijkl} shoud be independent of compressibility effects. T_{ijkl} can therefore be estimated on the

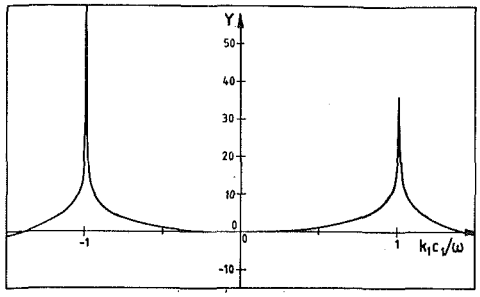

Fig. 2 Plot of

$$Y = 20\log_{10}\left|\frac{\omega/c_1}{E'(0)+U'(0)k_1/\omega}\right|$$

versus nondimensional wavenumber for flow over a rigid wall with $M = 0.01$, $\omega\delta/c_1 = 1$, $k_2 = 0$

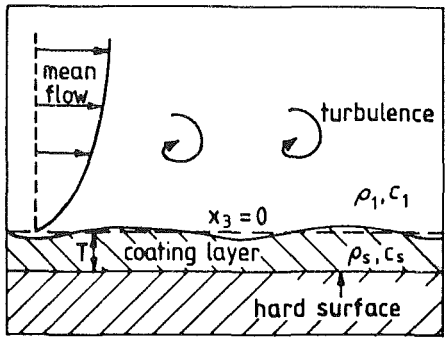

Fig. 3 A coating layer over a hard surface

basis of incompressible flow theory. We will nondimensionalize the integral in (29) and write:

$$\int e^{ik_1x_1+\gamma_1x_3-i\gamma_1y_3'}T_{ijkl}(y_3,y_3',\mathbf{k},\omega)dy_3dy_3' = \rho_1^2U_1^3\delta_1^5Q_{ijkl}(\delta_1\mathbf{k},\delta_1\omega/U_1) \quad (31)$$

Then the pressure spectrum simplifies to:

$$P(\mathbf{k},\omega) = \frac{D_i^+D_j^+D_kD_l}{|E'(0)+U'(0)k_1/\omega-\rho_1\omega^2/Z|^2} \times \rho_1^2U_1^3\delta_1^5Q_{ijkl}(\delta_1\mathbf{k},\delta_1\omega/U_1) \quad (32)$$

$D_i^+D_j^+D_kD_l|E'(0)+U'(0)k_1/\omega-\rho_1\omega^2/Z|^{-2}$ describes how the turbulent field Q_{ijkl} radiates sound within the boundary layer over the flexible surface. The product $D_i^+D_j^+D_kD_l$ describes the propagation of the different directional elements, but the main structure of the surface pressure spectrum comes from the $|E'(0)+U'(0)k_1/\omega-\rho_1\omega^2/Z|^{-2}$ term.

In the low Mach number limit, equation (27) shows that:

$$E'(0)+U'(0)k_1/\omega-\rho_1\omega^2/Z = -i\gamma_1(1+MB) - 2\omega k_1\delta_1M/c_1-\rho_1\omega^2/Z. \quad (33)$$

Without a mean flow profile and for a hard surface, $E'(0)+U'(0)k_1/\omega-\rho_1\omega^2/Z = -i\gamma_1$, which vanishes for spectral elements with sonic phase speeds. The mean flow profile therefore has most effect on the pressure spectrum near $\gamma_1 = 0$ where the leading order term in (33) vanishes. Then the $-i\gamma_1MB$ term is negligible since both γ_1 and M are small and the dominant effect of the mean flow profile is contained in the term $-2\omega k_1\delta_1M/c_1$. This was verified by numerical calculations for a tanh-velocity profile $U_1\tanh(y_3/\delta)$. Integration shows that for such a mean flow velocity variation the displacement thickness δ_1 is equal to $\delta\log_e2$. The values of $E'(0)+U'(0)k_1/\omega$ calculated numerically were compared with $-i\gamma_1-2\omega k_1\delta_1M/c_1$ for a Mach number of 0.01, $\omega\delta/c_1 = 1$, and good agreement was obtained for a range of values of k_1c_1/ω.

The major effect, therefore, of the boundary-layer profile is independent of the details of the boundary layer depending only on its integrated effect through the displacement thickness δ_1 ($= \int_0^\infty(1-U/U_1)dy_3$). We now see that the vortex sheet analogy developed by Dowling [4] is able to describe the effect of a mean flow profile on sonic or supersonic spectral elements for all boundary layers, not just for boundary layers which are thin in comparison with the wavelength, $2\pi c_1/\omega$, as suggested in that paper. We can understand this physically because the main influence of the flow profile is on spectral elements with nearly sonic phase speeds for which $\gamma_1 \simeq 0$, and these modes have infinitely long wavelengths in a direction normal to the surface. In particular by including an arbitrary mean flow profile and making no further approximations other than assuming the Mach number to be small, we have found where the equivalent vortex sheet should be placed. It is at a height above the surface equal to the displacement thickness of the boundary layer.

4 The Wall-Pressure Spectrum on Various Surfaces

Equation (32) describes the influence of the surface structure and mean flow profile on the wall-pressure spectrum. In this section the form of the pressure spectrum is investigated for a couple of simple surfaces.

4.1 A Hard Surface. The normal displacement always vanishes on a hard surface and so Z is infinite. From (32) the surface pressure spectrum is given by:

$$P(\mathbf{k},\omega) = \frac{D_i^+D_j^+D_kD_l}{|E'(0)+U'(0)k_1/\omega|^2} \times \rho_1^2U_1^3\delta_1^5Q_{ijkl}(\delta_1\mathbf{k},\delta_1\omega/U_1) \quad (34)$$

$|E'(0)+U'(0)k_1/\omega|^{-2}$ is plotted as a function of k_1c_1/ω in Fig. 2 for a flow with a velocity profile $U(y_3) = U_1\tanh(y_3/\delta)$ and M = 0.01, $\omega\delta/c_1 = 1$. In order to interpret these results we will consider the low Mach number limit.

Equation (33) gives:

$$E'(0)+U'(0)k_1/\omega = -i\gamma_1(1+MB)-2\omega k_1\delta_1M/c_1 \quad (35)$$

correct to order M. The denominator in (34) is therefore small near $\gamma_1 \simeq 0$, but it can only vanish when γ_1 is purely imaginary. Then the first term on the right-hand side of (35) is real and negative, and so from (35) $E'(0)+U'(0)k_1/\omega$ only vanishes if ω and k_1 have opposite signs, i.e., for downstream propagating modes. For upstream propagating modes $E'(0)+U'(0)k_1/\omega$ is always nonzero. The pressure spectrum therefore has a double pole near $\gamma_1 = 0$ for downstream propagating spectral components, but it is always finite for upstream propagating elements.

The curve in Fig. 2 clearly demonstrates that the predicted pressure spectrum is larger for downstream propagating modes with sonic phase speeds than it is for upstream propagating modes. Roebuck and Richardson (1981, private communication) have observed this in underwater experiments.

Just as in Dowling [4] we can interpret the singularity for downstream propagating spectral elements as being due to modes which are supersonic within the slowly moving fluid in the boundary layer but subsonic in the faster moving fluid outside it. The energy in these modes therefore remains trapped near the boundary layer, i.e., within a disc near the surface, and conservation of energy then suggests that downstream of the source the pressure disturbance will only decay like the inverse square-root of distance from the source, while upstream the disturbance will decay more rapidly. Hence the pressure decays more slowly with distance downstream of a source in the boundary layer than in a uniform stream, and this accounts for the stronger singularity in the pressure spectrum under an infinite region of turbulence.

It has been shown (Dowling [8]) that in the absence of a mean flow profile certain coating layers can have a benefical

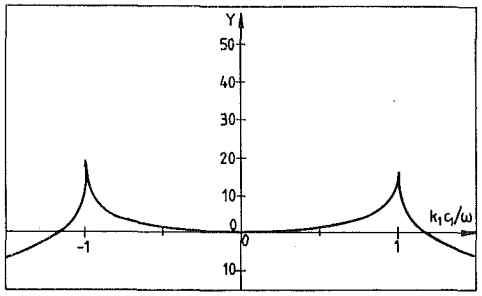

Fig. 4 Plot of

$$Y = 20\log_{10}\left|\frac{\omega/c_1}{E'(0)+U'(0)k_1/\omega-\rho_1\omega^2/Z}\right|$$

versus nondimensional wavenumber for a high-speed coating layer over a hard surface. $M = 0.01$, $\omega\delta/c_1 = 1$, $\omega T/c_1 = 0.5$, $c_s = 1.2c_1$, $\rho_s = 1.2\rho_1$, $k_2 = 0$

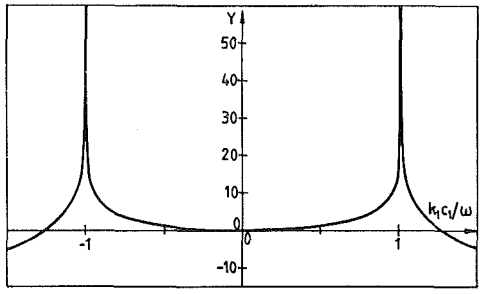

Fig. 5 Plot of

$$Y = 20\log_{10}\left|\frac{\omega/c_1}{E'(0)+U'(0)k_1/\omega-\rho_1\omega^2/Z}\right|$$

versus nondimensional wavenumber for a low-speed coating layer over a hard surface. $M = 0.01$, $\omega\delta/c_1 = 1$, $\omega T/c_1 = 0.5$, $c_s = 0.9c_1$, $\rho_s = 1.2\rho_1$, $k_2 = 0$

effect on the surface pressure spectrum. We now go to investigate the effect of a coating layer over a hard surface.

4.2 A Coating Layer. We model the coating by a fluid layer of thickness T with density ρ_s and sound speed c_s. A sketch of the coating layer on a hard surface is given in Fig. 3. The impedance of the composite surface can be calculated in a straightforward way and we find:

$$Z = -\frac{\rho_s\omega^2}{\gamma_s}\cot\gamma_s T \tag{36}$$

where $\gamma_s = (\omega^2/c_s^2 - k_1^2 - k_2^2)^{1/2}$. The pressure spectrum on the surface of the coating $x_3 = 0$ can then be obtained immediately from (32). In fact the pressure spectrum on the hard surface is of more practical interest since it can be compared more directly with the pressure on the uncoated plate. The relationship between the pressures on these two surfaces is:

$$\tilde{p}(-T,\mathbf{k},\omega) = \tilde{p}(0,\mathbf{k},\omega)\sec\gamma_s T \tag{37}$$

and so the wall pressure spectrum on the hard surface is:

$$P(\mathbf{k},\omega) = \frac{|\sec\gamma_s T|^2 D_i^+ D_j^+ D_k D_l}{|E'(0)+U'(0)k_1/\omega-\rho_1\omega^2/Z|^2} \times \rho_1 U_1^3\delta_1^5 Q_{ijkl}(\delta_1\mathbf{k},\delta_1\omega/U_1) \tag{38}$$

where Z is given in (36). $|\sec\gamma_s T|^2|E'(0) + U'(0)k_1/\omega - \rho_1\omega^2/Z|^{-2}$ is plotted in Figs. 4 and 5 for different coating properties using values of $E'(0,\mathbf{k},\omega)$ obtained by numerical integration. We will explain these results by investigating the low Mach number, thin coating layer limit analytically.

When $c_s \gg |\omega|T$ and M is small:

$$E'(0)+U'(0)\frac{k_1}{\omega}-\frac{\rho_1\omega^2}{Z} \simeq -i\gamma_1(1+MB)$$

$$-2\omega k_1\delta_1\frac{\mathrm{M}}{c_1}+\frac{\rho_1}{\rho_s}\left(\frac{\omega^2}{c_s^2}-k_1^2-k_2^2\right)T \tag{39}$$

This becomes small near $\gamma_1 = 0$, but can only vanish near there if:

$$\frac{\rho_1 T}{\rho_s c_1}\left(\frac{c_1^2}{c_s^2}-1\right)-2\frac{k_1\delta_1}{\omega}\mathrm{M}>0 \tag{40}$$

Hence a coating with a sound speed higher than that in the surrounding fluid can eliminate the singularity that occurs on an uncoated hard surface for spectral elements propagating downstream with an approximately sonic phase speed. This is seen clearly by comparing Figs. 2 and 4.

The inequality in (40) shows that a low-sound-speed coating can have an adverse effect and introduce new singularities into the surface pressure spectrum for upstream propagating modes which would be finite for an uncoated hard surface. This is illustrated in Fig. 5. A comparison of Figs. 2 and 5 shows that the low-sound-speed coating has introduced a new singularity into the surface pressure spectrum.

5 Conclusions

An expression for the low-wavenumber wall pressure spectrum under a turbulent boundary layer has been derived in a way which brings out explicitly the effects of the mean flow profile and the surface flexibility. It is found that the hard wall pressure spectrum has a singularity for spectral elements that propagate downstream with approximately sonic phase speeds, but that it is finite for all upstream propagating modes. It is shown that a coating with a sound speed greater than that of the fluid can eliminate the singularities in the pressure spectrum for these downstream propagating modes, but that a low-sound-speed coating has an adverse effect.

This work has been carried out with the support of Topexpress Ltd and the Procurement Executive, Ministry of Defence.

References

1 Chase, D. M., and Noiseux, C. F., "Turbulent Wall Pressure at Low Wave-Numbers: Relation to Nonlinear Sources in Planar and Cylindrical Flow," *Journal of the Acoustical Society of America*, Vol. 72, 1982, pp. 975–982.

2 Ffowcs Williams, J. E., "Surface-Pressure Fluctuations Induced by Boundary-Layer Flow at Finite Mach Number," *Journal of Fluid Mechanics*, Vol. 22, 1965, pp. 507–519.

3 Bergeron, R. F., "Aerodynamic Sound and the Low-Wavenumber Wall-Pressure Spectrum of Nearly Incompressible Boundary-Layer Turbulence," *Journal of the Acoustical Society of America*, Vol. 54, 1973, pp. 123–133.

4 Dowling, A. P., "Flow-Acoustic Interaction Near a Flexible Wall," *Journal of Fluid Mechanics*, Vol. 128, 1983, pp. 181–198.

5 Morse, P. M., and Feshbach, H., *Methods of Theoretical Physics*, McGraw-Hill, 1953.

6 Chase, D. M., "Recent Modeling of Turbulent Wall Pressure and Fluid Interaction With a Compliant Boundary," ASME *Journal of Vibration, Acoustics, Stress and Reliability in Design*, Vol. 106, 1984, pp. 328–333.

7 Michalke, A., "On Spatially Growing Disturbances in an Inviscid Shear Layer," *Journal of Fluid Mechanics*, Vol. 23, 1965, pp. 521–544.

8 Dowling, A. P., "The Low Wavenumber Wall Pressure Spectrum on a Flexible Surface," *Journal of Sound and Vibration*, Vol. 88, 1983, pp. 11–25.

M. J. Tan

S. G. Bankoff

Chemical Engineering Department,
Northwestern University,
Evanston, Ill. 60201

On the Fragmentation of Drops

Fragmentation of mercury drops falling through a bubbly aqueous liquid by a pressure shock wave was investigated by means of a shock tube capable of operating at driver pressures up to 3 MPa. The responses to moderately strong shock waves (up to 1.7 MPa) were photographed by a high-speed camera at rates of up to 4400 frames per second. The results show the existence of a critical Weber number, $(We)_{cr} = 17$, for drop fragmentation. Qualitative characterization of the shock-drop interactions for single mercury drops is provided.

Introduction

When a hot liquid (fuel) is brought into contact with a cold vaporizable liquid (coolant), an explosive interaction, which is termed a vapor explosion or a fuel-coolant interaction (FCI), may take place. Such interactions have been observed between a variety of low-melting-point molten metals (aluminum, tin, lead, etc.) and water [1–5], and between LMFBR materials, i.e., molten uranium dioxide and liquid sodium [6]. It is widely believed that a coherent interaction implies the existence of a propagation process which couples the explosive regions to the unexploded regions [7]. In this context, fine fuel fragmentation and mixing are essential since they produce new interfacial area, thereby enabling the rapid heat transfer necessary for sustained propagation of the pressure wave. Among the various fragmentation mechanisms which have been proposed in recent years, one group can be characterized as purely hydrodynamic, in which fragmentation is due to the velocity difference between the fuel drops and the coolant [7]. The hydrodynamic fragmentation mechanisms have particular relevance to the detonation model of Board et al. for FCI's [8]. In this detonation model the velocity difference is induced by the passage of shock waves. Since the magnitude of this shock-induced velocity difference decreases continuously under the action of interfacial drag and virtual inertia, estimates of the characteristic fragmentation and velocity re-equilibration times are required to assess the possibility of high-efficiency interactions.

Drop fragmentation in shock-induced gas flows has been studied quite extensively in connection with problems in the field of aerodynamics. Taylor [9] found that the shape of a liquid drop accelerating in a high speed air stream was nearly spherical at the windward surface, but more or less flat at the opposite surface. He proposed a boundary-layer stripping mechanism to analyze the mass loss. This analysis was extended by Ranger and Nicholls [10] to compare with their experimental data on drop displacements and breakup times for water drops in high-speed air flows. These authors showed that the dimensionless breakup time $\tau_b = t_b u_r \epsilon^{1/2}/D_o$ could be expressed as τ_b = constant ~ 5, where D_o is the initial equivalent drop diameter, ϵ is the density ratio of the continuous phase (gas) to the dispersed phase (liquid), and u_r is the relative speed between the phases. Waldman et al. [11] pointed out that the boundary-layer stripping mechanism alone could not account for complete drop destruction within experimentally observed breakup times. In their experiments two modes of breakup were identified: first, a gradual stripping mode, followed by a catastrophic mode in which the drops were rapidly shattered. The dimensionless breakup times for the catastrophic mode were correlated to the Weber number $We = \rho_c u_r^2 D_o/2\sigma$, by the equation $\tau_b = 38\ We^{-1/4}$, where ρ_c is the density of the continuous phase (gas), and σ is the interfacial tension.

Fishburn [12] suggested that Taylor instability coupled with aerodynamic flattening of the drops could increase the surface areas and thus enhance the stripping rate. In the same spirit, Harper et al. [13] provided a theory for drop breakup while leaving the effects of mass loss or boundary-layer stripping out of consideration. They showed that an initially spherical drop suddenly exposed to an external pressure field was unstable to small disturbances for Bond numbers $Bo = \rho_d a D_o^2/4\sigma$ above a critical value $(Bo)_{cr} = 11.2$, where a is the acceleration, and ρ_d is the density of the dispersed phase (liquid). However, on a time scale appropriate to the effects of aerodynamic deformation, the acceleration could be balanced exactly by the first mode of an axisymmetric external pressure distribution, thereby allowing the remaining pressure modes to deform the drop from its initially spherical shape. They thus suggested a quasi-stable region for Bond numbers up to 10^5, in which the drop response was dominated by deformation. For $Bo > 10^5$, the acceleration became the controlling factor, and the liquid drop disintegrated by means of unstable piercing of the wavy surface. Experiments by Simpkins and Bales [14] conformed qualitatively to this theoretical prediction. The observed times for the onset of Taylor instability were given by these authors as

$$\tau_b = 11\ Bo^{-1/4} \tag{1}$$

In their modeling of the FCI's, Board et al. [8] employed equation (1) to predict the fragmentation behavior in a uranium dioxide-sodium system. Since the continuous-to-dispersed phase density ratios involved in FCI's are several orders of magnitude larger than those in the liquid-gas systems, the separation between the fragmentation time and the velocity re-equilibration time is smaller in the former

Contributed by the Fluids Engineering Division and presented at the Winter Annual Meeting Miami Beach, Fla., November 17–22, 1985, of The American Society of Mechanical Engineers. Manuscript received by the Fluids Engineering Division, May 20, 1983. Paper No. 85-WA/FE-1.

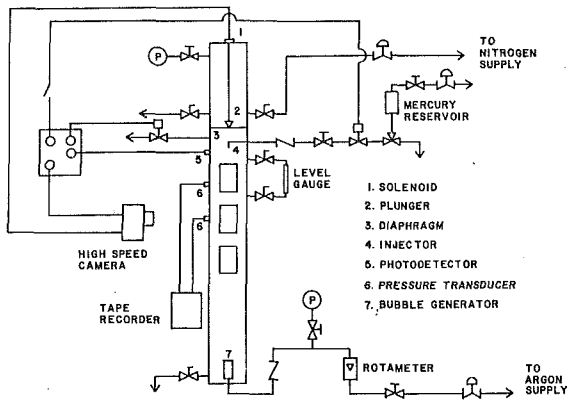

Fig. 1 Schematic diagram of the experimental setup

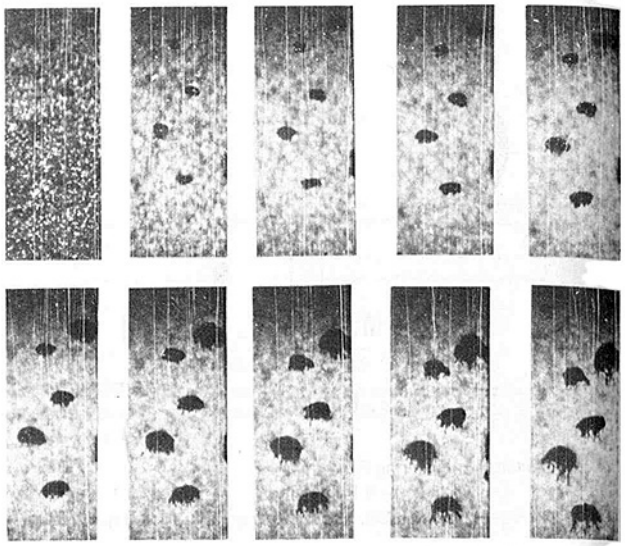

Fig. 2 Mercury drop responses for Run 8. The shock progresses downward. The shock front is approximately at the middle of frame 1. The time separation between each frame is 450 μs.

systems than in the latter systems. This indicates that the possibility of different behaviors for the two systems cannot be excluded. However, there are few studies of hydrodynamic fragmentation in dispersions of two liquids. Patel and Theofanous [15], using a shock-tube technique, investigated fragmentation of liquid drops (mercury, gallium, and acetylene tetrabromide) in water. They observed that, for the mercury-water pair and for Bond numbers in the range $52 < \mathrm{Bo} < 2810$, one could not distinguish between the stripping mode and the catastrophic mode for the shock-induced drop fragmentation. Rather, the mercury drops appeared to experience a symmetric blowup. The X-ray data of Theofanous et al. [16] showed that the symmetric blowup was effected by the superposition of a drop-flattening mechanism and an entrainment mechanism. On the basis of these observations, Patel and Theofanous [15] correlated their data in terms of the time characteristic of the growth of unstable Taylor waves

$$\tau_b = 0.83\ \mathrm{Bo}^{-1/4} \tag{2}$$

On the other hand, Baines and Buttery [17] obtained velocity differences between mercury drops and water by imposing an impulsive motion on a vessel containing these materials. They found that the general behavior of an initially-stationary drop was very similar to that of a water drop in shock-induced air flows, with both capillary wave growth and boundary-layer stripping contributing to the fragmentation process. The difference between the results of these two studies serves to underline the necessity of obtaining more information about differential velocity fragmentation for liquid-liquid systems.

In this paper, an experimental investigation of drop fragmentation for the mercury-gas bubbly mixture system is presented. The effects of gas bubbles in the liquid coolant on the fragmentation process are examined. A shock tube capable of operation at driver pressures of up to 3 MPa was used. The response of falling mercury drops to moderately strong shock waves was photographed by a high-speed movie camera at rates up to 4400 frames per second. A qualitative characterization of the shock-drop interactions for single mercury drops is provided.

2 Experimental Methods

A schematic diagram of the experimental setup is shown in Fig. 1. The test section consisted of a vertical shock tube. A detailed description of the shock tube can be found in reference [18]. The mercury-drop injector, which was located 11.5 cm below the diaphragm and 28 cm above the first window section, consisted of a 3.2 mm OD stainless-steel tube. The injection amount and timing were controlled by a normally-closed solenoid valve and a precision metering valve. A photodetector was mounted 2 cm below the injector to monitor the passage of the drops. The photographic system was a rotating-prism type high-speed movie camera (Photec IV-A), which was equipped with a 45 mm f/2.8 lens, in conjunction with two quartz-halogen projection lamps (GE Quartzline ELH). With this system and 100-ft reversal-acetate films, a maximum speed of 6500 frames per second was obtained. For pressure measurements, two miniature voltage-type quartz transducers (PCB-111A24) were flush mounted in the wall of the window section where pictures were taken. Pressure histories were recorded on a magnetic tape recorder (HP-3968A).

For each experimental run, the driver section was

Nomenclature

a = acceleration of the drop
Bo = Bond number
C_D = drag coefficient
c_1 = sound speed in the region ahead of the shock
D_o = initial equivalent diameter of the drop
g = acceleration of gravity
k = wave number
n = exponential growth rate
p_{21} = shock pressure ratio
T = dimensionless time
t = time
T_b = dimensionless fragmentation time
t_b = fragmentation time
u_{ro} = initial relative velocity
u_2 = mixture velocity in the region behind the shock
v = dimensionless volume
We = Weber number
X = dimensionless Cartesian space coordinate
x = Cartesian space coordinate
α_1 = void fraction in the region ahead of the shock
ϵ = density ratio of the continuous phase to the dispersed phase
λ_{cut} = cut-off wavelength
λ_{max} = fastest-growing wavelength
ρ_c = density of the continuous phase
ρ_d = density of the dispersed phase
σ = surface tension
τ_b = dimensionless breakup time

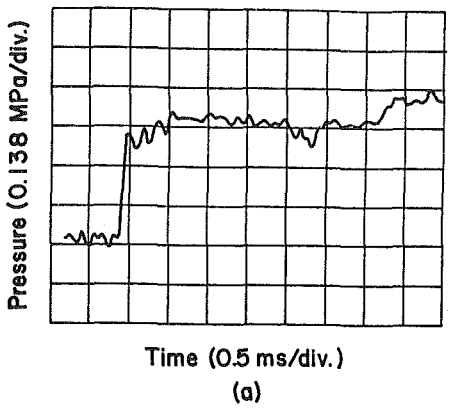

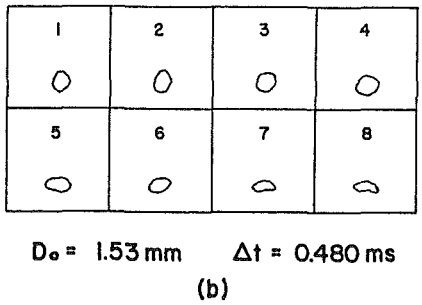

Fig. 3 Pressure history and typical drop response for Run 4

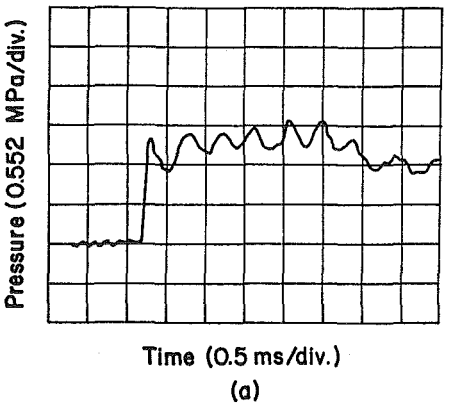

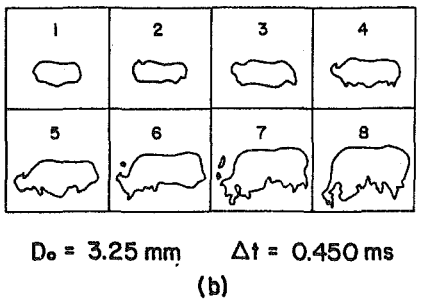

Fig. 4 Pressure history and typical drop response for Run 9

pressurized with high-pressure nitrogen. A pointed plunger, driven by a push-type solenoid mounted at the top of the driver section, was used to rupture the diaphragm. The driven section was partly filled with a glycerol-water-argon mixture. The distances between the free surface of the mixture and the tip of the mercury-drop injector were in the range from 3 cm to 6 cm. The gas bubbles were generated at the bottom of the test section by injecting argon through a stainless-steel sparger. In the liquids used in the experiments, the diameters of most of the bubbles lay between 0.3 mm and 0.8 mm. The initial void fraction was measured by means of a level gauge.

Table 1 Experimental value of pertinent quantities in drop fragmentation

Run	$100\alpha_1$	p_{21}	u_2 m/s	No. of drops
1	1.34 ± 0.38	8.67 ± 0.29	3.01 ± 15%	1
2	1.34 ± 0.38	13.02 ± 0.34	3.85 ± 14%	2
3	1.34 ± 0.38	15.84 ± 0.38	4.31 ± 14%	2
4	1.34 ± 0.38	4.82 ± 0.27	2.11 ± 14%	4
5	1.50 ± 0.38	17.76 ± 0.27	4.95 ± 13%	1
6	1.56 ± 0.42	12.57 ± 0.26	4.16 ± 14%	6
7	1.68 ± 0.42	14.99 ± 0.28	4.79 ± 13%	3
8	1.75 ± 0.42	15.42 ± 0.26	4.94 ± 12%	5
9	1.82 ± 0.42	15.64 ± 0.27	5.08 ± 12%	1
10	2.47 ± 0.55	10.27 ± 0.32	4.68 ± 12%	1
11	2.87 ± 0.55	12.35 ± 0.26	5.60 ± 10%	2
12	2.88 ± 0.55	3.96 ± 0.27	2.60 ± 11%	2
13	2.92 ± 0.55	10.01 ± 0.31	5.02 ± 0%	1
14	2.95 ± 0.55	4.51 ± 0.26	2.92 ± 11%	2
15	2.95 ± 0.55	7.68 ± 0.28	4.28 ± 10%	2
16	2.98 ± 0.55	8.73 ± 0.30	4.66 ± 10%	1
17	3.00 ± 0.69	14.81 ± 0.27	6.38 ± 12%	5
18	3.21 ± 0.68	10.72 ± 0.31	5.37 ± 11%	1
19	3.23 ± 0.68	13.27 ± 0.35	6.11 ± 11%	1

The experiments were carried out as follows. First, the solenoid valve of the mercury injection system was opened manually. Upon detecting the passage of a drop, the photodetector sent a signal simultaneously to start the camera and close the solenoid valve. Following the passage of a predetermined length of film, the event synchronizer in the camera actuated the solenoid plunger automatically, thereby rupturing the diaphragm and initiating a shock wave. For the driver pressures involved, which were up to 2.1 MPa, the duration of the uniform flow, which was the time interval between the arrival of the initial shock and subsequent reflection shock, was at least 3.5 ms. Synchronization of events was achieved by adjusting the height of the mixture in the test section and the time-delay setting on the camera. The time origin for the shock-drop interactions was determined from the photographs, as the arrival of a shock wave immediately changed the amount of light transmitted through the mixture.

3 Results and Discussions

Figure 2 is a typical photographic sequence showing the mercury drop response to the shock-induced flow. The histories of the pressure and corresponding drop response for two experiments are reproduced in Figs. 3 and 4. Other such results can be found in reference [18]. The appearance of a steep front of rise time less than 0.2 ms, followed by an approximately level plateau in the pressure history shown here, is typical for all experiments. Based on such pressure histories, the mixture velocity immediately behind the shock front, u_2, can be calculated by means of the shock condition [18].

$$u_2 = \alpha_1 c_1 [(p_{21} - 1)(1 - p_{21}^{-1})]^{1/2} \tag{3}$$

where α_1 and c_1 are, respectively, the void fraction and speed of sound in the mixture ahead of the shock, and p_{21} is the shock pressure ratio. The values of α_1, p_{21}, and u_2 for nineteen experiments are given in Table 1.

The drop responses after the passage of the shock waves can be broadly divided into two groups. In the first group, the responses are confined to purely oscillating motion. The change in drop volume is too slow to be significant within the time span of interest. This is the case represented by Fig. 3(*b*). In the second group, the drops appear to expand rapidly in directions both transverse and parallel to the flow. While the drops are expanding in this way, their leeward surfaces gradually deform to bear resemblance to an array of spikes, whereas their windward surfaces remain nearly smooth. This behavior is typified in Fig. 2. and represented by Fig. 4(*b*). It should be pointed out that the drop responses in the second

Table 2 Calculated values of pertinent quantities in drop fragmentation

Drop	D_o, mm (±10%)	We	T_b (±10%)	T_b' (±10%)	a, m/s2	λ_{cut},mm	λ_{max},mm
1-1	2.43	21 ± 7	1.98	-	702 ± 33%	1.30	2.25 ± 16%
2-1	1.64	27 ± 9	2.70	4.72	2000 ± 32%	0.77	1.34 ± 16%
2-2	1.59	26 ± 8	3.40	4.93	2072 ± 32%	0.76	1.31 ± 16%
3-1	2.26	46 ± 15	1.76	3.19	1791 ± 32%	0.81	1.41 ± 16%
3-2	3.04	58 ± 19	2.16	-	1273 ± 32%	0,97	1.67 ± 16%
4-1	1.73	6 ± 2	-	-	407 ± 32%	1.70	2.95 ± 16%
4-2	1.35	5 ± 2	-	-	557 ± 32%	1.46	2.52 ± 16%
4-3	1.49	5 ± 2	-	-	494 ± 32%	1.55	2.68 ± 16%
4-4	1.53	6 ± 2	-	-	476 ± 32%	1.58	2.73 ± 16%
5-1	2.90	73 ± 22	1.20	2.53	1742 ± 30%	0.82	1.43 ± 15%
6-1	1.54	29 ± 9	1.50	2.64	2404 ± 31%	0.70	1.22 ± 16%
6-2	1.82	33 ± 10	1.29	2.78	1999 ± 31%	0.77	1.33 ± 15%
6-3	2.11	37 ± 11	1.30	3.16	1684 ± 31%	0.84	1.45 ± 16%
6-4	1.68	31 ± 10	1.75	2.82	2183 ± 31%	0.74	1.28 ± 16%
6-5	2.05	36 ± 11	1.73	3.99	1740 ± 31%	0.82	1.43 ± 16%
6-6	1.51	28 ± 9	2.47	3.41	2461 ± 31%	0.69	1.20 ± 16%
7-1	2.07	51 ± 15	1.38	2.82	2376 ± 29%	0.71	1.22 ± 15%
7-2	2.57	61 ± 18	1.25	2.09	1860 ± 29%	0.80	1.38 ± 15%
7-3	1.95	48 ± 14	1.87	3.77	2544 ± 29%	0.68	1.18 ± 15%
8-1	3.24	80 ± 23	1.33	2.55	1529 ± 28%	0.88	1.52 ± 14%
8-2	1.86	50 ± 14	2.33	3.85	2879 ± 28%	0.64	1.11 ± 14%
8-3	2.35	61 ± 17	1.30	3.64	2215 ± 28%	0.73	1.27 ± 14%
8-4	2.98	74 ± 21	1.86	2.86	1684 ± 28%	0.84	1.45 ± 14%
8-5	2.62	67 ± 19	1.28	2.28	1952 ± 28%	0.78	1.35 ± 14%
9-1	3.25	85 ± 24	0.94	2.18	1619 ± 28%	0.85	1.48 ± 14%
10-1	2.73	61 ± 17	0.85	1.52	1638 ± 28%	0.85	1.47 ± 14%
11-1	2.19	76 ± 19	1.79	4.01	3172 ± 25%	0.61	1.06 ± 12%
11-2	2.26	78 ± 19	1.73	3.11	3054 ± 25%	0.62	1.08 ± 12%
12-1	2.04	12 ± 3	-	-	562 ± 27%	1.45	2.51 ± 14%
12-2	3.01	15 ± 4	-	-	339 ± 27%	1.87	3.24 ± 14%
13-1	3.13	80 ± 20	0.78	1.51	1642 ± 25%	0.85	1.47 ± 12%
14-1	2.20	16 ± 4	-	-	679 ± 26%	1.32	2.29 ± 13%
14-2	2.47	18 ± 5	2.88	-	586 ± 26%	1.42	2.46 ± 13%
15-1	4.53	73 ± 18	0.50	1.40	719 ± 25%	1.28	2.22 ± 12%
15-2	3.28	57 ± 14	1.01	1.86	1065 ± 25%	1.05	1.83 ± 12%
16-1	3.43	72 ± 18	0.71	1.69	1240 ± 25%	0.98	1.69 ± 12%
17-1	2.06	95 ± 27	0.71	1.94	4520 ± 28%	0.51	0.89 ± 12%
17-2	1.98	92 ± 26	1.13	2.30	4700 ± 28%	0.50	0.87 ± 12%
17-3	2.04	95 ± 27	1.48	3.00	4546 ± 28%	0.51	0.88 ± 12%
17-4	2.26	104 ± 29	1.02	2.46	4075 ± 28%	0.54	0.93 ± 12%
17-5	2.25	103 ± 29	1.44	2.86	4087 ± 28%	0.54	0.93 ± 12%
18-1	2.03	68 ± 18	0.89	3.18	3326 ± 27%	0.60	1.04 ± 13%
19-1	2.68	117 ± 31	2.42	4.58	3256 ± 27%	0.60	1.05 ± 13%

*Uncertainty in λ_{cut} is the same as in λ_{max} at 20:1 odds.

group are in accordance with the observations of Patel and Theofanous [15]. Figures 5(*b*) and 6(*b*) show the variations of dimensionless apparent volume with dimensionless time for the drops depicted in Figs. 3(*b*) and 4(*b*), respectively. The apparent volume is calculated from the projected area of the drop, assuming axisymmetry. The dimensionless time T is defined as $T = tu_{ro}/D_o$, where t is the real time and u_{ro} is the initial relative velocity between the drop and the mixture.

Because of the presence of residual gas bubbles which tend to obscure the field of view, it is not possible to observe in detail the interactions between the drop and the mixture, but it can be deduced from the photographs and volume variations that mixing occurs continuously for the drops which experienced expansion-type deformation. On the other hand, the production of misty wakes, stripping of liquid filaments from the equator of the drop, and the appearance of surface waves on the windward surface of the drop, which are typical for drop fragmentation in liquid-gas systems, are not evident in the experiments. In view of this difference, the characterization of fragmentation time, which for liquid-gas systems was defined to correspond to the complete disintegration of the parent drop, requires an alternative approach here. In fact, the major concerns in modeling FCI's regarding the shock-induced fragmentation are the initial drop configuration and the mixing characteristics, inasmuch as the effects of energy transfer must be allowed for at later times. Thus, in the context of FCI's, fragmentation of the mercury drops can be considered essentially complete if the apparent drop volume has increased above a critical value. The determination of this critical value would require information about the energy transfer mechanisms between the relevant constituents involved in FCI's. In this paper, the critical value is tentatively regarded as a parameter, as a qualitative representation of the extent of mixing is provided. For those experiments amenable to this criterion, the dimensionless fragmentation times T_b and T_b', which correspond to critical

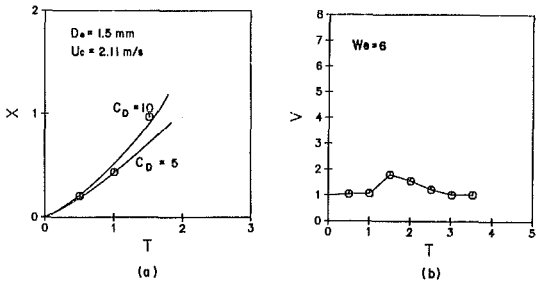

Fig. 5 Variations of the dimensionless displacement and the apparent volume for Drop 4-4. (Uncertainty in $X = \pm 10$ percent, in $V = \pm 14$ percent, in $T = \pm 17$ percent at 20:1 odds.)

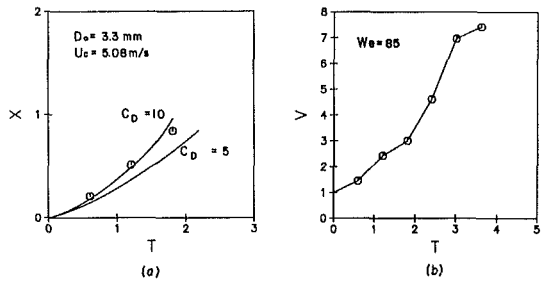

Fig. 6 Variations of the dimensionless displacement and the apparent volume for Drop 9-1. (Uncertainty in $X = \pm 10$ percent, in $V = \pm 14$ percent, in $T = \pm 16$ percent at 20:1 odds.)

dimensionless apparent volumes of 2 and 4, respectively, are given in Table 2.

In general, immediately following the passage of the shock front, the mixture velocity rises impulsively to u_2, while the drop velocity remains virtually unchanged. Subsequently, the mixture decelerates and the drop accelerates as a result of momentum interchange. If the total mass of the mixture compared to that of the drop is very large, the deceleration of the mixture is negligible. Hence, the drop is accelerated from its free-fall velocity until momentum equilibrium is attained, while the mixture velocity behind the shock remains constant at its initial value u_2. For water drops in shock-induced air flows, where the change in relative velocity before extensive fragmentation occurs is small, the acceleration of the drop is approximately constant [10,14]. By assuming constant drop mass and shape, the drag coefficient, C_D, can be estimated from

$$\frac{1}{2}\rho_c u_{ro}^2 C_D \frac{\pi}{4} D_o^2 = \rho_d \frac{\pi}{6} D_o^3 \frac{d^2x}{dt^2} \tag{4}$$

The values of C_D obtained in this way are in the range from 2 to 3 [10, 14]. For liquid-liquid systems, however, a considerable decrease in the relative velocity, and thus the acceleration of the drop, in the time span of interest is experienced, owing to the larger continuous-to-dispersed phase density ratios involved in such systems. Patel and Theofanous [15] have proposed a method to allow for the variation of drag force caused by the change in relative velocity and suggested that a drag coefficient of 2.5 is not unreasonable for their mercury-water data. Following this approach, a modified method, in which the effects of gravity, virtual inertia, and Basset force also have been taken into consideration, has been developed [18]. Typical drop trajectories calculated by means of this method, as well as the corresponding experimental drop displacement data based on the windward stagnation point, are shown in Figs. 5(*a*) and 6(*a*). Other such results can be found in reference [18]. It is apparent that there is considerable scatter in the measured data, especially at earlier times, which may be partly due to the difficulty in resolving the shape of the original drops. As

described above, the drops in the experiments either oscillate continuously or expand rapidly in all directions. Therefore, the calculated results, which are based on the assumption that the mass and shape of the drops remain unchanged, are useful only if regarded as order-of-magnitude estimates. With this in mind, it is thus deduced that the effective drag coefficient for the present experiments is approximately 5. The initial acceleration, based on a C_D of 5, and the Weber number for each drop in the experiments are given in Table 2.

From the values of the dimensionless fragmentation times shown in Table 2 and the histories of drop response, it is evident that there exists a critical Weber number which characterizes drop responses. For Weber numbers below the critical value, the drops would only oscillate, while for Weber numbers above the critical value, the drops would experience an expansion-type deformation. Based on present data, the critical Weber number is $(\mathrm{We})_{cr} = 17$. Moreover, in the experiments with $\mathrm{We} > (\mathrm{We})_{cr}$, there appears to be a systematic variation of dimensionless fragmentation time with Weber number, namely T_b decreases as We increases. This trend, together with the fact that no stripping has been observed in the experiments, suggests that a possible mechanism for mixing is Taylor instability.

In Taylor instability theory, the exponential growth rate of an interfacial disturbance in the linear region is given by [19]

$$n = \left[\frac{ka(\rho_d - \rho_c)}{\rho_d + \rho_c} - \frac{\sigma k^3}{\rho_d + \rho_c} \right]^{1/2} \tag{5}$$

where k is a wave number of the disturbance. It follows from equation (5) that the cut-off wavelength, λ_{cut}, and the fastest growing wavelength, $\lambda_{\max}$, for instability are

$$\lambda_{\mathrm{cut}} = 2\pi \left[\frac{\sigma}{a(\rho_d - \rho_c)} \right]^{1/2} \tag{6}$$

and

$$\lambda_{\max} = 2\pi \left[\frac{3\sigma}{a(\rho_d - \rho_c)} \right]^{1/2} \tag{7}$$

In Table 2 are also given the values of λ_{cut} and $\lambda_{\max}$ calculated from equations (6) and (7). The compatibility of D_o with λ_{cut} and $\lambda_{\max}$ lends support to the statement that mixing may have occurred as a result of drop penetration by unstable Taylor waves.

For liquid-gas systems, Taylor instability manifests itself as the windward surfaces of the drops assume a bubble-and-spike configuration at later times. As noted above, however, the windward surfaces of the drops appear to be smooth at all times. The bubble-and-spike shape has only been observed on the leeward halves of the drops. This seemingly opposite behavior may be explained with the concept of boundary-layer separation [20]. When the shock-induced flow is started, the boundary layers on both sides of the drop surfaces are very thin, because the liquid inside the drop is free to move tangentially. The motion of the mixture in the first instant is very nearly irrotational everywhere, and remains so as long as the boundary layer remains thin. The pressure in this irrotational flow field decreases along the drop windward surface and increases along the drop leeward surface, and so the mixture is accelerated on the upstream part and decelerated on the downstream part of the drop. The initial flow field developed inside the drop would resemble that of Hill's spherical vortex [21], and the mixture would flow around the edge (equator) of the drop with an increasingly high peak in velocity at the edge. As the flattening of the drop proceeds continuously, however, the strong deceleration of the mixture flowing from the drop edge toward the real stagnation point would at some instant lead to the reversal of flow in the boundary layer there and to the separation of the boundary layer from the drop edge. The external pressure field then would cause the mixture in the immediate neighborhood of the drop leeward surface to move in the reverse direction, and thus to move toward the drop. Hence, the detached boundary layer would be rolled up into a spiral under the action of this induced velocity field. As a consequence mixing may occur at the drop edge, and the tangential motion along the drop leeward surface of the liquid inside the drop would diminish, or perhaps stop completely. The drop leeward surface then would experience an effective acceleration which is directed from the mixture toward the drop.

In the range of initial accelerations covered here, the ratio of D_o to $\lambda_{\max}$ does not exceed 3. This implies that tangential motion along the drop windward surface would inhibit the growth of Taylor instability induced by the initial acceleration. It seems likely that the combined effects of the flow reversal in the mixture in the vicinity of the drop leeward surface and the lack of tangential motion inside the drop along this surface would eventually lead to unstable growth of interfacial disturbances on the leeward surface of the drop. Chang and Bankoff [22] have indicated that for the mercury-water pair the spike velocity can become infinite in very short times (~ 0.5 ms for ~ 100 g). The time scales for the growth of spikes observed in the experiments are in fair agreement with this theoretical prediction. In addition, the separation of boundary layer from the drop edge is consistent with the X-ray data of Theofanous et al. [16], wherein a vortex sheet orginating from the drop edge has been observed.

In view of the above discussions, the dimensionless fragmentation times are correlated to the Weber number as

$$T_b = 1.16\ \mathrm{We}^{-1/4} \epsilon^{-1/2} \tag{8}$$

and

$$T_b' = 2.23\ \mathrm{We}^{-1/4} \epsilon^{-1/2} \tag{9}$$

It should be remarked that, instead of the Weber number, the effects of acceleration on drop fragmentation are usually considered in terms of the Bond number. Since the two parameters are approximately related to each other through the drag coefficient. $\mathrm{Bo} = 3/8\ C_D \mathrm{We}$, it becomes a matter of convenience as to which one is appropriate in a mathematical formulation.

Both equations (8) and (9) compare favorably with equation (2). This serves to indicate that the fragmentation time is an order of magnitude smaller in liquid-liquid systems than in liquid-gas systems. As a final remark, because of limitations of the presently employed photographic technique, whereby the shapes of the drops could only be determined in a rather rough way, conclusive evidence of the occurrence of Taylor instability and quantitative characterization of the mixing process seem unlikely. Such information can only be obtained from more detailed description of the size variation and mass distribution of the drop conglomerate. In the light of this and the exclusion of thermal effects, the correlations presented here should be used with caution.

4 Conclusions

Experiments to investigate the shock-induced drop fragmentation in liquid-liquid systems have been performed. For mercury-gas-bubbly mixture systems, the general responses of the mercury drops show that there exists a critical Weber number, $(\mathrm{We})_{cr} = 17$, for drop fragmentation. For Weber numbers below this critical value, the drop oscillates at all times and no fragmentation occurs during the time span of interest. Above this critical Weber number the drop fragmentation is characterized by rapid expansion in directions both transverse and parallel to the flow. The production of misty wakes, stripping of liquid filaments from the equator of the drop, and the appearance of surface waves on the windward surface of the drop, which are typical for

drop fragmentation in liquid-gas systems, are not evident. This agrees with the previous results reported by Patel and Theofanous [15] and suggests that drop fragmentation is preceded by mixing which may be initiated by Taylor instability. The present results are characterized qualitatively by the extent of mixing, and the characteristic times are correlated to the Weber number. Although the shocks investigated in this study were rather weak (pressures up to 1.7 MPa), the lengths of the mixing zone were short (of the order of 0.3 m). This suggests that the presence of void could reduce drastically the pressure requirement for shock-induced hydrodynamic fragmentation. Hence, substantial fragmentation of molten uranium dioxide in liquid water may not require very strong shock waves.

Acknowledgment

This work was supported by a grant from the National Science Foundation under the U.S.-U.S.S.R. Cooperative Research Program in Heat Transfer.

References

1 Long, G., "The Explosions of Molten Aluminum in Water—Cause and Prevention," *Metal Prog.*, Vol. 71, No. 5, 1957, pp. 107–112.

2 Brauer, F. E., Green, N. W., and Mesler, R. B., "Metal/Water Explosions," *Nucl. Sci. Eng.*, Vol. 31, 1968, pp. 551–554.

3 Witte, L. C., Cox, J. E., and Bouvier, J. E., "The Vapor Explosion," *J. Metals*, Vol. 22, Feb. 1970, pp. 39–44.

4 Cho, D. H., Armstrong, D. R., and Gunther, W. H., "Molten Material-Coolant Interactions," *Trans. Am. Nucl. Soc.*, Vol. 13, 1970, p. 385.

5 Board, S. J., Farmer, C. L., and Poole, D. H., "Fragmentation in Thermal Explosions," *Int. J. Heat Mass Transfer*, Vol. 17, 1974, pp. 331–339.

6 Anderson, R. P., and Armstrong, D. R., "Laboratory Tests of Molten-Fuel-Coolant Interactions," *Trans. Am. Nucl. Soc.*, Vol. 15, 1972, pp. 313–314.

7 Bankoff, S. G., "Vapor Explosions," *Proceedings of the Japan-U.S. Seminar on Two-Phase Flow Dynamics*, Kobe, Japan, 1979, pp. 227–248.

8 Board, S. J., Hall, R. W., and Hall, R. S., "Detonation of Fuel-Coolant Explosions," *Nature*, Vol. 254, 1975, pp. 319–321.

9 Taylor, G. I., "The Shape and Acceleration of a Drop in a High-Speed Air Stream," in *The Scientific Papers of G. I. Taylor*, Vol. 3, G. K. Batchelor (ed.), Cambridge University Press, Cambridge, England, 1963, p. 457.

10 Ranger, A. A., and Nicholls, J. A., "Aerodynamic Shattering of Liquids Drops," *AIAA J.*, Vol. 7, 1969, pp. 285–290.

11 Waldman, G. D., Reinecke, W. G., and Glenn, D. C., "Raindrop Breakup in the Shock Layer of a High-Speed Vehicle," *AIAA J.*, Vol. 10, 1972, pp. 1200–1204.

12 Fishburn, B. D., "Boundary Layer Stripping of Liquid Drops Fragmented by Taylor Instability," *Acta Astronautica*, Vol. 1, 1974, pp. 1267–1284.

13 Harper, E. Y., Grube, G. W., and Chang, I., "On the Breakup of Accelerating Liquid Drops," *J. Fluid Mech.*, Vol. 52, 1972, pp. 565–591.

14 Simpkins, P. G., and Bales, E. L., "Water-Drop Response to Sudden Accelerations," *J. Fluid Mech.*, Vol. 55, 1972, pp. 629–639.

15 Patel, P. D., and Theofanous, T. G., "Hydrodynamic Fragmentation of Drops," *J. Fluid Mech.*, Vol. 103, 1981, pp. 207–223.

16 Theofanous, T. G., Saito, M., and Efthimiadis, T., "Fuel Coolant Interactions on Hydrodynamic Fragmentation," *Proceedings of the International Meeting on Fast Reactor Safety Technology*, Seattle, 1979, pp. 1568–1577.

17 Baines, M., and Buttery, N. E., "Differential Velocity Fragmentation in Liquid-Liquid Systems," CEGB Report RD/B/N4643, 1979.

18 Tan, M. J., "Propagation of Pressure Waves in Bubbly Mixtures and Fragmentation of Accelerating Drops," PhD dissertation, Northwestern University, Evanston, Illinois, 1982.

19 Bellman, R., and Pennington, R. H., "Effects of Surface Tension and Viscosity on Taylor Instability," *Quart. Appl. Math.*, Vol. 12, 1954, pp. 151–162.

20 Schlichting, H., *Boundary Layer Theory*, 7th ed., McGraw-Hill, New York, 1979, p. 28.

21 Milne-Thomson, L. M., *Theoretical Hydrodynamics*, 5th ed., Macmillan, New York, 1968, p. 578.

22 Chang, I. M., and Bankoff, S. G., "Nonlinear Taylor Instability of a Plane Interface between Two Incompressible Fluids with Interfacial Mass Transfer," *AIChE J.*, Vol. 29, 1983, pp. 95–100.

Journal of Fluids Engineering

Technical Briefs

A Note on the Response Equations for Hot-Wire Anemometry

M. K. Swaminathan,[1] G. W. Rankin,[1] and K. Sridhar[1]

The various heat transfer laws describing the response of the hot-wire to the velocity normal to its axis have been evaluated on a common basis to judge their effectiveness in representing the raw calibration data. The models compared were the King's law, the exponent power-law, the extended power-law and the polynomial heat transfer law. These models were compared in the high and low velocity ranges of 0–100 m/s and 0–35 m/s, respectively. The criteria chosen for comparison were the minimum sum of the errors squared in the velocity and the estimated uncertainties in the calibration constants evaluated. The results indicate that the differences in the various models based on the sum of the errors in velocity, are not significant. However, when an uncertainty analysis for the constants are included in the study, the extended power-law proves to be robust in both the velocity ranges besides yielding a low error in the velocity. The fourth order polynomial law produces the lowest error in velocity, but the uncertainty in the constants evaluated are considerable. The nonlinear method of calibration together with the criterion of minimizing the errors in velocity offers no significant improvement in a statistical sense as compared to the linear method and the criterion of minimizing the errors in E^2.

Nomenclature

A, B, C, and D = calibration constants
A_0, B_0, C_0 = best estimates of calibration constants
A_1, B_1, C_1 = estimate of the constants after indexing one of the variables
E = output voltage of the constant temperature anemometer
ΔE = estimated uncertainty in E
i = subscript to indicate a set of data points
N = number of data points
U = free stream velocity
ΔU = estimated uncertainty in U
X = a value or a number
$\bar{X}$ = mean of a set of N values of X
σ = standard deviation in U
Σ = symbol representing summation

Introduction

One of the most important problems of hot-wire anemometry is the accurate interpretation of the signal. The purpose of calibration is to determine this response as a function of the velocity vector, the probe-support geometry and the fluid and wire properties. For practical applications a smoothing process is applied to the raw calibration data obtained from a hot-wire probe in a real flow situation over a velocity range. The most commonly used technique to smooth the data is based on the use of analytical expressions or heat transfer laws. Since the true response of the hot-wire is not known, these expressions are only approximate. This together with the fact that the raw data contain uncertainties of measurements, require that more attention be given to the process of choosing the appropriate heat transfer law and the method of curve fitting if good accuracy is to be obtained.

King [1] was the first to obtain an analytical expression which governs the cooling of an electrically heated hot-wire based on a theoretical investigation of idealized flow around an infinitely long wire. This law can be expressed as

$$E^2 = A + BU^{0.5} \tag{1}$$

where E is the measured voltage output of the bridge, U is the cooling velocity normal to the wire, and A and B are the calibration constants. Davies and Bruun [2], based on their experiments, concluded that the exponent of U was a strong function of velocity and hence the values of A and B found for a low range of velocity was not appropriate for a high velocity range. Hence, they suggested the use of the exponent power law

$$E^2 = A + BU^C \tag{2}$$

following the work of Collis and Williams [3]. Collis and Williams first determined C to be 0.42 which was different from the 0.5 value suggested by King. This equation, though seemingly accurate, considerably increased the computational efforts. This is because the coefficient C occurs nonlinearly. Hence, a trial and error approach was adopted to determine all the constants. Swaminathan et al. [4] effectively used the nonlinear iterative technique to simultaneously evaluated all the constants involved in equation (2) and introduced the idea that the criterion for least squares fit ought to be to reduce the errors involved in U. The nonlinear calibration technique consists of rearranging equation (2) in the form

$$U = ((E^2 - A)/B)^{1/C} \tag{3}$$

and expanding this nonlinear equation in a Taylor series about initial estimates of the calibration constants A, B, and C. An iterative procedure using the Newton-Raphson technique then yields the calibration constants by minimizing the errors in U. This technique has been proved to be more systematic, accurate and provides better constants than the conventional approach of [2]. Siddall and Davies [5] put forth an alternate expression for the response of the hot-wire in the form

[1] Research Fellow, Associate Professor, and Professor, respectively, Department of Mechanical Engineering and Fluid Dynamics Research Institute, University of Windsor, Windsor, Ontario, Canada N9B 3P4.

Contributed by the Fluids Engineering Division of The American Society of Mechanical Engineers. Manuscript received by the Fluids Engineering Division, March 26, 1984.

$$E^2 = A + BU^{0.5} + CU \tag{4}$$

They compared the above equation with that of (1) in the high velocity range of 0 – 160 m/s. Equation (4) was especially suited for representing calibration data over a wide velocity range and was less complicated to fit and apply than equation (2). George et al. [6] introduced the polynominal heat transfer law in the form

$$U = A + BE + CE^2 + DE^3 + \ldots\ldots \tag{5}$$

The ease of applying equation (5) for computation and linearization of the response for the digital purposes, presents some advantages. Bruun and Tropea [7] compared the performance of some of these expressions in the low velocity range of 2–40 m/s. The availability of various heat transfer laws for the hot-wire makes it difficult for the experimenter to choose the appropriate one for his purpose. However, attempts to compare the heat transfer models, experimentally, by Siddal and Davies and Bruun and Tropea are lacking for the following reasons. Siddal and Davies compared only King's law and their extended power law and that too in the high velocity range. Further, the criterion used was minimum sum of errors squared in E^2. The other authors restricted themselves to the low velocity range of 2–40 m/s. The polynomial heat transfer law has not yet been compared with any of the accepted analytical expressions. For these reasons and other reasons to be listed below, these investigations are incomplete and hence results drawn are inconclusive.

The problem of calibration involves consideration of several factors such as the correct choice of the analytical expression, the curvefitting technique and the need to specify certain criteria for optimization. All these factors are interrelated and must be taken together to evaluate the relative merits of each equation. This has not been done by the above mentioned authors. The use of hot-wires in turbulence measurements requires that the sensitivity ($\partial E/\partial U$) as well as the mean velocity be accurately measured from the calibration. The choice of a heat transfer model, so far, seems to have been made on the basis of mathematical complexity and the goodness of fit. A choice based on the mathematical complexity is no longer valid since even the most difficult equation (2) has been solved by a simple procedure [4]. Goodness of fit is determined based on the value of the standard deviation, which is defined and given by

$$\text{standard deviation} = \sqrt{\sum_{i=1}^{N} (X_i - \bar{X})^2 / N} \tag{6}$$

where X_i is a set of N numbers with a mean value of $\bar{X}$. The sufficiency of using this criterion alone has to be investigated. Since, the calibration constants evaluate are to be used for computing velocities, turbulence quantities, etc., there should be a criterion to evaluated these constants as accurately as possible. This can only be done if an uncertainty analysis is included in the study. This would help in estimating the uncertainties associated with the parameters. This consideration has been lacking in all the previous studies reported. Therefore, the purpose of this note is to systematically compare these laws by including all factors of influence and to investigate if including an uncertainty analysis will give a different perspective. Further, when comparisons are being made between models, based on the result of curvefitting, a statistical approach must be taken to verify whether the differences, if any, are significant.

Calibrations of the hot-wire were performed in both the high and low velocity ranges. These calibration data were analyzed using the models listed in conjunction with the least squares method. However, since the criterion for selecting the calibration constants are arbitrary, both the minimum errors in U and E^2 were investigated. The uncertainty in the estimated parameters were determined by the method suggested by Moffatt [8] as described in the next section. The details of the experiment, the results and discussion follow.

Experiment, Results, and Discussion

The calibration experiments were carried out in the potential core of the jet facility described in [4] using a DISA (55P11) hot-wire probe and the DISA M system. The velocities were measured using a Pitot-static probe. The nominal velocity ranges chosen were 0–35 m/s and 0–100 m/s. Using the procedure given by Kline and McLintock [9] the estimated uncertainty in the measurement of velocity was less than ± 1 percent. The accuracy with which voltages can be measured is specified by the manufacturer of the voltmeter. This value, ± 0.3 percent, has been assumed to be the uncertainty in the measurement of voltages. The raw calibration data was curvefitted using the computer software developed on an IBM 3031 computer. The determination of uncertainties in the parameters of the models were carried out by the procedure similar to the one given by Moffatt [8]. This method is valid irrespective of whether the approach is a linear or a nonlinear parameter estimation. In this method, if

$$E = f(U; A, B, C) \tag{7}$$

and the uncertainties in E and U are known as ΔE and ΔU, then it is a simple matter to carry out uncertainty analysis on the computer based data reduction program. In principle, using the raw calibration data, (E_i, U_i) with $i = 1, N$, the best estimate A_0, B_0, C_0 is determined using the program. Then one of the variables, say E_1, is indexed by the amount ΔE and new values A_1, B_1, C_1 are calculated along with the differences $(A_1 - A_0)$, $(B_1 - B_0)$ and $(C_1 - C_0)$. This process is repeated for every value of each variable and the contributions squared and accumulated to yield the required uncertainties in the parameters. This forms a common basis of comparison of the performance of the various heat transfer laws. The results and other pertinent details for high and low velocity ranges are given in Table (1) and Table (2), respectively. As can be seen the various models have been compared taking into account factors such as various curvefitting techniques and criteria. The standard deviation reported is that of velocity in all the cases.

In the high velocity range (Table 1), comparison of the σ for the various models indicate that they differ from one another by less than one standard deviation. This should indicate that the differences in σ is not significant in a statistical sense. However, for the three parameter estimate, the exponent and extended power law models yield the lowest σ. Comparison of the uncertainties in the estimated constants shows that King's law yields the lowest uncertainties in the calibration constants. In the polynomial heat transfer model, equation (5), the independent variable E has been replaced by E^2. This change seems to provide lower errors in velocity for a given order of the polynominal. The reason for this can also be seen by rewriting King's law, equation (1), as

$$U^{0.5} = (1/B)E^2 - (1/B)A$$

$$U = (1/B^2)E^4 - (2A/B^2)E^2 + (A/B)^2 \tag{8}$$

Equation (8) has the form of (5), the polynomial heat transfer model. In the low velocity range (Table 2) the sum of the errors squared of the King's law model differs by at least one standard deviation from the rest. Hence the difference can be considered to be significant. The other observations made are valid in the low range as well.

The decision as to which model is to be preferred should be based on both the σ as well as the uncertainty in the estimation of the parameters. In addition, further considerations such as the data processing instruments available, the ease of data reduction for turbulence measurement needs to be taken into account. The use of the polynomial heat transfer law requires that higher order voltage correlations be measured. If

Table 1 Comparison of the heat transfer laws in high velocity range

#	HEAT TRANSFER LAW	CRITERIA FOR LEAST SQUARES FIT	METHOD OF CURVE FITTING	NO. OF PARA-METERS	PARAMETERS A	B	C	D	σ	ESTIMATED PERCENTAGE UNCERTAINTIES IN A	IN B	IN C	IN D	IN σ
1	KING'S LAW $E^2 = A+B\sqrt{U}$	MINIMUM SES IN E^2	LINEAR	2	8.18	2.01	-	-	0.74	0.49%	0.50%	-	-	47.70%
2	FLOATING EXPONENT POWER LAW	MINIMUM SES IN E^2	LINEAR- TRIAL AND ERROR	3	4.49	3.72	0.40	-	0.64	14.70%	9.14%	2.50%	-	57.81%
	$E^2 = A+BU^C$	MINIMUM SES IN U	NON-LINEAR - ITERATION	3	4.07	3.93	0.39	-	0.64	16.71%	7.60%	2.56%	-	56.25%
3	EXTENDED POWER LAW $E^2 = A+BU^{\frac{1}{2}}+CU$	MINIMUM SES IN E^2	POLYNOMIAL FIT	3	6.61	2.42	-0.027	-	0.64	3.30%	2.47%	14.80%	-	56.25%
4 POLYNOMIAL IN E^2	QUADRATIC $U = A+B(E^2) + C(E^2)^2$	MINIMUM SES IN U	POLYNOMIAL FIT	3	42.34	-6.29	0.30	-	0.66	16.84%	10.20%	4.70%	-	64.13%
	3rd Order $U = A+B(E^2) +C(E^2)^2 +D(E^2)^3$	MINIMUM SES IN U	POLYNOMIAL FIT	4	-52.78	6.22	-0.25	0.0078	0.66	110.71%	126.05%	140.00%	65.00%	68.07%

Table 2 Comparison of heat transfer laws in low velocity range

#	HEAT TRANSFER LAW	CRITERIA FOR LEAST SQUARES FIT	METHOD OF CURVE FITTING	NO. OF PARA-METERS	PARAMETERS A	B	C	D	σ	ESTIMATED PERCENTAGE UNCERTAINTIES IN A	IN B	IN C	IN D	IN σ
1	KING'S LAW $E^2 = A+B\sqrt{U}$	MINIMUM SES IN E^2	LINEAR	2	5.68	2.27	-	-	0.18	0.35%	0.20%	-	-	61.11%
2	FLOATING EXPONENT POWER LAW	MINIMUM SES IN E^2	LINEAR-TRIAL AND ERROR	3	4.10	3.27	0.43	-	0.10	5.37%	4.59%	2.05%	-	110%
	$E^2 = A+BU^C$	MINIMUM SES IN U	NON-LINEAR-ITERATION	3	3.97	3.35	0.42	-	0.096	7.56%	2.69%	2.86%	-	115%
3	EXTENDED POWER LAW $E^2 = A+BU^{\frac{1}{2}}+CU$	MINIMUM SES IN E^2	POLYNOMIAL FIT	3	4.97	2.62	-0.04	-	0.096	1.69%	1.60%	12.50%	-	112%
4 POLYNOMIAL IN E^2	QUADRATIC $U = A+B(E^2) + C(E^2)^2$	MINIMUM SES IN U	POLYNOMIAL FIT	3	12.68	-3.07	0.22	-	0.11	13.49%	7.82%	3.64%	-	127%
	3rd Order $U = A+B(E^2) +C(E^2)^2 +D(E^2)^3$	MINIMUM SES IN U	POLYNOMIAL FIT	4	-2.36	-0.037	0.022	0.0044	0.10	438%	HIGH	680%	75%	250%

analogue linearization of the hot-wire is to be carried out using the standard commercially available linearizer, such as the DISA 55D10, then use of the extended or polynomial laws lead to errors. Even though the criterion that errors in velocity should be minimized yields lower errors in an absolute sense, the differences are insignificant. This leads to considerable errors in the parameter estimated. This can be seen from the errors in the estimates using the polynomial approach. The polynomial model shows the highest errors in the parameter estimates. In a statistical sense the nonlinear technique seems to offer no particular advantage other than the determination of all the constants simultaneously without trial and error.

In view of the results presented, it is seen that the extended power law yields a compromise between low standard deviation in U and low uncertainties in A, B, and C for both of the velocity ranges. The added advantage of using the polynomial curvefitting technique can also be seen. However, if one prefers to look at the problem of choosing a heat transfer model from a somewhat physical reasoning based on King's law rather than as a regression problem, the exponent power law comes closer.

Conclusions

The raw calibration data on the hot-wire obtained in the high and low velocity ranges have been analyzed using the various heat transfer models and the least squares curve fitting technique. To compare and evaluate the laws both the σ and the uncertainty in the estimated parameters have been considered. The results indicate that the extended power law yields the best compromise between low σ and low uncertainty in the estimated parameters. The polynomial model yields the lowest σ for higher orders, but the uncertainties in the parameter estimations are considerable. From the statistical point of view, the differences in the values of σ for the various models are not significant.

References

1 King, L. V., "On the Convection of Heat From Small Cylinders in a Stream of Fluid," *Phil. Trans. Roy. Soc.*, Vol. 214A, 1914, pp. 373–432,

2 Davies, P. O. A. L., and Bruun, H. H., "The Performance of Yawed Hot-Wire," *Proceedings of a Symposium on Instrumentation and Data Processing for Industrial Aerodynamics*, N.P.L., 1968.

3 Collis, D. C., and Williams, M. J., "Two-Dimensional Convection From Heated Wires at Low Reynolds Numbers," *J. Fluid Mech.*, Vol. 6, 1959, pp. 357–389.

4 Swaminathan, M. K., Bacic, R., Rankin, G. W., and Sridhar, K., "Improved Calibration of Hot-Wire Anemometers," *J. Phy. E:Sci. Instrum.*, Vol. 16, 1983, pp. 335–338.

5 Siddall, R. G., and Davies, T. W., "An Improved Response Equation for Hot-Wire Anemometry," *Int. J. Heat Mass Tranfer*, Vol. 15, 1972, pp. 367–368.

6 George, W. K., Beuther, P. D., and Ahmad, M., "Polynomial Calibrations and Quasi-Linearization of Hot Wires,'" Turbulence Research Laboratory Report, SUNY Buffalo, Sept. 1981.

7 Bruun, H. H., and Tropea, C., "Calibration of Normal, Inclined and X-array Hot-Wire Probes," Report SFB 80/M/170, Ausbreitungsund Transportvorgänge in Strömungen, Universität, Karlsruhe, Nov. 1980.

8 Moffatt, R., Stanford University (private communication).

9 Kline, S. J., and McLintock, F. A., "Describing Uncertainties in Single-Sampled Experiments," *Mechanical Engineering*, Vol. 3, 1953.

The Dissipation Rate Correlation and Turbulent Secondary Flows in Noncircular Ducts

C. G. Speziale[1]

The pressure-driven mean turbulent flow of a viscous fluid through straight ducts of noncircular cross section is not unidirectional like its laminar counterpart. A nonzero mean flow occurs in the transverse planes of the duct which is referred to as secondary flow (see Fig. 1). Despite the fact that this secondary flow is small in magnitude (approximately one percent of that of the axial mean velocity), it nevertheless has a profound effect on the overall flow by leading to distortions of the axial flow with considerable friction losses. Nikuradse [1] was the first to observe experimentally the structure of the turbulent secondary flows in rectangular and triangular ducts. However, more than thirty years elapsed before the first detailed measurements of the turbulence structure in noncircular ducts were made [2–4]. Subsequently, Gessner and Jones [5] made more extensive measurements of turbulent flow in a rectangular duct and, from a simplified analysis of the Reynolds equation along a secondary flow streamline, concluded that "secondary flow is the result of small differences in magnitude of opposing forces exerted by the Reynolds stresses and static pressure gradients in planes normal to the axial flow direction".

In recent years, a significant effort has been directed toward the calculation of turbulent secondary flows in rectangular and triangular ducts. Most of the earliest work in this direction tended to be heavily empirical [6–7]. However, there has been a substantial amount of work done recently in the calculation of secondary flows by utilizing the Reynolds stress transport equations in some modified form [8–12]. While this work does represent an important first step in the calculation of turbulent secondary flows, it is still rather empirical. Furthermore, no effort has been made to account for the contributions that the higher-order turbulence correlations make in the generation of secondary flows without ad hoc empiricisms. The purpose of the present paper is to examine more precisely the role that various turbulence correlations play in the generation of secondary flows and to utilize this information in the development of better turbulent closure models. A preliminary investigation along these lines was presented in Speziale [13].

The fully-developed turbulent flow of an incompressible Newtonian fluid in a straight duct of non-circular cross-section will be considered (c.f., Fig. 1). Here, the axial mean pressure gradient $\partial \bar{P}/\partial z = -G$ is constant and is maintained by external means. The duct is sufficiently long so that there exists an interior section where the mean flow properties are independent of the axial coordinate z. For fully-developed turbulent flow, the mean velocity vector $\bar{\mathbf{v}}$ is three-dimensional, i.e., $\bar{\mathbf{v}}$ is of the form

$$\bar{\mathbf{v}} = \bar{v}_x \mathbf{i} + \bar{v}_y \mathbf{j} + \bar{v}_z \mathbf{k} \tag{1}$$

where $\bar{v}_x$ and $\bar{v}_y$ constitute the secondary flow and $\bar{v}_z$ represents the axial flow. As a result of the presence of secondary flow, fluid particles undergo a spiraling motion down the duct in contrast to the rectilinear motion that occurs in the laminar case. A modified vorticity-stream function formulation can be utilized for this problem as follows [13]:

$$\rho\left(\bar{v}_x \frac{\partial \bar{v}_z}{\partial x} + \bar{v}_y \frac{\partial \bar{v}_z}{\partial y}\right) = G + \mu \nabla^2 \bar{v}_z + \frac{\partial \tau_{xz}}{\partial x} + \frac{\partial \tau_{yz}}{\partial y} \tag{2}$$

$$\rho\left(\bar{v}_x \frac{\partial \bar{\omega}_z}{\partial x} + \bar{v}_y \frac{\partial \bar{\omega}_z}{\partial y}\right) = \mu \nabla^2 \bar{\omega}_z + \frac{\partial^2(\tau_{yy} - \tau_{xx})}{\partial x \partial y} + \frac{\partial^2 \tau_{xy}}{\partial x^2} - \frac{\partial^2 \tau_{xy}}{\partial y^2} \tag{3}$$

$$\nabla^2 \psi = \bar{\omega}_z \tag{4}$$

$$\bar{v}_x = -\frac{\partial \psi}{\partial y}, \quad \bar{v}_y = \frac{\partial \psi}{\partial x} \tag{5}$$

where $\bar{\omega}_z = \partial \bar{v}_y/\partial x - \partial \bar{v}_x/\partial y$ is the axial mean vorticity, ρ is the fluid density, μ is the shear viscosity, ψ is the secondary flow stream function, and τ is the Reynolds stress tensor.

Equations (2)–(5) must be solved subject to the boundary conditions

$$\bar{\mathbf{v}} = 0, \quad \psi = 0, \quad \tau = 0 \tag{6}$$

on the wall of the duct. As a result of (4) and the no-slip condition (6), it is quite clear that secondary flows result from a nonzero axial mean vorticity (i.e., if $\bar{\omega}_z = 0$, then $\psi = 0$ and $\bar{v}_x = \bar{v}_y = 0$). Consequently, the term

$$\frac{\partial^2(\tau_{yy} - \tau_{xx})}{\partial x \partial y} + \frac{\partial^2 \tau_{xy}}{\partial x^2} - \frac{\partial^2 \tau_{xy}}{\partial y^2}, \tag{7}$$

which serves as an axial vorticity source term in (3), is the cause of secondary flow.

It follows that if $\tau_{yy} - \tau_{xx} = 0$, for all x, y-coordinate systems, then $\tau_{xy} = 0$ (this is a direct consequence of the plane Reynolds stress transformation equations). Thus, if the axial mean velocity gives rise to a transverse normal Reynolds stress

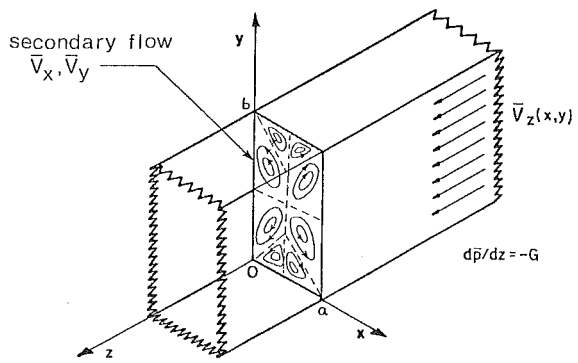

Fig. 1 Fully-developed turbulent flow in a rectangular duct

[1] George W. Woodruff School of Mechanical Engineering, Georgia Institute of Technology, Atlanta, GA 30332.

Contributed by the Fluids Engineering Division of THE AMERICAN SOCIETY OF MECHANICAL ENGINEERS. Manuscript received by the Fluids Engineering Division, April 10, 1984.

References

1 King, L. V., "On the Convection of Heat From Small Cylinders in a Stream of Fluid," *Phil. Trans. Roy. Soc.*, Vol. 214A, 1914, pp. 373–432,

2 Davies, P. O. A. L., and Bruun, H. H., "The Performance of Yawed Hot-Wire," *Proceedings of a Symposium on Instrumentation and Data Processing for Industrial Aerodynamics*, N.P.L., 1968.

3 Collis, D. C., and Williams, M. J., "Two-Dimensional Convection From Heated Wires at Low Reynolds Numbers," *J. Fluid Mech.*, Vol. 6, 1959, pp. 357–389.

4 Swaminathan, M. K., Bacic, R., Rankin, G. W., and Sridhar, K., "Improved Calibration of Hot-Wire Anemometers," *J. Phy. E:Sci. Instrum.*, Vol. 16, 1983, pp. 335–338.

5 Siddall, R. G., and Davies, T. W., "An Improved Response Equation for Hot-Wire Anemometry," *Int. J. Heat Mass Tranfer*, Vol. 15, 1972, pp. 367–368.

6 George, W. K., Beuther, P. D., and Ahmad, M., "Polynomial Calibrations and Quasi-Linearization of Hot Wires,'" Turbulence Research Laboratory Report, SUNY Buffalo, Sept. 1981.

7 Bruun, H. H., and Tropea, C., "Calibration of Normal, Inclined and X-array Hot-Wire Probes," Report SFB 80/M/170, Ausbreitungsund Transportvorgänge in Strömungen, Universität, Karlsruhe, Nov. 1980.

8 Moffatt, R., Stanford University (private communication).

9 Kline, S. J., and McLintock, F. A., "Describing Uncertainties in Single-Sampled Experiments," *Mechanical Engineering*, Vol. 3, 1953.

The Dissipation Rate Correlation and Turbulent Secondary Flows in Noncircular Ducts

C. G. Speziale[1]

The pressure-driven mean turbulent flow of a viscous fluid through straight ducts of noncircular cross section is not unidirectional like its laminar counterpart. A nonzero mean flow occurs in the transverse planes of the duct which is referred to as secondary flow (see Fig. 1). Despite the fact that this secondary flow is small in magnitude (approximately one percent of that of the axial mean velocity), it nevertheless has a profound effect on the overall flow by leading to distortions of the axial flow with considerable friction losses. Nikuradse [1] was the first to observe experimentally the structure of the turbulent secondary flows in rectangular and triangular ducts. However, more than thirty years elapsed before the first detailed measurements of the turbulence structure in noncircular ducts were made [2–4]. Subsequently, Gessner and Jones [5] made more extensive measurements of turbulent flow in a rectangular duct and, from a simplified analysis of the Reynolds equation along a secondary flow streamline, concluded that "secondary flow is the result of small differences in magnitude of opposing forces exerted by the Reynolds stresses and static pressure gradients in planes normal to the axial flow direction".

In recent years, a significant effort has been directed toward the calculation of turbulent secondary flows in rectangular and triangular ducts. Most of the earliest work in this direction tended to be heavily empirical [6–7]. However, there has been a substantial amount of work done recently in the calculation of secondary flows by utilizing the Reynolds stress transport equations in some modified form [8–12]. While this work does represent an important first step in the calculation of turbulent secondary flows, it is still rather empirical. Furthermore, no effort has been made to account for the contributions that the higher-order turbulence correlations make in the generation of secondary flows without ad hoc empiricisms. The purpose of the present paper is to examine more precisely the role that various turbulence correlations play in the generation of secondary flows and to utilize this information in the development of better turbulent closure models. A preliminary investigation along these lines was presented in Speziale [13].

The fully-developed turbulent flow of an incompressible Newtonian fluid in a straight duct of non-circular cross-section will be considered (c.f., Fig. 1). Here, the axial mean pressure gradient $\partial \bar{P}/\partial z = -G$ is constant and is maintained by external means. The duct is sufficiently long so that there exists an interior section where the mean flow properties are independent of the axial coordinate z. For fully-developed turbulent flow, the mean velocity vector $\bar{\mathbf{v}}$ is three-dimensional, i.e., $\bar{\mathbf{v}}$ is of the form

$$\bar{\mathbf{v}} = \bar{v}_x \mathbf{i} + \bar{v}_y \mathbf{j} + \bar{v}_z \mathbf{k} \tag{1}$$

where $\bar{v}_x$ and $\bar{v}_y$ constitute the secondary flow and $\bar{v}_z$ represents the axial flow. As a result of the presence of secondary flow, fluid particles undergo a spiraling motion down the duct in contrast to the rectilinear motion that occurs in the laminar case. A modified vorticity-stream function formulation can be utilized for this problem as follows [13]:

$$\rho\left(\bar{v}_x \frac{\partial \bar{v}_z}{\partial x} + \bar{v}_y \frac{\partial \bar{v}_z}{\partial y}\right) = G + \mu \nabla^2 \bar{v}_z + \frac{\partial \tau_{xz}}{\partial x} + \frac{\partial \tau_{yz}}{\partial y} \tag{2}$$

$$\rho\left(\bar{v}_x \frac{\partial \bar{\omega}_z}{\partial x} + \bar{v}_y \frac{\partial \bar{\omega}_z}{\partial y}\right) = \mu \nabla^2 \bar{\omega}_z + \frac{\partial^2(\tau_{yy} - \tau_{xx})}{\partial x \partial y} + \frac{\partial^2 \tau_{xy}}{\partial x^2} - \frac{\partial^2 \tau_{xy}}{\partial y^2} \tag{3}$$

$$\nabla^2 \psi = \bar{\omega}_z \tag{4}$$

$$\bar{v}_x = -\frac{\partial \psi}{\partial y}, \quad \bar{v}_y = \frac{\partial \psi}{\partial x} \tag{5}$$

where $\bar{\omega}_z = \partial \bar{v}_y/\partial x - \partial \bar{v}_x/\partial y$ is the axial mean vorticity, ρ is the fluid density, μ is the shear viscosity, ψ is the secondary flow stream function, and τ is the Reynolds stress tensor.

Equations (2)–(5) must be solved subject to the boundary conditions

$$\bar{\mathbf{v}} = 0, \quad \psi = 0, \quad \tau = 0 \tag{6}$$

on the wall of the duct. As a result of (4) and the no-slip condition (6), it is quite clear that secondary flows result from a nonzero axial mean vorticity (i.e., if $\bar{\omega}_z = 0$, then $\psi = 0$ and $\bar{v}_x = \bar{v}_y = 0$). Consequently, the term

$$\frac{\partial^2(\tau_{yy} - \tau_{xx})}{\partial x \partial y} + \frac{\partial^2 \tau_{xy}}{\partial x^2} - \frac{\partial^2 \tau_{xy}}{\partial y^2}, \tag{7}$$

which serves as an axial vorticity source term in (3), is the cause of secondary flow.

It follows that if $\tau_{yy} - \tau_{xx} = 0$, for all x, y-coordinate systems, then $\tau_{xy} = 0$ (this is a direct consequence of the plane Reynolds stress transformation equations). Thus, if the axial mean velocity gives rise to a transverse normal Reynolds stress

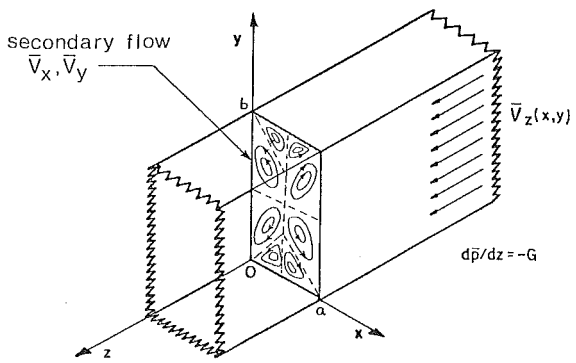

Fig. 1 Fully-developed turbulent flow in a rectangular duct

[1] George W. Woodruff School of Mechanical Engineering, Georgia Institute of Technology, Atlanta, GA 30332.

Contributed by the Fluids Engineering Division of THE AMERICAN SOCIETY OF MECHANICAL ENGINEERS. Manuscript received by the Fluids Engineering Division, April 10, 1984.

difference $\tau_{yy}-\tau_{xx}$ which is zero for all x, y-coordinate systems, the axial vorticity source term will vanish, i.e.,

$$\frac{\partial^2(\tau_{yy}-\tau_{xx})}{\partial x\partial y}+\frac{\partial^2\tau_{xy}}{\partial x^2}-\frac{\partial^2\tau_{xy}}{\partial y^2}=0 \tag{8}$$

Rectilinear mean turbulent flows would then occur in noncircular ducts.

The following necessary condition has thus been proven: Turbulent secondary flows will occur in ducts of noncircular cross-section only if the axial mean velocity gives rise to some nonzero difference in the transverse normal Reynolds stresses. While this result is qualitatively consistent with previous work on the subject, it is more concise and establishes a direct causal relationship between the existence of a non-zero transverse normal Reynolds stress difference $\tau_{yy}-\tau_{xx}$ and the development of secondary flow.

In order to determine the role that various higher-order turbulence correlations play in the generation of secondary flows, we will make use of the Reynolds stress transport equation which takes the general form [14]:

$$\frac{D\tau_{kl}}{Dt}+\tau_{mk}\frac{\partial\bar{v}_l}{\partial x_m}+\tau_{ml}\frac{\partial\bar{v}_k}{\partial x_m}=\rho\frac{\partial(\overline{u_ku_lu_m})}{\partial x_m}+\overline{u_k\frac{\partial p}{\partial x_l}+u_l\frac{\partial p}{\partial x_k}}+2\rho\nu\overline{\frac{\partial u_k}{\partial x_m}\frac{\partial u_l}{\partial x_m}}+\nu\nabla^2\tau_{kl} \tag{9}$$

In (9), $\mathbf{u}$ is the fluctuating velocity, p is the fluctuating pressure, $\nu\equiv\mu/\rho$ is the kinematic viscosity, an overbar represents the ensemble mean, and the operator D/Dt is defined by

$$\frac{D}{Dt}=\frac{\partial}{\partial t}+\bar{\mathbf{v}}\cdot\nabla \tag{10}$$

The higher-order turbulence correlations on the right-side of (9) given by

$$A^{(1)}_{klm}\equiv\overline{u_ku_lu_m}\,,$$

$$A^{(2)}_{kl}\equiv\overline{u_k\frac{\partial p}{\partial x_l}+u_l\frac{\partial p}{\partial x_k}}\,,\quad A^{(3)}_{kl}\equiv\nu\overline{\frac{\partial u_k}{\partial x_m}\frac{\partial u_l}{\partial x_m}} \tag{11}$$

are, respectively, referred to as the third-order diffusion correlation, the pressure gradient-velocity correlation, and the dissipation rate correlation. In the absence of the higher-order turbulence correlations, (9) reduces to

$$\frac{D\tau_{kl}}{Dt}+\tau_{mk}\frac{\partial\bar{v}_l}{\partial x_m}+\tau_{ml}\frac{\partial\bar{v}_k}{\partial x_m}=\nu\nabla^2\tau_{kl} \tag{12}$$

and, thus, the fully-developed axial mean velocity $\bar{v}_z$ gives rise to a transverse normal Reynolds stress difference that satisfies the equation

$$\nabla^2(\tau_{yy}-\tau_{xx})=0 \tag{13}$$

Equation (13) is obtained by setting $\bar{\mathbf{v}}=\bar{v}_z\,\mathbf{k}$ in (12) and then differencing the xx and yy - components while making use of the fact that the flow is fully-developed and independent of the axial coordinate z. As a result of the no slip condition (6) for the Reynolds stress tensor, (13) has the unique solution $\tau_{yy}-\tau_{xx}=0$ which violates the necessary condition for the development of secondary flows. Hence, we can conclude that secondary flows arise exclusively from the higher-order turbulence correlations.

In Speziale [13], the modeled terms for the higher-order turbulence correlations that give rise to secondary flows were determined for several turbulent closure models that are currently popular. To be specific, it was proven that in the Rotta-Kolmogorov model, secondary flows are generated by the third-order diffusion correlation and the pressure-diffusion correlation whereas, in the Launder model, they are generated by the third-order diffusion correlation and the pressure-strain correlation. In this paper, it will be demonstrated that all of these currently popular turbulence models are deficient in that the dissipation rate correlation does not give rise to secondary flows. From equation (9), it is clear that the axial mean velocity $\bar{v}_z$ gives rise to a transverse normal Reynolds stress difference that can be approximated by the equation

$$\nu\nabla^2(\tau_{yy}-\tau_{xx})=2\rho\nu\left[\overline{\frac{\partial u_x}{\partial x}\frac{\partial u_x}{\partial x}}+\overline{\frac{\partial u_x}{\partial y}\frac{\partial u_x}{\partial y}}+\overline{\frac{\partial u_x}{\partial z}\frac{\partial u_x}{\partial z}}-\overline{\frac{\partial u_y}{\partial x}\frac{\partial u_y}{\partial x}}-\overline{\frac{\partial u_y}{\partial y}\frac{\partial u_y}{\partial y}}-\overline{\frac{\partial u_y}{\partial z}\frac{\partial u_y}{\partial z}}\right]+2\left(\overline{u_x\frac{\partial p}{\partial x}}-\overline{u_y\frac{\partial p}{\partial y}}\right) \tag{14}$$

in the near wall region since the effects of turbulent diffusion can be neglected there. The right-hand side of (14), which serves as a source term for the transverse normal Reynolds stress difference, is directly responsible for the generation of secondary flows as a result of the necessary condition derived earlier and the fact that secondary flows emanate from the neighborhood of the duct walls. The first term on the right side of (14) is the transverse dissipation rate difference. Recent large-eddy simulations of turbulence [15] have indicated that there can be significant anisotropies in the dissipation rate correlation near solid boundaries – a state of affairs which would give rise to a non-negligible transverse dissipation rate difference in non-circular ducts. Hence, it appears that the dissipation rate correlation in turbulent duct flow can contribute to the generation of secondary flows.

It will now be demonstrated that in *all* of the currently popular second-order closure models, the dissipation rate correlation does not lead to the generation of secondary flows. In the Rotta-Kolmogorov model, the dissipation rate correlation is taken to be of the isotropic form

$$\nu\overline{\frac{\partial u_k}{\partial x_m}\frac{\partial u_l}{\partial x_m}}=\frac{1}{3}\frac{K^3}{\lambda}\delta_{kl} \tag{15}$$

where $K^2=-\tau_{kk}/2\rho$ is the local turbulent kinetic energy per unit mass, and λ is the length scale of turbulence which is obtained from a modeled version of the contracted transport equation for the two-point double-velocity correlation [16]. This closure relation yields a transverse dissipation rate difference that is zero, i.e., the substitution of (15) into (14) (neglecting the pressure gradient-velocity correlation) yields the equation

$$\nabla^2(\tau_{yy}-\tau_{xx})=0 \tag{16}$$

which has the unique solution $\tau_{yy}-\tau_{xx}=0$. Thus, the dissipation rate correlation in the Rotta-Kolmogorov model does not give rise to secondary flows.

In the generalized Launder model, the dissipation rate correlation is taken to be of the form

$$\nu\overline{\frac{\partial u_k}{\partial x_m}\frac{\partial u_l}{\partial x_m}}=\frac{1}{3}\frac{K^3}{\lambda}\left[(1-f_s)\delta_{kl}-\frac{3f_s}{2\rho K^2}\tau_{kl}\right] \tag{17}$$

where f_s is a dimensionless function of the Reynolds number, and λ is the length scale of turbulence which in this case is constructed from a modeled version of the transport equation for the scalar dissipation rate [17]. For high Reynolds number turbulence, f_s is taken to be zero. In the generalized Launder model, the dissipation rate correlation gives rise to a transverse normal Reynolds stress difference that satisfies the equation

$$\nu\nabla^2(\tau_{yy}-\tau_{xx})=\frac{K}{\lambda}f_s(\tau_{yy}-\tau_{xx}) \tag{18}$$

which has the unique solution $\tau_{yy}-\tau_{xx}=0$. Hence, the dissipation rate correlation in the generalized Launder model does

not lead to the generation of secondary flows which is contrary to the results derived herein.

It is now clear that the currently popular turbulent closure models are deficient in the modeling of the dissipation rate correlation in so far as secondary flows are concerned. This deficiency can be corrected within the usual context of second-order closures. By making use of the usual underlying assumption in second-order closure models that the departure from isotropy in the higher-order turbulence correlations is not very large, the following representation was derived in Speziale [18] by asymptotic and invariance arguments

$$\nu \overline{\frac{\partial u_k}{\partial x_m} \frac{\partial u_l}{\partial x_m}} = C_1 \frac{K^3}{\lambda} \delta_{kl} - \frac{C_2 K}{\rho \lambda} \tau_{kl} + \frac{C_3}{\rho^2 K \lambda} \tau_{km} \tau_{ml} \tag{19}$$

where C_1, C_2, and C_3 are dimensionless constants. This equation differs qualitatively only in the last term from the expression proposed by Hanjalic and Launder [17] and is almost identical to that proposed by Lin and Wolfshtein [19] using statistical arguments. However, it will now be shown that this last term can give rise to secondary flows. The direct substitution of (19) into (14) yields the following equation for the transverse normal Reynolds stress difference that the dissipation rate correlation gives rise to:

$$\nu \nabla^2 (\tau_{yy} - \tau_{xx}) = \frac{2C_2 K}{\lambda} (\tau_{yy} - \tau_{xx}) - \frac{2C_3}{\rho K \lambda} (\tau_{yy}^2 + \tau_{yz}^2 - \tau_{xx}^2 - \tau_{xz}^2) \tag{20}$$

However, this equation *cannot* have the solution $\tau_{yy} - \tau_{xx} = 0$ for turbulent flow in noncircular ducts since $\tau_{yz} \neq \tau_{xz}$, in general, as is obvious from simple symmetry arguments [5]. Hence, the closure relation (19) gives rise to a non-zero transverse normal Reynolds stress difference which can lead to the generation of secondary flows.

The calibration of the constants C_1, C_2, and C_3 and the application of this model to the calculation of turbulent secondary flows in noncircular ducts constitutes a major computational effort which must await future research. However, as demonstrated in this paper, the dissipation rate correlation in all of the currently popular turbulent closure models does not give rise to the development of secondary flows which appears to be inconsistent with results that are a rigorous consequence of the Navier-Stokes equations. This deficiency should be corrected if secondary flows are to be calculated more accurately, particularly for turbulent flows where the Reynolds numbers are not extremely high.

References

1 Nikuradse, J., "Untersuchungen uber die Geschwindigkeitsverteilung in Turbulenten Stromungen," *VDI Forschungsheft*, Vol. 70, 1926, p. 1229.

2 Hoagland, L. C., "Fully Developed Turbulent Flow in Straight Rectangular Ducts – Secondary Flow, Its Cause and Effect on the Primary Flow," Ph.D. thesis, Massachusetts Institute of Technology, 1960.

3 Leutheusser, H. J., "Turbulent Flow in Rectangular Ducts," *Proceedings ASCE, Journal of the Hydraulics Division*, Vol. 89, 1963, pp. 1–19.

4 Brundrett, E., and Baines, W. D., "The Production and Diffusion of Vorticity in Duct Flow," *J. Fluid Mech.*, Vol. 19, 1964, pp. 375–394.

5 Gessner, F. B., and Jones, J. B., "On Some Aspects of Fully-Developed Turbulent Flow in Rectangular Channels," *J. Fluid Mech.*, Vol. 23, 1965, pp. 689–713.

6 Ligget, J. A., Chiu, C. L., and Miao, L. S., "Secondary Currents in a Corner," ASME *J. Heat Transfer*, Vol. 95, 1973, pp. 453–457.

7 Krajewski, B., "Determination of Turbulent Velocity Field in a Rectilinear Duct with Non-Circular Cross-Section," *Int. J. Heat Mass Transfer*, Vol. 13, 1970, pp. 1819–1824.

8 Launder, B. E., and Ying, W. M., "Fully Developed Turbulent Flow in Ducts of Square Cross Section," Report TM/TN/A/11, Department of Mechanical Engineering, Imperial College of Science and Technology, London, 1971.

9 Naot, D., Shavit, A., and Wolfshtein, M., "Numerical Calculation of Reynolds Stresses in a Square Duct with Secondary Flow," *Warme und Stopubertragung*, Vol. 7, 1974, pp. 151–161.

10 Gessner, F. B., and Emery, A. F., "A Reynolds Stress Model for Turbulent Corner Flows – Part I: Development of the Model," ASME JOURNAL OF FLUIDS ENGINEERING, Vol. 98, 1976, pp. 261–268.

11 Gessner, F. B., and Po, J. K., "A Reynolds Stress Model for Turbulent Corner Flows – Part II: Comparisons Between Theory and Experiment," ASME JOURNAL OF FLUIDS ENGINEERING, Vol. 99, 1977, pp. 269–277.

12 DeMuren, A. and Rodi, W., "Calculation of Turbulence-Driven Secondary Motion in Non-Circular Ducts," *J. Fluid Mech.*, Vol. 140, 1984, pp. 189–222.

13 Speziale, C. G., "On Turbulent Secondary Flows in Pipes of Non-Circular Cross-Section," *Int. J. Eng. Sci.*, Vol. 20, 1982, pp. 863–872.

14 Hinze, J. O., *Turbulence*, McGraw-Hill Book Co., New York, 1975.

15 Moin, P. and Kim, J., "Numerical Investigation of Turbulent Channel Flow," *J. Fluid Mech.*, Vol. 118, 1982, pp. 341–377.

16 Mellor, G. L., and Herring, H. J., "A Survey of the Mean Turbulent Field Closure Models," *AIAA J.*, Vol. 11, 1973, pp. 590–599.

17 Hanjalic, K., and Launder, B. E., "Contribution Towards a Reynolds Stress Closure for Low Reynolds Number Turbulence," *J. Fluid Mech.*, Vol. 74, 1976, pp. 593–610.

18 Speziale, C. G., "Closure Models for Rotating Two-Dimensional Turbulence," *Geophys. Astrophys. Fluid Dynamics*, Vol. 23, 1983, pp. 69–84.

19 Lin, A. and Wolfshtein, M., "Theoretical Study of the Reynolds Stress Equations," in *Turbulent Shear Flows I*, 1979, F. Durst et al., eds., Springer, pp. 327–343.

Journal of Fluids Engineering

Discussion

The Effect of Elbow Restraint on Pressure Transients[1]

R. E. Schwirian.[2] The authors are to be commended for demonstrating, by analysis and experiment, the importance of pipe motion on the transient fluid pressures within a piping system. There are a number of things which have tended to obscure this issue in the past. One is the belief that differences between calculations and test measurements can be attributed solely to an "elbow" effect. While an "elbow" effect does exist (cf. Walker and Phillips, authors' reference [5]), it is usually only significant for acoustic wavelengths of the same order as or less than the distance around the elbow. Waterhammer wavelengths for which "elbow" effects have been observed are typically greater than this. The authors rightly conclude that such observations are probably due largely to non-rigid elbow restraints.

Another factor which tends to be misleading is that modal analyses of piping-fluid systems frequently show that many modes can be approximately characterized as either "acoustical" or "structural" in nature. This tendency has been used as a justification for separating the analytical problem into independent waterhammer and structural pieces. However, as the authors demonstrate, this separation is not generally valid for pulse-type transients, where many frequencies are involved, and where "acoustical" and "structural" frequencies are of the same order of magnitude. In such cases, energy exchange between the fluid and structure can readily occur.

Contrary to what one might intuitively expect, we have found that methodologies which account for fluid-structure interaction effects in piping dynamical analysis not only provide greater accuracy, but can also provide greater convenience to the analyst. The reason for this is that the two step waterhammer-structural approach involves two analyses rather than one, and necessitates what is usually a cumbersome transfer of results from the waterhammer analysis to the structural model. Considering this, and the importance of the fluid-structure interactive effects demonstrated by the authors, perhaps those in the business of analyzing the effects of fluid dynamics on piping system dynamics (and vice-versa) would do well to consider incorporating fluid-structure interaction effects into their analytical models.

John S. Walker.[3] Elbows are the sites of strong fluid-structure interaction for fluid transients. In treating solitary or periodic transients, one can ask what part of the original wave is transmitted through the elbow and what part is reflected back toward the source. However, the interaction is more complex than simple acoustic transmission and reflection. The compressive energy in the fluid transient can be temporarily transferred to the kinetic energy and strain energy of the elbow and adjacent lengths of pipe. When the structure returns the energy to the fluid, it may be more diffused or more concentrated, depending on the dynamic matching between the fluid and structure. All of these points are well illustrated by the analytical and experimental results presented in this paper which is indeed a valuable contribution to the literature.

This paper considers a single elbow with four different levels of external constraints. The constraints can also be inherent in the elbow. An elbow with a small radius of curvature and a thick wall is inherently constrained for fluid-structure interactions because of its small strains for a given fluid pressure and because of its inertia. An elbow with a large radius of curvature and a wall thickness comparable to that of the pipe is inherently unconstrained. The effects of elbow radius of curvature and wall thickness on solitary and periodic fluid transients were investigated in a series of experiments carried out approximately ten years ago.[4] These experimental results were compared with analytical results generated by the method of characteristics in a manner similar to that used in the present paper. The present paper solves four equations and treats the elbow as a single element. The previous analysis[5] solves eight equations for the fluid pressure, fluid axial velocity, axial tube displacement, transverse displacement of the tube centerline, rotation of the tube cross section about the diameter perpendicular to the plane of the elbow, tube bending moment resultant, tube shear resultant, and tube axial force resultant. The equations were integrated along the characteristics through the elbow with a number of points in the elbow itself. The previous research was concerned primarily with very short times for pressure increases in solitary transients and with very short periods for periodic transients, namely pressure rise times and periods comparable to the time for a sound wave to travel one pipe diameter. For longer times and longer periods, a number of the extra four variables considered in the previous research are not important.

Authors' Closure

We are grateful for the discussions by Drs. Walker and Schwirian, both of whom have made major contributions to

[1] By D. C. Wiggert, R. S. Ortwell, and F. J. Hatfield, published in the September, 1985 issue of the JOURNAL OF FLUIDS ENGINEERING, Vol. 107, pp. 402-406.

[2] Westinghouse MNC 310, Pittsburgh, Pa. 15230.

[3] Department of Theoretical and Applied Mechanics, University of Illinois, Urbana, IL 61801.

[4] Valentin, R. A., Phillips, J. W., and Walker, J. S., "Reflection and Transmission of Fluid Transients at an Elbow," *Proceedings of the Fifth International Conference on Structural Mechanics in Reactor Technology*, 1979.

[5] Phillips, J. W., and Walker, J. S., "A Study of Classical Waterhammer Theory," T.&A.M. Report No. 411, Department of Theoretical and Applied Mechanics, University of Illinois at Urbana-Champaign, 1976.

the understanding of dynamic behavior of liquid-filled pipe systems.

Indeed, our work uses an analysis of bend response formulated by Walker and Phillips [5]. Following a suggestion in that paper, we simplified their general model for our specific application. Whatever success we may have had in developing an analytical model that predicts observed response of the experimental piping is directly attributable to the accuracy of the Walker and Phillips bend analysis.

As engineering researchers, we prefer to believe that natural phenomena may be described by relatively simple laws. Therefore, we are encouraged by Dr. Schwirian's observation that the more comprehensive mathematical model simplifies the analysis.